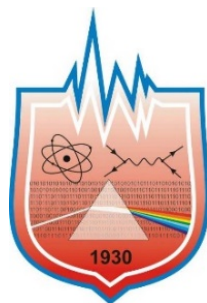


INTER-ACADEMIA 2021



Gomel
2021

Francisk Skorina Gomel State University

INTER-ACADEMIA 2021

The 19th International Conference on Global Research and Education

(Gomel, Belarus, 20 – 22 October, 2021)

Collection of abstracts

Scientific electronic publication

Gomel
F. Skorina Gomel State University
2021

ISBN 978-985-577-797-8

© Francisk Skorina
Gomel State University

UDC 378.4

Inter-Academia 2021 [Electronic resource] : The 19th International Conference on Global Research and Education (Gomel, Belarus, 20 – 22 October, 2021) : collection of abstracts / Francisk Skorina Gomel State University ; editorial board : S. A. Khakhomov (chief editor) [et al.]. – Electronic text data (11 MB). – Gomel : F. Skorina Gomel State University, 2021. – System requirements: IE from version 11 and higher or any current browser, access speed from 56 kbit. – Access mode: <http://conference.gsu.by>. – The title from the screen.

The collection contains abstracts from the reports of The 19th International Conference on Global Research and Education “Inter-Academia 2021”, in the following areas: bio- and environmental engineering; electric and electronic engineering; intelligent and soft computing techniques; internet based education, distance learning; manufacturing technology; material science and technology, smart materials; measurement, identification, and control; metamaterials and metasurfaces; modeling and diagnostics; multimedia and E-learning techniques and materials; nanotechnology and nanometrology; photonics; plasma physics.

It is addressed to researchers, postgraduates, undergraduates, students.

The materials are published in accordance with the original prepared by the editorial board, with the participation of the publishing house.

Editorial Board:

S. A. Khakhomov (chief editor),
I. V. Semchenko (deputy chief editor), O. M. Demidenko, D. L. Kovalenko,
A. A. Sereda, T. V. Lozovskaya.

F. Skorina Gomel State University
246028, Gomel, 104 Sovetskaya str.
tel. (232) 50-49-03, 50-38-59
<http://www.gsu.by>

© Francisk Skorina
Gomel State University, 2021

GENERAL CHAIRS

Igor V. Semchenko, Oleg M. Demidenko, Alexander V. Rogachev

HONORARY COMMITTEE

Host Rector

Sergei A. Khakhomov, Francisk Skorina Gomel State University,
Belarus

and Rectors

- **Kazuyuki Hizume**, Shizuoka University
- **Marek Stevcek**, Comenius University, Slovakia
- **János Józsa**, Budapest University of Technology and Economics,
Hungary
- **Krzysztof Zaremba**, Warsaw University of Technology, Poland
- **Lambert T. Koch**, Wuppertal University, Germany
- **Tudorel Toader**, Alexandru Ioan Cuza University, Romania
- **Leonids Ribickis**, Riga Technical University, Latvia
- **Martin Bares**, Masaryk University, Czech Republic
- **Anastas Gerdjikov**, Sofia University, Bulgaria
- **Levente Kovacs**, Óbuda University, Hungary
- **Volodymyr A. Buhrov**, Taras Shevchenko National University of
Kyiv, Ukraine
- **Andrey P. Shevchik**, St. Petersburg State Technological Institute,
Russia
- **Eugenijus Valatka**, Kaunas University of Technology, Lithuania
- **Igor Sarov**, Moldova State University, Moldova

INTERNATIONAL ADVISORY CONFERENCE COMMITTEE

- **Annamária R. Várkonyi-Kóczy** (Óbuda University, Hungary)
- **Arturs Medvids** (Riga Technical University, Latvia)
- **Gheorghe Popa** (Prof. Emeritus, Alexandru Ioan Cuza University,
Romania)
- **Evgenia Benova** (Sofia University, Bulgaria)
- **Dumitru Luca** (Prof. Emeritus, Alexandru Ioan Cuza University,
Romania)
- **Hidenori Mimura** (Shizuoka University, Japan)
- **Hiroshi Mizuta** (University of Southampton, England)
- **Kenji Murakami** (Shizuoka University, Japan)
- **Leonid Poperenko** (Taras Shevchenko National University of Kyiv,
Ukraine)

- **Lucel Sirghi** (Alexandru Ioan Cuza University, Romania)
- **Masaaki Nagatsu** (Prof. Emeritus, Shizuoka University, Japan)
- **Masashi Kando** (Prof. Emeritus, Shizuoka University, Japan)
- **Michiharu Tabe** (Prof. Emeritus, Shizuoka University, Japan)
- **Kazuhiko Hara** (Shizuoka University, Japan)
- **Nobuyuki Araki** (Prof. Emeritus, Shizuoka University, Japan)
- **Noriko Matsuda** (Shizuoka University, Japan)
- **Nicoleta Dumitrascu** (Alexandru Ioan Cuza University, Romania)
- **Ryszard Jablonski** (Warsaw University of Technology, Poland)
- **Jan Maciej Kościelny** (Warsaw University of Technology, Poland)
- **Małgorzata Kujawińska** (Warsaw University of Technology, Poland)
- **Sergiusz Łuczak** (Warsaw University of Technology, Poland)
- **Roman Szewczyk** (Warsaw University of Technology, Poland)
- **Adam Woźniak** (Warsaw University of Technology, Poland)
- **Sergei Khakhomov** (Gomel State University, Belarus)
- **Stefan Matejčík** (Comenius University, Slovakia)
- **Valdis Kokars** (Riga Technical University, Latvia)
- **Giedrius Laukaitis** (Kaunas University of Technology, Lithuania)
- **Maxim M. Sychov** (Saint Petersburg State Institute of Technology, Russia)
- **Volodymyr Gnatyuk** (National Academy of Sciences of Ukraine)
- **Yoshimasa Kawata** (Shizuoka University, Japan)
- **Jun Kondoh** (Shizuoka University, Japan)

LOCAL ORGANIZING COMMITTEE

- **Dmitry Kovalenko**, Francisk Skorina Gomel State University, Belarus
- **Andrey Samafalov**, Francisk Skorina Gomel State University, Belarus
- **Andrey Sereda**, Francisk Skorina Gomel State University, Belarus
- **Oksana Deruzhkova**, Francisk Skorina Gomel State University, Belarus
- **Tatyana Lozovskaya**, Francisk Skorina Gomel State University, Belarus

CONFERENCE TOPICS

1. Bio- and environmental engineering;
2. Electric and Electronic engineering;
3. Intelligent and soft computing techniques;
4. Internet based education, distance learning;

5. Manufacturing technology;
6. Material science and technology, smart materials;
7. Measurement, identification, and control;
8. Metamaterials and metasurfaces;
9. Modeling and diagnostics;
10. Multimedia and E-learning techniques and materials;
11. Nanotechnology and nanometrology;
12. Photonics;
13. Plasma physics;
14. iA Young Researcher;
15. Precision engineering;
16. Robotics;
17. Signal and Image processing.

Content

To go to the text of the materials, click on the hyperlink
on the corresponding report

Unit 1 “Bio- and environmental engineering”

Abdilalizadeh L., Ardabili S., Mosavi A., Várkonyi Kóczy A. R. Investigating urban sustainability by emphasizing on the approaches for reducing fuel consumption using intelligent transportation system.....	15
Abdilalizadeh L., Ardabili S., Mosavi A., Várkonyi Kóczy A. R. Environmental risk management by achieving sustainable development goals in architecture and urban engineering.....	15
Dovydenko E. M., Avdeeva E. V., Laznev K. V., Petkevich A. V., Rogachev A. A. Application of additive technology to create universal carriers of cellular structures.....	16
Fedosenko-Becker T. N., Becker M., Berger M. Comparison and selection of the greenhouse gas accounting method for a model region in Germany.....	18
Hashimoto K., Sakata H., Tripathi S. R. In vivo measurement of dielectric properties of human skin using attenuated total reflection terahertz time domain spectroscopy.....	20
Les A., Molokanov A., Shvidkiy S., Creanga D. The proton beam influence on the sensitivity of wheat plantlets to AgNP pollution-preliminary results.....	22
Motrescu I., Ciolan M. A., Calistru A. E., Jitareanu G., Miron L. D. Evaluation of heavy metal contamination in Mytilus sp. shells.....	24
Zelenska K., Zelenska T., Vynohradova-Anik O., Aoki T. Analysis of color coordinates in dried blood spots under aging for forensic medical applications.....	26

Unit 2 “Electric and Electronic engineering”

Khajishvili M. R., Gomidze N. Kh., Shainidze J. J. 3D fluorescence spectroscopy of liquid media via internal reference method.....	29
Mitsuyoshi R., Kondoh J. Transportation and measurement of droplet using surface acoustic wave for digital microfluidic system application.....	30
Moraru D., Tamura Y., Iwatsuki Y., Yamaguchi K. Probing of deep states by band-to-band tunneling in nanoscale silicon-on-insulator Esaki diodes.....	33
Nakagawa H., Yamada R., Hashimoto M., Yamaguchi T., Onuma T., Honda T., Nakano T., Aoki T. Evaluation of radiation detection characteristics by α -Ga ₂ O ₃	35
Pandy C., Yamaguchi K., Neo Y., Mimura H., Tabe M., Moraru D. Theoretical study of the impact of a donor-acceptor pair on tunneling current in Si nanodiodes.....	37
Rakos B. A Fluorescent protein-based AND gate for photon-coupled protein logic.....	39
Shubbar M., Rakos B. An angle-sensitive, nickel bolometer-based, adaptive infrared pixel antenna.....	41
Yamaguchi K., Tabe M., Moraru D. First-principles study of bandgap electronic states under electric field in silicon nanowires with discrete dopants.....	43

Unit 3 “Intelligent and soft computing techniques”

Kase H., Takagi K., Tabata K., Aoki T. Applications for effective representation of imaging with X-ray CT.....	46
Košťál I. A parallelization of instance methods of a .NET application that search for required structured data stored in a skip list.....	47
Tabrizchi H., Razmara J., Mosavi A., Várkonyi-Kóczy A. R. Deep learning applications for COVID-19: a brief review.....	49
Tusor B., Tóth T. J., Várkonyi-Kóczy A. R. Intelligent pantry: a low-cost smart storage manager for food spoilage prevention.....	49

Unit 4 “Internet based education, distance learning”

Sereda A. A., Shalupaev S. V., Nikitjuk Yu. V. The use of design automation tools in training young specialists in radio electronics..... 52

Unit 5 “Manufacturing technology”

Azhagar A., Sakai K., Shizuka H., Hayakawa K. Effects of process parameters on the dissimilar friction stir welded joints between aluminum alloy and polycarbonate..... 54

Unit 6 “Material science and technology, smart materials”

Athithya S., Ikeda H., Navaneethan M., Harish S., Archana J. Investigation on influence of Cu doping on thermoelectric performance of tin-selenide-based nanostructures..... 57

Balabanov S. V., Makogon A. I., Koshevaya K. S., Sychev M. M. Isotropy mechanical properties products with geometry triple periodic minimal surfaces (TPMS)..... 59

Bekarevich R., Pihosh Y., Tanaka Y., Nishikawa K., Matsushita Y., Hiroto T. Mechanism of double-step conversion reaction in nanostructured tungsten trioxide anode for Li-ion batteries. 61

Dolgin A. S., Bogdanov S. P., Leibgam V. The role of the dispersed composition of the diamond matrix in the preparation of a composite by infiltration with molten silicon..... 63

Dorokhina A. M., Kominami H., Bakhmetyev V. V., Aoki T., Morii H. Research of morphology and luminescence of particles based on yttrium fluorides for medical usage..... 64

Filippov V. V., Kashko I. A., Tuchkovskii A. K., Kovalenko D. L., Vaskevich V. V., Gaishun V. E. NiO and NiO:Al films for solar cells: a compromise between electrical conductivity and transparency..... 67

Hatescu I., Borcia C., Borcia G. Behavior of electron-beam irradiated polyethylene and polystyrene..... 69

Kalaiarasan K., Sidharth D., Alagar Nedunchezian A. S., Rajasekaran P., Shimomura M., Arivanandhan M., Ikeda H., Hayakawa Y., Jayavel R. Effect of Ag substitution on enhancing the thermoelectric performance of nanostructured SnSe.....	71
Keskinova M. V., Sychov M. M., Hara K. One-step microwave synthesis of Eu ²⁺ -doped silicate and chlorinesilicate phosphors mixture for application in light sources.....	73
Kovalenko D. L., Gaishun V. E., Vaskevich V. V., Aleshkevich N. A., Kosenok Ya. A., Tyulenкова O. I., Ignatenko O. V. Development of sapphire-like glass by sol-gel technology.....	75
Kovalenko D. L., Dobromir M., Vaskevich V. V., Semchenko A. V., Luca D., Sidski V. V., Tyulenкова O. I. Sol-gel synthesis of TiO ₂ nanotubes based on ZnO nanorods, for use in solar cells.....	77
Kulyk O. P., Tkachenko V. I., Andrieieva O. L., Podshyvalova O. V., Gnatyuk V. A., Aoki T. Investigation of the convection effect on the inclusion motion in thermally stressed crystals.....	79
Makogon A. I., Balabanov S. V., Koshevaya K. S., Sychev M. M. Impact of modeling method on geometry and mechanical properties of samples with TPMS structure.....	81
Moskvichyov M. I., Vaskevich V. V., Semchenko A. V., Sidski V. V., Kravets V. A., Tkachenko V. V., Zalessky V. B. Synthesis of scintillating glass materials containing yttrium niobate crystallites activated with terbium ions.....	83
Piliptsou D. G., Pobiya A. S., Rogachev A. V. Structure and optical properties of a-C coatings doped with nitrogen and silicon....	85
Piliptsou D. G., Rogachev A. V., Jiang X.-H., Fedosenko N. N., Kulesh E. A. Structure and properties of metal-carbon a-C coatings alloyed with Ti, Zr and Al with a high concentration.....	87
Semchenko A. V., Sidski V. V., Tyulenкова O. I., Gaishun V. E., Kovalenko D. L., Ayvazyan G. Y., Hakhoyan L. A. Characteristics of nanocomposite sol-gel films on black silicon surface.....	89
Shalini V., Harish S., Ikeda H., Archana J., Navaneethan M. Enhancing the seebeck coefficient of Zn-doped MoS ₂ grown over carbon fabrics via band engineering.....	91
Shumskaya A. E., Novik H. A., Zhidko T. V., Filippovich L. V., Ignatovich J. V., Rogachev A. A. Polyaniline-based food quality markers.....	93

Sidski V. V., Semchenko A. V., Danilchenko K. D., Tyulenkova O. I. AFM topography of ZnO _x :MgO nanocomposite sol-gel films on the surface of silicon.....	96
Sychov M. M. Digital materials science.....	98
Uesugi K., Ishiguro K., Oishi R., Matsui M. The effect of SiO ₂ content rate in simulated lunar regolith on ablation plume temperature and the feasibility assessment of Al ₂ O ₃ reduction.....	99
Yiming Liu, Kontsevaya I. I., Rogachev A. A., Xiaohong Jiang, Yarmolenko M. A. Vacuum coatings based on miramistin and their biological properties.....	102

Unit 7 “Measurement, identification, and control”

Armetta F., Ciaramitaro V., Chirco G., Lo Re G., Midiri M., Hreniak D., Caponetti E., Saladino M. L. Discovering the <i>Sicilian byzantine Icons</i> through a combination of imaging and spectroscopic techniques.....	105
--	-----

Unit 8 “Metamaterials and metasurfaces”

Faniayeu I. A., Fanyaev I. A., Asadchy V. S. Optical chirality enhancement with dielectric metasurfaces.....	108
Semchenko I., Samofalov A., Kravchenko A., Khakhomov S. Production and experimental study of a weakly reflecting absorbing metamaterial based on planar spirals in the microwave range.....	109
Slepiankou D., Balmakou A., Khakhomov S., Semchenko I. Modeling of a three-peak absorber in the 9 – 13 GHz range.....	111

Unit 9 “Modeling and diagnostics”

Arsentev M. Yu., Sysoev E. I., Makogon A. I. Investigation of acoustic wave propagation in complex geometry.....	115
Emelyanov V. A., Shershnev E. B., Nikitjuk Y. V., Sokolov S. I. Optimization of quartz glass laser polishing parameters using the computational experiment planning method.....	117

Kobayashi R., Sakai H., Matsui M. Investigation of the effect of observation window on the sensitivity enhancement in the multi-pass cell outside the expansion wave tube chamber.....	119
Nikitjuk Y. V., Serdyukov A. N., Aushev I. Y. Simulation of laser splitting of bilayer structures made of silicon wafers and glass substrates.....	121
Nikitjuk Y. V., Serdyukov A. N., Prokhorenko V. A., Aushev I. Y. The use of artificial neural networks for determining the parameters of laser processing of fused quartz.....	123
Nikitjuk Y. V., Bayevich G. A., Myshkovets V. N., Maximenko A. V., Aushev I. Y. Characterization of laser welding of steel 30XГCH2A by combining artificial neural networks and finite element method.....	125
Rituraj R., Várkonyi-Kóczy A. R. Modeling and optimization of a microgrid for a midrise apartment and industry.....	127
Timoshenko M. V., Balabanov S. V., Sychev M. M., Nikiforov D. I. Development of material for 3D printing based on thermoplastic elastomer.....	129

Unit 10 “Multimedia and E-learning techniques and materials”

Aksionova N. Project architecture and data model for AR application development.....	132
Ota S. R. Online lesson “Academic English I” for students.....	134

Unit 11 “Nanotechnology and nanometrology”

Dobromir M., Konrad-Soare C. T., Apetrei R. P., Airinei A., Semchenko A. V., Kovalenko D. L., Luca D. Two-steps formation of ZnO-loaded TiO ₂ nanotube array films with enhanced photocatalytic performance.....	136
Fesenko O., Tsebriienko T., Yaremkevych A., Sidski V. V., Semchenko A. V., Gaishun V. E., Kovalenko D. L., Khakhomov S. A. Raman investigation of multiferroic BiFeO ₃ and Bi _{1-x} Sm _x FeO ₃ materials synthesized by the sol-gel method.....	138

Firmansyah T., Wibisono G., Rahardjo E. T., Kondoh J. Localized surface plasmon resonance liquid sensors based on array gold nanoparticles fabricated on 36XY-LiTaO ₃ substrate.....	140
Jinxing Cao, Xiaohong Jiang, Rogachev A. V. Studies of magnesium – hydroxyapatite micro/nano film for drug sustained release.....	142
Konrad-Soare C. T., Dobromir M., Stoian G., Luca M., Ciobanu A., Luca D. Photocatalytic activity and wettability of TiO ₂ nanotube arrays coupled with WO ₃ and ZnO.....	144
Rudnikov A. S., Pobiya A. S. Heat treatment effect on the mechanical properties of nanostructured carbon coatings.....	146
Semchenko A. V., Sidski V. V., Tyulenкова O. I., Shepelina A. Yu., Kiselev D. A., Pilipenko V. A. Piezoelectric properties of SrBi ₂ (Ta _x Nb _{1-x}) ₂ O ₉ thin films synthesized by the sol-gel method.....	148
Sirghi L., Besleaga A. Atomic force spectroscopy experiments with amino-functionalized silicon AFM tips and samples.....	150
Tifui G., Teodoroff-Onesim S., Sirghi L. Atomic force microscopy indentation of supported lipid bilayers.....	152

Unit 12 “Photonics”

Kawauchi T., Ohtake G., Koyama C., Uchida H., Takeya K., Tripathi S. R. High power terahertz wave emission using DAST crystal.....	156
---	-----

Unit 13 “Plasma physics”

Bîrleanu E., Mihaila I., Topala I., Borcia G. Oxidation and stability of polymers treated by atmospheric-pressure plasma.....	159
Costin C. Velocity distribution functions at plasma boundary.....	161
Yahaya A. G, Okuyama T., Kristof J., Blajan M. G., Shimizu K. The physicochemical/electrical properties of plasma activated medium by dielectric barrier discharge microplasma.....	163

Unit 14 “iA Young Researcher”

Buzhan A. V., Kapshai V. N. Green functions of relativistic quasipotential equations for complex values of energy.....	166
Kapshai V. N., Grischechkina A. A. Partial two-particle equations in the relativistic configurational representation for scattering p-states in the case of a superposition of two δ -function potentials.....	166
Kapshai V. N., Shamyna A. A., Talkachov A. I. Analysis of the spatial distribution of the second-harmonic radiation generated in a thin surface layer of a spheroidal dielectric particle.....	168
Kapshai V. N., Talkachov A. I., Shamyna A. A. Maxima of the power density of the second-harmonic generation from a linear structure of long cylindrical dielectric particles.....	171
Miyake T., Nakagawa H., Masuzawa T., Yamada T., Nakano T., Takagi K., Aoki T., Mimura H. Diamond radiation detector with built-in boron-doped neutron converter layer.....	173
Paulenko A. V., Grischechkin Yu. A. Numerical solution of the two-dimensional Logunov-Tavkhelidze equation with the sum of two separable potentials in the momentum representation.....	175
Toyoda K., Takagi K., Kase H., Takagi T., Tabata K., Terao T., Morii H., Koike A., Aoki T., Nogami M., Hitomi K. Spatial resolution of X-ray Imaging using 80 μ m pitch TlBr Detector.....	178

Unit 1 “Bio- and environmental engineering”

Investigating urban sustainability by emphasizing on the approaches for reducing fuel consumption using intelligent transportation system

L. ABDILALIZADEH¹, S. ARDABILI²,
A. MOSAVI³, A. R. VÁRKONYI KÓCZY³

¹ Master of Art (MA) urban Planning, Urban development department, faculty of art and architecture, Islamic Azad University Science and Research Branch, Tehran, Iran.

² Department of Biosystem Engineering, University of Mohaghegh Ardabili, Ardabil, Iran

³ John von Neumann Faculty of Informatics, Obuda University, 1034 Budapest, Hungary

Abstract

In the current situation, the city is regarded as a suitable place, and urbanization is the most desirable way of life. This tendency to urbanization has accelerated urban population growth, disproportionate urban expansion, and created environmental problems including increased pollution from transportation reduced fuel consumption, and, subsequently, reduced emissions of the most serious threats. Urban sustainable development, as a common way to reduce these adverse effects, can be effective by improving and enhancing the economic, social, and environmental conditions of the city. This can be achieved through multidisciplinary approaches by taking into account various aspects of ecological development such as safety, health, industrial metabolism, landscape, and awareness. Along with this important and necessary approach to reduce fuel consumption in the transportation field, which is the main objective of the present study, various approaches and methods have been proposed by researchers. But with the advent of ICT and intelligent transportation systems, these techniques and approaches have taken a new direction. Nowadays, solutions to reduce fuel consumption by using intelligent transportation systems have become one of the most popular areas of science. This study aims to evaluate the dimensions of urban ecology to attain the quality of a sustainable urban environment and provide suggestions for reducing the harmful effects on the environment by the transportation system.

Environmental risk management by achieving sustainable development goals in architecture and urban engineering

L. ABDILALIZADEH¹, S. ARDABILI²,
A. MOSAVI³, A. R. VÁRKONYI KÓCZY³

¹ Master of Art (MA) urban Planning, Urban development department, faculty of art and architecture, Islamic Azad University Science and Research Branch, Tehran, Iran.

² Department of Biosystem Engineering, University of Mohaghegh Ardabili, Ardabil, Iran

³ John von Neumann Faculty of Informatics, Obuda University, 1034 Budapest, Hungary

Abstract

In today's world, the increasing progress of technology and urban construction has increased the variety of unknown hazards to the environment. This has led organizations to find a way to reduce these risks. In this regard, environmental risk assessment and sustainable development in architecture and urban engineering can be a good tool for achieving sustainable development goals. Risk Management is a new branch of management science

that found its new place in a variety of trends, including finance and capital, investment, trade, insurance, industrial, civil, military and safety projects, health and environmental management has found its place. Therefore, the study aims to review environmental risk management by introducing the performance of William Fine, and PHA approaches in Environmental Risk Assessment and to achieve Sustainable development goals in architecture and urban engineering. It helps us to promote sustainable development in harmony with nature while reducing the level of environmental risks.

Application of additive technology to create universal carriers of cellular structures

E. M. DOVYDENKO, E. V. AVDEEVA, K. V. LAZNEV,
A. V. PETKEVICH, A. A. ROGACHEV

*State Scientific Institution «Institute of Chemistry of New Materials of the NAS of Belarus»
Fr. Skoriny st., 36, 220141, Minsk, Republic of Belarus, avdeeva.katerina86@mail.ru*

Abstract

In order to obtain biocompatible carriers with mechanical properties close to living tissues, 3D printing was performed with sodium alginate and chitosan hydrogels on a modified 3D printer based on the Wanhao Duplicator 4S (China) by installing a special extrusion head – a syringe extruder. The optimal compositions of sodium alginate and chitosan hydrogels for printing in a "supporting" agar and gelatin gel for fixing print objects have been determined.

Optimal speeds of movement of the extruder-syringe for 3D printing with sodium alginate hydrogel into agar "supporting" gel 9 – 11 mm/s, for sodium alginate into gelatinous "supporting" gel – 2 mm/s, for chitosan into "supporting" gel with the addition of $(\text{NH}_4)_2\text{HPO}_4$ – 6 – 8 mm/s.

Introduction

Sodium alginate and chitosan, which are biocompatible materials, have high elasticity and strength [1–4] and make it possible to form structures for growing living cells on the surface and in the volume of a printed sample, seem to be the most interesting as the main components for creating universal carriers of cellular structures. The technology of layer-by-layer construction of a print object inevitably imposes limitations on the size of the object's elements and its shape. When selecting 3D printing parameters, an important problem remains to obtain a product that will accurately repeat an adjusted computer model. Technological modes of operation of the extrusion of the 3D printer have a great influence on the accuracy of the reproduction of printing products [3].

The work is devoted to obtaining biocompatible carriers with mechanical properties similar to living tissues by extrusion 3D printing. Test printing was carried out with biocompatible hydrogels of sodium alginate and chitosan in order to determine the optimal concentrations of components and printing parameters.

Materials and methods

Sodium alginate solutions in distilled water and chitosan solutions in acetic acid 0.5% v were used as extruded material. The printing process from sodium alginate was carried out in a volume of "supporting" gel from agar or gelatin with CaCl_2 or $(\text{NH}_4)_2\text{HPO}_4$ in distilled water (Fig. 1).

For printing, an upgraded 3D printer was used, created on the basis of the Wanhao Duplicator 4S (PRC) by installing a special extrusion head - a syringe extruder. The original models were built in the form of a Menger sponge (a fractal cube with an edge length of 0.3 cm and hole sizes of 0.1×0.1 ; 0.3×0.3 and 0.8×0.8 cm²) using the KOMPAS program. 3D. Printing parameters were set using the KISSlicer program: layer height 0.5 mm, filling density 100%,

hydrogel temperature and table temperature 25 °C, printing speed 2 – 11 mm/s, syringe needle diameter 0.3 mm.

Printing was carried out for the following compositions: sodium alginate (1 – 2 wt.% In an aqueous solution), agar (0.3 – 0.4 wt.% In 0.15 wt.% In a CaCl₂ solution), gelatin (1.0 – 2.0 wt.% in CaCl₂ solution), CaCl₂ (0.15 wt%); chitosan (1.5 – 3 wt.% in 0.5% acetic acid solution) in a "supporting" gel (NH₄)₂HPO₄ (20 g/l).

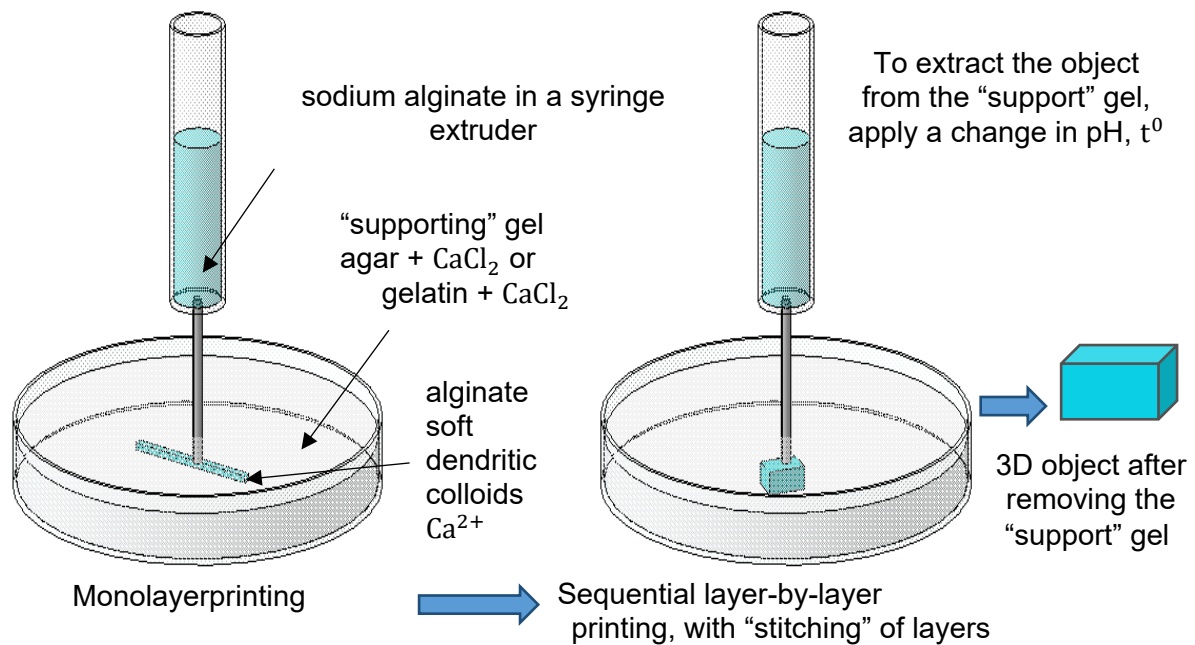


Fig. 1. Diagram of the process of obtaining objects from a hydrogel by 3D printing

Results and Discussions

Print quality is determined by the stability and fidelity of the printed model. The accuracy of the model and the homogeneity of the structure of the print object are greatly influenced by the speed of extrusion of the material and the movement of the extruder-syringe during printing. Test printing with biocompatible sodium alginate and chitosan hydrogels at optimal concentrations of components that allow the hydrogels to create stable crosslinking was carried out under various printing parameters. Using the modified KISSlicer software for a 3D printer, various speeds of movements of the extruder-syringe during printing were adjusted: the outer perimeter of the model, inner filling, and material supply.

The speed of material feeding during the formation of the inner filling of the model, as well as when printing the outer perimeter, affects the reliability of fixing the material inside the volume of the "supporting" suspension. The best reproduction of the model was observed with the following print parameters (table 1).

Table 1. Optimal printing modes for hydrogels

Extrusive hydrogel composition	Maintenance gel composition	Print speed of internal filling of the model, mm / s	Print speed of the outer perimeter of the model, mm / s	Hydrogel extrusion rate, ml / sec
sodium alginate	agar + CaCl ₂	9 – 11	9 – 11	1.3
sodium alginate	gelatin + CaCl ₂	2	2	1.3
chitosan	(NH ₄) ₂ HPO ₄	6 – 8	6 – 8	1.3

Conclusion

The possibility of using a water-based sodium alginate hydrogel and chitosan in an aqueous solution of acetic acid for 3D printing is presented.

Optimal speeds of movement of the extruder-syringe based on Wanhao Duplicator 4S have been determined for 3D printing with sodium alginate hydrogel in agar “supporting” gel 9 – 11 mm/s, for sodium alginate in gelatinous “supporting” gel – 2 mm/s, for chitosan in “supporting” gel with the addition of $(\text{NH}_4)_2\text{HPO}_4$ – 6 – 8 mm/s.

The presented technological approaches can be used for 3D printing of volumetric objects for biomedical applications.

References

- [1] Preparation of macroporous alginate-based aerogels for biomedical applications / S. Quraishi et al. // J. Supercrit. Fluids. 2015.
- [2] A denatured collagen microfiber scaffold seeded with human fibroblasts and keratinocytes for skin grafting / M. Kempf et al. // J. Biomaterials. 2011. Vol. 32. (21). P. 4782 – 4792.
- [3] Dovydenko, E. M. Optimization of 3D printing parameters with sodium alginate hydrogel / E. M. Dovydenko, V. E. Agabekov, S. A. Chizhik // Ves. Nat. acad. Navuk Belarus. Ser. fiz.-tekhn. navuk. – 2019. – T. 64, No. 1. – P. 7 – 13. <https://doi.org/10.29235/1561-8358-2019-64-1-7-13>.
- [4] A chitosan thermogel for delivery of ropivacaine in regional musculoskeletal anesthesia / Patricia L. Foley et al. // J. Biomaterials. 2013. – Vol. 34. P. 2539 – 2546.

Comparison and selection of the greenhouse gas accounting method for a model region in Germany

T. N. FEDOSENKO-BECKER¹, M. BECKER², M. BERGER¹

¹ *Institute for the Transformation of the Energy System (ITE), West Coast University of Applied Sciences, Markt 18, 25746 Heide, Germany*

² *Eco.income engineering GmbH, Billwerder Neuer Deich 12, 20539 Hamburg, Germany*

Abstract

Following the sustainable development trends, Germany is moving towards an energy transformation. This complex process requires serious planning and an interdisciplinary approach. Within the framework of the German project “WESTKUESTE100” the roadmaps to complete CO₂-neutrality in a model region will be offered. The first step to creating realistic scenarios is to analyze the existing accounting methods of greenhouse gas emissions and to adapt the chosen methods for specific purposes. This work describes an approach to the selection and adaptation of a climate gas emission accounting method for a model region in order to create scenarios for the energy transformation.

Introduction

The problem of climate change is getting more serious year by year and there is still no clear defined realistic solution. One of the most iconic visualizations of the climate change in the world is the Mauna Loa continuous record of carbon dioxide concentration [1] (see Fig. 1). The complexity of the problem is justified by its multiple dimensions, therefore, it is only possible to slow down the climate change by an interdisciplinary scientific approach: technology, society and politics.

The European Union (EU) is going to take on a pioneering role with regard to the global existential challenges and to become the first CO₂-neutral continent by 2050. The “European Green Deal” – a new growth strategy, presented by the EU Commission in December 2019, should help the EU to achieve a modern, resource-efficient and competitive economy [2].

Germany has recognized that its long-term competitiveness and future viability can only be secured through economic activities geared towards innovation, sustainability, environmental protection, and social needs. Therefore, it is essential to transform the existing energy systems fundamentally.

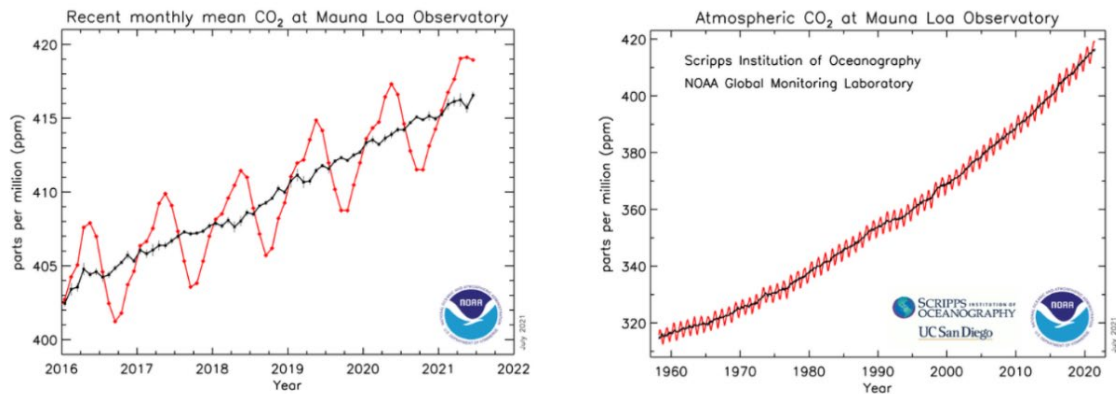


Fig. 1. Monthly mean carbon dioxide measured at Mauna Loa Observatory. The red lines represent the monthly mean values, centered on the middle of each month. The black lines represent the monthly mean values after correction for the average seasonal cycle [1]

Discussion and Methodology

The German federal government, with its energy and climate concepts, has given a significant impetus in the direction of energy transformation and, among other things, has set the central goals of reducing greenhouse gas emissions by at least 80% by 2050 compared to 1990 and providing 60% of gross final energy consumption from the renewable energies by 2050 [3], [4]. According to the presentation of the problem in the description of the project “WESTKUESTE100”, these goals can only be achieved in case of successful promotion of the energy system decarbonization across all sectors and in particular addressing the associated issues of a temporally, regionally, and materially independent use of renewable energies.

The new German climate protection targets open up a number of options of combining non-fossil and low-fossil technologies and process management. A big step to the sustainability in heating, industrial processes, as well as construction and transport sectors can be made by modelling a regional economy on an industrial scale [5]. Energy efficiency potentials and their implementation play a major role here. For this, among many other things, several realistic scenarios, which consider how a fluctuating electricity supply can be used economically for CO₂-reduced production, will be developed. The development of roadmaps up to complete CO₂-neutrality in a model region is one of the tasks of the German project “WESTKUESTE100”.

The development of realistic scenarios requires the methodological basics of accounting for greenhouse gas emissions. At this stage, various international and national accounting tools and regulations have to be examined and compared. This work examined the accounting methods suitable for a chosen model region (Schleswig-Holstein in Germany) in detail. The main focus is on BSKO (accounting system for municipalities), GPC (Green Gas Protocol), Covenant of Mayors for Climate & Energy, and on the interaction between the method and the roadmap derived.

Conclusions

This investigation shows that the accounting methods follow different approaches when considering individual sectors, as well as when applying the polluter-pays principle or territorial principle within the individual sectors. A uniform and thus comparable accounting methodology

is, of course, indispensable for creating applicable scenarios. A problem here is the intention to achieve the most complete and precise coverage of the respective sectors for the development of meaningful scenarios on the one hand, as well as the availability of the data sources and the required data quality for this purpose on the other hand. A review of the data shows that the availability is not guaranteed, especially for the sectors of industry-related emissions, as well as agriculture and waste. For other sectors such as final energy-based stationary emissions, data are generally available, but the quality of the data is limited. This can impair the informative value of the accounting and thus the meaningfulness of the scenarios designed on the basis of this accounting. For this reason, a uniform method for determining the data quality of the accounting has been established.

References

- [1] Global Monitoring Laboratory, Earth System Research Laboratories, "Trends in Atmospheric Carbon Dioxide". Available online at: <https://gml.noaa.gov/ccgg/trends/> checked on 09/07/2021.
- [2] Ministerium für Energiewende, Landwirtschaft, Umwelt, Natur und Digitalisierung, "Bericht der Landesregierung: Energiewende und Klimaschutz in Schleswig-Holstein - Ziele, Maßnahmen und Monitoring 2020" (Schleswig-Holsteinischer Landtag, 19. Wahlperiode, Drucksache 19/2291, 06/2020, pp. 9-10), (in German).
- [3] Bundesministerium für Wirtschaft und Energie, "Energiekonzept für eine umweltschonende, zuverlässige und bezahlbare Energieversorgung (2010)". Available online at: <https://www.bmwi.de/Redaktion/DE/Downloads/E/energiekonzept-2010.html> checked on 09/07/2021, (in German).
- [4] Bundesministerium für Umwelt, Naturschutz nukleare Sicherheit, "Der Klimaschutzplan 2050 – Die deutsche Klimaschutzlangfriststrategie". Available online at: <https://www.bmu.de/themen/klima-energie/klimaschutz/nationale-klimapolitik/klimaschutzplan-2050/#c8418> checked on 09/07/2021, (in German).
- [5] Bioenergy International, "Westküste 100 renewable hydrogen project secures EUR 30 million in funding". Available online at: <https://bioenergyinternational.com/heat-power/westkuste-100-renewable-hydrogen-project-secures-eur-30-million-in-funding> checked on 09/07/2021.

In vivo measurement of dielectric properties of human skin using attenuated total reflection terahertz time domain spectroscopy

K. HASHIMOTO¹, H. SAKATA¹, S. R. TRIPATHI^{1,2}

¹*Department of Mechanical Engineering, Shizuoka University, 3-5-1 Johoku, Hamamatsu, Shizuoka 432-8561, Japan*

²*Graduate School of Science and Technology, Shizuoka University, 3-5-1 Johoku, Hamamatsu, Shizuoka 432-8561, Japan*

Abstract

The applications of terahertz (THz) waves have increased rapidly in different fields such as homeland security, non-destructive testing and next-generation high-speed communication. With the rapid development of such applications, encounters between THz waves and humans are expected to become common. Therefore, it is important to know the terahertz properties of human skin to understand the interaction of terahertz waves with human skin. In this study, we developed attenuated total reflection terahertz time domain spectroscopy and measured the refractive index and absorption coefficient of skin in the frequency range of 200 GHz to 2 THz. This information helps understand the terahertz wave interaction with human skin and other possible biomedical applications of terahertz waves, such as the assessment of skin hydration.

Introduction

Terahertz waves refer to electromagnetic waves in the frequency range of 0.1 to 3 THz. Terahertz waves can be used in various applications such as homeland security, non-destructive testing and evaluation, biomedical engineering, and pharmaceutical science [1]. Moreover, terahertz communication systems have attracted tremendous attention owing to their ability to satisfy the increasing demand for high-speed data transfer. With the rapid development of such applications, encounters between THz waves and humans are expected to become common. Therefore, it is essential to know the terahertz properties of human skin to understand the interaction of terahertz waves with human skin [2]. Moreover, the dielectric properties of human skin are important to assess skin hydration, identify skin cancer and monitor the healing process of scars in the skin [3]. Terahertz time domain spectroscopy in transmission mode is widely used to characterize a variety of samples. However, the characterization of biological samples using terahertz time domain spectroscopy in transmission geometry is difficult due to the strong water absorption of terahertz waves. Therefore, here we developed terahertz time domain spectroscopy in attenuated total reflection geometry, and we measured the dielectric properties of human skin *in vivo*. We measured the complex refractive index of the skin in the terahertz frequency region from several human subjects.

Experiment

We developed a terahertz time domain spectroscopy system in attenuated total reflection mode (ATR THz-TDS), consisting of two photoconductive antennas as a terahertz wave emitter and a detector. Both of them are excited by femtosecond fiber laser ($\lambda=780$ nm, average power =20 mw, pulse width <100 fs, repetition rate = 50 MHz). The THz wave emitted by the photoconductive antenna was guided by parabolic mirrors and incident on the Silicon prism. The terahertz wave undergoes total internal reflection at the boundary between Silicon and air, and finally, the terahertz wave is detected by another photoconductive antenna. The frequency resolution of the system is 24 GHz, and the maximum dynamic range is 65 dB. This system can measure both refractive index (n) and absorption coefficient (α) of sample in a frequency range of 100 GHz to 2 THz. In this study, we recruited several volunteers for the measurement. All subjects gave their informed consent to the research, and the Shizuoka University Ethics committee approved the research. During the measurement, an index finger was placed on the Silicon prism for the measurement as shown in Fig.1. A reference time domain terahertz pulse was measured without placing anything on the prism, whereas the sample data was measured by placing the subject's index finger on the prism. Both reference and sample time domain pulses were transformed to frequency domain using fast Fourier transform, and corresponding intensity and phase spectra were obtained. Finally, refractive index and absorption coefficient of the sample were calculated [4]. Fig. 2 shows the average refractive index (n) and absorption coefficient (α) of skin measured from all human subjects. These results are comparable to those published in previous reports by other measurement techniques.

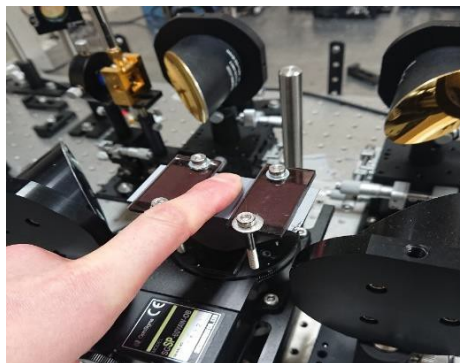


Fig. 1. Experiment system

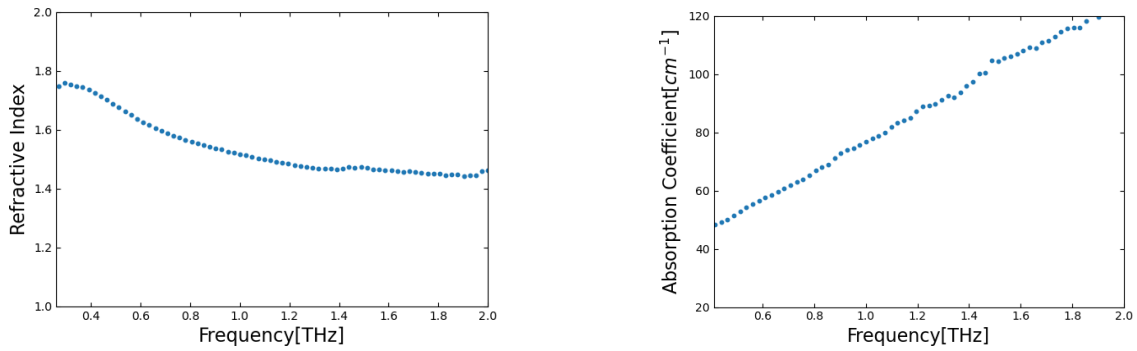


Fig. 2. Refractive index (n) and absorption coefficient (α) of the human skin

Summary

We measured the refractive index and absorption coefficient of human skin in a frequency range of 0.1 to 2 THz by using a terahertz time domain spectroscopy in attenuated total reflection mode (ATR THz-TDS). The results show that the index of refraction decreases with frequency, and the values for the absorption coefficient increase with frequency. This result is helpful in many biomedical applications of terahertz waves and to understand THz wave interaction with human skin.

References

- [1]. P. U. Jepsen, D. G. Cooke, M. Koch. "Terahertz spectroscopy and imaging-Modern techniques and applications" *Las. Phot. Rev.* vol. 5, no. 1 pp. 124-166 (2011).
- [2]. S. R. Tripathi, P. B. Ishai and K. Kawase "Frequency of the resonance of human sweat duct in normal mode of radiation" *Bio. Med. Opt. Exp.* vol. 9, pp. 1301-1308, (2018).
- [3]. J. Wang et al, "THz in vivo measurements: the effects of pressure on skin reflectivity" *Biomed. Opt. Exp.* vol.9, Issue 12, pp. 6467-6476(2018).
- [4]. A. Nakanishi, Y. Kawada, T. Yasuda, K. Akiyama, H. Takahashi, "Terahertz time domain attenuated total reflection spectroscopy with an integrated prism system" *Rev. Sci. Inst.* 83, 033103 (2012).

The proton beam influence on the sensitivity of wheat plantlets to AgNP pollution-preliminary results

A. LES¹, A. MOLOKANOV², S. SHVIDKIY², D. CREANGA¹

¹ Alexandru Ioan Cuza University, Physics Faculty, 11 Blvd. Carol I, Iasi, Romania

² Joint Institute for Nuclear Research, Dubna, Russia

Abstract

Proton beam treatment of wheat seeds was carried out to study the sensitivity of young plantlets further grown from seeds to environmental stress caused by nanoparticulate silver. The laboratory experiment evidenced diminished contents of assimilatory pigments lacking silver nanoparticles (AgNP) but higher values for diluted AgNP suspension.

Introduction

Due to its antibacterial features, silver is widely used in sanitation, cosmetics, pharmacy, wastewater treatment, etc., in the form of nanoparticles (AgNP). In Europe, the estimated production of Ag NPs is about 0.6 – 55 tones/year [1]. The fate of these nanoparticles is to finally reach the water, soil and air, polluting the biosphere. As another study [2] showed that proton beam exposure could change the young plantlet sensitivity to soil salinity, we searched

for the influence of proton exposure of cereal seeds (wheat) on the respective seedling sensitivity to AgNP pollution.

Experiment

The proton beam energy at the point of irradiation of the samples was 150 MeV, the average LET (Linear Energy Transfer) was $dE/dx = 0.539 \text{ keV}/\mu\text{m}$ at the Bragg peak. Proton beam dosimetry was based on the recommendations of the International Atomic Energy Agency (IAEA). The irradiation was carried out on dry seeds at the Dubna Institute for Nuclear Research. The irradiation dose was chosen as above 89 Gy.

After that, the wheat seeds were arranged on paper filters embedded with distilled water in Petri dishes and let to grow in controlled conditions in laboratory, 12 h light:12 h darkness, at $24^{\circ}\pm 1\text{C}$. The germinated seeds were supplied with appropriate volumes of silver nanoparticle suspensions: native suspension and 10:100 diluted one for ten days. AgNP suspension was synthesized by photochemical reduction with citrate [3]. The seedlings were grown in the same controlled conditions of lightning and temperature. According to the literature procedure, the green tissue was biochemically analyzed to estimate the assimilatory pigment contents (chlorophylls and carotenes) [4].

Results

The results showed that in the lack of AgNP supply, the contents of assimilatory pigments decreased by up to 40%. The administration of AgNP suspensions influenced the chlorophyll and carotene biosynthesis mechanisms with an increase of all assimilatory pigments contents for the diluted suspension but with a diminution for native AgNP suspension (Fig. 1).

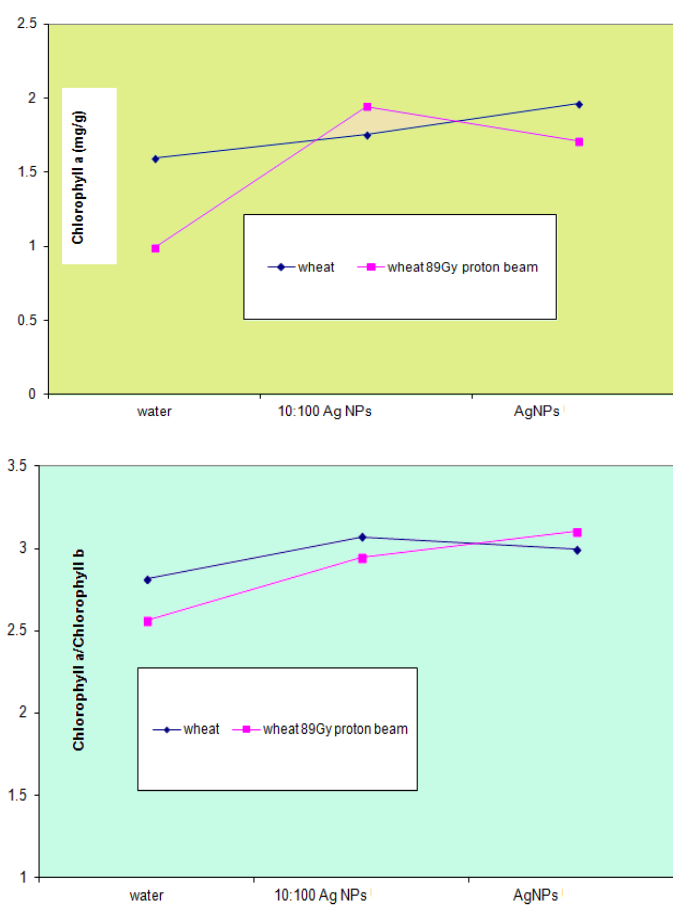


Fig 1. The content of chlorophyll a and photosynthesis efficacy

The photosynthesis efficacy as given by the content ratio of chlorophyll *a*/chlorophyll *b* was found to increase in the seedlings supplied with silver nanoparticles.

Conclusion

This could be a basis for new bionanotechnology involving cereal seeds treated with a proton beam in order to change their sensitivity to silver nanoparticle pollution. New irradiation doses with protons will be tested as well as other silver nanoparticles suspensions.

Acknowledgement

This research was partially supported by J.I.N.R-RO projects 2019 – 2021

References

- [1] Piccinno, F., Gottschalk, F., Seeger, S., Nowack, B., “Industrial production quantities and uses of ten engineered nanomaterials in Europe and the world”, *J. Nanopart. Res.*, 14, 9, 1 – 11, 2012.
- [2] Oprica, L., Grigore, M. N., Caraciuc, I., Gherghel, D., Mihai, C. T., Vochita, G., “Impact of proton beam irradiation on the growth and biochemical indexes of barley (*Hordeum vulgare* L.) seedlings grown under salt stress”, *Plants*, 9, 9,1234, 2020.
- [3] Oprica, L., Andries, M., Sacarescu, L., Popescu, L., Pricop, D., Creanga, D., Balasoiu, M., “Citrate-silver nanoparticles and their impact on some environmental beneficial fungi”, *Saudi J. Biol. Sci.* 27, 12, 3365 – 3375, 2020.
- [4] Lichtenthaler, H. K., Welburn, A. R. “Determinations of total carotenoids and chlorophylls a and b of leaf extracts in different solvents”, *Biochem. Soc. Trans.*, 11, 5, 591 – 592, 1983.

Evaluation of heavy metal contamination in *Mytilus* sp. shells

I. MOTRESCU^{1,2}, M. A. CIOLAN³, A. E. CALISTRU^{2,4},
G. JITAREANU^{2,4}, L. D. MIRON⁵

¹*Sciences Department, Iasi University of Life Sciences, Romania*

²*Research Institute for Agriculture and Environment,
Iasi University of Life Sciences, Romania*

³*Research Center on Advanced Materials and Technologies, Science Department,
Institute of Interdisciplinary Research, Alexandru Ioan Cuza University of Iasi, Romania*

⁴*Pedotechnics Department, Iasi University of Life Sciences, Romania*

⁵*Clinics Department, Iasi University of Life Sciences, Romania*

Abstract

Shellfish, such as *Mytilus*, are filter feeders, accumulating elements from the aquatic environment where they develop. Among these are heavy metal contaminants found in the water as a result of anthropogenic pollution. The mollusks metabolize these elements both into the consumable part and the crystalline structure of the shells, in different amounts. Thus, these heavy metals are a possible threat to human consumption of shellfish. In this paper, we use physical methods for fast detecting heavy metals of some *Mytilus* sp. shells and discuss the relevance and efficiency of these methods for bio-safety.

Introduction

The consumption of shellfish has been increasing in the past decades, due to the nutritional benefits of these foods [1–4]. On the other hand, toxic concentrations of chemical contaminants can be present in some shellfish as a result of bioaccumulation from the contaminated water mainly due to anthropogenic sources (industrialization, urbanization, agricultural activities) [5, 6]. Elements such as copper, iron, zinc, selenium are essential macro-nutrients for the life of these organisms; however, due to pollution, these elements can be found in the marine environments in high concentrations, along with some non-essential

and toxic elements such as cadmium, chromium, lead, arsenic, mercury [5–8]. Because some of the fixation takes place in the edible part, the shellfish consumption could pose risks for human consumption.

In our previous work we studied the biomineralization and bioaccumulation processes in *Mytilus* sp. shells, such as using them as environmental monitors. Based on the premises mentioned above, in this work we focus on determining the distribution of some heavy metal elements inside the shells using environmental scanning electron microscopy (ESEM) coupled with energy dispersive X-ray spectroscopy (EDAX) for elemental mapping and relative concentrations measurements. Higher resolution absolute evaluation of heavy metal composition was performed with High Resolution X-Ray Fluorescence Spectroscopy (XRF). Simple detection of heavy metal concentrations without using sophisticated and environmental and user non- friendly chemical protocols could be a rapid indication of toxic elements presence in dangerous concentrations in the edible part of these mollusks and could aid to rising alerts for consumers.

Materials and Methods

For these experiments, *Mytilus galloprovincialis* (Mediterranean mussel or blue mussel) samples originating from three aquaculture locations in Europe (1 – Adriatic Sea, 2 – Aegean Sea, and 3 – Black Sea) were commercially procured. The samples were cleaned (pure water, then ethanol) and imaged by ESEM using Quanta 450 electron microscope from FEI coupled with energy dispersive X-ray spectroscopy (EDAX). The data was compared with absolute values determined with XRF performed with Tiger 8 spectrometer from Bruker, Germany.

Results

Mytilus galloprovincialis lives on the Atlantic coast of Europe and the Mediterranean and Black seas. For the results presented in this work, the shells were in a similar ontogenetic state; the size of the shells was as follows: 1 – 6.8 ± 0.5 (cm), 2 – 6.77 ± 0.45 (cm), and 3 – 6.82 ± 0.4 (cm), respectively. To study the elemental distribution in different parts of the shells, ESEM analysis coupled with EDAX was performed. First, an average spectrum was obtained to identify in each case the relative presence of different elements. Subsequently, different areas on the analyzed surfaces were mapped to image the distribution of specific elements.

Fig. 1 shows the results for a surface on the outer part of the shell (periostacum) from sampling location 1 with separate distribution of some elements (C, O, N, Ca, Pb). The exposed outer layers show calcium carbonate and organic matrix, nitrogen being an indication of the latter. Lead appears uniformly distributed without any preference for the organic part or carbonate crystalline structure. Similar behavior was found for other trace metals (e.g., Fe, Cd, Cu, Zn) (data not shown here).

In the inner part of the shells, we were able to image the aragonite tablets with mineral bridges in between. The lead relative concentration was insignificant, seemingly in this case being more fixed towards the exterior of the shells. An opposite trend was found for Al which seems to be found in much smaller quantities towards the outer part than the nacre.

XRF measurements confirmed the presence of contaminants such as Al, Fe, Co, Ni, Cu, Zn, As, Sr, Ba, Pb, U in different concentrations depending on the environment from where the samples originated. More results and discussions will be presented during the conference.

Conclusions

The results confirm that the presented methods can be used for the fast detection of heavy metal contaminants in mollusk shells, which can be very important especially since the contamination in the shells mirrors the one in the consumable part.

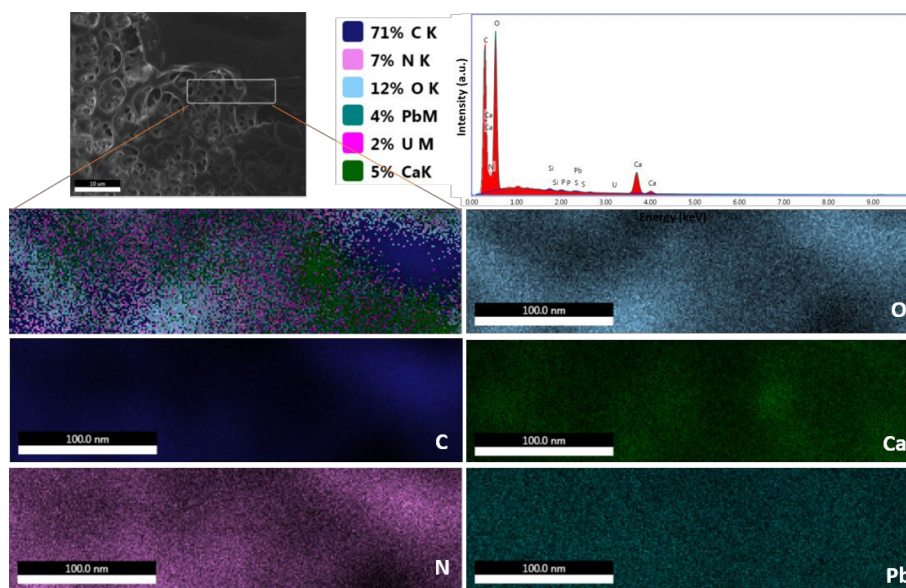


Fig. 1. EDAX elemental mapping for an area on the periostacum of a sample collected from area 1

References

- [1] Food and Agriculture Organization of the United Nations [Electronic resource] / Official site – URL: <http://www.fao.org/>.
- [2] Souci, S. W.; Fachman, W.; Krant, H. Food composition and nutritional tables, 7th ed. (Medpharm Scientific: Stuttgart, Germany, 2008, pp.1300).
- [3] Venugopal, V.; Gopakumar, K. Shellfish: Nutritive Value, Health Benefits, and Consumer Safety. *Compr. Rev. Food Sci. Food Saf.* 16, pp.1219 – 1242 (2017).
- [4] Khan, B. M.; Liu, Y. Marine Mollusks: Food with benefits. *Compr. Rev. Food. Sci. Food Saf.* 18, pp.548 – 564 (2019).
- [5] Bashir, I.; Lone, F. A.; Bhat, R. A.; Mir, S. A.; Dar, Z. A.; Dar, S. A. Concerns and Threats of Contamination on Aquatic Ecosystems. In *Bioremediation and Biotechnology*; Hakeem, K., Bhat., R., Qadri, H., Eds.; (Springer, Cham: Switzerland; 2020, pp.1 – 26).
- [6] Abdallah, M. A. M. Bioaccumulation of Heavy Metals in Mollusca Species and Assessment of Potential Risks to Human Health, *Bull. Environ. Contam. Toxicol.* 90, pp.552 – 557 (2013).
- [7] Millward, G.; Turner, A.; He, X. Metal Pollution. In *Encyclopedia of Ocean Sciences*, 3rd ed.; Cochran, J. K., Bokuniewicz, H. J., Yager, P. L., Eds.; (Academic Press. Elsevier, 2019, Volume 6, pp. 342 – 349).
- [8] Milenkovic, B.; Stajic, J. M.; Stojic, N.; Pucarevic, M.; Strbac, S. Evaluation of heavy metals and radionuclides in fish and seafood products. *Chemosphere* 229, pp. 324 – 331 (2019).

Analysis of color coordinates in dried blood spots under aging for forensic medical applications

K. ZELENSKA¹, T. ZELENSKA², O. VYNOHRADOVA-ANIK³, T. AOKI¹

¹Research Institute of Electronics, Shizuoka University, Japan

²Kyiv Regional Bureau of Forensic Medical Examination, Kyiv, Ukraine

³Physiology Department, Bogomolets National Medical University, Kyiv, Ukraine

Abstract

The color of a dried blood spot depends on the hemoglobin state and its amount in the aged spot. Digital images of the dried blood spots were analyzed in order to estimate color

components depending on storage time. A level of chromaticity coordinate of g-component is almost stable while r- and b-components compete because of different contribution of hemoglobin states.

Introduction

Blood stains revealed at crime scenes can provide valuable information to solve the case in forensic medicine. After determining the blood in the spots, the most interesting question is to determine their age and spread the objects in time, even without specifying the exact date of their formation.

Experimental Details and Results

As known, hemoglobin can change its form under various factors in living beings and under the aging of dried blood spots. In aged bloodstains, hemoglobin is usually present in the modified form of hematoporphyrin. The samples of dried blood spots were taken on white medical gauze and stored in a dark dry place during different periods of time (0 – 10 days and 0 – 90 days). Typical samples are shown on the inserts in Fig. 1.

Digital images of the dried blood spots were analyzed in order to estimate color components depending on the storage time. Changing in color components was based on the hemoglobin form modifications. Color values from the images were extracted in the RGB color space. The following parameters were obtained:

- chromaticity coordinates

$$r = \frac{R}{R+G+B}, \quad g = \frac{G}{R+G+B}, \quad b = \frac{B}{R+G+B};$$

- effective color parameter

$$\bar{K} = \frac{R/R_{white}}{G/G_{white} B/B_{white}};$$

- relative color coordinates

$$R_G = \frac{R}{G}, \quad R_B = \frac{R}{B}, \quad R_{BG} = \frac{R_B}{R_G}.$$

When a blood stain gets to a forensic medical examiner, during the first few days after its formation, the blood dye will mainly be in the state of oxyhemoglobin with an admixture of a small amount of methemoglobin. As this period increases, the amount of methemoglobin in the spot increases, and oxyhemoglobin decreases. With significant destruction of hemoglobin, hemichromes and hematoporphyrins are formed. The color of the dried blood spot depends on the hemoglobin state and its amount in the aged spot. As known, oxyhemoglobin has orange-red color, deoxyhemoglobin – magenta-red color, and methemoglobin – bluish chocolate-brown color. The ratio of the color components of the blood dye colors can be represented in the RGB system and is shown in Table 1.

Table 1. Color characterization of hemoglobin in different states

Hemoglobin state	Oxyhemoglobin	Deoxyhemoglobin	Methemoglobin
Color	Orange-red	Magenta-red	Bluish chocolate-brown
RGB coordinates ratio	R>G=B	R>B>>G	R≥B>G

Fig. 1 represents digital images of the samples of blood stains and corresponding chromaticity coordinates in arbitrary units depending on the number of storage days. The G-component

level is almost stable while R- and B-components compete, confirming changes in the contribution of different states of hemoglobin associated with R- and B-components scatter from each other (see left-hand insert of red circles). It should be mentioned that storage of a blood stain in a glass container leads to the retention of the R-component in 3 hours almost on the same level as just after deposition because of the limited air flow.

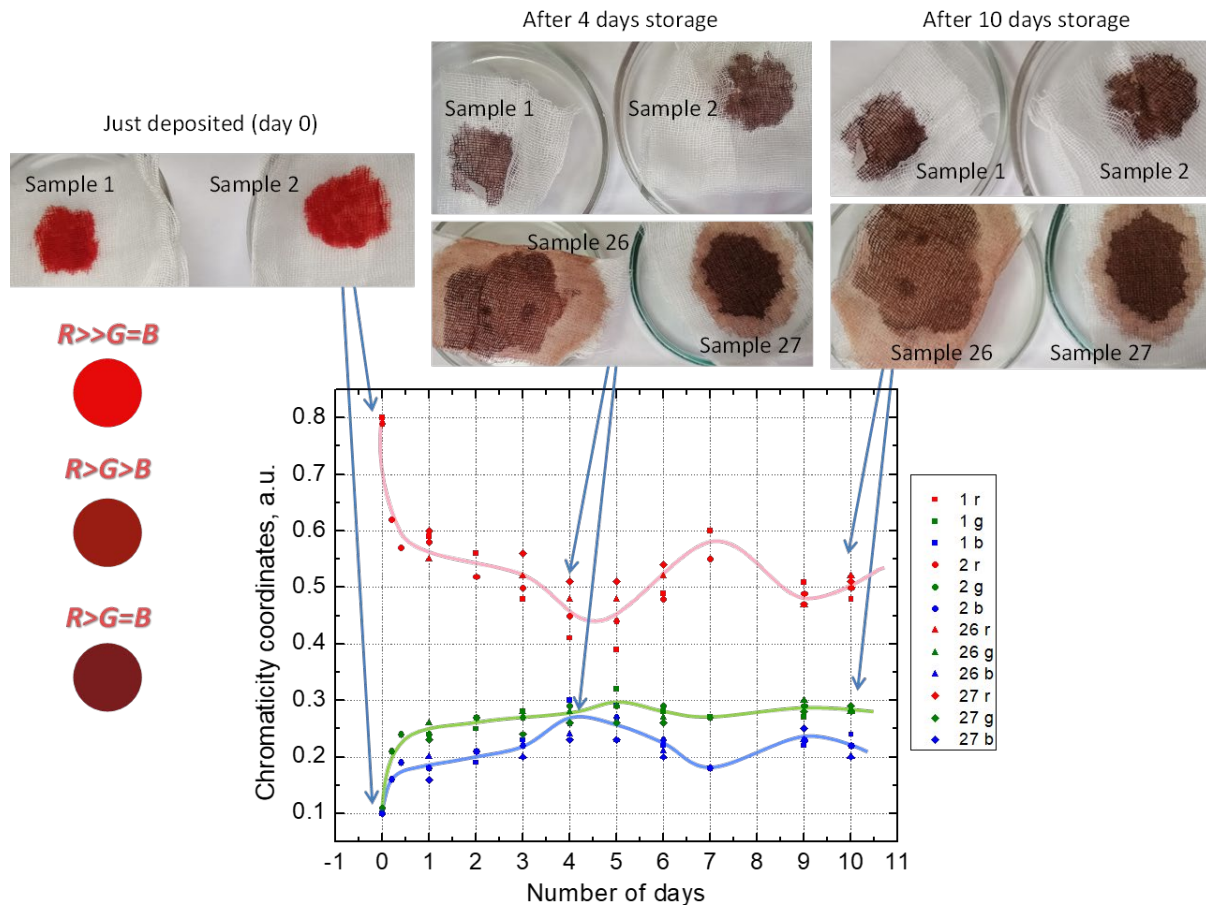


Fig.1. Dependence of chromaticity coordinates on the number of storage days in air for samples 1, 2, 26 and 27

Conclusion

Deterioration of the R-component with respect to G- and B-components contribution under drying a blood stain on air was observed. Relative color coordinates under storage demonstrate an increase in G- and B-component that can be corresponded to the hemoglobin state modification and appearance of deoxyhemoglobin and methemoglobin.

Acknowledgements

This research was partly supported by 2020 – 2021 Cooperative Research at Research Center of Biomedical Engineering, Japan, adopted as 2021 Cooperative Research at RIE, Shizuoka University (Grant No. 2057).

Unit 2 “Electric and Electronic engineering”

3D fluorescence spectroscopy of liquid media via internal reference method

M. R. KHAJISHVILI, N. KH. GOMIDZE, J. J. SHAINIDZE
Batumi Shota Rustaveli State University, Georgia

Abstract

Common methods of analyzing the chemical composition of a substance include many existing optical methods. Selecting an effective and optimal method from numerous optical methods and adapting it to the properties of the investigated substance is one of the most urgent tasks of modernity. Scientists are trying to study the substances – bioananoagents that surround humanity and develop methods and approaches that are used in one way or another to study the materials. The properties of materials are determined by considering both the main components and the compounds. In addition, often the properties of the materials depend on the distribution of the compounds or components in their volume.

Introduction

Today, the growing interest in laser fluorescence spectroscopy is due to its practical application in laser communication, ecology, and medicine. Medical imaging, for example, is one of the major problems in medicine.

A number of works have already been done to increase the characteristics of the detected signal. For example, spectra of emission radiation intensity of blood plasma were measured in Revaz Turmanidze's master thesis [1], where a partially coherent laser beam fell on the blood plasma placed in the cuvette, and the intensity of the scattered laser radiation was also intensified.

Paper [2] discussed the relationship of stochastic shifts in solutions and gases to the wavelength of the absorbed light. Scattering from water molecules (Raman scattering) were studied in [3]. Fluorescence characteristics such as fluorescence attenuation and damping dependence on wavelength, quantum yield, and fluorescence damping time are discussed in [4]. Paper [5] studies fluorescence anisotropy and fluorescent energy transfer conditions.

Paper [6] shows that partial spatial coherence of the source reduces scintillation. The partial coherence function of a partially coherent Gaussian source is highlighted in [7]. In Kakha Makharadze's doctoral dissertation [8], the characteristics of the Gaussian beam are studied, such as average intensity, beam width, phase front radius of curvature, wave front coherence radius. Partial spatial coherence beam radius coherence analysis is presented in [9].

Under weak and strong turbulence conditions, an analytical image of the partially spatial coherence beam intensity correlation function was obtained in [10]. Paper [11] presents Rittov's method in an atmosphere with low turbulence. Paper [12] investigates the scintillation effect for a partially temporal coherence wave.

Within grant project №FR-152-9-240-14 [13–15] was taken spectra using spectrometer StellarNet Black-Comet (190 – 900 nm) which captures relative echo-intensity intensities of laser beams scattered from an optically dense random phase screen.

However, the difficulty is otherwise to evaluate the statistical characteristics of the signal detected through a heterogeneous environment and visualize the spectral image. Environmental statistics cause these difficulties. For example, the detection of fluorescence signals in complex environments and the visualization of spectral images are associated with significant difficulties because the complex composition of the environment (petroleum, petroleum products, organic compounds, etc.) determines the overlap of spectra and reduces the ability to decipher useful information. It becomes important to increase the quality of the

signal registered on the detector and to determine the factors that are responsible for this quality. This is the subject of this work.

References

- [1] Turmanidze R. Evaluation of the correlation function of the fluctuation of the laser beam intensity in the blood. Master thesis. Batumi, 2017.
- [2] Stokes G. G. Über die Veränderung der Brechbarkeit des Lichts, *Annalen der Physik*, B. 163 (11), 1852, S. 480 – 490.
- [3] Berlman I. B. 1971. *Handbook of fluorescence spectra of aromatic molecules*, 2nd ed. Academic Press, New York.
- [4] Korotkova O., Andrews L. C. “Speckle propagation through atmospheric turbulence: effects of partial coherence of the target”, (SPIE pr., 2002).
- [5] Bernard V. *Molecular Fluorescence: Principles and Applications*. – Wiley-VCH Verlag GmbH, 2001.
- [6] Banakh V. A., Buldakov V. M., Mironov V. L. “Intensity fluctuations of a partially coherent light beam in a turbulent atmosphere”, *Opt. Spectrosk.*, 54, 1054 – 1059 (1983).
- [7] Fante L. “Intensity fluctuations of an optical wave in a turbulent medium, effect of source coherence”, *Opt. Acta*, 28, 1203 – 1207 (1981).
- [8] Gomidze N. Kh., Shashikadze Z. Kh., Makharadze K. A., Khajishvili M. R. About fluorescence excitation spectrums. 6th International Conference on Advanced Optoelectronics and Lasers. Conference Proceedings. 9 – 13 September (2013), Sudak, Ukraine, pp. 317 – 319.
- [9] Belenkii M. S., Kon A. I., Mironov V. L. Turbulent distortions of the spatial coherence of a laser beam, *Kvantovaya Electron. (Moscow)*, 4, 517 – 523 (1977).
- [10] Leader J. C. "Intensity fluctuations resulting from a spatially partially coherent light propagating through atmospheric turbulence", *J. Opt. Soc. Am. A*, Vol.69, 1, 73 – 84 (1979).
- [11] Mandel L., Wolf E. *Optical Coherence and Quantum Optics* (Cambridge University Press, Cambridge, 1995).
- [12] Joseph R. Lakowicz Z. *Principles of Fluorescence Spectroscopy* / R. J. Lakowicz. – N.Y.: Springer Science, 2006. – 960 p.
- [13] Gomidze N. Kh., Shashikadze Z. Kh., Makharadze K. A., Khajishvili M. R. About fluorescence excitation spectrums. 6th International Conference on Advanced Optoelectronics and Lasers. Conference Proceedings. 9 – 13 September (2013), Sudak, Ukraine, pp. 317 – 319.
- [14] Gomidze N. Kh., Khajishvili M. R., Makharadze K. A., Jabnidze I. N., Surmanidze Z. J. About Statistical Moments of Scattered Laser Radiation from Random Phase Screen. *International Journal of Emerging Technology and Advanced Engineering*. ISSN 2250-2459 (ISO 9001:2008 Certified), Vol. 6, Issue 4, pp.237 – 245, 2016.
- [15] Gomidze N. Kh., Makharadze K. A., Khajishvili M. R., Shashikadze Z. Kh. About Numerical Analyses of Sea Water with Laser Spectroscopy Method. 2011 XXXth URSI General Assembly and Scientific Symposium, 30TH 2011 (5 VOLS), pp. 1620 – 1624, ISBN 978-1-4244-5117-3.

Transportation and measurement of droplet using surface acoustic wave for digital microfluidic system application

R. MITSUYOSHI¹, J. KONDOH^{1,2}

¹ *Shizuoka University, Graduate School of Integrated Science and Technology,*

² *Shizuoka University, Graduate School of Science and Technology*

Abstract

Nonlinear acoustic phenomena are caused by a surface acoustic wave (SAW) and a liquid. The principal is based on the radiated longitudinal wave from the SAW at the solid and liquid interface. Transportation and mixing are well-known phenomena. Those phenomena are important to realizing a digital microfluidic system (DMFS) application. For the DMFS application, integration of a measurement function is necessary. In this paper, sound velocity was measured using the radiated longitudinal wave. The velocity measurements depend on

the shape of the droplet. To keep the constant shape, slippery liquid-infused porous surface treatment was carried out. The improvement of the estimated velocity was confirmed with the treatment.

Introduction

Acoustic wave devices, such as surface acoustic waves (SAW) and film bulk acoustic waves, play an important role in a mobile communication system [1]. The SAW devices have been applied to sensors and microfluidics [2, 3]. When SAW propagates at the interface between solid and liquid, longitudinal waves are radiated into the liquid. The nonlinear acoustic phenomena, such as acoustic streaming and acoustic radiation force, are caused by the longitudinal wave. A droplet on the SAW device is transported by the radiation force acting at the water and air interface. The droplet on the SAW device is not only transported but also mixed due to the longitudinal wave. For droplet transportation, measurements of the droplet position are also important. We proposed the position measurement method [4]. The method is based on the longitudinal wave propagation path in the droplet and can also be applied to measure the sound velocity. In this paper, transportation of the droplet and measurement of sound velocity using the SAW device are discussed. Normally, the droplet shape is varied after the transportation [3]. It is necessary to estimate the propagation path after the droplet transportation. Therefore, keeping the droplet shape during transportation is important. In this paper, slippery liquid-infused porous surface (SLIPS) [5] was adapted to avoid changing the shape and found that it is suitable for the purpose.

Method

The SAW device was fabricated on 128° rotated Y-cut X-propagating LiNbO₃ (see Fig. 1). The metal materials of the interdigital transducer (IDT) were gold/chromium. The center frequency was 50 MHz. The measurement setup is shown in [3, 4]. A sinusoidal signal of 50 MHz and pulse signal were mixed and applied to the SAW device. The frequency of the pulse signal was fixed at 10 kHz. The duty cycle was 50% for the droplet transportation and 1% for the sound velocity measurement. The propagation surface was treated to realize the SLIPS [5]. The used sample was glycerol-water mixtures.

Sound velocity V_L was estimated from the following equation.

$$f(V_L) = \frac{1}{2} \pi (r + h)(1 + b) + \frac{V_L}{V_{SAW}} \left(X - \frac{2T}{\pi} V_L \right) - T_t V_L \quad (1)$$

$$T_t = \frac{L}{V_L} + \frac{A+B}{V_{SAW}}, \quad T = \frac{T_r + T'_r}{2} - T_t, \quad b = \frac{r-h}{r+h}$$

Where, V_{SAW} is the phase velocity of the SAW, T_r and T'_r are the reflected times from the droplet measured by IDT1 and IDT2, respectively. The other parameters are shown in Fig. 1. Eq. (1) was derived using the Newton-Raphson method.

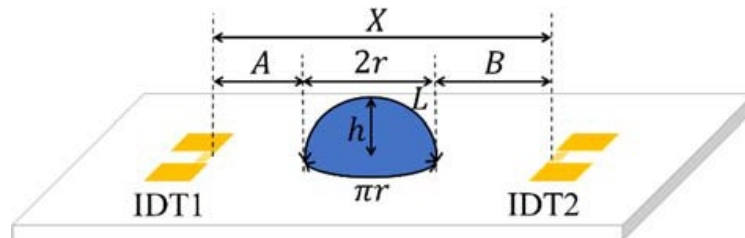


Fig. 1. Schematic of SAW device used

Results and discussion

We measured three different cases: 1) before droplet transportation, 2) after droplet transportation without the SLIPS, and 3) after droplet transportation with the SLIPS. The

transportation distance was 5 mm. The results are shown in Fig. 2. Literature values are also shown in the figure. At the low concentration, the results of 1) and 3) agree with the literature values. The results of 2), however, do not agree. Also, measurement errors for 2) are wide. The reason is explained from the droplet shape as shown in Figs. 3 and 4. In the case of 2), the contact angle decreases after the transportation, and the shape of the droplet is not hemisphere. As shown in Fig. 1, eq. (1) was derived for the hemispherical droplet. Droplet transportation on the SLIPS, change of the droplet shape is small, as shown in Fig. 4. Therefore, the measured results after the transportation agree with ones before the transportation.

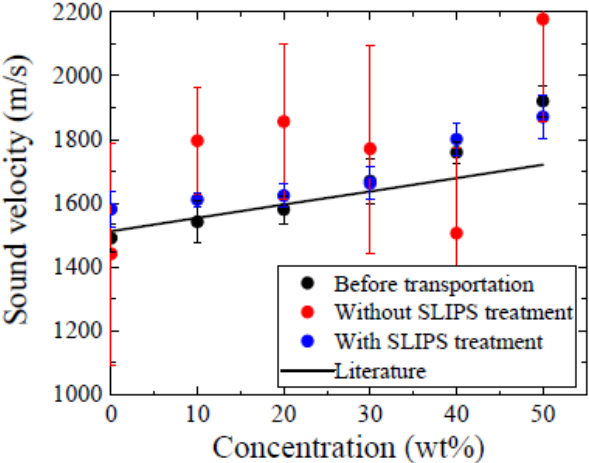


Fig. 2. Measured results of sound velocity for three cases as a function of concentration of glycerol-water mixture

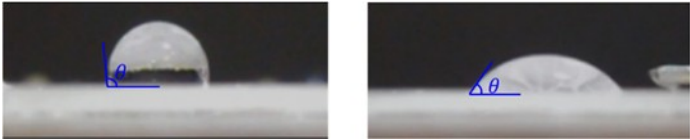


Fig. 3. Droplet manipulation without SLIPS treatment. (a) before and (b) after transportation



Fig. 4. Droplet manipulation on SLIPS. (a) before and (b) after transportation

Conclusion

Droplet transportation and sound velocity measurements were simultaneously carried out. The SLIPS treatment to avoid the droplet shape change during transportation is an effective method. In this paper, a single droplet is transported and measured. For the actual application, however, two or more droplets will be manipulated and mixed. During the mixture process, liquid properties are changed. The sound velocity measurements are required in those cases. This is our next work.

References

[1] C. K. Campbell, "Surface Acoustic Wave Devices for Mobile and Wireless Communications" (Academic, San Diego, CA, 1998).

- [2] J. Kondoh “A liquid-phase sensor using shear horizontal surface acoustic wave devices” *Electron. Commun. Jpn.* 96 [2], pp. 41 – 49 (2013).
- [3] J. Kondoh, “Nonlinear acoustic phenomena caused by surface acoustic wave and its application to digital microfluidic system” *Jpn. J. Appl. Phys.* 57, 07LA01 (2018).
- [4] S. Tsunogaya and J. Kondoh, “Observation of reflected and transmitted waves caused by acoustic streaming in droplet on surface acoustic waves devices” *Jpn. J. Appl. Phys.* 57, 07LD03 (2018).
- [5] J. T. Luo, N. R. Gerald, G. McHale, G. G. Wells, and Y. Q. Fu, “Slippery Liquid-Infused Porous Surfaces and Droplet Transportation by Surface Acoustic Wave” *Phys. Rev. Appl.* 7, 014017 (2017).

Probing of deep states by band-to-band tunneling in nanoscale silicon-on-insulator Esaki diodes

D. MORARU^{1,2a}, Y. TAMURA², Y. IWATSUKI², K. YAMAGUCHI²

¹*Research Institute of Electronics, Shizuoka University, 3-5-1 Johoku, Hamamatsu, Japan*

²*Graduate School of Integrated Science and Technology, Shizuoka University*

^a*E-mail: moraru.daniel@shizuoka.ac.jp*

Abstract

Band-to-band tunneling (BTBT) is a fundamental transport mechanism that can be activated in highly-doped *pn* diodes, so-called Esaki diodes [1, 2]. In silicon, the indirect-bandgap nature poses some difficulties because phenomena such as phonon assistance are needed for momentum conservation purposes. In that sense, transport through deep, localized energy states in the depletion layer [3, 4] can be of interest as an alternative to direct BTBT transport between the leads. Here, we present an analysis of silicon-on-insulator (SOI) Esaki diodes with nanoscale dimensions, in which excess current (at forward biases) contains current features that can be related to such deep states. The analysis also covers the role of a nanoscale *i*-layer inserted between the p^+ and n^+ leads in tuning the BTBT tunneling rate.

Introduction

Silicon is the main platform for electronics and a promising material for future generations, involving new transport mechanisms such as band-to-band tunneling (BTBT), explored for tunnel field-effect transistors (TFETs). However, differently from the conventional transistors involving uni-polar transport, BTBT involves transport between conduction and valence bands, and so the tunneling rate is suppressed because of the need for phonon assistance required for momentum conservation. This is due to the indirect-bandgap nature of Si. As such, direct-bandgap semiconductors are generally more attractive for BTBT applications.

It can be expected, however, that Si can exhibit new properties in highly-doped nanoscale structures. First, quantum confinement and dielectric confinement can significantly modify the band structure of Si. Second, the high degree of doping needed to create nanoscale depletion-layers can introduce deep energy states, which can mediate the BTBT transport.

Here, we present several results of electrical characteristics for nanoscale tunnel (Esaki) diodes fabricated in silicon-on-insulator (SOI) substrates. The low-temperature measurements allow BTBT “spectroscopy” of deep states and an analysis of the impact of *i*-layer (between leads).

Device structure and measurement setup

The experimental devices were fabricated using CMOS-compatible methodology, using Clean Room techniques, and are shown schematically in Fig. 1. Fig. 1 also shows the measurement circuit. For these devices, the p^+n^+ (and p^+-i-n^+) diodes were fabricated laterally, in an SOI substrate, by selective doping at high concentrations: with Boron (B)

for p -type, $N_A \approx (3\sim 9) \times 10^{19} \text{ cm}^{-3}$, and Phosphorus (P) for n -type, $N_D \approx (1\sim 3) \times 10^{20} \text{ cm}^{-3}$, depending on the design.

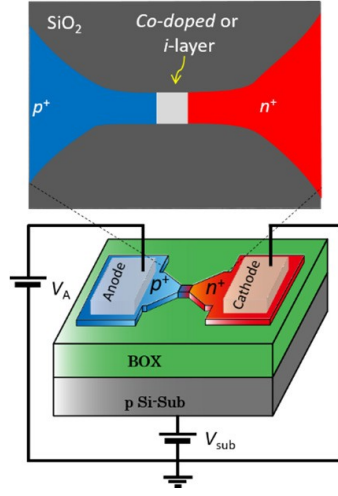


Fig. 1. (a) Schematic illustration of a lateral p^+-n^+ (or p^+-i-n^+) diode, containing either a co-doped or i -layer region between the leads. Devices are fabricated in silicon-on-insulator (SOI), and the p -type substrate can be used as a gate (i.e., controlling the potential in the top Si layer, mainly in the depletion-layer or i -layer)

We focus on analyzing devices as shown in Fig. 1, without top or side gates, using V_p as anode bias (and V_{sub} as backgate voltage, in some cases). Considering the doping concentrations indicated above, the depletion-layer width is expected to be on the order of 20 nm, which should allow the observation of BTBT transport. Furthermore, we focus on the forward-bias regime, where BTBT transport is expected to occur either directly between the bands (at lower biases) or mediated by deep bandgap states (at higher biases) before the onset of the regular diode current.

Results

Most measurements were taken at a low temperature, as shown in Fig. 2(a).

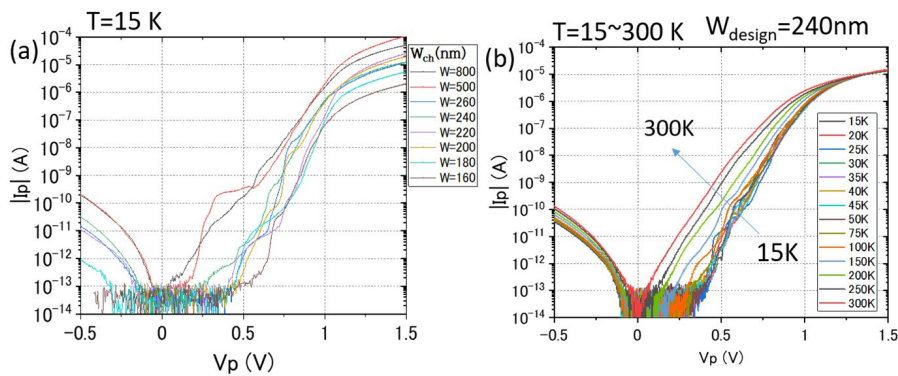


Fig. 2. (a) $|I_p|$ - V_p characteristics ($T=15 \text{ K}$) for thin SOI pn diodes with different widths (given by the designed values). Current steps are observed in forward-bias regime, around $V_p=0.5 \text{ V}$. (b) Temperature dependence for one device (designed width 240 nm) in the range 15 – 300 K

The results show the current-voltage (I_p - V_p) characteristics in both reverse- and forward-bias regimes (with $|I_p|$ shown on the vertical axis). Data is displayed for different values of the width of the Si constriction in which the pn diodes were fabricated (designed width: 160~800 nm, with actual width being significantly smaller). For most devices, reverse-

current flows with large levels, which suggests that the depletion-layer width is small; however, all devices shown here do not exhibit the typical negative differential conductance (NDC) peak in the forward-bias regime. This may be due to a relatively low N_A (estimated to be $3.9 \times 10^{19} \text{ cm}^{-3}$), i.e., because the Fermi level within the p -lead may not be sufficiently deep below the valence band edge to allow direct BTBT. However, at higher V_p , all the devices exhibit current steps, with the current level overall showing a systematic dependence on the width. This regime corresponds to the so-called “excess current” mechanism, which involves deep bandgap states as stepping stones in the BTBT transport. Typically, such a mechanism is reported as contributing to a non-zero current background that deteriorates the peak-to-valley ratio in Esaki diodes. In these SOI pn diodes, with reduced dimensionality, the observation of the clear current steps suggests that a small number of energy states can contribute to BTBT transport and can be revealed by such BTBT-“spectroscopy”.

As the temperature increases, the current steps are broadened and disappear at intermediate temperatures, as observed in Fig. 2(b) for one device (with a designed width of 240 nm). This behavior is common for most devices, and further analysis of the T -dependence can reveal the distribution of the energy states involved in BTBT transport. Such states can be expected to arise from the clustering of donors and/or acceptors at the edges of the depletion-layer (or i -layer). Further systematic analysis of such a mechanism will be presented later.

Conclusion

We presented data representative for thin silicon-on-insulator Esaki diodes, in which current steps appear in the forward-bias region (excess-current region). These current steps indicate band-to-band tunneling transport mediated, most likely, by dopant-induced states at the edges of depletion-layer (or i -layer for $p^+ - i - n^+$ diodes). Band-to-band tunneling “spectroscopy” allows a deeper understanding of the distribution of these energy states and their impact on device operation. In the future, such understanding can provide new concepts for overcoming the limitations of BTBT devices by specifically considering the new nature of highly-doped nanoscale Si.

This work is partly supported by Grant-in-Aid for Scientific Research (KAKENHI JP19K04529) from MEXT. We thank Prof. M. Tabe and Dr. G. Prabhudesai for many critical discussions and support.

References

- [1] L. Esaki and Y. Miyahara, *Solid State Electron.* **1**, 13 (1960).
- [2] H. Schmid *et al.*, *Nano Lett.* **12**, 699 (2012).
- [3] M. Tabe *et al.*, and D. Moraru, *Appl. Phys. Lett.* **108**, 093502 (2016).
- [4] G. Prabhudesai, *et al.*, and D. Moraru, *Appl. Phys. Lett.* **114**, 243502 (2019).

Evaluation of radiation detection characteristics by $\alpha\text{-Ga}_2\text{O}_3$

H. NAKAGAWA¹, R. YAMADA², M. HASHIMOTO², T. YAMAGUCHI², T. ONUMA²,
T. HONDA², T. NAKANO¹, T. AOKI¹

¹ *Research Institute of Electronics, Shizuoka University, Japan*

² *Department of Applied Physics, School of Advanced Engineering,
Kogakuin University, Japan*

Abstract

In this study, we report on the radiation detection characteristics of $\alpha\text{-Ga}_2\text{O}_3$ semiconductor radiation detector for evaluation possibility of radiation detection. The $\alpha\text{-Ga}_2\text{O}_3$ sample was

grown on a c-plane sapphire substrate by mist chemical vapor deposition (mist-CVD) and the radiation detection characteristics were evaluated. The α -Ga₂O₃ detector exhibited good sensitivity in the current-time change measurement with ²⁴¹Am α -particle irradiation. Moreover, the detection pulse signal of ²⁴¹Am α -particle was able to be obtained at room temperature. These results show α -Ga₂O₃ has the radiation sensitivity and the possibility for application as a room temperature radiation detector.

Introduction

Gallium oxide (Ga₂O₃) is expected to be applied to optoelectronics, sensing systems, power devices, etc. Ga₂O₃ has six different polymorphs. The α -Ga₂O₃ with corundum structure of these polymorphs is grown by mist chemical vapor deposition (mist-CVD) [1]. Since α -Ga₂O₃ is a wide-gap (~ 5.3 eV) semiconductor, it can be operated as a radiation detector at room temperature due to low thermal noise. However, the radiation detection characteristics of α -Ga₂O₃ semiconductors have not been evaluated sufficiently.

This study evaluated the radiation detection characteristics of α -Ga₂O₃ fabricated by mist-CVD to confirm its potential as a radiation detector. For the evaluation, the current-time change measurement and the pulse signal detection measurement were performed with ²⁴¹Am α -particle irradiation condition. The results confirm that α -Ga₂O₃ has good sensitivity of α -particles.

Experimental and Results

This study evaluated the radiation detection characteristics of α -Ga₂O₃, which was fabricated by mist-CVD. The current-time change measurement of the α -Ga₂O₃ was performed and analyzed by a semiconductor parameter analyzer under the irradiation of ²⁴¹Am α -particle source. Fig. 1 (a) shows the result of current-time change measurement under the ²⁴¹Am irradiation and dark condition at applied bias voltage of 10 V. As the result, current value increased with ²⁴¹Am irradiation.

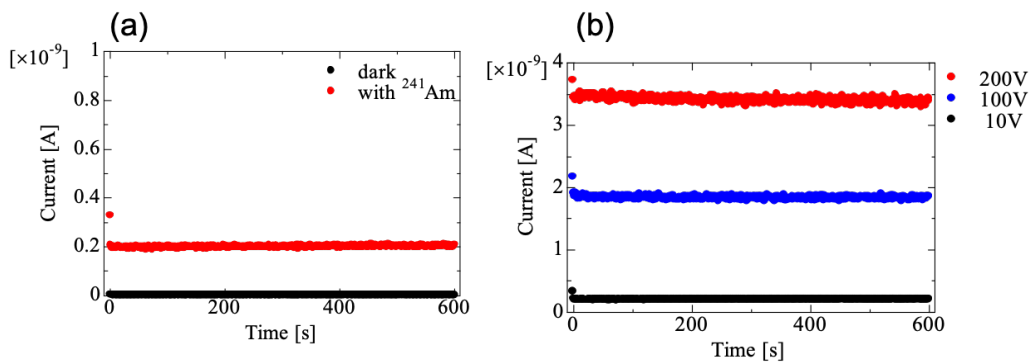


Fig. 1. Current-time change measurement of α -Ga₂O₃ (a) under the ²⁴¹Am α -particle irradiation and dark condition at bias voltage of 10 V and (b) depend on bias voltage

This result shows that the electron-hole pairs were generated by α -particles and collected as a detection current. The bias voltage dependence of current-time change measurement was shown in fig. 1 (b). The current value increased with an increase in bias voltage. It indicates that the increase of bias voltage leads to increase in the carrier drift velocity. Moreover, the detection pulse signals from a charge-sensitive amplifier connected to the α -Ga₂O₃ detector were confirmed by the oscilloscope with ²⁴¹Am α -particle source. Fig 2 shows the α -particle detection pulse signal at the applied bias voltage of 5 V and 10 V, respectively. The pulse height of the signal shows the number of electron-hole pairs generated by the α -particles managed to be collected. The pulse height at the voltage of 10 V was higher than that at 5 V. The increase in the carrier collection efficiency was confirmed by increasing the applied bias voltage.

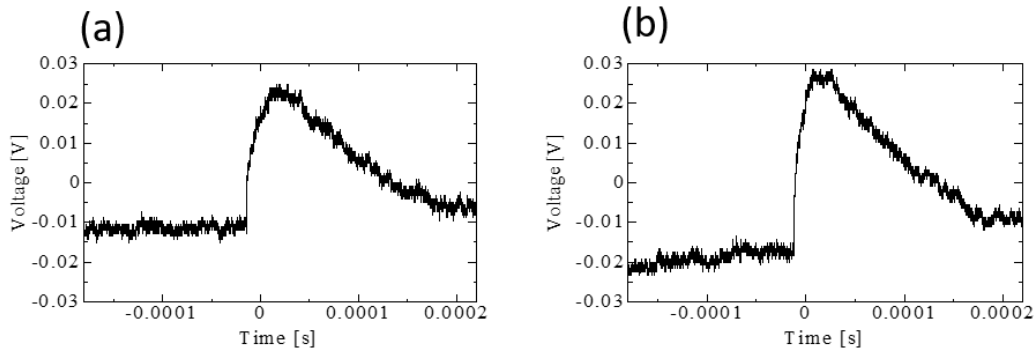


Fig. 2. Detection pulse signal of ^{241}Am α -particles at applied bias voltage of (a) 5 V and (b) 10 V

Conclusion

This study evaluates the radiation detection characteristics of $\alpha\text{-Ga}_2\text{O}_3$. In the current-time change measurement, the current value increased with the α -particle source comparing with dark condition. This result shows that the electrons and holes generated by the α - managed to be obtained as the detection current. Moreover, the detection pulse signal of α -particle can be obtained. These results indicate that $\alpha\text{-Ga}_2\text{O}_3$ has good sensitivity to α -particles. $\alpha\text{-Ga}_2\text{O}_3$ has the potential to be used as a room temperature radiation detector.

References

- [1] K. Akaiwa, and S Fujita “Electrical Conductive Corundum-Structured $\alpha\text{-Ga}_2\text{O}_3$ Thin Films on Sapphire Tin-Doping Grown by Spray Assisted Mist Chemical Vapor Deposition” Jpn. J Appl. Phys, 51 070203 (2012).

Theoretical study of the impact of a donor-acceptor pair on tunneling current in Si nanodiodes

C. PANDY^{1,2}, K. YAMAGUCHI², Y. NEO¹, H. MIMURA¹, M. TABE¹, D. MORARU^{1,a}

¹Research Institute of Electronics, Shizuoka University, 3-5-1 Johoku, Hamamatsu, Japan

²Graduate School of Integrated Science and Technology, Shizuoka University

^aE-mail: moraru.daniel@shizuoka.ac.jp

Abstract

Tunnel diodes are semiconductor devices that operate based on the band-to-band tunneling (BTBT) mechanism [1], a process that holds promise for future electronics. In Si, due to its indirect bandgap nature, the BTBT requires phonon assistance for momentum conservation. However, as device dimensions are reduced [2], discrete dopants at fronts of the depletion region can become critical in providing pathways for BTBT through localized or extended states. Here, we provide a theoretical study of the impact of a donor-acceptor pair on BTBT current, using a semi-empirical simulation approach [3]. It is found that such a system can enhance the current, and the main factors involved in this enhancement are identified distinctly.

Introduction

Band-to-band tunneling (BTBT) in silicon is a promising alternative mechanism for sub-thermal swing devices, such as tunnel field-effect transistors (TFETs). In Si, this mechanism is hindered by the necessity for phonon assistance to conserve the momentum in tunneling between the bands in such an indirect-bandgap material. It can be expected that the presence of dopant-induced states in the depletion region can relax this condition. In [4], *ab initio*

simulations are used for studying the effect of a donor-acceptor pair on the band structure under electric field, with implicit effects on the transmission probability. The current paper investigates the role of a donor-acceptor pair directly in the current in the simplified tunnel-diode layout.

Device structure and simulation details

The simplified structure of the devices is illustrated in Fig. 1, with electrically-doped leads (p^+ and n^+) sandwiching a central region (without or with a discrete pair of a phosphorus (P) donor and a boron (B) acceptor, as shown in Fig. 1(a) or Fig. 1(b), respectively), all within a $\langle 100 \rangle$ Si nanowire. The electrical doping method is represented by a jellium-like uniform distribution of extra charges in the Si leads, corresponding to high dopant concentrations $N_D=N_A= 2 \times 10^{20} \text{ cm}^{-3}$. The cross-section size is 1.5 nm, while the central region is typically 3.25 nm in length.

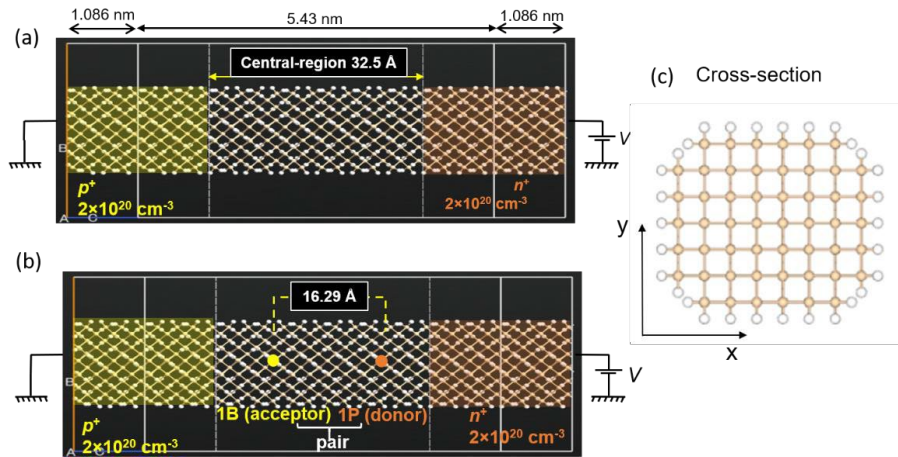


Fig. 1. Atomistic views of p^+-n^+ diodes with leads electrically-doped corresponding to dopant concentrations $N_{D,A}=2 \times 10^{20} \text{ cm}^{-3}$. All dangling bonds are passivated with H-atoms in the entire structure. Bias circuits are shown for IV simulations. The cases correspond to p^+-n^+ diodes with the central region: (a) without discrete dopants; (b) with a P-B pair.

(c) Cross-sectional view of the nanowire

Geometry optimization (after substitutional doping) using an in-built optimizer with maximum forces of 0.05 eV/\AA and simulation of current-voltage characteristics for structures shown in Fig. 1 are carried out with Quantum-ATK software [5]. A non-equilibrium Green's function (NEGF) method is used to calculate the current through the nanostructured devices. In addition, the local density of states (LDOS) spectra is used to understand the modification in the overall band structure due to the donor-acceptor pair.

Results

IV characteristics are simulated typically at room temperature ($T=300 \text{ K}$), and Fig. 2(a) shows a comparison between the results obtained without dopants and with a donor-acceptor (D-A) pair, with inter-dopant distance, $d_{D-A}=16.29 \text{ \AA}$. First, both characteristics exhibit the behavior of tunnel diodes, i.e., a negative differential conductance (NDC) peak in forward bias regime and a relatively larger current in the reverse-bias regime. However, it should be noted that phonon scattering is not included in these simulations.

Second, it can be seen that the presence of a D-A pair leads to an overall current enhancement by more than an order of magnitude (for this D-A configuration). This result suggests the positive effect of such front-side dopants in the current enhancement. It will be argued that there are several key factors in further tuning this contribution, mainly the dopant-lead coupling and the alignment of dopant-induced energy states. Figures 2(b) and 2(c) show the LDOS

spectra for $V=0.2$ V across the central region (within the lead extensions) for the two cases: (b) without discrete dopants; (c) with a D-A pair. It can be noticed that the D-A pair makes the tunnel barrier narrower. Further analysis, covering multiple D-A configurations, will be presented and can provide more insights into the impact of such discrete dopants on BTBT transport.

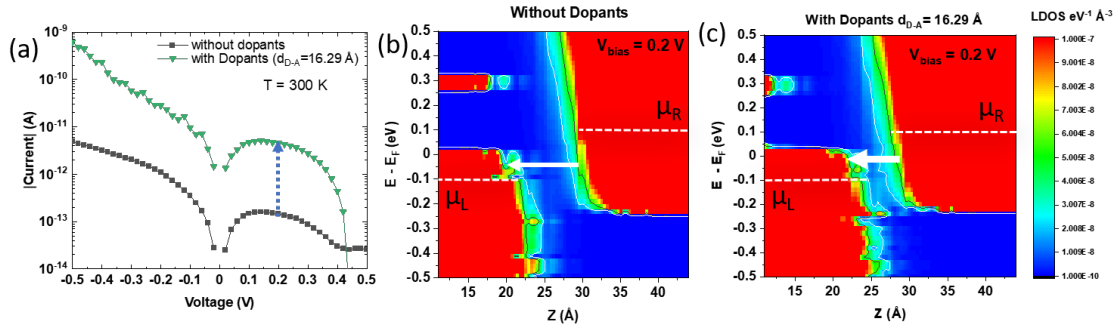


Fig. 2. (a) $|I_p|-V_p$ (current-voltage) characteristics simulated at $T=300$ K for p^+-n^+ diodes without and with a pair of discrete dopants (D-A pair, in this case distanced at 16.29 Å). Current increase, indicated by the arrow, is observed for the case containing a D-A pair. (b)-(c) Local density of states (LDOS) spectra for the two cases at $V=0.2$ V: (b) without discrete dopants; (c) with a discrete D-A dopant pair. Same LDOS range is valid for both graphs

Conclusion

We report a semi-empirical simulation analysis of the impact of a donor-acceptor pair on band-to-band tunneling current by using simplified p^+-n^+ diodes formed in Si nanostructures. By monitoring directly, the BTBT current, an enhancement is observed when a donor-acceptor pair is introduced between the leads. Further analysis of various configurations can reveal the key factors that lead to such enhancement, allowing a deeper understanding of the atomistic effects in future ultimately downscaled BTBT Si devices.

This work is partly supported by Grant-in-Aid for Scientific Research (KAKENHI JP19K04529) from MEXT.

References

- [1] L. Esaki and Y. Miyahara, *Solid State Electron.* **1**, 13 (1960).
- [2] H. Schmid *et al.*, *Nano Lett.* **12**, 699 (2012).
- [3] P. Vogl, H. P. Hjalmarson, and J. D. Dow, *J. Phys. Chem. Solids* **44**, 365 (1983).
- [4] K. Yamaguchi, M. Tabe, and D. Moraru, submitted to *inter-Academia* 2021.
- [5] S. Smidstrup *et al.*, *J. Phys. : Condens. Matter* **32**, 015901 (2020).

A Fluorescent protein-based AND gate for photon coupled protein logic

B. RAKOS

*Department of Automation and Applied Informatics,
Budapest University of Technology and Economics, Hungary*

Abstract

We propose a fluorescent protein AND gate, which can serve as nanometer-scale building block in photon-coupled, protein-based logic circuits. The structure has numerous advantages with respect to previously introduced photoswitchable protein logic gates, such as its simplicity

and faster response time. Furthermore, it can be accomplished with only a single molecule, and fluorescence is the sole requirement, which broadens the choices with respect to photoswitchable proteins. Besides its operational principle, readily available protein AND gates are introduced, and their integration into photon-coupled protein circuits is discussed, as well. We believe that the present work brings the realization of terahertz-speed molecular circuits yet another step closer.

Introduction

The continuous demand for improvements of computing power, combined with the need for sustainable development stimulates the creation of faster, smaller, lower power consuming and dissipating electronic elements in logic circuits, and processors. The application of proteins in such architectures is a potentially promising way due to their numerous advantages [1–4], and they may lead to the development of terahertz-speed computing circuits. Reversibly photoswitchable fluorescent proteins (RSFPs) [5–7] are particularly favorable in this respect [8–10].

RSFPs are a subgroup of proteins, which can be switched between different forms by light with well-defined frequencies, and at least one of their forms has fluorescent properties. Due to the robustness of photon coupling, logic circuits based on photon-coupled RSFPs promise an outstanding stability besides other advantageous properties [8–10].

In previous works, the operation of logic gates in photon-coupled RSFP architectures was based on photoswitching combined with fluorescence [8, 9]. Although such arrangements can be made very fast (terahertz frequencies), each of the two processes (photoswitching and fluorescence) contribute to the speed constraints. This is particularly true in the case of presently existing RSFPs, where the photoswitching process is relatively slow. In this study, we focus on an AND gate, based exclusively on fluorescence. Since the operation of the proposed gate relies on only one process, faster response is expected, therefore its application in photon-coupled RSFP arrangements can further improve the computing speed.

Operational principle

When a fluorescent protein (FP) is subjected to radiation with a well-defined frequency, it emits photons with another specific frequency. The excitation and emitted frequencies are characteristics of the particular molecule. Since in the case of FPs, the only speed-limiting factor is fluorescence lifetime (can be on the order of picoseconds), their incorporation into photon-coupled RSFP protein architectures can boost the speed of the logic circuit. Furthermore, it improves the choice of readily-available proteins as building blocks of such arrangements.

Let us assume that the absence of radiation is treated as logic '0', and its existence means logic '1'. If the sources of the incident exciting radiation on the FP serve as inputs, and the emitted radiation is the output, the molecule operates as a binary OR gate. In the absence of input photons, the FP doesn't emit fluorescent radiation, therefore the output is logic '0'. However, if any of the input sources emit photons with the excitation frequency, the protein demonstrates fluorescence, therefore its output becomes logic '1'.

If RSFP-based inverting gates are applied in the circuit besides the FP-based OR gates, universal binary logic architectures can be designed. We will discuss this method in detail, and the implementation of the aforementioned gates with the aid of readily-available molecules, as well.

Conclusion

In this work, we introduced a fluorescent protein-based AND gate, which can be incorporated into photon-coupled, reversibly photoswitchable fluorescent protein logic architectures. Its two major potential advantages are the improved speed and improved choice of elementary building blocks of such circuits. We will discuss the details of the integration of the proposed gate into photon-coupled protein arrangements, capable of universal computations. Moreover, readily-available proteins suitable for such purposes will be introduced.

References

- [1] Rakos B., "Simulation of Coulomb-coupled, protein-based logic" *J. Auto. Mob. Robot. Intell. Syst.* 2009, 3(4), pp. 46 – 48.
- [2] Rakos B., "Modeling of dipole–dipole-coupled, electric field-driven, protein-based computing architectures" *Int. J. Circ. Theor. App.*, 2015, 43(1), pp. 60 – 72.
- [3] Rakos B., "Pulse-driven, photon-coupled, protein-based logic circuits" *Adv. Intel. Syst. Comput.*, 2016, 519, pp. 123 – 127.
- [4] Rakos B., "Multiple-valued computing by dipole–dipole coupled proteins", *Int. J. Circ. Theor. App.*, 2019, 47(8), pp. 1357 – 1369.
- [5] Ando R., Mizuno H., and Miyawaki A., "Regulated fast nucleocytoplasmic shuttling observed by reversible protein highlighting" *Science*, 2004, 306, pp. 1370 – 1373.
- [6] Stiel A. C., Trowitzsch S., Weber G., Andresen M., Eggeling C., et al., "A bright-state structure of the reversibly switchable fluorescent protein Dronpa guides the generation of fast switching variants" *Biochem. J.*, 2007, 402, pp. 35 – 42.
- [7] Henderson J. N., Ai H. W., Campbell R. E., and Remington S. J., "Structural basis for reversible photobleaching of a green fluorescent protein homologue" *Proc. Natl. Acad. Sci. U. S. A.*, 2007, 104, pp. 6672 – 6677.
- [8] Rakos B., "Pulse-driven, photon-coupled, protein-based logic circuits" *Adv. Intel. Syst. Comput.*, 2016, 519, pp. 123 – 127.
- [9] Rakos B., "Photon-coupled, photoswitchable protein-based OR, NOR logic gates" *Adv. Intel. Syst. Comput.*, 2017, 660, pp. 99 – 103.
- [10] Rakos B., "Modeling and simulation of photon-coupled, fluorescent photoswitchable protein logic", *Int. J. Circ. Theor. App.*, 2020, 48, pp. 2130 – 2140.

An angle-sensitive, nickel bolometer-based, adaptive infrared pixel antenna

M. SHUBBAR, B. RAKOS

*Department of Automation and Applied Informatics,
Budapest University of Technology and Economics, Hungary*

Abstract

The present study proposes an infrared pixel antenna combined with readily-available, angle-sensitive, nickel bolometers. The antenna can automatically optimize itself for the direction of the incident mid-infrared radiation. The structure is expected to improve the performance of infrared sensors used in several areas, such as medicine, telecommunication, and military. Furthermore, it can boost the efficiency of infrared energy harvesting applications, such as rectenna (antenna-rectifier) systems.

Introduction

The development of infrared (IR) sensors faces several challenges related to the cooling requirements, spectral response, responsibility, sensor size and the control of frequency and spatial domains [1]. Their integration with antennas is a potential solution for such limitations, which offers good control of the spatial and frequency domains. Furthermore, the antenna-coupled structures promise spatially compact sensors and large collection areas [2]. K. Kim et al. [3] reports a detectivity seven times higher than that of conventional microbolometers when the sensors are integrated together with 3D feed horn antennas. G. Jayaswal [4] and A. M. A. Sabaawi [5] introduce a bowtie antenna for IR field capture, and they propose a metal-insulator-metal (MIM) diode for rectification of high-frequency currents.

Recently, reconfigurable antennas have gained considerable research interest in order to manipulate the antenna characteristics, suppress excessive noise, and avoid jamming signals, hence maximizing the power transfer [6]. One of the most attractive reconfigurable antenna type is the pixel antenna [7, 8]. It operates in a similar way similar to an LCD screen, which

can display any shape [8]. Such antennas consist of a two-dimensional grid, composed of small metallic patches (pixels), interconnected by switches. By activating or deactivating these switches, the surface, shape, physical length of the antenna can be rearranged, and its current distribution can be altered, which results in the modification of its frequency and radiation characteristics. This reconfiguration principle provides high flexibility and reconfigurability [3–5]. Due to its numerous advantages, in this work, we propose a pixel antenna design. Another important part of our present angle-sensitive antenna design is the bolometer. Bolometers change their resistance if they are irradiated, therefore, they can be applied as radiation-controlled switches. Mohammedi et al. [11] propose an angle-sensitive bolometer design, based on a nickel-metal thin film. Nickel has one of the highest temperature coefficients of resistance (TCR) among available metals. The resistance of the device is in the range of few tens of Ohms in the absence of radiation. The resistance of the structure depends on the angle of incidence of the radiation besides its intensity.

Proposed structure

The proposed pixel antenna is composed of a 3×3 grid of square pixels with $w=1.5\ \mu\text{m}$ side length, separated by a $0.8\ \mu\text{m}$ gap (see fig. 1). The grid structure is located on a SiO_2 layer with an optimized thickness of $0.8\ \mu\text{m}$. The antenna is fed by a $50\ \Omega$ microstrip line with a $0.4\ \mu\text{m}$ width, located on the same side of the substrate. The feed line is backed by a rectangular ground plane with dimensions of $4.9\ \mu\text{m} \times 2\ \mu\text{m}$, placed on the other side of the SiO_2 layer. Both the ground plane and the SiO_2 layer are supported by a $600\ \mu\text{m}$ thick silicon substrate. Small metallic connections are incorporated to interconnect any two adjacent pixels in the grid. Two orientational types of bolometers were used to interconnect the pixels and sensing the different angle of incidence. Six of them were placed in the horizontal direction, and the other six bolometers were placed in the vertical direction.

We will show through simulations that the proposed antenna operates in the mid-infrared band. Furthermore, the simulated characteristics confirm that the structure automatically adapts itself to the direction of the incident radiation, and some of the switched states show evidence of the gain enhancement with respect to the case when all of the pixels are connected.

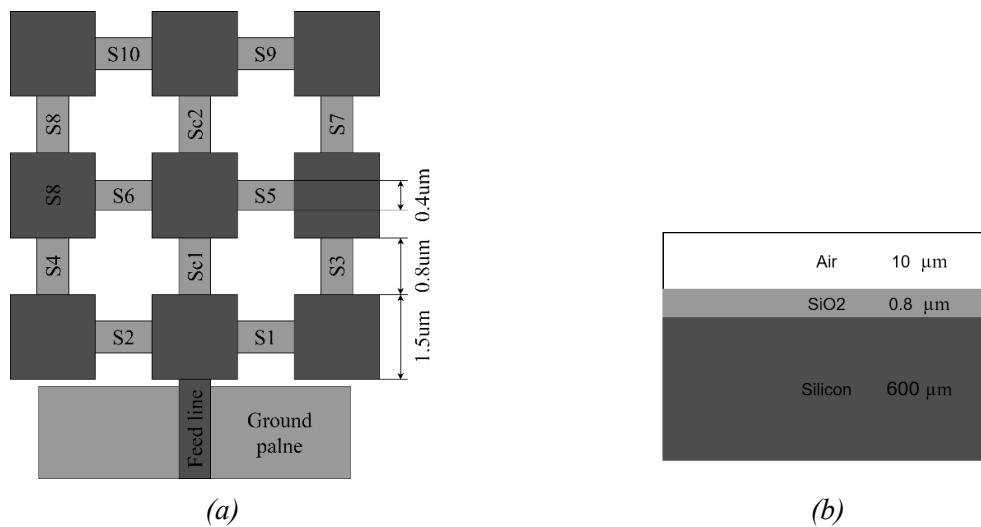


Fig. 1. Antenna geometry (a) and substrate arrangement (b)

Conclusion

A flexible, inexpensive, easily implementable, self-adapting antenna structure was presented in this study. The arrangement is suited for mid-infrared frequencies. The proposed design shows gain enhancement towards the direction of the incident radiation. Its operation will be discussed in detail, backed by simulations.

References

- [1] M. Mubarak, O. Sidek, M. Abdel-Rahman, M. Mustaffa, A. Mustapa Kamal, and S. Mukras, "Nano-Antenna Coupled Infrared Detector Design", *Sensors*, vol. 18, no. 11, p. 3714, Oct. 2018, doi: 10.3390/s18113714.
- [2] J. Alda and G. D. Boreman, *Infrared antennas and resonant structures*. Bellingham, Washington, USA: SPIE Press, 2017.
- [3] K. Kim et al., "3D-feed horn antenna-coupled microbolometer," *Sensors and Actuators A: Physical*, vol. 110, no. 1 – 3, pp. 196 – 205, Feb. 2004, doi: 10.1016/j.sna.2003.09.018.
- [4] G. Jayaswal, A. Belkadi, A. Meredov, B. Pelz, G. Moddel, and A. Shamim, "Optical rectification through an Al₂O₃ based MIM passive rectenna at 28.3 THz", *Materials Today Energy*, vol. 7, pp. 1 – 9, Mar. 2018, doi: 10.1016/j.mtener.2017.11.002.
- [5] A. M. A. Sabaawi, C. C. Tsimeridis, and B. S. Sharif, "Bow-tie nano-array rectenna: Design and optimization," in *2012 6th European Conference on Antennas and Propagation (EUCAP)*, Prague, Czech Republic, Mar. 2012, pp. 1975 – 1978. doi: 10.1109/EuCAP.2012.6206439.
- [6] L. Han, C. Wang, W. Zhang, R. Ma, and Q. Zeng, "Design of Frequency- and Pattern-Reconfigurable Wideband Slot Antenna", *International Journal of Antennas and Propagation*, vol. 2018, pp. 1 – 7, 2018, doi: 10.1155/2018/3678018.
- [7] D. Rodrigo, B. A. Cetiner, and L. Jofre, "Frequency, Radiation Pattern and Polarization Reconfigurable Antenna Using a Parasitic Pixel Layer", *IEEE Trans. Antennas Propagat.*, vol. 62, no. 6, pp. 3422 – 3427, Jun. 2014, doi: 10.1109/TAP.2014.2314464.
- [8] D. Rodrigo and L. Jofre, "Frequency and Radiation Pattern Reconfigurability of a Multi-Size Pixel Antenna", *IEEE Trans. Antennas Propagat.*, vol. 60, no. 5, pp. 2219 – 2225, May 2012, doi: 10.1109/TAP.2012.2189739.
- [9] R. George, C. R. S. Kumar, and S. A. Gangal, "Design of a frequency reconfigurable pixel patch antenna for cognitive radio applications", in *2016 International Conference on Communication and Signal Processing (ICCSP)*, Melmaruvathur, Tamilnadu, India, Apr. 2016, pp. 1684 – 1688. doi: 10.1109/ICCSP.2016.7754451.
- [10] M. Tewari, A. Yadav, and R. P. Yadav, "Frequency reconfigurable antenna: Using pixel ground," in *2016 International Conference on Recent Advances and Innovations in Engineering (ICRAIE)*, Jaipur, India, Dec. 2016, pp. 1 – 6. doi: 10.1109/ICRAIE.2016.7939590.
- [11] E. Mohammadi, B. Behzadnezhad, and N. Behdad, "An Angle-Sensing Infrared Detector Using a Two-Element Biomimetic Antenna Array," *IEEE Trans. Antennas Propagat.*, vol. 66, no. 11, pp. 5818 – 5826, Nov. 2018, doi: 10.1109/TAP.2018.2863112.

First-principles study of bandgap electronic states under electric field in silicon nanowires with discrete dopants

K. YAMAGUCHI^{1,2a}, M. TABE¹, D. MORARU^{1,2}

¹*Research Institute of Electronics, Shizuoka University, 3-5-1 Johoku, Hamamatsu, Japan*

²*Graduate School of Integrated Science and Technology, Shizuoka University*

^a*E-mail: yamaguchi.kensuke.15@shizuoka.ac.jp*

Abstract

Low-dimensional Si tunnel diodes show a significantly different transport behavior than conventional (large-scale) devices due to dopant individuality. In this research, we aim to understand the role of energy states which can be induced in the bandgap by the interaction between a donor-atom and an acceptor-atom in Si nanostructures. By means of *ab initio* (first-principles) simulations, we investigate the correlations between the internal electric field, which is induced by the dopant atoms, and the external electric field applied from outside. We find that a high electric field makes the bandgap small because of a phenomenon equivalent to the Franz-Keldysh effect, even in such a small Si nanostructure. The effect is increased by the internal electric field, which is induced by dopant atoms.

Introduction

In recent years, since the switching speed of MOSFETs approaches a fundamental limitation, the research on tunnel FETs (TFETs) has become critical to realize faster switching based on the band-to-band tunneling (BTBT) mechanism [1]. However, BTBT in Si requires the assistance of phonons due to its indirect-bandgap nature. For this reason, enhancement of tunneling current cannot be easily achieved. In our previous research, we found that, in low-dimensional Esaki diodes, current is steeply enhanced due to BTBT transport via discrete dopant-induced energy-levels, most likely formed by a pair of a boron (B) acceptor and a phosphorus (P) donor in the depletion layer [2]. Also, we reported from *ab initio* simulations that the tunnel (transmission) current could be increased by a preferential position of a P-B pair [3].

In this work, we investigate the effect induced by the dopant atoms on the energy states in the bandgap of Silicon nanowires using LDOS (Local Density of States) under the external electric field. By identifying the energy states of the dopants and tuning them using the external electric field, it can be expected that extended states between donor and acceptor can significantly contribute to further current enhancement.

Method for simulation

The simulation was carried out using an open-source *ab initio* simulation package, OpenMX [4]. All simulations are carried out by using generalized gradient approximation (GGA) PBE. The threshold value for the self-consistent field (SCF) iteration is 10^{-6} Hartree. In order to confirm the effect of a P-B pair, we used Si nanowires with diameters of 1.5 nm, length of 6 nm, as shown in Fig. 1. A pair of dopants are located at several distances from each other along the z-axis, in parallel to the direction of the external electric field. All dangling bonds around the Si nanoplates are passivated by hydrogen. The Si nanowires are embedded in a large supercell with ~ 20 Å of vacuum layer in order to prevent interactions from neighboring supercells. DOS calculations were performed under the external electric field after structure optimization.

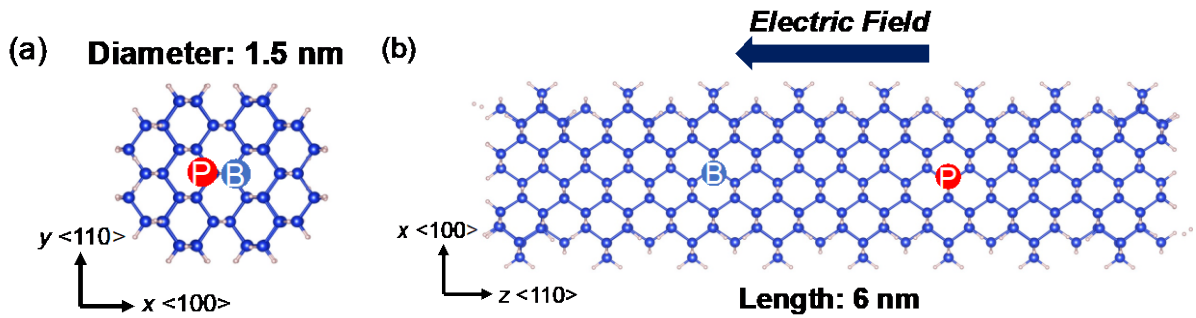


Fig. 1. Silicon nanowire with boron (B) and Phosphorus (P): (a) XY plane view, (b) XZ plane view

Results

The LDOS spectra are shown in Figs. 2(a) and (b), corresponding to the zero-electric field and an electric field of 2.5 V/nm, respectively. At the zero-electric field, a built-in potential can be observed between phosphorus (P) and boron (B) atoms (Fig. 2(a)). The dopant states can also be broadly distributed around each dopant, although significant hybridization with Si states is also expected [5]. On the other hand, extended states are shown in the bandgap between the dopants under the high external electric field (Fig. 2(b)). It is suggested that “gap-states” might be formed between the dopants. However, from a comparison between Figs. 2(a) and 2(b), the gap-states appear to be due to the electronic-state hybridization of states from dopant- and silicon-atoms.

In addition to this, we found that the bandgap decreases gradually in Si nanostructure, as the external electric field increases. This occurs because of the high electric field, which is

equivalent to the “Franz-Keldysh effect” reported for bulk semiconductors. Such a phenomenon occurs even when there is no dopant in the nanostructure. However, the bandgap narrowing is more significant when a pair of dopants is present in the nanostructure, as compared to the non-doped structure. In particular, the inter-dopant distance of 11.6 Å corresponds to the narrowest bandgap obtained in this simulation. This result indicates that preferential positions (distances) of a donor-acceptor pair would lead to obtaining the narrowest bandgap (and likely the highest transmission). On the other hand, the overall trend is relatively similar between co-doped and non-doped structures. Therefore, the difference might come from the internal electric field induced by a pair of dopants. Further analysis will be discussed in the presentation.

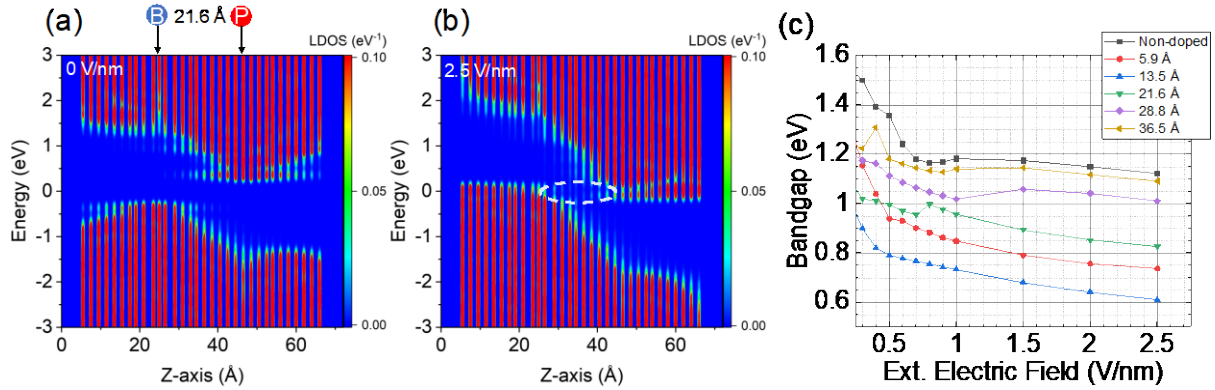


Fig. 2. LDOS spectra for a co-doped Si nanostructure at: (a) zero-electric field; (b) an electric field of 2,5 V/nm. “Gap-states” formed in the bandgap under electric field are encircled. (c) Comparison between estimated bandgap and electric field for several inter-dopant distances and for the non-doped structure

Conclusion

By *ab initio* simulations of Si nanowires, co-doped with a donor-acceptor pair, it is found that an external electric field can assist in enhancing the interaction between a donor-atom and an acceptor-atom. We also found that the bandgap around the co-doped region of the Si nanowires is generally decreased under application of the external electric field. This result suggests the possibility of utilizing such fundamental physics for current enhancement in band-to-band tunneling devices.

Acknowledgements

This work was partially supported by Grants-in-Aid for Scientific Research (KAKENHI No. JP19K04529) from the Ministry of Education, Culture, Sports, Science and Technology (MEXT), Japan. We acknowledge the ACCMS, Kyoto University for providing access to their supercomputer for computation resources.

References

- [1] A. M. Ionescu and H. Riel, *Nature* **479**, 329 (2011).
- [2] M. Tabe, *et al.*, *Appl. Phys. Lett.* **108**, 093502 (2016).
- [3] M. Manoharan *et al.*, JSAP Spring Meeting 2017.
- [4] See <http://www.openmx-square.org/> for the details of DFT method as implemented in OpenMX.
- [5] L. T. Anh, D. Moraru, M. Manoharan, M. Tabe, and H. Mizuta, *J. Appl. Phys.* **116**, 063705 (2014).

Unit 3 “Intelligent and soft computing techniques”

Applications for effective representation of imaging with X-ray CT

H. KASE¹, K. TAKAGI², K. TABATA², T. AOKI^{1,2}
¹Graduate School of Medical Photonics, Shizuoka University,
²Research Institute of Electronics, Shizuoka University

Abstract

X-ray CT technology is currently advanced and provides high contrast and low noise imaging and material identification. Recent technology by AR (Augmented Reality) and VR (Virtual Reality) cannot represent large information by photon counting technology because it has intensity information and energy information. Moreover, the user could not observe internal structure and cross-section images. Two representing systems, by AR, and Spatial Reproduction Display with Motion capture, have been proposed. These systems organize information and allow users to observe the object at any angle intuitively and confirm the cross-sectional image. These problems have been solved and could bring further innovations, such as coloring objects by composition.

Introduction

The technology of X-ray CT is currently advanced and used in various situations. Photon counting technology changed X-ray imaging to provide high contrast and low noise imaging and material identification. On the other hand, AR (Augmented Reality) and VR (Virtual Reality) technologies have also been developed, and it is now possible to represent the data captured by X-ray CT in a virtual space. However, the amount of information that is obtained by photon counting technology, such as composition information of the imaged object is large, and current representation methods simply represent surface information and do not represent data such as internal structures and cross sections that the observer wants to see.

Proposal Systems

Therefore, two methods to effectively represent the data captured by X-ray CT have been proposed. The first one is to use AR to display the 3D objectified imaging data on the screen of a mobile device, allowing the observer to observe the object and its cross-section in the direction of 2π solid angle. The other method is to use a spatial reproduction display and motion capture to allow the user to intuitively understand the internal structure of the object and observe its cross-section by holding the stereoscopic 3D object in their hands and rotating or moving in the virtual space. The system of transferring data is described in Fig. 1 and Fig. 2.

Result and conclusion

On the AR system, the AR image can be displayed according to the angle with the 3D-AR marker so that users can check the cross-sectional image of the object at any 2π solid angle. On the system using spatial reproduction display and motion capture, users can move the 3D data in all directions: up, down, left, right, front and back, and rotate it 360 degrees' view and confirm cross-section of the data, so that understand the internal structure of the material intuitively. These proposed methods have solved the problems that information obtained by photon counting technology is large and conventional representation could not display internal structures and cross-sections of the object. This system will be able to bring further innovations in the future, such as coloring objects according to their composition.

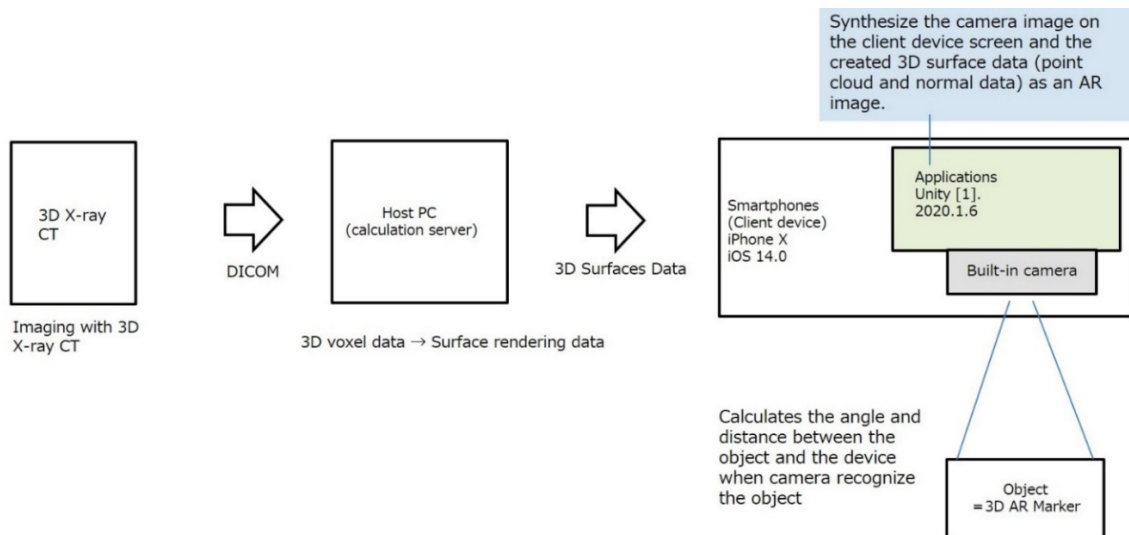


Fig. 1. Proposal system of representing data using AR

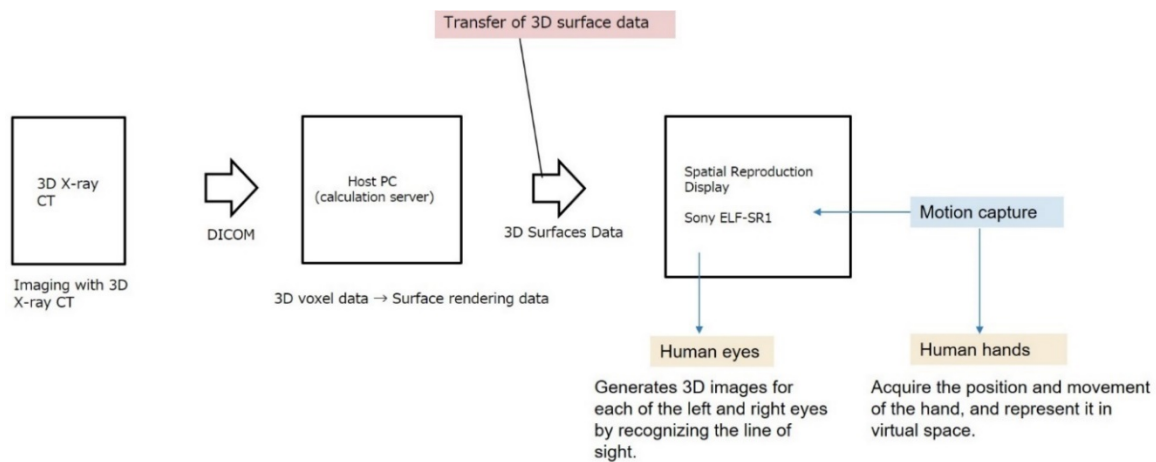


Fig. 2. Proposal system of representing data using Spatial Reproduction Display and Motion capture

A parallelization of instance methods of a .NET application that search for required structured data stored in a skip list

I. KOŠŤÁL

University of Economics in Bratislava, Faculty of Economic Informatics, Department of Applied Informatics, Dolnozemska cesta 1, 852 35 Bratislava, Slovakia, e-mail: igor.kostal@euba.sk

Abstract

The skip list is a more memory efficient version of a single level linked list. Searching for the required data elements in a skip list is more efficient than in a single level linked list because a skip list allows us to skip to the searched element in it. We have created a C# .NET application that uses a skip list with structured data in its data elements. This application can perform search operations within these data elements using serial, threaded, and parallelized instance methods, and simultaneously it is able to measure the execution times of particular methods. By comparing these times, we have examined the execution efficiency of parallelized instance methods of the object of the .NET application compared to threaded and serial

instance methods of the same object. The results and evaluation of this examination are listed in the paper.

Introduction

A single level linked list (a simple list) is a dynamic data structure that is used for storing data in applications. However, there are also multi-level linked lists (called skip lists [4]) that are more complicated for creating but searching for the required data elements in them is more efficient because they allow us to skip to the searched element in them.

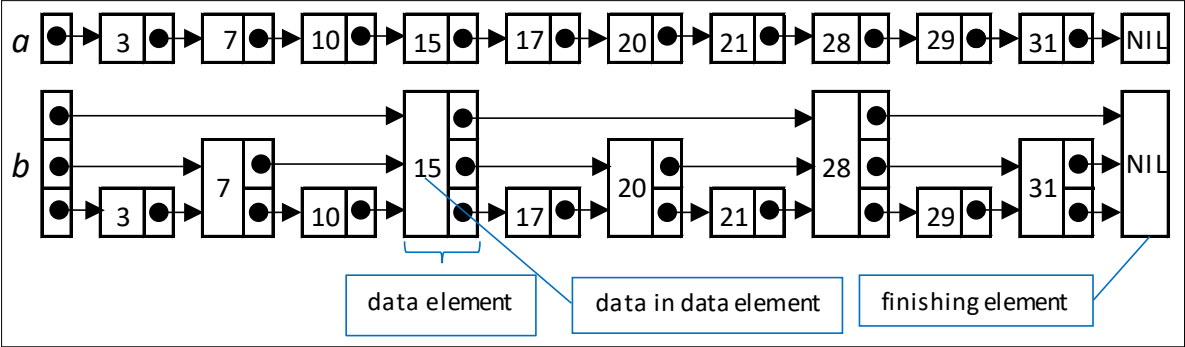


Fig. 1. The simple list (a) and the skip list (b) with simple, unstructured data in their data elements [4]

We dealt with a comparison of execution efficiency of the use of a skip list and simple list in a C# .NET Application [1]. This application had the same structured data of students stored in the data elements of its skip and simple list. The results of the comparison of the execution times of the search operations and the insertion operation performed by our .NET application in the skip list and execution times of the same operations performed by the same application but in a simple list clearly illustrate that the use of the skip list in this application was with a bigger number of data elements containing structured data, significantly more efficient [1]. We were interested in now, how to parallelize search operations in a skip list with the structured data of students in its data elements. We have created a C# .NET application that uses a skip list with such data elements. This application parallelizes the execution of search instance methods in its instance methods, and at the same time, measures the execution times of its serial and parallel instance methods. By comparing these times, we have examined the execution efficiency of parallelization of search instance methods of our C# application. The results and evaluation of this examination are listed in the paper.

Parallel Programming in the .NET Framework

In parallel programming in the .NET Framework, we know two kinds of parallelism – data and task parallelism. Data parallelism refers to scenarios in which the same operation is performed concurrently (that is, in parallel) on elements in a source collection or array. The term task parallelism refers to one or more tasks running concurrently. A task represents an asynchronous operation, and in some ways, it resembles the creation of a new thread or *ThreadPool* work item but at a higher level of abstraction. [2] Data and task parallelism are used in a parallelized code of our .NET application.

C# .NET Application, Experiment, and Its Results

Our .NET application was developed in the C# language in the development environment Microsoft Visual Studio 2019 Enterprise for the Microsoft .NET Framework version 4 and for the Microsoft Windows 10 operating system. The .NET application has the structured data of students stored in the data elements of a skip list. This application can perform search operations within these data elements using serial, threaded, and parallelized instance methods, and simultaneously it is able to measure the execution times of particular methods.

We performed the experiment to measure the execution efficiency of parallelized instance methods of the object of the .NET application compared to threaded and serial instance methods of the same object. Then we evaluated and described the results of the experiment.

Conclusion

In the conclusion we discuss the experiment and its results.

References

- [1] Košťál, I., "Comparison of Execution Efficiency of the Use of a Skip List and Simple List in a .NET Application", Recent Advances in Technology Research and Education Proceedings of the 17th International Conference on Global Research and Education Inter-Academia – 2018 (Springer Nature Switzerland AG 2019, Springer, Cham, 2019, pp. 252 – 259).
- [2] Microsoft Corporation, "Documentation", (Microsoft Corporation, 2021), retrieved from <https://docs.microsoft.com>, (2021, July 11).
- [3] Niemann, T., "Sorting and Searching Algorithms" (epaperpress.com, 1999).
- [4] Pugh, W., "Skip Lists: A Probabilistic Alternative to Balanced Trees" Communications of the ACM, 33(6), pp. 668 – 676. (1990).

Deep learning applications for COVID-19: a brief review

H. TABRIZCHI¹, J. RAZMARA¹, A. MOSAVI², A. R. VÁRKONYI-KÓCZY³

¹ *Department of Computer Science, Faculty of Mathematical Sciences,
University of Tabriz, Tabriz, Iran*

² *John von Neumann Faculty of Informatics, Obuda University, Budapest, Hungary*

³ *Institute of Software Design and Software Development,
Obuda University, Budapest, Hungary*

Abstract

Since December 2019, coronavirus disease (COVID-19) has affected most parts of human life. With the progression of time, COVID-19 was declared by the world health organization as an outbreak. Deep learning has been praised as one of the top methods in image-based healthcare applications. For this reason, a great number of research works have been proposed for the development of smart image-based diagnosis devices for the detection of COVID-19. This paper elaborates on summarizing the state-of-the-art research works related to deep learning applications for COVID-19 medical image processing to shed light on the accelerated use of Deep Learning for COVID-19 research.

Intelligent pantry: a low-cost smart storage manager for food spoilage prevention

B. TUSOR^{1,2,a}, T. J. TÓTH^{1,b}, A. R. VÁRKONYI-KÓCZY^{1,2,c}

¹ *Department of Mathematics and Informatics, J. Selye University, Bratislavská Str. 3322,
P.O. BOX 54. 945 01, Komárno, Slovakia*

² *Software Engineering Institute, Óbuda University, Bécsi Str. 96/b, 1034, Budapest, Hungary*
^atusorb@ujs.sk, ^btothj@ujs.sk, ^cvarkonyi-koczy@uni-obuda.hu

Abstract

Home storage of various perishable goods (e.g., food items, sanitary products, medical supplies, etc.) is an integral part of any household. It gains even more importance in

unexpected events such as pandemics when people tend to stock up for months ahead. However, with higher amounts of perishable items, the probability of food spoilage (and thus, food waste) occurring is also higher unless each item is carefully accounted for. This paper presents a novel smart storage framework for tracking the expiration date and location of stored items and providing users with information and warnings about the goods in the storage using cheap, affordable devices. Furthermore, the system can act as an advisor about replenishing supplies by learning the consumption habits and priorities of its users.

Introduction

In the past decades, smart home environments have become more and more affordable, giving average households more control over their home faculties. Pantries are perhaps one of the most important parts of each household, storing various perishable goods ranging from food items, sanitary products to medical supplies, etc. In case of unexpected events such as pandemics, when there is a danger of shortage of any of these products, it is a good idea to keep a healthy amount of stocks. However, with higher amounts of perishable items, the probability of food spoilage (and thus, food waste) occurring is also higher unless each item is carefully accounted for. Another problem is the localization of the items in question.

This paper presents the Intelligent Pantry (iPantry), a novel smart storage framework for tracking the expiration date and location of stored items and providing users with information and warnings about the goods in the storage. The framework is an Intelligent Space (iSpace [1]) application: the central computing module of the system, the so-called iPantry Manager, is based on the DIND (Distributed Intelligent Networking Device) schema, which the iSpace is built upon.

Fig 1. shows the architecture of the proposed Smart Storage framework.

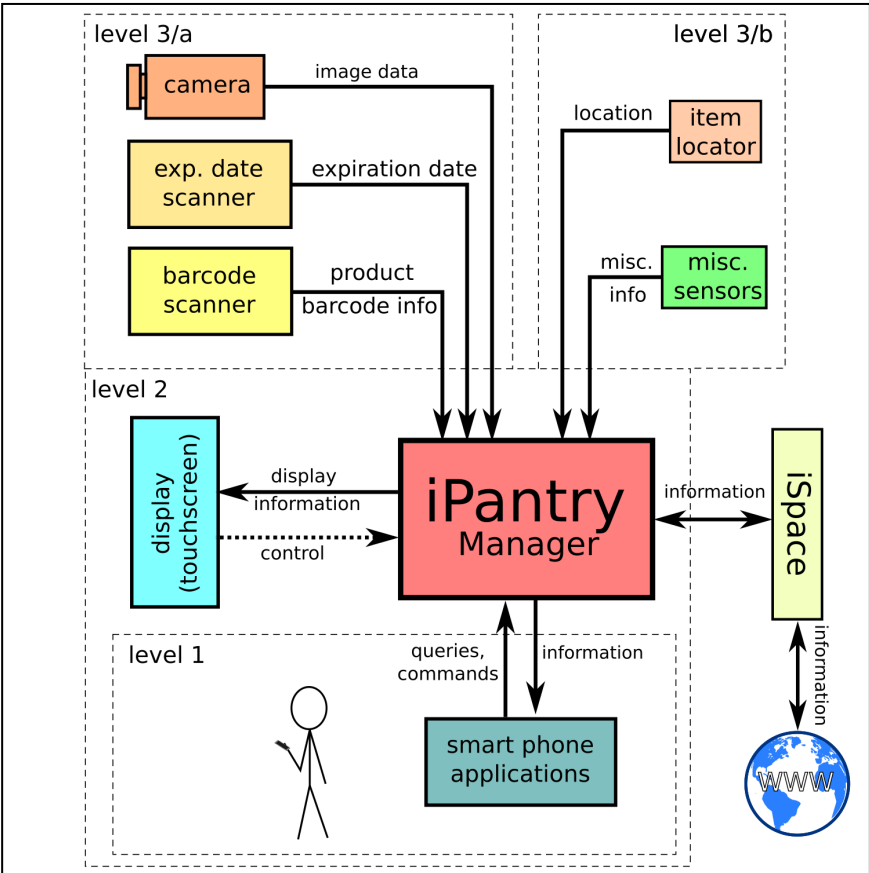


Fig. 1. The general architecture of the Intelligent Pantry framework

Given the complexity and cost of the various functionalities of the system, the framework can be distinguished into different levels. At level 1, the most cost-effective implementation is a smart phone application, which can provide the basic functions, i.e., keeping track of the stocks (expiration and presumed location). The user can manually enter each item, take note of its expiration date and the location it has been deposited to, and thus, the system can provide warnings on the approaching expiration date, as well as help locate the items in question. The user habit and preference learning, which is done using fuzzy inference machines, can also be implemented in most modern smartphones. Of course, this level has the least amount of convenience. Furthermore, the access is also restricted to a single person.

At level 2, the main processing functions and the database (the iPantry Manager module) are implemented in a suitable low-cost (single board) computer, like the Raspberry PI 4B [2]. Multiple users can access it through smartphone applications, as well as optional interfaces (such as touch-based displays).

Level 3 is divided into more two parts, both of which add more functionality (and thus, more comfort and convenience) for the user, but the two parts can still be used without each other. Level 3/a can provide barcode scanners and image data for easier (and faster) product registration, as well as expiration date scanners for expiration date registration. Lastly, level 3/b can provide further aid with locating given items (e.g., through RFID localization [3]), and provide further information (e.g., using weight scales in the storage compartment to see if there has been any access to said compartment, and as a result, a change in the content).

The framework is made to be compatible with the general iSpace architecture. Thus, it can connect to other iSpace applications in the household (such as a Smart Fridge Agent [4], so they can keep in contact in order to implement a complex system that can account for perishable items inside and outside of the fridge).

Conclusion

This paper presents an iSpace-based novel smart storage framework for average homes, primarily for the tracking of the expiration date and location of stored items and providing users with information and warnings about the goods in the storage using cheap, affordable devices. Various options are explored in order to create a system that can be tailored to the needs (and financial situation) of the user. Furthermore, the system can advise the user in the replenishment of the stocks, for which a fuzzy logic-based inference is used.

Acknowledgement

This publication the result of the Research & Innovation Operational Programme for the Project: "Support of research and development activities of J. Selye University in the field of Digital Slovakia and creative industry", ITMS code: NFP313010T504, co-funded by the European Regional Development Fund.

References

- [1] Hashimoto, H., "Intelligent space: Interaction and intelligence", *Artificial Life and Robotics*, vol.7, no.3, pp. 79 – 85 (Sep., 2003).
- [2] Gay, W. W. "Raspberry Pi Hardware Reference". (2014) DOI: 10.1007/978-1-4842-0799-4.
- [3] Huang, S. and Shi, Z. H. "An Application of Autonomous Learning Multimodel System for Localization in Industrial Warehouse Storage Rack". (2019) pp. 519 – 522. DOI: 10.1109/ICMLA.2019.00097.
- [4] Tusor, B. Gubo, S., Kmet', T., Tóth, J. T. "Augmented Smart Refrigerator – An Intelligent Space Application". (2020) DOI: 10.1007/978-3-030-36841-8_17.

Unit 4 “Internet based education, distance learning”

The use of design automation tools in training young specialists in radio electronics

A. A. SEREDA, S. V. SHALUPAEV, Yu. V. NIKITJUK
Francisk Skorina Gomel State University, Gomel, Republic of Belarus

Abstract

The paper considers the stages of mastering the computer-aided design of printed circuit boards for students of radio engineering specialties. The scheme allows a recent graduate to more effectively master the phases of constructing electronic devices and acquire professional skills in the development of printed wiring elements.

Introduction

Using classical methods and means of “manual” design, it is currently impossible to carry out quality and timely production design engineering. The complexity of the designed objects makes it impossible to produce sufficiently high-quality design documentation within a reasonable period of time. The design automation system is intended to carry out the design process with an optimal distribution of functions between the developer and the PC and to ensure maximum automation of all design procedures.

Phases of mastering systems for designing printed wiring elements

To develop any electronic device, it is necessary to go through several phases: develop the concept of the future product, its input and output parameters, operating modes and then develop the electrical circuits of the device, implement them on printed circuit boards, design the frame product, and much more. Computer-aided design systems are widely used to optimize this process. They allow preliminary computer modeling of the operation of circuit schematics, the optimal layout of radioelements on a printed circuit board and tracing the conductors, and, if necessary, make design changes before manufacturing a prototype.

Currently, there are numerous software packages to automate the processes of circuit simulation. These are Sprint-Layout, Eagle, DipTrace, ExpressPCB, TARGET 3001, FreePCB, Kicad, DesignSpark PCB, SoloPCB Design, PCB123, TopoR, Pad2Pad, PCB-Investigator, EDWinXP, P-CAD, Mentor Graphics PADS, ZenitPCB, CADSTAR Express, ZofzPCB 3D Gerber Viewer, PCBWeb, CometCAD, Layo1 PCB, PCB Elegance, NI Ultiboard, CAM350, BoardMaker3, GerberLogix, PCB Artist, VUTRAX, CADintPCB, etc. A brief description on each of them is provided by [1] and the official websites of the manufacturers. Each of them has its own advantages and disadvantages. Some packages are free, but they have a limited feature set (for example, GerberLogix); some are focused on a narrow range of tasks (for example, only for the development of a drawing of conductors, as in Layo1 PCB and Sprint-Layout, or only for modeling electrical circuits); others have good functionality, but a rather complex interface, etc.

Specialists in radio electronics should have experience in various software products that allow to development of an electronic device of any complexity in the shortest possible time and as efficiently as possible. Laboratory workshops facilitate the process. Teachers and students majoring in radio engineering can use them not only during laboratory classes but also as practical reference guides for self-study and mastering, as well as for distance learning. While studying the principles of designing electronic devices, the future specialist needs to follow the "simple-to-complex" principle, consistently mastering the principles of designing printed circuit boards. For example, the first projects can be performed with Sprint-Layout software. It has a simple, intuitive interface but a limited feature set in automating the layout of elements and

tracing conductors, designing multilayer boards, importing electrical circuits, etc. So, it is ideal for a beginner radio amateur and allows mastering the steps and features of the manual and semi-automatic design of printed circuit boards without building 3D models of radioelements and the possibility of importing electrical circuits into the project. On receiving basic skills in such a software product, it is easier for a young specialist to master professional design packages that allow developing a multilayer board project using vias, signal and ground layers, the ability to import electrical circuits, etc. For example, the second software product to learn could be Ultiboard by National Instruments. Here you can import electrical circuits from the Multisim program, develop 3D models of radioelements, create vias, prohibition zones, and much more. After mastering this product, a future specialist can move on to mastering professional end-to-end design programs that allow all phases of the electronic device development to be implemented in a single project, i.e., to export a developed circuit diagram to a module for designing printed circuit boards, place the resulting three-dimensional models in a 3D modeling module and convert them to drawings for design documentation. Altium Designer can be such a software product. At the same time, some of the specialized interface elements, functions, menu items will be easier to understand and master for a specialist who has already become familiar with easier software packages.

Conclusion

The concept described above was implemented in laboratory workshops for students of the Department of Radiophysics and Electronics at Francisk Skorina Gomel State University. Starting with simpler design systems in the early years of study and mastering more professional software packages in senior years, graduates become specialists in radio electronics and can work effectively in the electronics industry. Fig. 1 shows the development results of projects in different design systems.

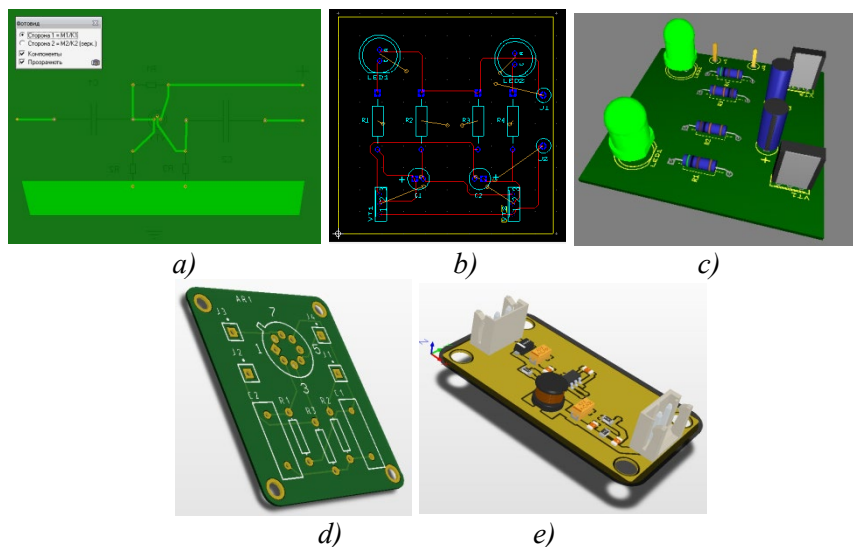


Fig. 1. The result of project development in different design systems:
a) – Sprint – Layout; b), c) – Ultiboard; d), e) – Altium Designer

References

- [1] PCB design software [Electronic resource] / MMO “Electric soldering iron site” – URL: https://cxem.net/software/soft_PCB.php.

Unit 5 “Manufacturing technology”

Effects of process parameters on the dissimilar friction stir welded joints between aluminum alloy and polycarbonate

A. AZHAGAR, K. SAKAI, H. SHIZUKA, K. HAYAKAWA
*Graduate School of Science and Technology, Shizuoka University,
Johoku, Hamamatsu 432-8011, Japan.*

Abstract

Effects of processing parameters on weld interface and material flow during friction stir welding of dissimilar materials were investigated. The tapered cylindrical tool pin made of SKD11 was used to improve the in-process material flow behaviors during the process. In the experiments, 3 mm thick plates of AA2017 aluminum alloy and polycarbonate were used as materials for welding at a tool rotation speed of 1320 or 1760 rpm, travel speed of 60 mm/min, and tool offset of 2, 3 or 4 mm toward AA2017. The experiments found the suitable process parameters for the butt welded joint between the AA2017 and polycarbonate.

Introduction

Friction stir welding (FSW) is a solid-state joining process that uses a non-consumable tool to join two facing workpieces without melting the workpiece material. In this process, heat is generated from the friction between the rotating welding tool (including both the shoulder and the probe) and the material being welded, causing the material to soften at a temperature lower than its melting point. The softened material underneath the shoulder is further subjected to deformation by the rotational and transverse movements of the tool. Accordingly, the tool geometry has a considerable influence on the weld properties.

Derazkola et al. studied dissimilar joining of AA5058 and polycarbonate along with combination of tapered cylindrical tool pin geometry of FSW tool with a tilt angle of 2° is performed¹⁾. Moshwan et al. has performed the dissimilar joint between polycarbonate and AA7075 with tapered cylindrical tool pin profile²⁾. Khodabakshi et al. Have studied the dissimilar FSWeld joints on AA5058 and PMMA along with a combination of tapered cylindrical tool pin with tilt angle of 2° was performed³⁾. This paper investigates the effects of process parameters on the dissimilar friction stir welded joints between aluminum alloy and polycarbonate to clarify the suitable condition for sufficient joint efficiency.

Experiments

Aluminum alloy AA2017 (Al) and polycarbonate (PC) with dimensions of 100 mm x 50 mm x 3 mm were joined via FSW in a butt configuration. Tapered cylindrical tool pin made of SKD11 tool steel with shoulder diameter of 18 mm and tool pin height of 2.7 mm was used. Tool rotation speed of 1320 or 1760 rpm, travel speed of 60 mm/min, and plunge depth of 2.74 mm was adopted. The tool offset towards Al was varied as 2, 3 and 4 mm. The tensile tests were carried out after welding to evaluate joint efficiency. The specimens for the tests were prepared from three regions of the welded material (start, middle, and end), according to the size and procedure mentioned in ASTM E8.

Results and Discussion

Table 1 shows the resulting ultimate tensile strength of the joint to the process parameters of tool offset and rotational speed. It is observed that the tool offset of 3 and 4 mm leads to much lower tensile strength than the tool offset of 2 mm. Fig. 1 shows the material flow at the joint interface between Al and PC, where (a) to (f) show the results by the experimental conditions

(a) to (f) in Table 1. The highest and lowest ultimate tensile strengths of 33.4 MPa and 3.60 MPa were obtained from experimental conditions (f) and (b), in which the tool offset of 2 mm and 4 mm was used. The tool pin offset of 2 mm enhanced material flow along with the weld interface. From Fig.1 (e) and (f), non-uniform material flow along the weld zone due to high rotational speed and highly deformed material flow is observed. On the other hand, Fig.1 (a) and (b) show the shoulder influenced weld formation due to the improper material fusion between the two dissimilar materials and reduced tool pin interaction at the weld zone, which has led to lower tensile strength. Fig.1 (c) has exhibited a tunnel-like appearance throughout the weld joint due to tool pin progress. In Fig. 1 (d), regular Weld formation is observed.

Table 1. FSW process parameters with an ultimate tensile strength of joint

Experimental condition	Tool offset (mm)	Rotational speed (rpm)	Ultimate tensile strength (MPa)		
			(Start) Test 1	(Middle) Test 2	(End) Test 3
(a)	4	1760	4.49	3.70	3.80
(b)		1320	4.20	3.80	3.60
(c)	3	1760	5.60	4.60	4.40
(d)		1320	4.49	5.00	4.60
(e)	2	1760	33.10	4.80	4.49
(f)		1320	5.80	33.40	4.80

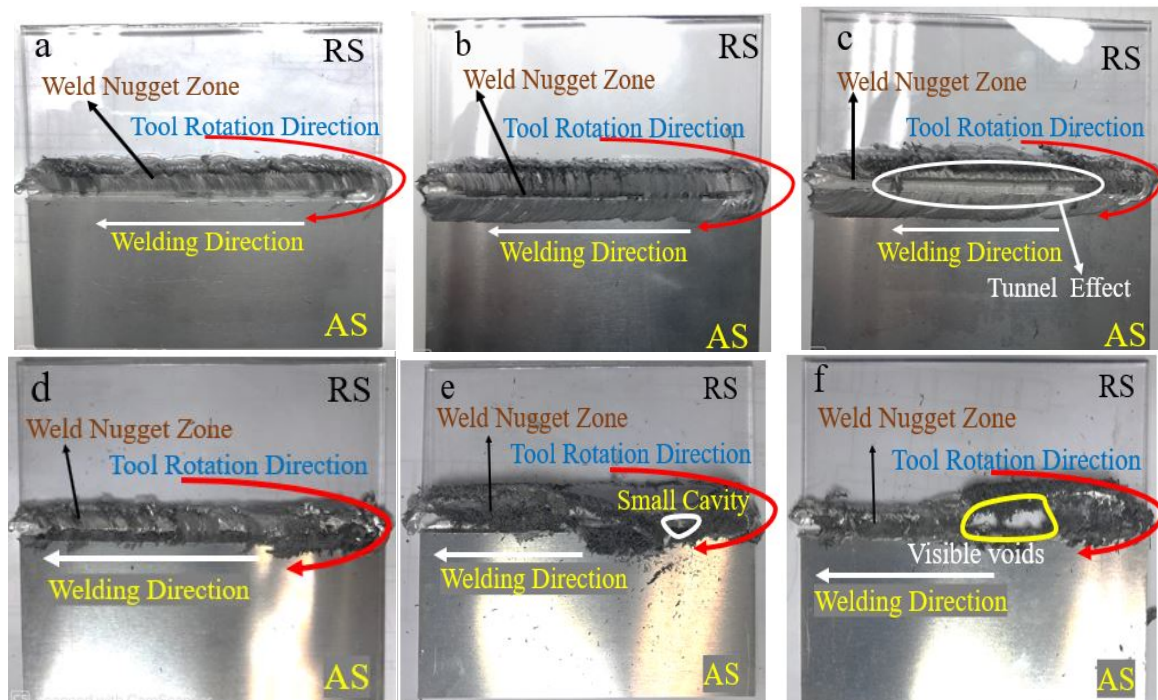


Fig. 1 Material flow at joint interface. (a) to (f) correspond to experimental condition (a) to (f) in Table 1

Conclusion

The effect of tool pin offset on joint efficiency was evaluated based on the tensile strength of the welded samples. The results showed that the FSW with a tool pin offset of 2 mm, the rotational speed of 1320 rpm, and travel speed of 60 mm/min recorded a higher tensile strength. Since the tool shoulder and pin enhanced the heat transfer, the decrease of the tool pin offset, which enhanced a smaller number of voids and defects in the weld surface and in terms increase weld strength. The findings of this study can be used to develop an improved

tool pins profile along with optimized process parameters that can produce superior dissimilar friction stir welds.

References

- [1] H. A. Derazkola, M. Elyasi, "The influence of process parameters in friction stir welding of Al-Mg alloy and polycarbonate", *J. Manuf. Process.*, 35 (2018), 88 – 98.
- [2] R. Moshwan, M. Sahifulddin, and F. Yusof, "Dissimilar friction stir welding between polycarbonate and AA7075 aluminum alloy", *Int. J. Mater. Res.*, 105 (2014), 1 – 9.
- [3] H. A. Derazkola, R. K. Fard, and F. Khodabakshi, "Effects of processing parameters on the characteristics of dissimilar friction-stir-welded joints between AA5058 aluminum alloy and PMMA polymer", *Int. Institute of welding.*, 62 (2018), 117 – 130.

Unit 6 “Material science and technology, smart materials”

Investigation on influence of Cu doping on thermoelectric performance of tin-selenide-based nanostructures

S. ATHITHYA^{1,3}, H. IKEDA^{3,4}, M. NAVANEETHAN^{1,2}, S. HARISH¹, J. ARCHANA¹

¹Functional Materials and Energy Devices, Department of Physics and Nanotechnology, SRM Institute of Science and Technology, Kattankulathur, Chennai, 603 203, Tamil Nadu.

²Nanotechnology Research Center, SRM Institute of Science and Technology, Kattankulathur, Chennai, 603 203, Tamil Nadu.

³Graduate School of Science and Technology, Shizuoka University, 3-5-1 Johoku, Naka-Ku, Hamamatsu, Shizuoka 432-8011, Japan.

⁴Research Institute of Electronics, Shizuoka University, 3-5-1 Johoku, Naka-Ku, Hamamatsu, Shizuoka 432-8011, Japan

Abstract

Tin selenide (SnSe) has attracted more interest as thermoelectric material due to the anharmonic nature and anisotropy. Thus, a high ZT of 2.6 has been achieved for a single crystalline SnSe. We have explored the effect of Cu doping on the nanostructured SnSe synthesized via the ball milling method. The presence of Cu as well as nanostructuring plays a crucial role in reducing thermal conductivity and enhancing power factor compared with pristine SnSe. Cu⁺ ions provide more hole carriers, which leads to enhance the electrical conductivity. The higher doping concentration of Cu contributes to a lower thermal conductivity of around 0.85 W/mK at 280 K, which is improved by one order of magnitude compared with pristine SnSe 1.8 W/mK at 280 K.

Introduction

Substantial increase in the world's population as well as the number of industries, the demand for energy also increases. The depletion of fossil fuels urges researchers to consider alternative ecological energy resources for energy harvesting [1]. Thermoelectric materials can realize the direct conversion between thermal and electrical energies, which are expected to be widely applied in the field of waste heat recovery and power generation. To evaluate the thermoelectric conversion efficiency of materials, a dimensionless figure-of-merit ZT has been defined as $ZT = S^2\sigma T/\kappa$, where S is the Seebeck coefficient, σ is the electrical conductivity, T is the absolute temperature, and κ is the thermal conductivity. A bulk polycrystalline SnSe-based material exhibited a peak ZT of ~1.2, which is very low compared to single crystalline SnSe (~2.6). Therefore, many researchers have focused on various strategies, such as carrier engineering, band engineering, defect engineering etc., in polycrystalline SnSe materials to enhance ZT [2]. Thus, due to the necessity of enhancement in thermoelectric properties of SnSe, we have chosen polycrystalline SnSe and selected the dopant as Cu to improve the power factor.

Results and discussions

XRD diffraction pattern of as-prepared sample is shown in Fig. 1(a) and shows that there is pristine SnSe matched with an orthorhombic pnma phase [JCPDS (48 – 1224)] [3]. In Figs. 1(b) – 1(d), the total thermal conductivity (κ_{total}) can be calculated by the equation $\kappa_{\text{total}} = D \cdot C_p \cdot \rho$, where C_p is the specific heat capacity at constant pressure, D is the thermal diffusivity and ρ is the density. It is found that the higher doping concentration (10 wt%) of Cu contributes to a low thermal conductivity around 0.85 W/mK, which is lower than pristine SnSe

(1.8 W/mK) at 280 K. The specific heat capacity of Cu-doped SnSe is lower than pristine SnSe. In addition, an increase in temperature leads to a decrease in thermal diffusivity.

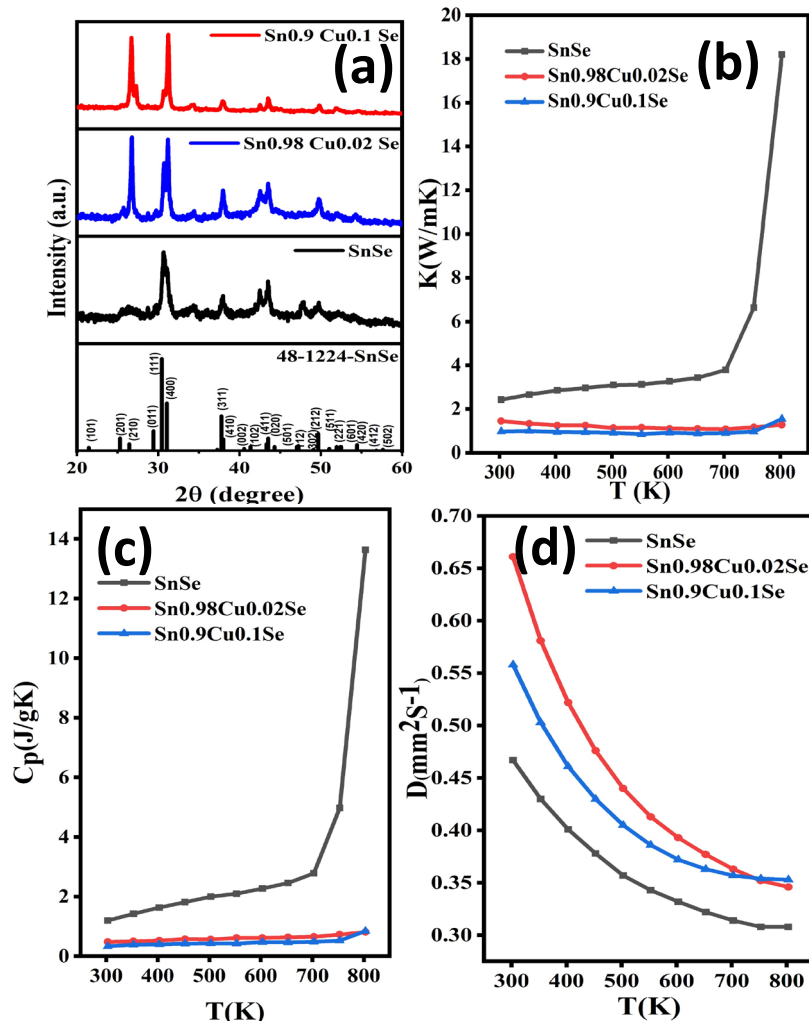


Fig. 1: (a) XRD pattern of SnSe and Cu-doped SnSe, temperature dependent of (b) total thermal conductivity (κ_{total}), (c) specific heat capacity (C_p), and (d) thermal diffusivity (D)

Conclusion

Pristine and Cu-doped SnSe materials were prepared by ball milling and their pelletization was carried out by hot pressing method. The structural analysis using XRD showed the existence of an orthorhombic pnma structure of SnSe. The higher doping concentration of Cu realized a low thermal conductivity of 0.85 W/mK at 280 K and improved by one order of magnitude compared with pristine SnSe 1.8 W/mK.

Reference

- [1] N. Toshima, Recent progress of organic and hybrid thermoelectric materials, Synth. Met. 225 (2017) 3 – 21. <https://doi.org/10.1016/j.synthmet.2016.12.017>.
- [2] H. Xi, L. Luo, G. Fraisse, Development and applications of solar-based thermoelectric technologies, Renew. Sustain. Energy Rev. 11 (2007) 923 – 936. <https://doi.org/10.1016/j.rser.2005.06.008>.
- [3] R. Maa, G. Liu, J. Li, Y. Li, K. Chen, Y. Han, M. Zhou, L. Li. Effect of secondary phases on thermoelectric properties of Cu₂SnSe₃, Ceramics International, 43(2017)7002 – 7010. <https://doi.org/10.1016/j.ceramint.2017.02.126>.

Isotropy mechanical properties products with geometry triple periodic minimal surfaces (TPMS)

S. V. BALABANOV¹, A. I. MAKOGON¹, K. S. KOSHEVAYA², M. M. SYCHEV^{1,2}

¹Institute of Silicate Chemistry RAS

²Saint-Petersburg State Technological Institute (Technical University)

Abstract

The impetuous development of science and technology makes ever-higher demands on structural materials. Therefore, the creation of new cellular materials with increased operational characteristics is a relevant task. Cellular structures make it possible to optimize the ratio between material strength and weight. This work presents several research results of the anisotropic mechanical properties of cellular structures with the geometry of triply periodic surfaces (TPMS) produced by additive manufacturing.

Introduction

Triply periodic minimal surfaces are surfaces with a minimal area bounded by a given contour, without self-intersections and unrestrictedly translating in a lattice of the third rank.

Paper [1] shows that products with TPMS geometry are able to dissipate energy in the most efficient way.

Theoretically, the direction of the load application should not have any effect. This research aims to study the isotropy of the mechanical properties of products with TPMS geometry.

The manufacture of products with TPMS geometry used additive technologies [2–3]. This study used selective laser sintering (SLS).

Experimental Procedure

An implicit method was used for the modeling of samples. A number of TPMS can be described by approximation equations. For the Schwarz P-surface; the equation has the form (1):

$$\cos(x)+\cos(y)+\cos(z)=t \quad (1)$$

Changing the parameter t allows to variate the geometry, and specifically the size of the repeating structural element and the properties of the resulting objects.

The samples with the Schwarz P-surface geometry were modeled; $t \in [-0.9; 0.9]$, the step is 0.3, (Fig. 1a). In order to assess the isotropy, samples were cut off by a cube rotated by 45°, Fig. 2, Fig. 1b.

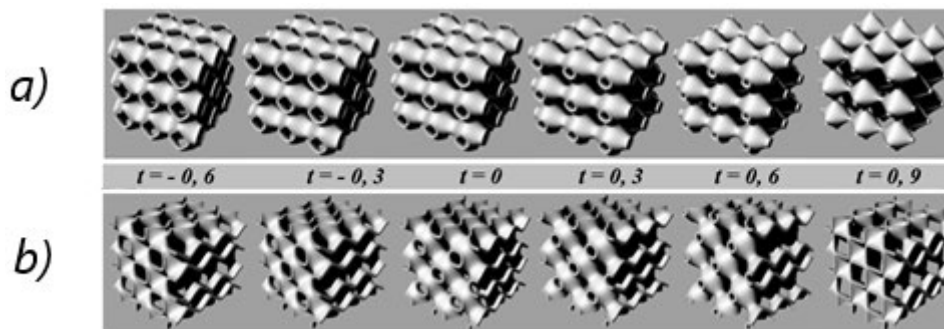


Fig. 1. Renders of 3D models with different parameter t

Based on the designed 3D models, samples were made, which were obtained by selective laser sintering (SLS technology) on an EOS FORMIGA P100 3D printer. The wall thickness of the samples is 0.8 mm. The dimensions of the samples are 30 × 30 × 30 mm.

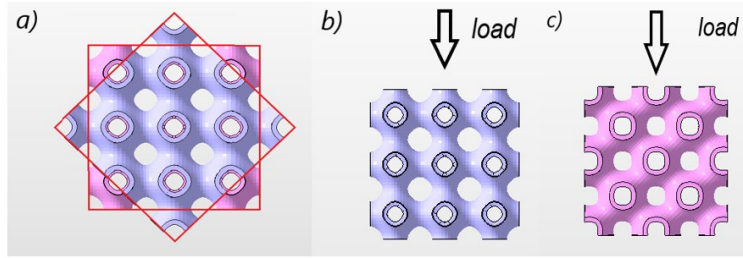


Fig. 2. Renders of 3D models of specimens with geometry "primitive Schwartz" a) 3D model at $t = 0$ & 3D model at $t = 0$ for loading at an angle b) Sample at $t = 0$ c) 3D model at $t = 0$ for loading at an angle

During the research of physical and mechanical properties, the samples were tested for compressive strength according to ISO 604:2002 on an electromechanical machine Shimadzu AG-X-50kN. Results of the tests reveal the strength characteristics of the specimen (Fig. 3).

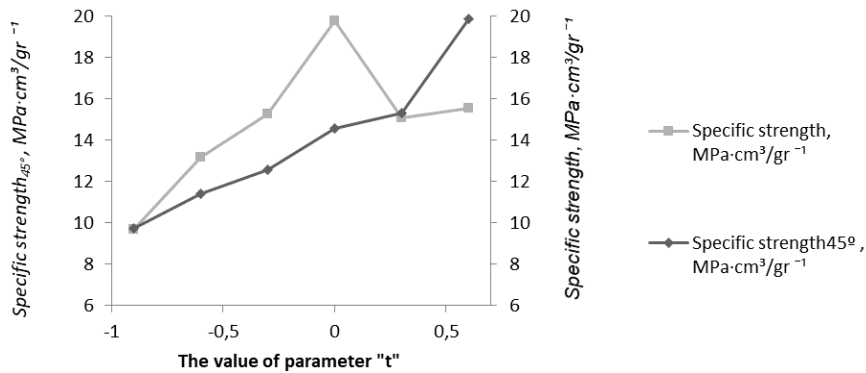


Fig. 3. Mechanical properties of products with TPMS geometry

Results and conclusion

Using method SLS 3D-printing, the samples with the Schwarz P-surface geometry with various parameter t were obtained. It is established that the growth of the samples' mechanical properties is observed at any loading angle at the value of the parameter " t " from -0.9 to 0. At $t = 0$, a maximum of specific mechanical characteristics is achieved, this is due to the fact that at $t \neq 0$, domains arise with non-zero mean curvature [2].

At $t = 0$, isotropy is preserved. When the parameter " t " differs from zero, the physical and mechanical properties of the structures decrease due to the loss of the properties of the minimum surfaces.

The study was supported by a grant from the Russian Science Foundation (project No. 20-73-10171).

References

- [1] von Schnering H. G., Nesper R., "Nodal surfaces of Fourier series; fundamental invariants of structured matter", Zeitschrift für Physik B Condensed Matter, 83, 3, pp. 407 – 412 (October 1991).
- [2] Balabanov, S. V., Makogon, A. I., Sychev, M. M. et al., "3D Printing and Mechanical Properties of Polyamide Products with Schwartz Primitive Topology", Technical Physics, 65, 2, pp. 211 – 215 (April, 2020).
- [3] Ambu R., Morabito A. E., "Modeling, Assessment, and Design of Porous Cells Based on Schwartz Primitive Surface for Bone Scaffolds", The Scientific World Journal, 2019, 7060847, pp. 1 – 16 (June, 2019).

Mechanism of double-step conversion reaction in nanostructured tungsten trioxide anode for Li-ion batteries

R. BEKAREVICH^{1,3}, Y. PIHOSH², Y. TANAKA¹,
K. NISHIKAWA¹, Y. MATSUSHITA¹, T. HIROTO¹

¹ National Institute for Materials Science, Tsukuba, Japan;

² The University of Tokyo, Tokyo, Japan;

³ Trinity College Dublin, Dublin, Ireland.

Abstract

Market demands raise the problem of developing lithium-ion batteries (LIBs) with high-energy densities, as LIBs with conventional anodes are limited by low reversible capacity of graphite. Tungsten oxide (WO₃), possessing high theoretical capacity, can potentially replace conventional anodes. However, large volumetric changes during the cycling lead to rapid degradation of WO₃-based electrodes. In this study, we report a binder-free nanostructured anode integrated with a current collector. Its controlled geometry minimized volumetric expansion effects and conferred high mechanical stability of anode. Detailed structural analyses supported by theoretical calculations revealed the appearance of the intermediate active phases during conversion reaction.

Introduction

Next-generation LIBs with high energy densities and improved safety features are essential to maintain the steadily increasing performance demands. [1] The energy density of batteries can be increased with the capacity increase of positive and/or negative electrode. [2] Many studies proposed to use transition metal oxides (TMOs) as a new type of conversion anode. WO₃ with its large gravimetric (693 mAh g⁻¹) and volumetric (5274 mAh cm⁻³) capacities stands out from other TMOs. In this study, we enhanced the properties of WO₃ anodes by directly creating an array of vertically aligned WO₃ nanorods (WO₃-NRs) on a Ti current collector using the glancing angle deposition technique. [3, 4] This study also addressed the lack of systematic research on the mechanisms of lithium insertion/removal during cycling. We quantitatively analyzed structural changes in the WO₃-NRs during the first two charge/discharge cycles to understand the reaction mechanisms in detail. We examined the WO₃ conversion mechanism via ex situ X-ray diffraction (XRD) analysis, scanning electron microscopy (SEM), X-ray photoelectron spectroscopy (XPS), and transmission electron microscopy (TEM) in combination with first principle calculations.

Results and discussion

Coin-type half-cells with Li foils as counter electrodes were used to investigate the electrochemical properties of the WO₃-NR anodes. A series of electrochemical measurements was conducted in the voltage window 0.01-2.5 V vs Li/Li⁺ to examine the cycling and rate performances of the WO₃-NR anodes. Similarly to the previous reports [5, 6], cyclic voltammetry (CV) indicated the presence of four cathodic peaks observed at 2.7, 2.42, 0.79, and 0.01 V during the first cycle of measurements. The peaks at 2.7 and 2.42 V indicated the intercalation of lithium ions into the WO₃ crystal lattice. The large peak at 0.79 V, which was absent in the second cycle, can be explained by the solid electrolyte interphase layer formation. The last peak at 0.01 V originated from the conversion reaction.

The detailed in situ and ex situ studies of the WO₃-NRs were performed to examine the charge/discharge mechanism in the WO₃-NR anodes. Each peak in the CV profiles is associated with an electrochemical reaction that was accompanied by a phase transformation in the electrode material. To detect the evidence of phase transformations, the freshly made coin cells were operated until the end of each peak during the first two cycles. The coin cells were then disassembled in an Ar-filled glovebox, and the cycled anodes were transferred to airtight holders for XRD and SEM-EDS analyses. Fully charged and discharged anodes were also

analyzed via XPS, STEM and electron energy loss spectroscopy (EELS). We found that tungsten oxide was cyclically converted into lithium oxide and atomic tungsten. During charging, secondary lithium tungstate phases (Li_xWO_y) were detected as active conversion materials.

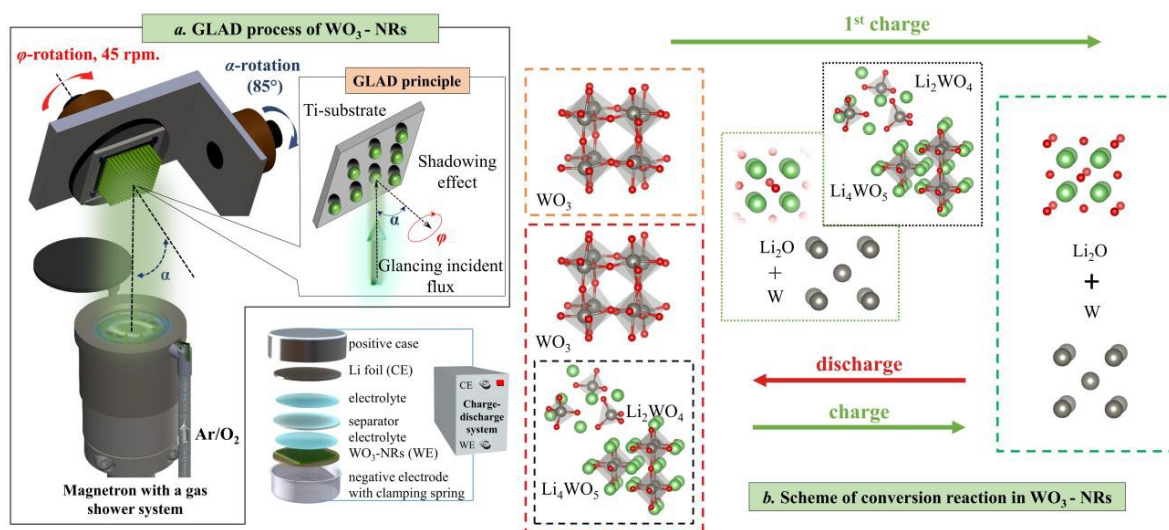


Fig. 1. Schematic illustration of the synthesis (a) and cycling (b) processes in the WO_3 -NR anodes

Conclusion

We have demonstrated a new approach for the fabrication of an efficient and mechanically stable anode for LIBs. The controlled geometry of the WO_3 -NRs minimized volumetric expansion effects, which conferred high mechanical stability to the anode. The nanostructure of the anode material facilitated the directional transport of electrons and ions and enabled high electron collection efficiency. This study revealed a new aspect of conversion reaction mechanism.

References

- [1] Z. Tu, S. Choudhury, M. J. Zachman, S. Wei, K. Zhang, L. F. Kourkoutis, and L. A. Archer, "Fast ion transport at solid-solid interfaces in hybrid battery anodes", *Nat. Energy* **3**, 310 – 316 (2018).
- [2] S. Goriparti, E. Miele, F. De Angelis, E. Di Fabrizio, R. Proietti Zaccaria, and C. Capiglia, "Review on recent progress of nanostructured anode materials for Li-ion batteries", *J. Power Sources* **257**, 421 – 443 (2014).
- [3] Y. Pihosh, I. Turkevych, K. Mawatari, J. Uemura, Y. Kazoe, S. Kosar, K. Makita, T. Sugaya, T. Matsui, et al., "Photocatalytic generation of hydrogen by core-shell $\text{WO}_3/\text{BiVO}_4$ nanorods with ultimate water splitting efficiency", *Sci. Rep.* **5**, 11141 (2015).
- [4] R. Bekarevich, Y. Pihosh, Y. Tanaka, K. Nishikawa, Y. Matsushita, T. Hiroto, H. Ohata, T. Ohno, T. Minegishi, et al., "Conversion Reaction in the Binder-Free Anode for Fast-Charging Li-Ion Batteries Based on WO_3 Nanorods", *ACS Appl. Energy Mater.* **3**, 6700 – 6708 (2020).
- [5] P. Li, X. Li, Z. Zhao, M. Wang, T. Fox, Q. Zhang, and Y. Zhou, "Correlations among structure, composition and electrochemical performances of WO_3 anode materials for lithium-ion batteries", *Electrochim. Acta* **192**, 148 – 157 (2016).
- [6] R. Pathak, A. Gurung, H. Elbohy, K. Chen, K. M. Reza, B. Bahrami, S. Mabrouk, R. Ghimire, M. Hummel, et al., "Self-recovery in Li-metal hybrid lithium-ion batteries via WO_3 reduction", *Nanoscale* **10**, 15956 – 15966 (2018).

The role of the dispersed composition of the diamond matrix in the preparation of a composite by infiltration with molten silicon

A. S. DOLGIN¹, S. P. BOGDANOV², V. LEIBGAM²

¹*Institute of Silicate Chemistry named after I. V. Grebenshchikov RAS*

²*St. Petersburg State Technological Institute (Technical University)*

Abstract

Diamond-silicon carbide composite is a new promising ceramic material with high hardness, strength, thermal conductivity and low density. The paper studies the effect of the dispersion of the diamond matrix of the composite on its properties.

Introduction

Diamond-silicon carbide composite is a promising material for various fields of application. Due to its high thermal conductivity, this composite can be used in the field of heat-conducting materials. Due to its low density and high mechanical characteristics (hardness, bending strength, sound speed, modulus of elasticity), this material is suitable as a ceramic substrate for combined armor in aviation [1–2].

Thus, knowledge of the dependence of the properties of the final product on the granulometric composition of the diamond matrix will make it possible to control the combination of material properties.

Manufacturing of samples from diamond-silicon carbide composite

To optimize the granulometric composition of the composition, polydisperse compositions were used. The grades of diamond powders of various fineness are taken as a basis: 3/2 microns, 7/5 microns, 10/7 microns, 14/10 microns, 28/20 microns, 50/40 microns, 100/80 microns, 250/200 microns (experiments 1 – 8).

Using the program “Main” according to Fuller's method, the granulometric composition of polydisperse mixtures from the available set of granularities was calculated to obtain a composition with the maximum density (experiments 9 – 19). The calculation results are presented in table. one.

Porous blanks were made from the selected powders, which were then impregnated with molten silicon:

- 1) mixing powders of different fineness with silicon carbide grinding bodies;
- 2) plasticizing the powder with a PEG15 solution;
- 3) granulating the resulting mixture through a 0.5 mm sieve;
- 4) forming discs at a pressure of 100 MPa;
- 5) drying of raw materials (heating up to 120°C according to a given program and holding for 5 hours);
- 6) siliconizing samples (sintering) - impregnation with molten silicon in a vacuum.

Density, porosity, hardness, and modulus of elasticity were measured for the synthesized composites. The structure and phase composition of the materials obtained have been studied.

Conclusion

In this work, samples were made from diamond powders of different granulometric compositions to study the effect of the dispersed composition on the mechanical characteristics of products. Using the “Main” program, according to Fuller's method, the optimal ratios between diamond powders of different dispersion were calculated to achieve maximum density and high mechanical characteristics. Powder compacts are siliconized by infiltration with molten silicon. The effect of the dispersity of the diamond matrix of the composite on its structure and mechanical properties has been studied.

Table 1. Disperse composition

Experience number	Composition of diamond compositions	Ratio of grain sizes of diamonds of basic grain sizes	Weight ratio between main grit sizes
1	ACM 3/2	-	-
2	ACM 7/5	-	-
3	ACM 10/7	-	-
4	ACM 14/10	-	-
5	ACM 28/20	-	-
6	AC6 50/40	-	-
7	AC6 100/80	-	-
8	AC160 250/200	-	-
9	AC6 100/80 + ACM 10/7	10/1	60/40
10	AC160 250/200 + ACM 28/20	10/1	50/50
11	AC160 250/200 + ACM 28/20	10/1	60/40
12	AC160 250/200 + ACM 28/20	10/1	70/30
13	AC6 100/80 + ACM 3/2	33/1	75/25
14	AC160 250/200 + ACM 10/7	25/1	75/25
15	AC160 250/200 + ACM 28/20+ ACM 10/7	25/3/1	65/25/10
16	AC160 250/200 + ACM 28/20+ ACM 10/7	25/3/1	61/12/27
17	AC160 250/200 + AC6 100/80 + ACM 10/7	25/10/1	30/40/30
18	AC160 250/200 + AC6 50/40 + ACM 10/7	25/5/1	50/20/30
19	AC160 250/200 + ACM 28/20+ ACM 3/2	100/10/1	60/20/20

Funding

The study was supported by a grant from the Russian Science Foundation (project No. 20-13-00054).

References

- [1] R. Simpkin, "Multi-layer Armour – A quantum Jump?", *Fifteen Nations Special*, number 1, pp. 29 – 33 (1981).
- [2] M. V. Kovalchuk, A. S. Oryshenko, V. Y. Shevchenko, "Synthesis of a new class of materials with a regular (periodic) interconnected microstructure", *Israel journal of chemistry*, volume 60, number 5 – 6, pp. 519 – 526 (2020).

Research of morphology and luminescence of particles based on yttrium fluorides for medical usage

A. M. DOROKHINA^{1,2}, H. KOMINAMI¹, V. V. BAKHMETYEV²,
T. AOKI³, H. MORII³

¹*Saint Petersburg State Technological Institute (Technical University)*

²*Shizuoka University, Japan*

³*ANSeeN Inc., Japan*

Abstract

The hydrothermal method is used to produce X-ray stimulated YF₃: Ce³⁺ nanophosphors with luminescence spectra and particle sizes suitable for photodynamic therapy. The influence of the synthesis media on the properties of particles is considered. The optimal duration of

hydrothermal synthesis in an ethylene glycol medium has been revealed. The effect of various stabilizers (PEG, PVP, and PEI) on morphology and luminescent properties has been studied.

Introduction

To ensure the applicability of phosphors in medicine, in particular, in the composition of pharmacological preparations for photodynamic therapy of oncological diseases (PDT), a phosphor is required with certain properties, such as particle size no more than 100 nm, excitation by radiation penetrating through the tissues of the body – X-ray or infrared (IR), and radiation in the absorption band of industrial photosensitizers. An important issue is also the biocompatibility of inorganic particles of REE fluorides with the body. This paper examines the effect of the time of hydrothermal synthesis on the morphology of YF_3 particles, as well as the role of various stabilizers in the luminescence properties and morphology. The work was carried out on X-ray excited $YF_3: Ce^{3+}$ phosphors. The synthesis was carried out by the hydrothermal method, since it avoids high temperatures leading to particle agglomeration.

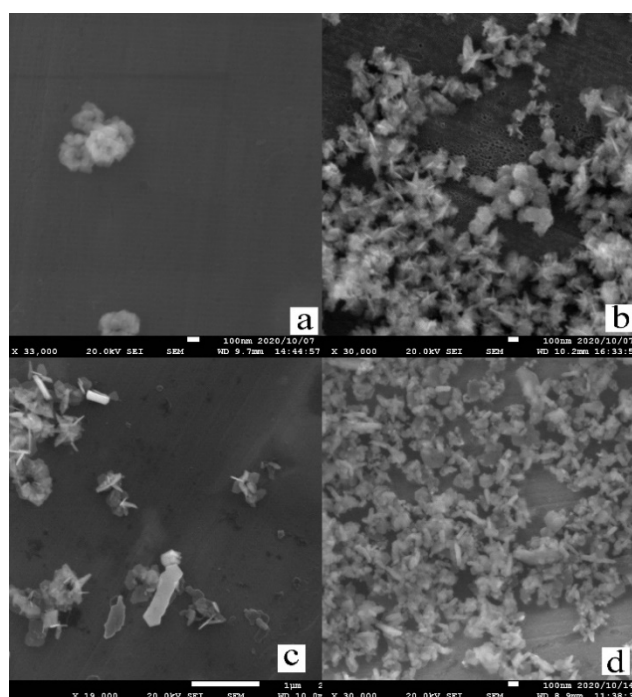


Fig. 1. Micrographs of $YF_3: Ce^{3+}$ phosphors with various surfactants: a – sample with PEG-2000 (magnification 100 nm), b – PVP (magnification 100 nm), c – PEI (magnification 1 μ m), d – PEG-20000 (magnification 100 nm)

The first stage of the research consisted in identifying the most favorable medium for obtaining the required phase and size - water or organic matter (ethylene glycol and ethanol). Research has shown that ethylene glycol has all the advantages: it prevents agglomeration, allows you to get the required phase. To determine the optimal synthesis time, the hydrothermal synthesis of YF_3 samples was carried out according to the same scheme - in an organic medium of ethylene glycol without the use of stabilizers for 4, 8, 12, 16, 20 hours. In the sources [1, 2], the synthesis was carried out for at least 20 hours. However, our study showed that it is possible to obtain a YF_3 sample that meets the necessary requirements (including nanosize) within 4 hours, moreover, without the use of stabilizers. Concurrent with the study of the synthesis duration, an experiment was carried out on the effect of various stabilizers on the properties of the $YF_3: Ce^{3+}$ phosphors (5%).

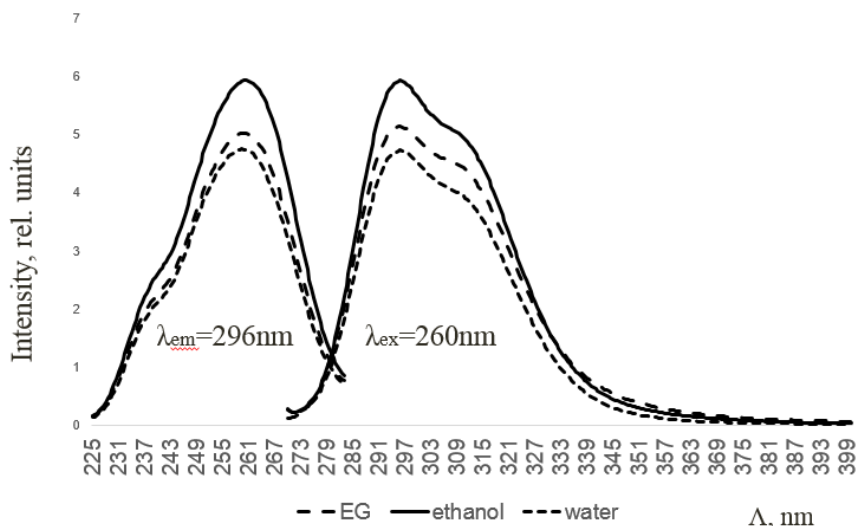


Fig. 2. Photoluminescence spectra (excitation and emission) of $YF_3:Ce$ 2%mol. samples synthesized in various media

Polyethylene glycol (PEG) with various average molecular weights (PEG-200, PEG-2000, PEG-20,000), polyethyleneimine (PEI Mw 60,000-80,000), polyvinylpyrrolidone (PVP Mw 1,300,000) were used as stabilizers. Scanning electron microscopy has shown that the most regular and smallest particles are synthesized with PEG-20,000. However, in terms of luminescence parameters, the most successful sample was synthesized with PEG-2000. Samples with PEI and PVP are needle-shaped, and the dimensions are noticeably larger than required. The synthesized nanophosphorus possessed effective X-ray luminescence with a maximum in the region of 300 nm, which makes it possible to use them in the composition of preparations for PDT.

Conclusion

As a result of the work carried out by the solvothermal method, nanophosphorus $YF_3:Ce^{3+}$ was synthesized in three ways – an aqueous medium, an ethylene glycol medium, and an ethanol medium.

It was shown that, in contrast to [1, 2], the duration of solvothermal areas could be less than 20 hours, in particular in the range of 16-18 hours.

It was found that, in contrast to synthesis in an aqueous medium, hydrothermal synthesis in an ethylene glycol medium using a stabilizer allows the synthesis of phosphors with smaller particles (less than 100 nm), which have a better shape close to spherical, which is more suitable for use in PDT.

In terms of particle size and X-ray luminescence characteristics, the synthesized phosphor $YF_3:Ce^{3+}$ is very promising for use in photodynamic therapy of oncological diseases.

References

- [1] Magnetic and upconverted luminescent properties of multifunctional lanthanide doped cubic $KGdF_4$ nanocrystals / L. W. Yang, Y. Y. Zhang, a J. J. Li, a Y. Li, a J. X. Zhong, a, Paul K. Chu // *Nanoscale*, 2010, 2, 2805 – 2810.
- [2] $NaGdF_4:Eu^{3+}$ Nanoparticles for Enhanced X-ray Excited Optical Imaging / L. Sudheendra, Gautom K. Das, Changqing Li, Daniel Stark, Jake Cena, Simon Cherry, Ian M. Kennedy // *Chem. Mater.* 2014, 26, 1881 – 1888.

NiO and NiO:Al films for solar cells: a compromise between electrical conductivity and transparency

V. V. FILIPPOV¹, I. A. KASHKO¹, A. K. TUCHKOVSKI¹, D. L. KOVALENKO²,
V. V. VASKEVICH², V. E. GAISHUN²

¹Belarusian State University of Informatics and Radioelectronics, Minsk, Belarus

²Francisk Skorina Gomel State University, Gomel, Belarus

Abstract

The paper presents sol-gel and thermal oxidation methods for producing thin NiO films. The high transparency of the films correlates with their low electrical conductivity. Small additions of Al can significantly increase the conductivity of the films, while the oxidation/annealing temperatures determine the transparency of the films.

Introduction

NiO films are well-known *p*-type transport materials for perovskite solar cells and LEDs with an optical bandgap of around 3.4-4.0 eV. Stoichiometric NiO is highly insulating at room temperature with a resistivity of $\sim 10^{13}$ Ohm·cm; the *p*-type conductivity may be obtained by introducing acceptor defects such as nickel vacancies and oxygen interstitials and/or by intentional doping with Li, K, and Cu ions. NiO transport film is more stable in comparison with organic films (typically PEDOT:PSS), and inverted solar cells with NiO show an impressive good result as follows from existing studies. The fabrication of high-performing *p*-type transparent conductive NiO and other oxides is difficult, even using a high-temperature process. The optical/electrical properties of films prepared by magnetron sputtering are very sensitive to the conditions and parameters of the deposition (pressure, the composition of the chamber atmosphere, etc.). In the paper, we used the sol-gel method and Ni and Ni doped with Al thin film thermal oxidation for producing stable NiO films with parameters suitable for use in perovskite solar cells. It is worth noting that electrical conductivity and optical transparency are seemingly mutually exclusive properties when considering metal oxides; it is intrinsically a difficult task to obtain a high *p*-type conductivity and acceptable transparency.

Results and discussion

Samples of thin NiO films were prepared by two methods: the sol-gel method and the method of thermal oxidation of the film Ni formed by high-frequency magnetron sputtering.

The technology of NiO thin film-forming by the sol-gel method included three stages. At the first stage, a film-forming solution based on nickel acetate ($\text{Ni}(\text{CH}_3\text{COO})_2$) is prepared, which is kept for full maturation at room temperature for three days. For the formation of NiO: Al-doped films, up to 5 wt.% of aluminum nitrate is added to the solution. At the second stage, substrates are coated with a solution by spin-coating. By changing the rotational speed of the centrifuge, the required thickness of the resulting NiO and NiO:Al films can be achieved. At the final stage, the samples are heat treated in a muffle furnace in air at a temperature of 300 °C for 90 minutes.

To obtain NiO films by thermal oxidation, we used glass substrates with a preformed conductive

FTO layer. Ni films were deposited on them by magnetron RF sputtering of a target in an Ar atmosphere. The discharge power was 300 W; the deposition time was 5 min. The pressure in the chamber during the operation of the RF magnetron was 1.08 – 1.12 Pa. Under the same conditions, mixed films of Ni with aluminum with a concentration of the latter up to 5% were deposited onto the substrates. For this, the nickel target in the vacuum chamber was partially covered with Al foil of various areas, depending on the required Al concentration in the Ni film. After that, the films were thermally oxidized / annealed at 250 °C, 300 °C, and 500 °C for 1 hour in an oxygen atmosphere. The rate of temperature rise was 15 deg / min. The initial Ni and Ni: Al films had a thickness of 32-36 nm, which, after oxidation / annealing, increased by $\sim 19\%$. A pure NiO film obtained by oxidizing Ni was actually an insulator and had an electrical

resistance of more than 200 MOhm (760 Ohm-cm). But at an Al concentration in the initial film of 0.3% and oxidation / annealing at 300 °C, the resistance of the NiO oxide film decreased by almost 20 times, and at a concentration of 3% – by almost 200 times. Another important characteristic of NiO films for use in inverted solar cells is transparency in the visible range of the spectrum.

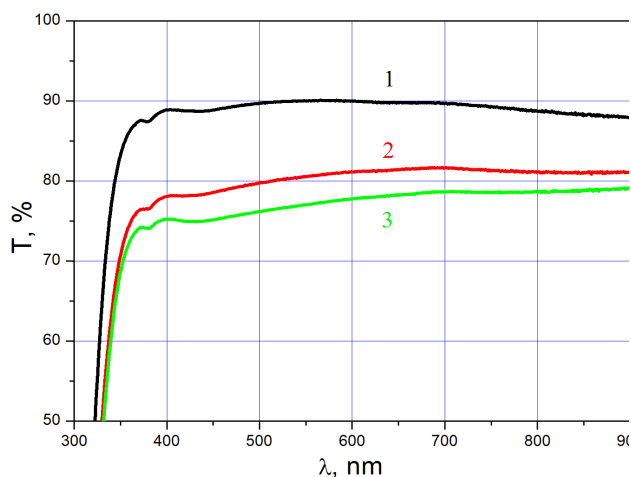


Fig. 1. Light transmission by the substrate – (1), freshly received NiO_x film – (2) and after storage in air for 10 days (3)

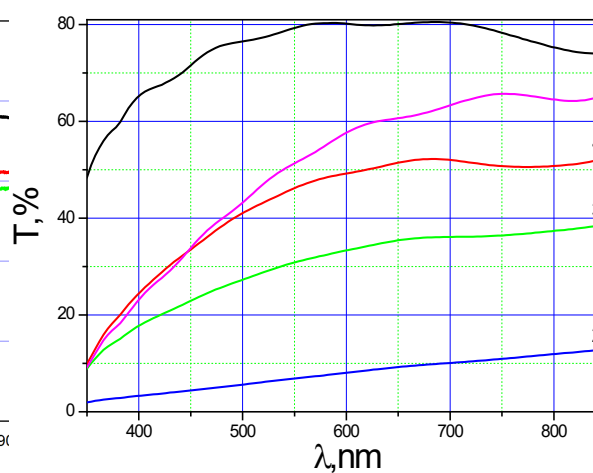


Fig. 2. Light transmission by the substrate – (1), Ni:Al film – (2) and samples at oxidation/annealing T: 250 – (3), 300 – (4) and – 500 (5) (°C); Al concentration is 0.3%

Figure 1 shows the transmission spectra of the substrate and NiO films obtained by the sol-gel method. NiO films have high transmission in the visible spectral range. However, the electrical resistance of the received films was also high: 2 to 10 MOhm-cm.

Figure 2 shows the transmission spectra of the substrate and NiO films with an Al concentration of 0.3%, obtained at different oxidation/annealing temperatures T. With an increase in T, the transparency of the NiO films increases due to the formation of AlNiO_x complexes. Conductivity, in this case, drops to 30 – 50 Ohm-cm. Photovoltaic cells with a NiO:Al p transport layer, the interface with perovskite of which was additionally treated with an aqueous solution of graphene oxide, showed an increase in the short-circuit current by 20%.

Conclusion

Thermal oxidation of Ni films with the addition of Al leads to the formation of NiO films, which are characterized by low electrical resistance. Thus, at an Al concentration of 3%, the resistance drops by almost 200 times compared to a film without Al additive. The transparency of the film is mainly determined by the temperature of thermal oxidation/annealing. By varying this temperature, annealing time, and Al concentration, stable NiO films with low light loss and low electrical resistance can be obtained.

References

- [1] D. Di Girolamo, F. Di Giacomo, F. Matteocci, A. G. Marrani, D. Dini and A. Abate “Progress, highlights and perspectives on NiO in perovskite photovoltaics”, Chem. Sci., Vol. 11, pp. 7746 – 7759 (2020).

Behavior of electron-beam irradiated polyethylene and polystyrene

I. HATESCU, C. BORCIA, G. BORCIA

Faculty of Physics, Alexandru Ioan Cuza University, Iasi, Romania

Abstract

The influence of electron-beam irradiation on low-density polyethylene (LDPE) and polystyrene (PS) was investigated, aiming to assess the reactions during the irradiation process, as chain scission, chain branching and cross-linking. Under mild irradiation conditions, similar dominant effects, creation of radicals and crosslinking, are shown for the two polymers, although these have different chemical structure and morphology. The crosslinked structure reinforces the rigidity and hardness of the material.

Introduction

When evaluating the behavior of a polymer material in a given working environment, one must take into account the particular dynamic nature of polymers, compared to other materials, due to their complex 3D structure, where both the chemical unit and the macromolecular chain play important roles. Thus, polymers present intrinsic internal mobility and any bulk or surface perturbation of the material may affect its mechanical and physico-chemical properties.

Several methods can be used to induce modifications of a polymer material in order to assess and control the evolution of the bulk and surface properties. Thus, the molecular structure of polymers and consequently their properties can be significantly modified by electron beam irradiation. The effects of electron beam irradiation on polymers are studied extensively, for various exposures, the delivered doses ranging from kGy to hundreds of kGy [1–3]. The main reactions during the irradiation process are chain scission, chain branching and cross-linking. Considering this, here the influence of electron-beam irradiation on low-density polyethylene (LDPE) and polystyrene (PS) was investigated. The two polymers, belonging to the carbonchain polymer class, have non polar structure, but bear differences in their structure, since PS presents pending aromatic groups and is amorphous, whereas LDPE has only hydrogen atoms bonded to each carbon atom and is semicrystalline.

The irradiation was carried out under mild conditions in order to identify the effects that may dominate in a given polymer, depending on several factors, such as the chemical structure and morphology of the polymer, as well as the irradiation conditions and the post-treatment.

Experimental

The samples were irradiated using an electron accelerator for clinical use (Varian TrueBeam STX). The output energy was 6 MeV, with a dose rate of 1000 M.U./min, ensuring 100 cGy at 1.3 cm depth for a field of 10x10 cm² and a source-to surface distance (SSD) of 100 cm. In order to achieve this dose, the samples (foils of 0.1 mm thick and 10x10 cm² surface) were placed under a solid water bolus 1.3 cm thick. Under these experimental conditions, the estimated planar fluence is of 4·10⁸ electrons/cm²·s [4]. The irradiation time was set to 100 min, so that the total dose delivered to the foil was 1000 Gy.

The irradiation was performed on commercial polymer films of low-density polyethylene (LDPE) and polystyrene (PS), (Goodfellow Ltd., Cambridge), 50 μm thick.

The chemical properties of the polymers were monitored by combining Fourier-transform infrared (FTIR) and X-ray photoelectron spectroscopy (XPS); the modifications in the crystalline/ amorphous structure were assessed by X-ray diffraction (XRD); the viscoelastic behavior was analyzed using dynamic mechanical analysis (DMA). Supplementary, the surface was tested by contact angle measurement.

Results and discussion

The repeat units of the two polymers are presented in Fig. 1. These represent non-polar structures with no bonded oxygen atoms. Nonetheless, the XPS analysis shows that the untreated samples present intrinsic low-level oxidized carbon atoms, which may reasonably

be attributed to carbon singly bonded to oxygen. This result is not surprising for commercial polymers.

Interestingly, after irradiation, all these functional groups are removed from the structure and no oxygen is detected by XPS, as shown by the atomic elemental compositions expressed as O/C presented in Table 1.

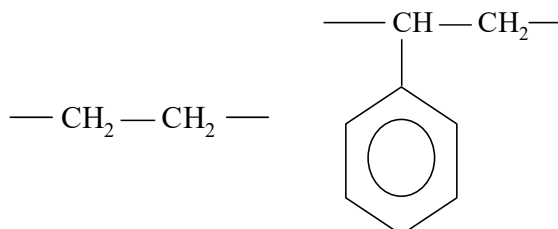


Fig. 1. Repeat units of PE and PS

Table 1. Atomic elemental composition for LDPE and PS, expressed as O/C

untreated LDPE	irradiated LDPE	untreated PS	irradiated PS
5.4/94.6	-/100	5.6/94.4	-/100

The removal of oxygen may imply chemical reactions conducting to the creation of radicals, which, on one side, may link to each other in the bulk and develop a crosslinked structure. On the other side, these radicals may behave differently at the surface, inducing a polar surface character. This is sustained by the water contact angle values, revealing an evolution from hydrophobic to slightly hydrophilic on both polymers.

Table 2. Contact angle of water on LDPE and PS surfaces

untreated LDPE	irradiated LDPE	untreated PS	irradiated PS
95°	80°	92°	82°

The XRD was carried out only for LDPE, which shows that irradiation has caused a small but detectable decrease in the intensity of the two characteristic XRD peaks, which could be consistent with an increase in amorphous character due to crosslinking. In this respect, the calculated areas of the two peaks are presented in Table 3.

Table 3. XRD for LDPE

I (arb. units)	untreated LDPE	irradiated LDPE
$2\theta = 21.48^\circ$	8452	8125
$2\theta = 23.82^\circ$	1604	1541

The mechanical properties of the polymers, investigated in (-150 to 200°C) temperature range, show that the effects of the irradiation are small, but detectable. Thus, there is some increase in the storage modulus and the glass transition temperature, which would imply some reduction in the mobility of the macromolecular chains, due to crosslinking.

Conclusion

The electron-beam irradiation of LDPE and PS, conducted under mild irradiation conditions, has dominant effects the creation of radicals and crosslinking. The effects are similar for the two polymers, although these have different chemical structure and morphology. The crosslinked structure reinforces the rigidity and hardness of the material.

References

- [1] A. Akhavan, F. Khoylou, N. Sheikh, H. Kazeminejad “Study of crystallization behaviour of electron beam irradiated polypropylene and high-density polyethylene”, *Rad. Phys. Chem.*, 187, art. no. 109582 (2021).
- [2] M. Rzepna, J. Sadlo, G. Przybytniak, A. Iuliano “Impact of electron beam treatment on copolymers of polylactide and poly(trimethylene carbonate) in an air atmosphere”, *J. Appl. Polym. Sci.*, 138(15), art. no. e50184 (2020).
- [3] P. Svoboda, K. Trivedi, K. Stoklasa, D. Svobodova, T. Ougizawa “Study of crystallization behaviour of electron beam irradiated polypropylene and high-density polyethylene”, *Roy. Soc. Open Sci.*, 8(3), pp. 1 – 23 (2021).
- [4] J. P. Gibbons et. al. “Monitor unit calculations for external photon and electron beams: Report of the AAPM Therapy Physics Committee Task Group No. 71”, *Med. Phys.*, 41(3), pp. 031501-(1-34) (2014).

Effect of Ag substitution on enhancing the thermoelectric performance of nanostructured SnSe

K. KALAIARASAN^{1,2}, D. SIDHARTH¹, A. S. ALAGAR NEDUNCHEZHIAN¹,
P. RAJASEKARAN², M. SHIMOMURA², M. ARIVANANDHAN¹, H. IKEDA^{2,3},
Y. HAYAKAWA³, R. JAYAVEL¹

¹Centre for Nanoscience and Technology, Anna University, Chennai 600025, India.

²Graduate School of Science and Technology, Shizuoka University,
Hamamatsu 432-8011, Japan.

³Research Institute of Electronics, Shizuoka University, Hamamatsu 432-8011, Japan.

Abstract

Nanostructured Sn_{1-x}Ag_xSe (x=0.02, 0.04, 0.08) materials were synthesised via mechanical milling followed by hydrogen decrepitation method. The structural, morphological, compositional and thermoelectric properties were investigated. The XRD analysis confirmed the crystal structure of SnSe. The prepared Sn_{1-x}Ag_xSe samples were pelletized via high pressure high temperature sintering (HPHTS) technique for thermoelectric measurements. Seebeck coefficient and electrical resistivity were measured as a function of temperature. It was found that the power factor of Sn_{0.92}Ag_{0.08}Se was 6.3 times higher than that of pristine SnSe.

Introduction

Thermoelectrics is a promising technology that can be employed for sustainable energy generation from waste heat. But the efficiency of the thermoelectric generator is very low. Hence an effective material is needed to improve the performance of thermoelectric generator. The efficiency of a thermoelectric material can be determined using dimensionless figure of merit $ZT = S^2\sigma/\kappa$, where S is the Seebeck coefficient, σ the electrical conductivity, κ the thermal conductivity, and T the absolute temperature. Several attempts were made to improve the performance of materials via nanostructuring, doping, phonon engineering, etc. Conventional methods involve solid state reaction followed by spark plasma sintering are highly sophisticated and expensive. Here, we introduced high pressure high temperature sintering (HPHTS) method to prepare nanostructured pellets for thermoelectric measurements which is simple and cost effective.

Experimental method

Elemental powders of Sn, Se and Ag were taken and mechanically milled under optimised conditions, and then the powders were collected. The samples were further processed by

hydrogen decrepitation technique at 673 K for 3 hours. Finally, the powders were collected and pelletized by HPHTS technique for thermoelectric measurements.

Results and Discussion

The XRD analysis confirmed the crystal structure of the prepared $\text{Sn}_{1-x}\text{Ag}_x\text{Se}$ samples. The sheet-like morphology of the samples was observed by SEM and TEM analysis. The thermoelectric properties of the pelletized nanostructures were analysed as a function of temperatures. Figure 1 shows the Seebeck coefficient, electrical resistivity and power factor of the samples, as a function of temperature. The Seebeck coefficient of the samples decreases with an increase in Ag substitution at lower temperature, and transition of positive to negative value of Seebeck coefficient occurs at higher temperature. Since Se has low melting point and high vapour pressure, it may be vaporous easily and thereby deficiency of Se occurs which increases the electron concentration by charge compensation. Hence, majority carriers change from holes to electrons at high temperature. The electrical resistivity of all the samples decreases with increasing temperature, which confirms the semiconducting behaviour. The $\text{Sn}_{0.92}\text{Ag}_{0.08}\text{Se}$ sample exhibits a power factor of $76.54 \mu\text{W}/\text{K}^2\text{m}$ which is about 6.3 times higher than that of pure SnSe.

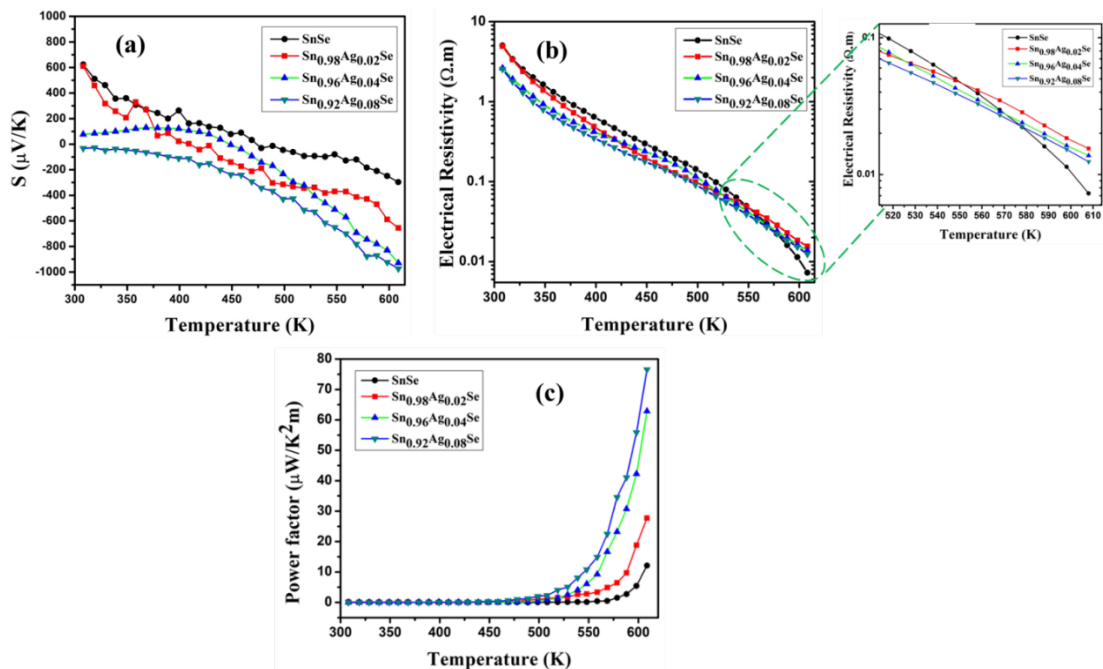


Fig. 1. Measured (a) Seebeck coefficient, (b) electrical resistivity and (c) power factor value, as a function of temperature

Conclusion

Nanostructured $\text{Sn}_{1-x}\text{Ag}_x\text{Se}$ ($x=0.02, 0.04, 0.08$) materials were synthesised via mechanical milling followed by hydrogen decrepitation method. The samples were pelletized for thermoelectric measurement using HPHTS technique. The obtained thermoelectric power factor values were compared with the pristine SnSe and found to be enhanced for $\text{Sn}_{0.92}\text{Ag}_{0.08}\text{Se}$, which was about 6.3 times higher than that of pristine SnSe. The experimental results demonstrated that the substitution of Ag at Sn site in SnSe is beneficial for improving the thermoelectric properties of SnSe.

References

- [1] Sidharth, D., Nedunchezian, A. A., Rajkumar, R., Devi, N. Y., Rajasekaran, P., Arivanandhan, M., Fujiwara, K., Anbalagan, G. and Jayavel, R. Enhancing effects of Te substitution on the

- thermoelectric power factor of nanostructured $\text{Sn}_x\text{Se}_{1-x}\text{Te}_x$. *Physical Chemistry Chemical Physics*, 21(28), pp.15725 – 15733, 2019.
- [2] Sidharth, D., Nedunchezian, A. A., Akilan, R., Srivastava, A., Srinivasan, B. Immanuel, P., Rajkumar, R., Devi, N. Y., Arivanandhan, M., Liu, C. J. and Anbalagan, G. Enhanced thermoelectric performance of band structure engineered $\text{Ge}_x\text{Se}_{1-x}\text{Te}_x$ alloys. *Sustainable Energy & Fuels*, 5(6), pp.1734 – 1746, 2021.

One-step microwave synthesis of Eu^{2+} -doped silicate and chlorinesilicate phosphors mixture for application in light sources

M. V. KESKINOVA^{1,2}, M. M. SYCHOV^{1,2}, K. HARA³

¹*Saint-Petersburg State Institute of Technology, Russia*

²*Institute of Silicate Chemistry of the Russian Academy of Sciences, Russia*

³*Shizuoka University, Japan*

Abstract

We have developed one-step microwave synthesis of Eu^{2+} -doped silicate and chlorinesilicate phosphors mixture, which can be used for light-sources application such as white-emitting diodes, luminescent lamps, and cathodoluminescent white light sources. The mixture of phosphors $\text{Sr}_2\text{SiO}_4:\text{Eu}^{2+}$, $\text{CaSrSiO}_4:\text{Eu}^{2+}$, $\text{Ca}_{10}\text{Si}_6\text{O}_{21}\text{Cl}_2:\text{Eu}^{2+}$, $\text{Ca}_6\text{Sr}_4(\text{Si}_2\text{O}_7)_3\text{Cl}_2:\text{Eu}^{2+}$ has a wide photoluminescence spectrum (around 150 nm) close to the sun-light, that provides a high value of color rendering index (93) in the light source based on this phosphors mixture.

Introduction

At present, an important task is the wider introduction of white light-emitting diodes (WLEDs) with a wide luminescence spectrum, a minimum content of short-wave radiation and a high color rendering index into lighting products. The most common phosphor for WLED is cerium-doped yttrium aluminum garnet (YAG:Ce). The disadvantage of WLED based on it includes an intense band in the blue region of the spectrum promoting suppression of the melatonin secretion, which plays an important role in controlling the circadian system maintaining the frequency of sleep and wakefulness in the human body [1]. In general, the spectrum of such WLEDs differs from the solar spectrum. Phosphors with such a solar spectrum do not exist; therefore, mixtures of phosphors with different spectral characteristics are used.

In this regard, development of synthesis technology of phosphors mixture by cost-effective one-step process providing high color rendering index of the samples which can replace YAG:Ce is under of the interest.

For this purpose, mixtures of silicate and chlorinesilicate phosphors doped with Eu^{2+} ions are suitable. They have high chemical and thermal stability and durability, and have a high quantum yield and radiation intensity [2]. The luminescence bands are wide enough and their combination makes it possible to achieve a high color rendering index for WLEDs based on these phosphors. For their synthesis, one can use the same set of starting materials, which opens up the possibility of simultaneously synthesizing several phosphors in one step. By varying the synthesis conditions, it is possible to obtain mixtures of phosphors with the required spectral characteristics.

The use of microwave technology is a current direction in reducing the energy and time costs for the synthesis of phosphors. Interaction of microwave energy with materials, due to the implementation of the ponderomotive effect and electrodiffusion, allows increasing the level of functional characteristics of phosphors [3 – 5].

Experiment

For phosphor preparation SiO_2 , $\text{SrCl}_2 \cdot 6\text{H}_2\text{O}$, $\text{Ca}(\text{OH})_2$, Eu_2O_3 powders were preliminarily ground in the mortar, sieved and mixed for 3 hours. The phosphor synthesis was performed in

the custom-made microwave furnace with the frequency of 2.45 GHz using the experimental setup with two layers of carbon between charge mixture for creating reducing atmosphere for the transition of Eu^{3+} into Eu^{2+} . The conditions of the synthesis were optimized in our works [3–5]. All samples were synthesized at 750 °C for 10 minutes.

X-ray diffraction analysis of the synthesized samples was performed using RigakuSmartLab3 apparatus. The phosphors were studied by measuring their photoluminescence (PL) emission spectra using AvaSpec-3648 spectrofluorimeter at 376 nm excitation wavelength. The color rendering index was measured using «TKA-VD»/01 spectrophotometer.

Results and discussions

According to x-ray diffraction analysis, the synthesized mixture consists of 4 luminescent phases: $\text{Sr}_2\text{SiO}_4:\text{Eu}^{2+}$, $\text{CaSrSiO}_4:\text{Eu}^{2+}$, $\text{Ca}_{10}\text{Si}_6\text{O}_{21}\text{Cl}_2:\text{Eu}^{2+}$ and $\text{Ca}_6\text{Sr}_4(\text{Si}_2\text{O}_7)_3\text{Cl}_2:\text{Eu}^{2+}$.

Firstly, the sample with 15 mol. % in the mixture was prepared. The spectrum of this sample is shown in Fig. 1, b. This spectrum does not match very well with solar spectrum because it has maximum at 562 nm corresponding to 5d-4f Eu^{2+} transitions in $\text{Ca}_6\text{Sr}_4\text{Si}_6\text{O}_{21}\text{Cl}_2$ phase and right bands corresponded 4f-4f Eu^{3+} transitions. For more similarity with solar spectrum, it was necessary to increase the influence of the left band at 516 nm corresponding to 5d-4f Eu^{2+} transitions in Sr_2SiO_4 phase and decrease the presence of Eu^{3+} by increasing of reducing atmosphere during the synthesis. For that purpose, the percentage of Ca^{2+} in the mixture was reduced and we have optimized the quantity of carbon used for the synthesis (optimum carbon quantity is 1 g for a layer).

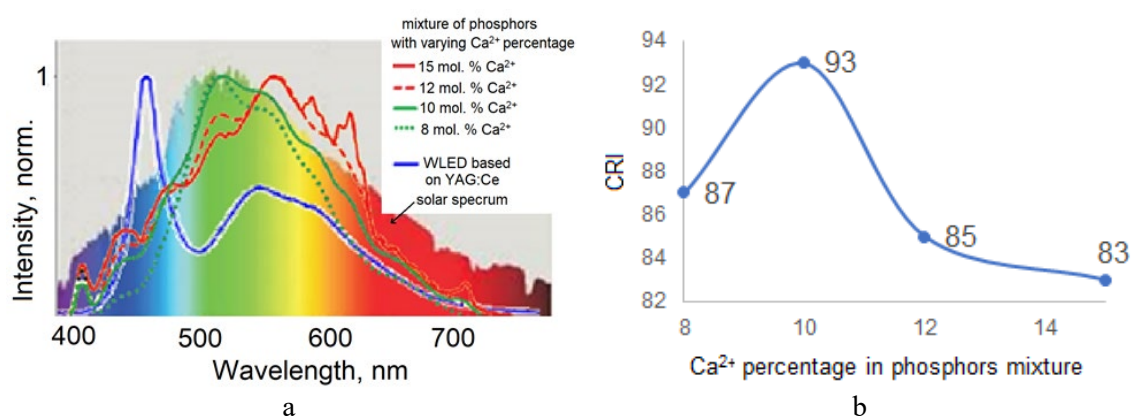


Fig. 1. a – PL spectra, b – Color rendering indexes of the phosphors mixtures

As a result, the mixture with higher color rendering index was synthesized (Fig. 1, b). The phosphor mixture with 10 % of Ca^{2+} has spectrum with maximum at 516 nm, HWHM 150 nm and color rendering index 93 and it is more similar to white light of the sun compared to the spectrum of WLED based on YAG:Ce.

The research was carried out within the state assignment of Ministry of Science and Higher Education of the Russian Federation (theme No. AAAA-A19-119022290092-5) and supported by RSF (project No. 20-13-00054).

Conclusion

By managing carbon content and Ca^{2+} percentage in the phosphor mixture $\text{Sr}_2\text{SiO}_4:\text{Eu}^{2+}$, $\text{CaSrSiO}_4:\text{Eu}^{2+}$, $\text{Ca}_{10}\text{Si}_6\text{O}_{21}\text{Cl}_2:\text{Eu}^{2+}$, $\text{Ca}_6\text{Sr}_4(\text{Si}_2\text{O}_7)_3\text{Cl}_2:\text{Eu}^{2+}$, the mixture with spectrum imitated solar spectrum and high color rendering index (93) was synthesized. The prepared mixture is perspective for the application in light sources.

References

- [1] M. Rea, M. Figueiro, A. Bierman and J. Bullough, Circadian light, Journal of Circadian Rhythms, V. 8, № 2, pp. 2 – 10 (2010).

- [2] Liu Fengxin, Fang Yongzheng, Zhang Na, Hou Jingshan, Zhang Lingyan, Yu Shengjie, Liu Shupe, Eu²⁺ and Dy³⁺ codoped (Ca,Sr)₇(SiO₃)₆Cl₂ highly efficient yellow phosphor, *Journal of Rare Earths*, V. 32, № 9, pp. 812 – 816 (2014).
- [3] M. V. Keskinova, K. A. Ogurtsov, M. M. Sychov, E. V. Kolobkova, I. A. Turkin, Y. Nakanishi, K. Hara, Synthesis of chlorine-silicate phosphors for white light-emitting diodes, *Advanced Materials Research*, V. 1117, pp. 48 – 51. (2015).
- [4] Igor A. Turkin, Mariia V. Keskinova, Maxim M. Sychov, Konstantin A. Ogurtsov, Kazuhiko Hara, Yoichiro Nakanishi, Olga A. Shilova, Microwave Synthesis of Eu-doped Silicate Phosphors, *JJAP Conf. Proc.*, Japan, pp. 011108-1 – 011108-6 (2016).
- [5] Igor A. Turkin, Mariia V. Keskinova, Maxim M. Sychov, Konstantin A. Ogurtsov, Kazuhiko Hara, Yoichiro Nakanishi, Olga A. Shilova Cathodoluminescent Properties and Particle Morphology of Eu-Doped Silicate Phosphors Synthesized in Microwave Furnace, *Advances in Intelligent Systems and Computing*, V. 519, pp 339 – 346 (2016).

Development of sapphire-like glass by sol-gel technology

D. L. KOVALENKO¹, V. E. GAISHUN¹, V. V. VASKEVICH¹, N. A. ALESHKEVICH¹,
YA. A. KOSENOK¹, O. I. TYULENKOVA¹, O. V. IGNATENKO²

¹*Francisk Skorina Gomel State University, Gomel, Belarus*

²*SSPA “Scientific-Practical Materials Research Centre of NAS of Belarus”, Minsk, Belarus*

Abstract

The paper describes the study of methods for converting precursors into optically transparent aluminum oxide and identifies the most promising methods for the synthesis of sapphire glasses.

Introduction

The development of technological processes of manufacturing transparent and strong polycrystalline materials for optical engineering was made possible only as a result of systematic fundamental research of the kinetics and mechanism of sintering processes. Studying the effect of temperature, pressure, the surrounding atmosphere, impurities, and thermal prehistory of the initial materials on the compaction process of powders during sintering led to the development of two methods for obtaining polycrystalline materials with a density close to theoretical, i.e., the density of a monocrystalline substance is both transparent and durable.

Currently, methods for the synthesis of alumina ceramics, which include elements of sol-gel synthesis, are widely used. Alkoxy technology is a promising method for producing finely dispersed aluminum oxide.

Results and discussion

Xerogels of aluminum oxide were obtained by the alkoxide sol-gel method from aluminum-tri-sec-butoxide. Isopropyl or butyl alcohol was used as a solvent for liquid-phase hydrolysis; the molar ratio of aluminum alkoxide to alcohol was 1:8. To carry out the hydrolysis process and subsequent gelation, the following reagents were added to the alcohol mixture based on aluminum alkoxide: nitric acid, aluminum acetylacacetate solution, alcoholic acrylamide solution, acrylic acid, citric acid, boron ethoxide, and ethanolamine. The maturation of the gels took place within 24 hours. The resulting xerogels dried at 40 – 50 °C for 3 – 5 days, depending on the geometry of gels. As a result of the rapid solvent evaporation rate, a xerogel had strain related to the capillary effect, resulting in cracking. Most xerogels formed during drying disintegrate into dense or unconsolidated agglomerates, depending on the type of the initial components. Suitable further drying, the gels were obtained using nitric acid, acrylamide, and boron ethoxide. Isopropyl or butyl alcohol was used as a solvent to reduce the viscosity of the system. Distilled water was used as a hydrolyzing agent. Acid hydrolysis was carried out in the

variant with an alkoxide sol-gel method. The formation of dense agglomerates was observed, which after drying, milled to nanopowder in a planetary mill. Depending on the type of initial components, the resulting xerogels desintegrate during drying into dense or loose agglomerates. The gel structure stabilizes the smallest particle size, preventing their rapid agglomeration. From these powders, blanks were formed by dry pressing in a steel mold on a hydraulic press at a pressure of 100 MPa. The pressed blanks were annealed for 1 hour at a temperature of 1000 °C. After that, the samples were sintered under the pressure of 5GPa (50 000 atmospheres) at the temperature of 500-600 °C.

Figures 1 shows the transmission spectra of typical samples of transparent ceramics.

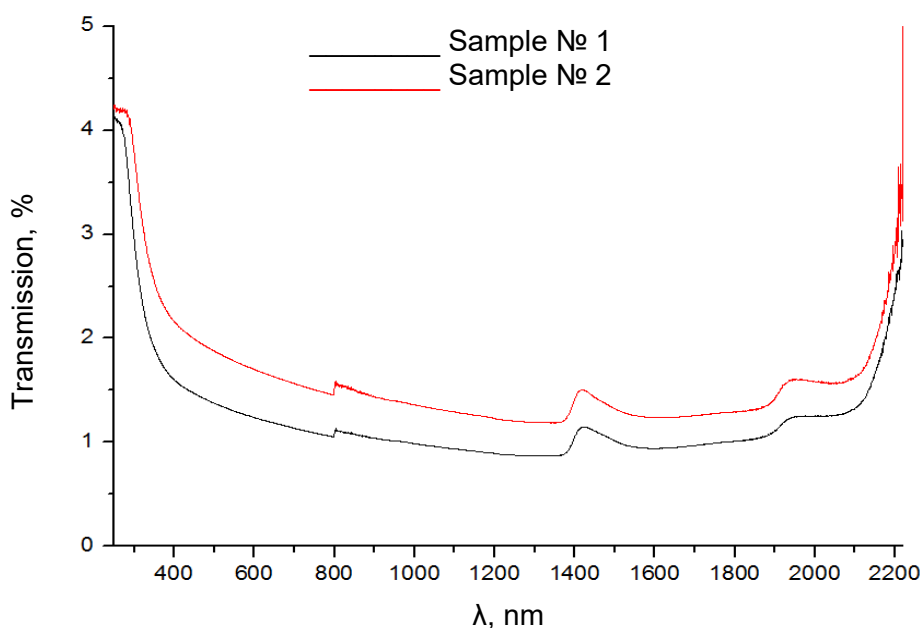


Fig. 1. The transmission spectra of samples №1 ($h=1,5$ mm) and №2 ($h=1,6$ mm) of transparent aluminum oxide ceramic samples prepared in GSU

Using the obtained powder to create products for chemical technologies can significantly reduce the total cost of equipment, production, and energy consumption compared to getting a single crystal counterpart. Table 1 shows the characteristics of transparent ceramic samples №1 and №2 synthesized by the sol-gel method and compares the features of the sol-gel silica glass and standard synthetic sapphire.

Table 1. Characteristic of transparent materials

Sample	Density, g/cm ³	Microhardness, MPa	Light transmission in the visible range, %
Quartz glass obtained by the sol-gel method	2.19	5128	90
Synthetic sapphire	3.98	20 000	95
Ceramic aluminum oxide (№1) GSU	4.15	9775	10 – 15
Ceramic aluminum oxide (№2) GSU	4.05	9272	15 – 20

Conclusion

The properties of the materials obtained by the sol-gel method are determined mainly by the composition and conditions of preparation of the gel, as well as its subsequent heat treatment regimes. An important task at this stage is to find the minimum time and temperature regime for the annealing of the crystalline phase of alumina and increase the strength of the preforms.

Samples of transparent ceramics were obtained from the aluminum nanopowders synthesized by the sol-gel process. The microhardness of the samples was about 104 MPa, the density of the sample was about 4.0 g/cm³. The light transmission was about 15 – 20 % in the visible range. It is essential to find “condensing” additives and optimal synthesis parameters that will make it possible to obtain sapphire glass with the high light transmission in the visible range with the minimum time and temperature conditions for annealing the samples.

Sol-gel synthesis of TiO₂ nanotubes based on ZnO nanorods, for use in solar cells

D. L. KOVALENKO¹, M. DOBROMIR², V. V. VASKEVICH¹, A. V. SEMCHENKO¹,
D. LUCA³, V. V. SIDSKI¹, O. I. TYULENKOVA¹

¹*Francisk Skorina Gomel State University, Sovetskaya 104, 246028, Gomel, Belarus*

²*Interdisciplinary Research, Department of Exact and Natural Sciences, Alexandru Ioan Cuza University of Iasi, 11 Carol I Blvd., 700506, Iasi, Romania*

³*Faculty of Physics, Alexandru Ioan Cuza University of Iasi, 11 Carol I Blvd., 700506, Iasi, Romania*

Abstract

This paper describes the sol-gel method for obtaining TiO₂ nanotubes on a sublayer of ZnO nanorods. The ZnO nanorod layer was pre-formed by the hydrothermal method. Optimal regimes have been determined for the formation of TiO₂-ZnO structures. An extended surface nano-morphology study of the obtained materials has been carried out.

Introduction

Obtaining materials in the form of nanotubes/nanofibers allows for the creation of mechanically strong three-dimensional structures with large surface/volume area ratios. One of the promising unconventional method for producing TiO₂ nanotubes is their synthesis by the sol-gel method on a sublayer of ZnO nanorods, obtained by the hydrothermal method. There are several advantages of this approach. The hydrothermal method makes it possible to fabricate homogeneous layers of ZnO nanorods and to vary their dimensional structure over a wide range. As a consequence, by changing the characteristics of the sublayer of ZnO nanorods, the properties of the resulting TiO₂ nanotubes can be varied, accordingly.

Synthesis of samples

Polished silicon plates and glass plates were used as substrates. The substrates were first ultrasonicated in acetone, then in ethanol for 10 minutes.

The TiO₂-ZnO materials were formed in three stages, each of them with specific procedures: *Stage one* consisted of: (a) growing a ZnO seed layer to substrates; (b) depositing a thin layer of ZnO on top of the surface by the sol-gel method. Thin films of ZnO were thus obtained from a sol based on zinc acetate Zn(CH₃COO)₂. The sol covers the substrate by spin-coating and distributed over the surface by centrifugation at a rotation speed of 2000 rpm. A third procedure (c) followed consisting of heat treatment in a muffle furnace at a temperature of 350 °C within 60 minutes. As a result, thin ZnO films, approximately 40 nm thick, were obtained.

The *second stage* followed for obtaining ZnO by the hydrothermal method. Chemical deposition from a zinc acetate solution (Zn(CH₃COOH)₂) was carried out on substrates with a seed ZnO layer. The substrates were kept for 2 hours at a temperature of 110 °C. At the end of the synthesis, the samples were carefully washed with distilled water and dried on air.

During the *third stage*, the preparation of TiO₂ nanotubes by the sol-gel method was carried out.

For the synthesis of a titanium-based nanotube, previously obtained on substrate samples with formed zinc oxide nanorods were dipped into a sol based on titanium isopropoxide (Ti[OCH(CH₃)₂]₄). Dip-coating with keeping the substrate at a certain temperature improves

the homogeneity of the penetration of titanium sol between zinc oxide nanorods. After that, the substrates were placed in a muffle furnace and kept at temperatures up to 500 °C for 60 minutes and cooled down up to room temperature with a furnace.

Results and discussion

Sample morphology was investigated by scanning electron microscopy (SEM) on a HITACHI S-4800 instrument. The dimensions of the prepared samples for SEM measurements were limited by the size of the microscope sample holder. The SEM images have shown the possibility of synthesizing one-dimensional zinc oxide nanostructures on substrates with a seed layer deposited by the sol-gel method.

Figure 1 shows an SEM image of a zinc oxide seed layer on a silicon substrate, deposited using the sol-gel method and an ordered array of zinc oxide nanorods formed on a zinc oxide seed layer.

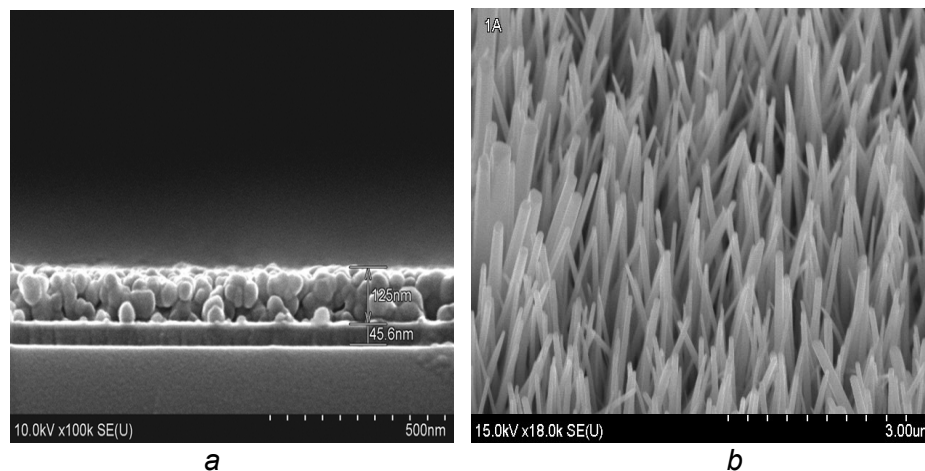


Fig. 1. SEM images of: a – zinc oxide seeding layer on substrate, b – ordered array of ZnO nanorods grown on a substrate with seed layer

It was established that the quality and morphology of the columnar zinc oxide nanostructures depend on the thickness of the seed sublayer (the best results were obtained with a seed layer thickness of 60 nm). In addition, it was found that a good crystalline quality of the seed layer is a necessary condition for growing dense ordered arrays of columnar nanostructures with a high-quality, oriented perpendicular to the substrate. The properties of nanorods are significantly improved upon annealing the seed layer in an oxygen atmosphere.

Figure 2 shows AFM images of ZnO/TiO₂ nanotubes on the surface of monocrystalline silicon.

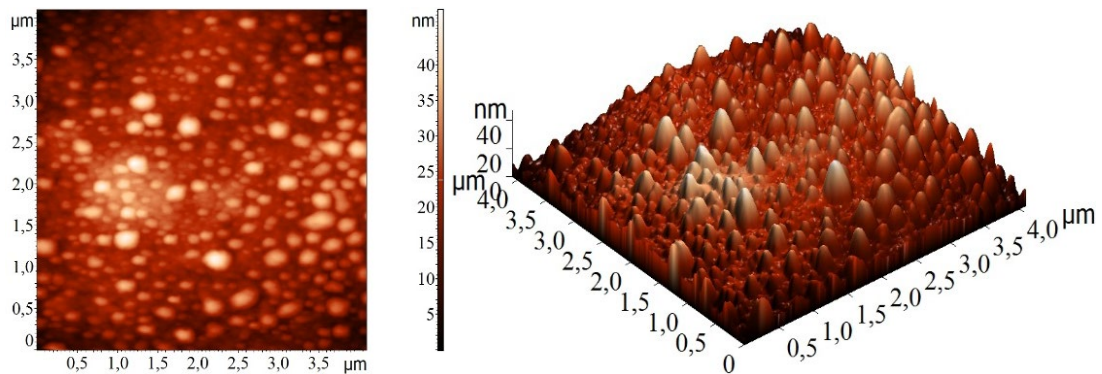


Fig. 2. AFM - images of ZnO/TiO₂ nanotubes

The results of surface studies show the presence of spherical structures. Data analysis confirmed a diameter of structures of 90 – 110 nm, and heights varying from 70 to 100 nm.

Conclusion

A sol-gel method for the preparation of TiO₂ nanotubes on a sublayer of ZnO nanorods, obtained by the hydrothermal method, has been developed. The temperature of hydrothermal synthesis affects the growth of columnar zinc oxide nanostructures. At a synthesis temperature below 80°C, the growth rate decreases, and the number of defects increases, and ZnO nanoparticles are formed. They have a structure similar to nanorods, but this temperature is insufficient for forming a rod-like structure. An increase in the annealing temperature of the obtained samples leads to the densification of the structures and a decrease in the outer diameter of the structures with 5 – 7% in the volume of the surface region.

Acknowledgements

This research was supported by the Belarusian Republican Foundation for Fundamental Research (Grant No. T20RA-019) and the Romania-Belarus AR-FRBCF-2020-2021 and Belarus-Romania T20RA-019 bilateral research grants.

Investigation of the convection effect on the inclusion motion in thermally stressed crystals

O. P. KULYK¹, V. I. TKACHENKO^{1,2}, O. L. ANDRIEIEVA^{1,2},
O. V. PODSHYVALOVA³, V. A. GNATYUK⁴, T. AOKI⁵

¹*V. N. Karazin Kharkiv National University, Kharkiv, Ukraine*

²*National Science Center "Kharkiv Institute of Physics and Technology", Kharkiv, Ukraine*

³*National Aerospace University "Kharkiv Aviation Institute", Kharkiv, Ukraine*

⁴*V. E. Lashkaryov Institute of Semiconductor Physics of the
National Academy of Sciences of Ukraine, Kyiv, Ukraine*

⁵*Research Institute of Electronics, Shizuoka University, Hamamatsu, Japan*

Abstract

The appearance and influence of convection in a liquid medium of inclusions on their motion in thermally stressed crystals are investigated, taking into account the temperature gradient direction with regard to diffusion processes. Using the example of water-soluble alkaline-halide crystals, the values of Rayleigh and Prandtl numbers were estimated, and the conditions of convective instability caused by the difference in temperature and solution concentration near the front and back surfaces of the inclusion were determined. It is shown that the contribution of convection to the processes of heat and mass transfer in a liquid medium of inclusions can result in a change in the kinetic laws of their motion in crystals.

Introduction

It is known that crystallization from solutions, melts, and high-density gaseous media can be accompanied by natural convection. Control of convective heat and mass transfer during crystallization is, as a rule, a complex technological process. The quality of grown crystals is determined by the perfection of their structure, stoichiometry and depends on the technological equipment level. The problem of controlling convective fluxes has become particularly important in connection with the growth of protein crystals from biological solutions (see [1] and references therein). Protein crystallization plays a vital role in structural biology, protein purification, drug transport, etc. High-quality crystals are required for X-ray studies of protein molecules, which are essential for understanding protein functions. One of the methods for obtaining such crystals is the vapor-diffusion technique of protein crystallization, in which

crystals are grown inside an evaporating drop. However, due to the variety of hydrodynamic processes in such a method, there are difficulties with its complete description and, accordingly, its wide application. In this work, the motion of liquid inclusions in thermally stressed crystals is investigated at such values of the crystal parameters and the temperature gradient direction when the contribution of convective processes can not only be described theoretically, but also recommendations for their detection in the experiment can be given.

Analysis of approaches

Solid crystalline surfaces have a stationary boundary layer in which transfer is carried out by ordinary diffusion for structural particles or thermal conduction for temperature. Diffusion transfer in the whole volume of the mother medium can occur, for example, during crystal growth in supersaturated solid solutions, gels, or under specially created conditions that suppress liquid convection: in weightlessness (under microgravity conditions), under the influence of magnetic fields, etc. Previously, we have studied the motion of liquid inclusions in inhomogeneously stressed crystals and described the peculiarities of microcrystallization in the inclusion volume [2, 3]. The enclosed and small volume of solution in inclusions allows us to create low under- and supersaturation in them and maintain a high degree of solution purity. At small values of thermodynamic driving forces, due to inhomogeneities in the density of linear structure defects (dislocations) or radiation point defects, unique conditions for diffusion heat and mass transfer are created in the inclusion. The study of the inclusion motion in the inhomogeneity due to the temperature gradient is the most interesting, both for the study of growth and dissolution processes and for applied material science. In this case, the motion of a saturated solution inclusion in a water-soluble crystal is impossible without sources of layers, i.e., steps at the intersection of the dissolving faces by screw dislocations [4]. It is considered that the motion of inclusions is limited by the processes of emission and assimilation of atoms rather than by their diffusion through the solution. Therefore, the large scatter of inclusion velocities depending on their size is explained solely by the difference in the morphology of dissolving faces. At the same time, as the results of this work have shown, along with the diffusion processes in the inclusion, convective instability [5] can arise due to the difference in temperature and concentration of the solution near the front and back surfaces. Due to the convective fluxes near these surfaces, intensification of the processes of atom emission and assimilation is possible, which should cause changes in the kinetics of inclusion motion.

Results and Discussions

Based on the concepts of the theory of convective stability of an incompressible liquid, a system of thermal convection equations was derived in the Boussinesq approximation for a liquid bounded by the inclusion volume in a homogeneous solid matrix. Using experimental data on the kinetics of motion and shape transformation of water solution inclusions in potassium chloride crystals under the temperature gradient, we obtained expressions for the inclusion velocity taking into account convection. The data on the parameters included in the convection equations, boundary conditions, and the expression for the inclusion velocity made it possible to analyze the conditions under which convective transfer in an inclusion can become decisive in comparison with diffusion transfer. The obtained results showed that the presence of convection in a liquid medium of inclusions resulted in a change in the kinetics of their motion under the temperature gradient. The expression for the inclusion velocity, depending on the parameters of the boundary problem being solved – Rayleigh and Prandtl numbers – makes it possible to control the conditions of transition from purely diffusion transfer of the matrix substance through the inclusion volume to convective mass transfer and vice versa. The developed concepts of the nature of convective processes depending on the thickness of the boundary layer near crystal surfaces, separated by a temperature gradient, can be used to control protein crystallization by the vapor-diffusion technique using controlled convective fluxes.

Conclusion

Analysis of solutions of the system of thermal convection equations for a liquid bounded by the inclusion volume in a homogeneous solid matrix has allowed us to describe the kinetic regularities of motion and shape transformation of liquid inclusions in thermally stressed crystals, taking into account the temperature gradient direction with regard to diffusion processes. The values of the Rayleigh and Prandtl numbers, obtained for water-soluble alkaline-halide crystals enable us to state that the process of microcrystallization in the inclusion volume, caused by the differences in temperature and solution concentration near the front and back surfaces of the inclusion, can be accompanied by convection, including under microgravity conditions.

References

- [1] T. K. Pradhan, P. K. Panigrahi “Suppressing convection strength using confinement during protein crystallization”, *Journal of Applied Physics*, 128, 8, pp. 084701-1-10 (March 2020).
- [2] A. P. Kulik, O. V. Podshyvalova, I. G. Marchenko, “Radiation-induced motion of liquid inclusions in alkali halide crystals”, *Problems of Atomic Science and Technology*, 120, 2, pp. 13 – 19 (March 2019).
- [3] O. P. Kulyk, L. A. Bulavin, S. F. Skoromnaya, V. I. Tkachenko “A model of induced motion of inclusions in inhomogeneously stressed crystals”, in: A.R. Varkonyi-Koczy (eds.) *Engineering for Sustainable Future. Inter-Academia 2019. Lecture Notes in Networks and Systems (LNNS)*, 101, pp. 326 – 339 (January 2020).
- [4] V. S. Kruzhanov, O. V. Podshyvalova “Defining the kinetic coefficients of dissolution using the experimental data on the motion of liquid inclusions in the crystals”, *Sov. Crystallography* 35, 6, 1534 – 1539 (November 1990).
- [5] O. L. Patochkina, Yu. G. Kazarinov, V. I. Tkachenko “Physical Model of the Dependence of the Nusselt number on the Rayleigh number”, *Technical Physics*, 61, pp. 1626 – 1632 (November 2016).

Impact of modeling method on geometry and mechanical properties of samples with TPMS structure

A. I. MAKOGON¹, S. V. BALABANOV¹, K. S. KOSHEVAYA², M. M. SYCHEV^{1,2}

¹Institute of Silicate Chemistry RAS

²Saint-Petersburg State Technological Institute (Technical University)

Abstract

Products based on triply periodic minimal surfaces (TPMS) are promising for use in various applied fields from mechanical engineering to medicine. Despite the fact that TPMS have been known for more than two centuries, their practical application became possible only in recent decades with the development of additive technologies. Computer modeling of products based on TPMS for 3D printing is a relevant problem. This paper investigates the impact of the modeling method on the geometry and mechanical properties of samples with TPMS structure.

Introduction

Triply periodic minimal surfaces (TPMS) are surfaces that are invariant with respect to translations in a lattice of the third rank and have a minimal surface bounded by a given contour. A direct consequence of minimality is zero mean curvature at each point. Schwartz described the first TPMS without self-intersections in 1865; in 1883, Neovius described another family of surfaces [1].

Fabrication of samples with TPMS structure is possible only with the help of additive technologies [2]. The first step in additive manufacturing is CAD modeling.

There are several methods for modeling TPMS:

- Group of methods based on discrete analytical geometry;
- Approximation Methods Based on the Weierstrass Representation.

It was shown in [3] that utilization of only the first term of the Fourier expansion is sufficient for applied problems. This approach is used in almost all works devoted to both experimental and computational studies of the properties of TPMS.

The aim of this work is to compare the properties of TPMS modeled by different methods.

Modeling of samples

Implicit method. An implicit function is a continuous scalar function in R^3 . The implicit surface of such a function is the locus of points at which the function has zero value. Positive values are inside the surface defined by the implicit function, and negative values are outside of it. Any TPMS can be described by the sum of an infinite number of terms of the Fourier series, TPMS can be approximated by periodic node surfaces (PNS) based on a finite number of trigonometric functions. The number of functions will determine the surface quality. In the work of von Schnering, it is shown that the main term of the Fourier series is sufficient.

For example, the Schwarz P-surface is described by the approximation equation (1):

$$\cos(x) + \cos(y) + \cos(z) = 0 \quad (1)$$

For implicit modeling Grasshopper-script was developed.

Discrete geometry method. To model the samples using discrete geometry methods, the boundary method was used, in which a simplicial complex and boundary conditions were specified, and the mesh was iteratively refined to minimize the surface energy. The Surface Evolver software package, developed by Kenneth Brakke [4] was used.

Fabrication of samples

Six samples with the geometry of Schwarz-P surface (three of each type) were fabricated using stereolithography on an Anycubic Photon 3D printer. The manufactured samples fit into a 30x30x30 mm cube and have a space filling degree of 0.18.

Mechanical testing

The samples were tested for compressive strength on a tabletop universal testing machine Shimadzu AG-50kNXD, at an air temperature of 25 °C and a loading rate of 5 mm/min. The samples were tested for compression on a tensile testing machine in accordance with ISO 604-2002, the strength of the samples was taken to be the first peak on the deformation curve, which corresponds to the transition of the sample to the region of plastic deformation. It is known that 3D printed products are characterized by a high anisotropy arising from the layered construction of samples. In this regard, the tests were carried out along the growth axis (along the Z axis).

Results and conclusion

As a result of mechanical tests, it was found that samples modeled using the boundary method have 9 % higher strength comparing to samples modeled using implicit functions ($2.36 \pm$ and $2.16 \pm$ Mpa, respectively). This can be explained by the fact that the boundary method allows one to obtain surfaces with zero mean curvature at each point, while the implicit method allows one to obtain only TPMS approximations, the curvature of which is close to zero, but there are regions where there are deviations. Presumably, the areas on the surface where the average curvature gradient occurs act as stress concentrators and lead to the destruction of the samples.

The study was supported by a grant of the Russian Science Foundation (project No. 20-73-10171).

References

- [1] E. R. Neovius, "Bestimmung zweier spezieller periodischer Minimalflächen", Akad. Abhandlungen, Helsingfors, 1883.

- [2] Balabanov S. V., Makogon A. I., Mechanical properties of 3D printed cellular structures with topology of triply periodic minimal surfaces, *Materials Today: Proceedings*, 30, 439 – 442, 2020.
- [3] von Schnering H. G., Nesper R. Nodal surfaces of Fourier series; fundamental invariants of structured matter. *Zeitschrift für Physik B Condensed Matter*. 1991;83(3):407 – 412.
- [4] Brakke K. A. The surface evolver. *Experimental Mathematics*. 1992;1(2):141 – 165.

Synthesis of scintillating glass materials containing yttrium niobate crystallites activated with terbium ions

M. I. MOSKVICHYOV¹, V. V. VASKEVICH¹, A. V. SEMCHENKO¹, V. V. SIDSKI¹,
V. A. KRAVETS², V. V. TKACHENKO³, V. B. ZALESSKY⁴

¹Francisk Skorina Gomel State University, Sovetskaya 104, Gomel, 246028, Belarus,

²Ioffe Institute, Politekhnicheskaya 26, St. Petersburg, 194021, Russia,

³UIIP NAS of Belarus, P. Brovki 19, Minsk, 220072, Belarus,

⁴SSPA "Optics, Optoelectronics and Laser Technology",
Logoiski trakt 22, Minsk, 220090, Belarus

Abstract

The method for obtaining sodium boron glass materials at reduced temperature containing yttrium niobate crystallites activated with terbium ions was developed. The performed studies of the structural and optical characteristics show the formation of M-YNbO₄ activated by terbium ions with a crystalline phase content of about 95%.

Introduction

Yttrium niobate is an X-ray phosphor that emits radiation when exposed to X-rays. This compound is widely used in medicine (fluoroscopy, tomography, and radiography) in industrial radiography in electronic detector systems [1]. Yttrium niobate has broad and dense absorption bands concentrated in the ultraviolet region. This luminescent radiation can be shifted towards longer wavelengths as a result of partial replacement of yttrium ions in the YNbO₄ inclusion crystal lattice. A promising direction is the development of technologies for the formation of optically homogeneous glass-crystalline materials containing niobates activated by rare-earth elements, especially at low temperatures (less than 1600 °C) [2].

Experimental

For the synthesis of glass crystalline materials, yttrium oxide (Y₂O₃), niobium oxide (Nb₂O₅), terbium oxide (Tb₄O₇), and sodium tetraborate (Na₂B₄O₇) were mixed in the required ratios, ground in a mortar for homogenization, and placed in a ceramic crucible for heat treatment. Heat treatment of the samples was carried out in a muffle furnace. The following stages of heat treatment were determined: 1 hour heating to 900 °C, 30 minutes holding at 900 °C and cooling to room temperature for 3.5 hours.

Results and discussion

The crystalline phase in the samples was determined by X-ray diffraction phase analysis and by the spectroscopic characteristics of the activator in the material. Crystalline phases M-YNbO₄, NaNbO₃ and YBO₃ were identified in the ratio of 95 %, 3 % and 2 % of the total crystalline phase in the sample volume.

The luminescent properties of a glass-crystalline material based on yttrium niobate doped with terbium ions were studied by the method of local cathodoluminescence.

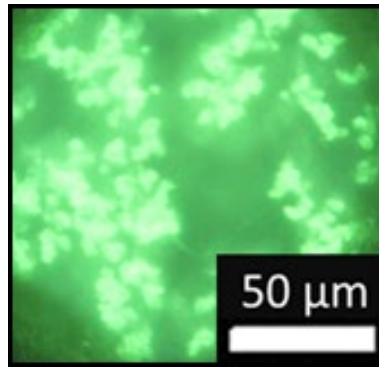


Fig. 1. Cathodoluminescent image of the obtained glass crystalline material

In the obtained sample of glass-crystalline material, two types of inclusions were observed (Fig. 1). According to the results of X-ray phase analysis, these inclusions are $\text{YNbO}_4:\text{Tb}^{3+}$ and $\text{YBO}_3:\text{Tb}^{3+}$, since the replacement of Na or Nb with rare earth elements in the NaNbO_3 crystal is unlikely. The first type of inclusions exhibits significantly more intense cathodoluminescence. Such inclusions are extremely rare (less than 1 % of the studied area of the sample), which are YBO_3 inclusions. The rest of the inclusions cover more than 50 % of the observed sample area, which are YNbO_4 inclusions.

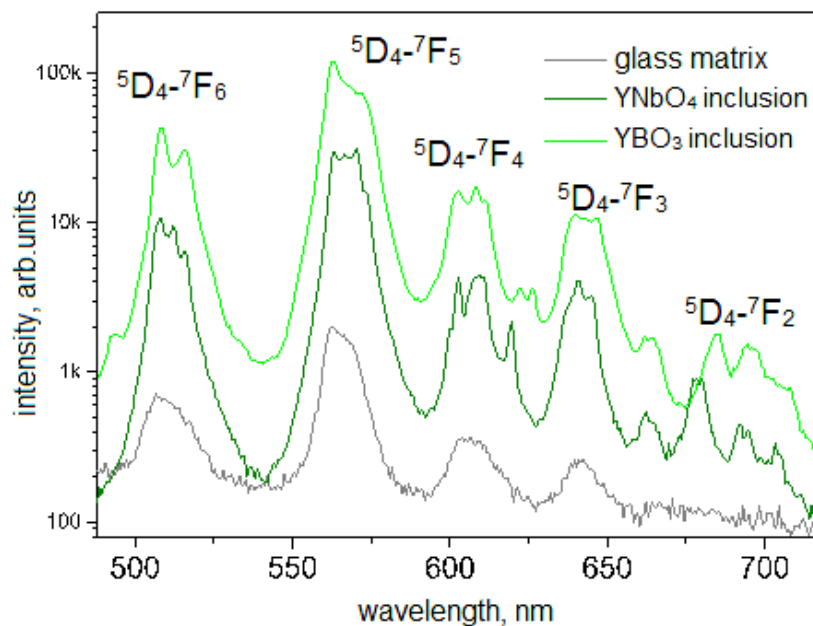


Fig. 2. Cathodoluminescence spectra of the obtained glass-crystalline material

The luminescence spectra in Fig.2 (green and light green) belong to $\text{YNbO}_4:\text{Tb}^{3+}$ and $\text{YBO}_3:\text{Tb}^{3+}$. The low-intensity spectrum in Fig.2 (gray) is characteristic of the terbium-activated amorphous matrix. Narrow luminescence bands correspond to Tb^{3+} emission. The CL spectrums show transitions corresponding to the Tb^{3+} luminescence in the spectrum. The most intense transitions are observed from the $^5\text{D}_4$ level. The most intense luminescence line at 563 nm corresponds to the $^5\text{D}_4 - ^7\text{F}_5$ transition.

Conclusion

Sodium-borate glass materials were synthesized at a temperature of 900 °C. It was found that crystallization of M-YNbO_4 , as well as NaNbO_3 and YBO_3 occurred in the synthesized samples. The content of the crystalline phase M-YNbO_4 was 95%, $\text{NaNbO}_3 - 3\%$, $\text{YBO}_3 - 2\%$. The

developed method makes it possible to obtain sodium-borate glass materials containing principally crystallites of yttrium niobate activated with terbium ions at a reduced temperature. XRD studies were performed using the equipment of the Federal Center for Collective Use "Materials Science and Diagnostics in Advanced Technologies" supported by the Ministry of Education and Science of the Russian Federation, (unique identifier RFMEFI62119X0021).

References

- [1] Yildirim, S., Demirci, S., Ertekin, K. et al., "Production, characterization, and luminescent properties of Eu^{3+} doped yttrium niobate–tantarate films", *J Adv Ceram*, 6, 1, pp. 33 – 42 (03, 2017).
- [2] Kravets, V. A., Ivanova, E. V., Orekhova, K. N. et al., "Low-Temperature Synthesis of Glass-Ceramics with $\text{YNbO}_4:\text{Eu}^{3+}$ Crystallites", *Optics and Spectroscopy*, 129, 2, pp. 245 – 251 (02, 2021).

Structure and optical properties of a-C coatings doped with nitrogen and silicon

D. G. PILIPTSOU, A. S. POBIYAHA, A. V. ROGACHEV
*Francisk Skorina Gomel State University,
104, Sovetskaya Street, 246028, Gomel, Belarus;
pdg_@mail.ru*

Abstract

Using a pulsed arc discharge, carbon coatings binary-doped with silicon and nitrogen are deposited on quartz and silicon substrates. The structure and phase composition of the coatings are studied by atomic force microscopy, Raman spectroscopy, and X-ray photoelectron spectroscopy. The optic band gap E_g and the refractive index of the coatings are determined depending on the alloying elements. The influence of nitrogen and silicon on the formation of the structure of the carbon matrix and the formation of chemical compounds in the coatings, leading to a change in the width optic band gap E_g , has been established. Changes in the roughness R_a and the size of the Csp^2 cluster are shown in the case of binary doping with nitrogen and silicon.

Introduction

The functional properties of coatings largely depend on their chemical, phase composition and morphology, and for carbon-based coatings they are determined by the sp^3/sp^2 ratio [1], the value of which can be changed both by regulating the deposition parameters and as a result of the formation of composite or multilayer coatings. Alloying with nitrogen leads to a change in the structure and properties of coatings (increase in wear resistance, decrease in internal stresses), which is recovered by the formation of chemical bonds between carbon and nitrogen atoms, and the incorporation of nitrogen into the structure of carbon chains [1]. Silicon alloying of a-C coatings causes a change in their structural-phase composition, optical and mechanical properties, and, which is especially important, electrophysical properties mainly due to the formation of chemical compounds [2]. With the joint introduction of nitrogen and silicon into the carbon coating, the formation of silicon nitrides, carbides and carbonitrides is possible, which affect the phase composition of the carbon matrix and change the properties. The aim of this work is to establish the effect of complex alloying of carbon coatings with nitrogen and silicon on their optical properties and to analyze the relationship between changes in properties and the phase composition of the carbon matrix.

Deposition technique

Using a pulsed vacuum arc discharge, carbon coatings doped with silicon, nitrogen, and binary doped with silicon and nitrogen are deposited on quartz and silicon substrates. The thickness

of the coatings was 86 ± 5 nm. The deposition of a-C:Si:N coatings was due to the sputtering of a composite cathode at a nitrogen pressure in the chamber equal to 10^{-2} Pa. Carbon coatings were applied at a discharge voltage of 350 V and a pulse repetition rate of 15 Hz. The absorption spectrum of a-C coatings in the visible and UV regions was studied using a Cary-50 (Varian) spectrophotometer. The optical band gap was determined according to the Tauc method [3]. The refractive index was measured by laser ellipsometry. Surface morphology was studied using a Solver P47 PRO scanning probe microscope. The structure of the coatings was established by Raman spectroscopy and photoelectron spectroscopy.

The results obtained and their analysis

It was found by atomic force microscopy that for a-C:Si:N₂ coatings, in comparison with single-component carbon layers, the roughness (Ra) increases with a simultaneous increase in the grain size, which is associated with the interaction between carbon, silicon and nitrogen and the formation of the SiN phase, which characterized by higher growth rates than Csp³ and Csp²-N. A change in the ID/G ratio and the width of the G-peak of the Raman spectrum of the C:N₂ coating indicates an increase in the size of Csp² clusters and an increase in the concentration of carbon atoms in the state with sp² bond hybridization. High ID/IG values for the a-C:Si coating in combination with a decrease in the G-peak width indicate an increase in the size of Csp² clusters and the degree of their ordering.

For a-C:N₂ and a-C:Si:N₂ coatings, lower values of the ID/IG ratio, an increase in the width of the G-peak in comparison with coatings obtained with assisted nitrogen ions, as well as a shift in the position of the G-peak to a more high wavenumbers. The change in the phase composition of the carbon matrix was determined by the XPS. It is shown that the sp³/sp² ratio is maximum for a-C coating. a-C:N₂ is characterized by an increase in the graphite component and the formation of C-N compounds, which determines an increase in absorption in the UV region (Fig. 1) and a decrease in the band gap E_g (Fig. 2), as well as a refractive index n=2.62. For the a-C:Si coating, at sufficiently large values of the sp³/sp² ratio, the formation of bonds of the C-Si and Si-O is observed in the structure, which lead to an increase in E_g to 2.86 eV, while the value of n reaches 2.72.

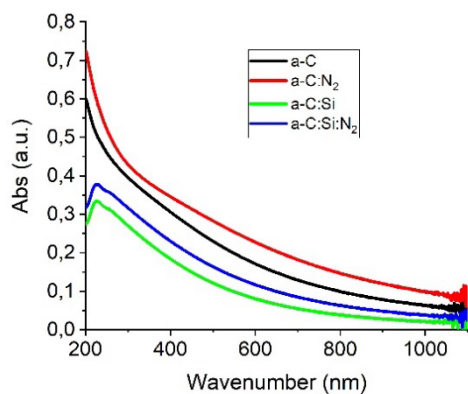


Fig. 1. Uv-Vis spectra for a-C films doped by Si and N

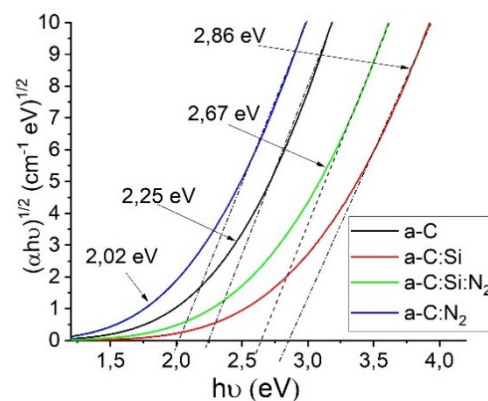


Fig. 2. Tauc plot of (ahv) versus photon energy hv for a-C films doped by Si and N

For a-C:Si:N₂ coatings, the formation of ternary SiN_xC_y compounds is possible, as well as an increase in C-N bonds due to the formation of pyridine-like compounds, which determines a decrease in the band gap (Fig. 2). It has been found that a change in E_g, which depends on the concentration of carbon atoms with an sp² bond, and an increase in the size of Csp² clusters, cause the formation of a broad absorption band in the UV region. Thus, a change in E_g and n is a sign of a change in their optical properties due to the formation of a cluster structure with different cluster sizes and sp²/sp³ bond ratios.

Conclusion

The regularities of the influence of complex alloying of carbon coatings with nitrogen and silicon on their optical properties have been determined. It was found that binary-doped carbon coatings have optical properties (E_g and n), the values of which are intermediate between the values characteristic of coatings doped with nitrogen and silicon. The decrease in the catalytic effect of silicon on the phase composition of the carbon matrix and, accordingly, the properties of the binary-alloyed coating is explained by its participation in the formation of chemical compounds with nitrogen.

References

- [1] D. G. Piliptsov, A. S. Rudenkov, P. A. Luchnikov, A. V. Rogachev, Jiao Xiao Hung, Zhou Bin, "Composite carbon coatings deposited from pulsed cathode plasma" [Kompozitsionnyye uglerodnyye pokrytiya, osazhdennyye iz impul'snoy katodnoy plazmy] (Moscow: Radiotekhnika, October 2020, 283 p.).
- [2] A. S. Chaus, X. H. Jiang, P. Pokorný, D. G. Piliptsov, A. V. Rogachev "Improving the mechanical property of amor-phous carbon films by silicon doping" *Diam. & Rel.Mat.* 82 137 – 142 (January, 2018).
- [3] Tauc, J.; Grigorovici, R.; Vancu, "Optical properties and electronic structure of amorphous germanium" *A. Phys. Stat. Solid* 15, 627 – 637 (March, 1966).

Structure and properties of metal-carbon a-C coatings alloyed with Ti, Zr and Al with a high concentration

D. G. PILIPTSOU¹, A. V. ROGACHEV¹, X.-H. JIANG²,
N. N. FEDOSENKO¹, E. A. KULESH^{1,a}

International Chinese-Belarusian Scientific Laboratory by Vacuum-Plasma Technologies,

¹*Francisk Skorina Gomel State University,*

104, Sovetskaya Street, 246028, Gomel, Belarus;

²*Nanjing University of Science and Technology,*

200, Xiaolingwei street, 210094, Nanjing, China

^a*katrinamillers29@mail.ru*

Abstract

The paper presents a comparative analysis of the structure and mechanical properties of carbon coatings, highly alloyed with metals Ti, Zr and Al. Coatings were deposited from combined flows of metal and carbon plasma with approximately the same mass content. The influence of the nature of the metal on the size of C_{sp^2} clusters and the degree of ordering of the carbon matrix has been determined by means of Raman spectroscopy. Using scanning electron microscopy, the features of the morphology of coatings due to the formation of a carbide phase have been evaluated. It is shown that the values of the Young modules (E) and the coefficient of elastic recovery (η) of the coatings are also determined by the nature of the metal phase: a higher hardness is achieved when alloying with titanium, and the η is achieved when alloying with aluminum.

Introduction

A promising method for changing the structure and properties of carbon coatings is their alloying with metals characterized by different chemical activity in relation to carbon [1]. As a rule, during the formation of metal-carbon coatings, the change in their properties depends on the nature and concentration of the metal, which determines the ratio of the main phases formed with their participation: solid solutions, chemical compounds, metal micro-nanoparticles [1]. At a high concentration of the metal introduced into the volume of the carbon coating, one should expect a slight decrease in hardness due to the formation of metal clusters;

however, in this case, an increase in the elasticity of the coatings, their thermal conductivity, and a decrease in internal stresses are possible. The role of the nature of the metal in such layers is manifested in a different effect on the phase composition and structure of the carbon matrix, changes in the size and ordering of sp^2 and sp^3 clusters. In this regard, the study of the morphological features, properties of carbon coatings, highly alloyed with metals of various nature, and their comparative analysis is of particular interest. The aim of this work is to determine the structural and morphological features, mechanical properties of highly alloyed Ti, Zr and Al carbon coatings.

Deposition technique

a-C:Me coatings were deposited from ionized flows of carbon and metal. Metals (Zr, Al, Ti) were used as the alloying metal. The deposition of the carbon component was carried out from a pulsed cathode plasma generated by a source with a frequency of 5 Hz. Metal evaporation was carried out by an electric arc method at currents of an arc evaporator, providing the same deposition rate of the metal component. The structure of the coatings was studied using a Senterra Raman microscope (Bruker). The morphology and the elemental composition of the coatings were investigated by scanning electron microscopy with EDS (S-4800 FE-SEM, Hitachi). The mechanical properties of the coatings were studied using a NanoScan 4D (Russia).

The results obtained and their analysis

The Raman spectrum of the a-C:Me coatings presents an asymmetric peak ranging from 1000 to 2000 cm^{-1} . The results of processing Raman spectra using Gaussian functions are shown in Table 1 and show the dependence of ratio I_D/I_G , position and width of the G peak on the type of alloying metal. a-C:Ti coating is characterized by a high value of I_D/I_G ratio, while the width of the G peak is minimal, and the position of its center is shifted to the region of low wavenumbers, which is a consequence of a decrease in the size of Csp^2 clusters and an increase in the degree of ordering of the carbon matrix [2]. The significant broadening of the G peak upon doping with aluminum is apparently associated with a higher content of solid solutions in the coating. In this case, there is a correlation between the values of the ratio I_D/I_G and the hardness of the coatings (Table 1).

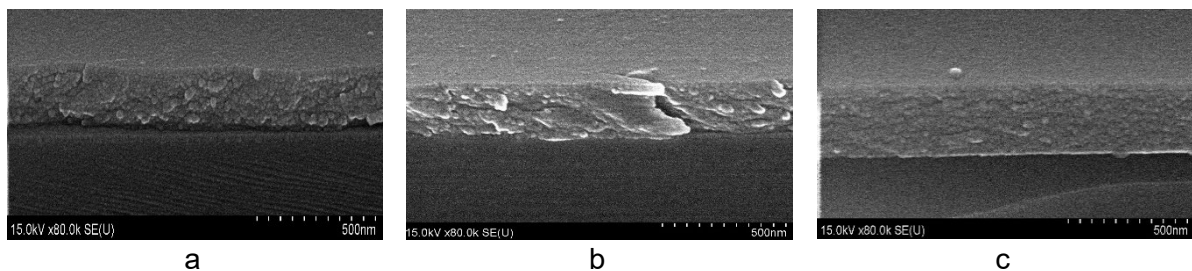


Fig. 1. SEM cross-image of coatings: a) a-C: Zr, b) a-C: Al, c) a-C: Ti

Fig. 1 shows the influence of the nature of the metal on the morphology of the coatings. Thereby for coatings doped with Ti and Zr (Figs. 1a and 1c), the formation of a structure with a grain of a spherical shape is characteristic, while the carbon coatings doped with Al have a fine-grain structure, characteristic of layers more homogeneous in their chemical composition.

Table 1. Elemental composition, structure and mechanical properties of coatings

Coating	C, wt. %	Me, wt. %	O, wt. %	d, nm	G peak position, sm^{-1}	Width G peak, sm^{-1}	Ratio I_D/I_G	H, GPa	E, GPa
a-C:Ti	53.8	45.0	1.2	262	1532.2	187.1	1.28	24.8	195.2
a-C:Zr	42.2	56.5	1.3	183	1535.5	211.2	0.78	20.2	178.6
a-C:Al	57.4	38.6	4.3	254	1487.3	235.8	1.08	20.8	187.1

The hardness of the a-C:Me coatings decreases in comparison with the a-C coating, which is determined by a change in both the structure of the carbon matrix and the formation of carbide and metal phases. It was found that the hardness of a-C:Al coatings is higher than that of a-C:Zr coatings, possibly due to the formation of Al_3O_x in the surface layer. It is known [1] that the chemical activity of Zr with carbon is much lower than that of titanium; therefore, in the structure of the a-C:Zr coating, metal prevails, the occupied volume of which is much higher than for a-C:Ti coating. The change in hardness, E and η depending on the depth of indentation, was established. The results obtained indicate the dependence of these parameters on the nature of the alloying metal and the peculiarities of the processes of chemical interaction between the elements. It was found that for a-C:Al coatings the η is maximum. For a-C:Ti and a-C:Zr, the mechanical properties change slightly over the layer depth.

Conclusion

The work established morphological features, phase composition and mechanical properties of carbon coatings doped with Zr, Al, Ti with a volume concentration of 38 to 56 %. It was found that a decrease in the size of C_{sp^2} clusters and an increase in the degree of ordering of the carbon matrix takes place in coatings doped with Zr, Al, and Ti, respectively. It is shown that in highly alloyed carbon coatings, the nature of the alloying metal has a decisive effect on the structure of the coating; the fineness of the coating is the highest when alloyed with aluminum. The hardness of the coatings is highest when alloyed with titanium; a-C:Al coatings are characterized by higher viscoelastic properties.

References

- [1] D. G. Piliptsov, A. S. Rudenkov, P. A. Luchnikov, A. V. Rogachev, Jiao Xiao Hung, Zhou Bin, "Composite carbon coatings deposited from pulsed cathode plasma" [Kompozitsionnyye uglerodnyye pokrytiya, osazhdennyye iz impul'snoy katodnoy plazmy] (Moscow: Radiotekhnika, October 2020, 283 p.).
- [2] Robertson, J. "Diamond-like amorphous carbon", Mater. Sci. Eng. R, 37, 4 – 6, pp. 129 – 281 (May, 2002).

Characteristics of nanocomposite sol-gel films on black silicon surface

A. V. SEMCHENKO¹, V. V. SIDSKI¹, O. I. TYULENKOVA¹, V. E. GAISHUN¹,
D. L. KOVALENKO¹, G. Y. AYVAZYAN², L. A. HAKHOYAN²

¹Francisk Skorina Gomel State University, Sovetskaya 104, Gomel, 246028, Belarus

²National Polytechnic University of Armenia, Yerevan, st. 105 Teryan, 0009, Armenia

Abstract

The structural and photoelectric characteristics of thin sol-gel ZnO, TiO₂, and SiO₂ films on the black silicon (b-Si) surface have been studied. It has been shown that it is preferable to use ZnO and TiO₂ films as passivating and protective films of solar cells based on b-Si, which have stable structural and optical properties and, at least, do not worsen the reflection of b-Si in the near infrared and visible regions of the solar radiation.

Introduction

Black silicon (b-Si) is a needle-like surface nanostructure [1, 2]. These needles increase the amount of light that is captured rather than reflected back from the surface. The combination of low reflectivity and the semi-conductive properties of Si found in b-Si make it a prime candidate for application in solar cells as an antireflection surface. The large surface area of

b-Si leads to a high surface recombination velocity and, therefore, efficient surface passivation by thin films is of utmost importance in employing b-Si in solar cells.

A wide variety of techniques for the deposit method of high quality ZnO, TiO₂, and SiO₂ passivating films on planar (without b-Si) Si surface have been reported, such as chemical vapor deposition, atomic layer deposition, pulsed laser deposition, sol-gel, sputtering and electrochemical deposition [3]. The general advantage of the sol-gel method is that it can be used for large area deposition and processed at a low temperature [4]. In addition, this method is easy in its composition control, it has a low cost and provides uniformity of the film's thickness.

This work presents the results of studying the structural and photoelectric (current-voltage and capacitance-voltage) characteristics of thin sol-gel ZnO, TiO₂, and SiO₂ passivating films on the b-Si surface.

Experimental

The b-Si on the front surfaces of Si wafers was fabricated by reactive ion etching method in a gas mixture of sulfur hexafluoride (SF₆) and O₂. The process pressure was 55mTorr and gas flow rates were 75 cm³/min and 40 cm³/min for SF₆ and O₂, respectively. Samples were placed on the water-cooled bottom electrode that was powered by a 13.56 MHz RF generator [2]. Etching of 10 min leads to a random nanostructure with an average needle height of 1.0 μm and width of 110 nm. The precipitation of ZnO, TiO₂, and SiO₂ nanocomposite films was performed by depositing a sol by centrifugal separation (the spin-coating procedure) [4, 5]. The thickness of the films was about 300 nm.

The cross-section and top-view morphology of the b-Si and thin films were observed by a scanning electron microscope (SEM) and Atomic Force Microscopy (AFM). Measurement of photoelectric characteristics (current-voltage and capacitance-voltage) was carried out under the influence of laser and UV radiation of different wavelengths. The optical reflectance of the samples was detected using a spectrophotometer T70 UV-VIS with an integrating sphere.

Results and discussion

SEM and AFM studies have shown that sol-gel films precisely reproduce the morphology of the b-Si surface without any voids or inclusions. Thus, these films can be concluded to be rather conformal, which is essential for efficient surface passivation.

Studies of the reflection spectrum of ZnO, TiO₂, and SiO₂ films on the b-Si surface showed that ZnO and TiO₂ films, especially in the long-wavelength visible region of the solar radiation, have the lowest optical reflectance, which is most likely due to the large number and small size of their grains. Therefore, it is preferable to use ZnO and TiO₂ sol-gel films as passivating and protective coatings in solar cells based on b-Si. These films not only retain low reflection of b-Si in the near infrared and visible regions of solar radiation, but also extend it to the short wavelength region of the spectrum.

Fig. 1 shows the current-voltage and capacitance-voltage characteristics of b-Si samples with TiO₂ films. The absolute values of the photocurrent in the b-Si / TiO₂ structures are insufficient for converting solar energy in practice (Fig. 1, a). However, the combined use of TiO₂ films and solar cells based on b-Si can facilitate the efficient use of the solar spectrum, for example, in tandem solar cells based on materials with different band gap. At negative bias voltages from -15 V to 0 V at a signal frequency of 1 MHz, the capacity of the b-Si / TiO₂ structure slightly decreases due to the rearrangement of metastable defects (Fig. 1, b). The extended slope of the experimental curves in the middle part of the capacitance-voltage characteristics is due to the presence of a significant density of surface states at the interface.

Conclusion

It is shown that the ZnO and TiO₂ films have stable structural properties and do not worsen the reflection of b-Si in a wide range of solar radiation. Only samples with a TiO₂ film have a noticeable photosensitivity. The functional possibilities of using b-Si/oxide film structures in

semiconductor devices for different applications are analyzed. It is preferable to use ZnO and TiO₂ sol-gel films as passivation and protective coatings in solar cells based on b-Si.

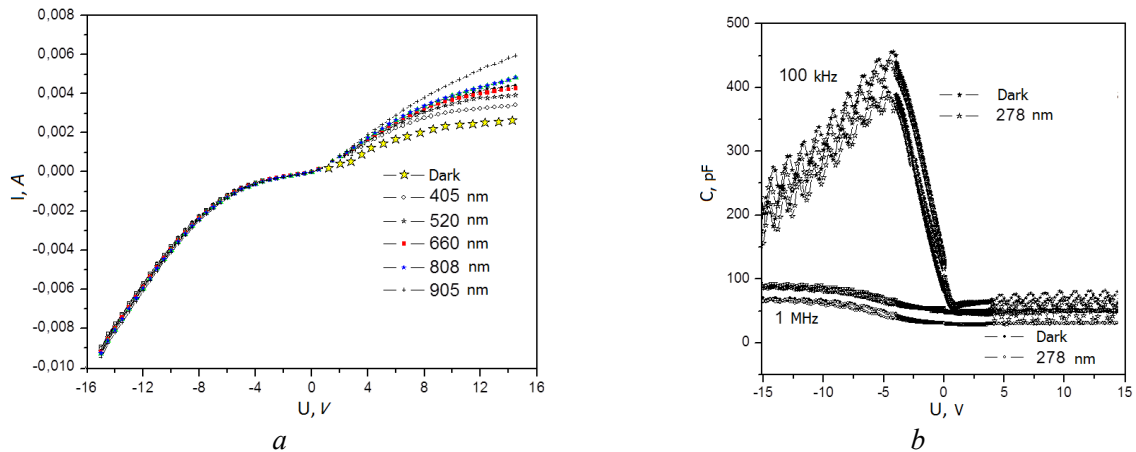


Fig. 1. Current-voltage (a) and capacitance-voltage (b) characteristics of b-Si samples with TiO₂ films

References

- [1] Jian L., Ting Zhang, Peng Zhang, and Shibin Li, "Review Application of Nanostructured Black Silicon", *Nanoscale Res. Letters*, vol. 15, pp. 1 – 10 (2018).
- [2] Ayvazyan G. Y., Barseghyan R. N., and Minasyan S. A., "Optimization of Surface Reflectance for Silicon Solar Cells", *Green Energy & Smart Grids. E3S Web of Conf.*, vol. 69, pp. 01008 – 010012 (2018).
- [3] Schmidt J., Peibst R., and Brendel R., "Surface Passivation of Crystalline Silicon Solar Cells: Present and Future", *Solar Energy Mat. and Solar Cells*, vol. 187, n. 1, pp/ 39 – 54 (2018).
- [4] Rogachev A. V., Gaishun V. E., Semchenko A. V., and Kovalenko D. L., "Sol-Gel Synthesis of Functional Nanostructured Materials for Electronic Devices", *Adv. Mat. Res.*, vol. 1117, pp. 164 – 167 (2015).
- [5] Rogachev A. V., Semchenko A. V., Sidsky V., Gaishun V. E., Kovalenko D. L., Gremenok V., Zaretskaya H., and Sudnik L., "Structural, Optical and Electrical Properties of ZnO:Al Thin Films Synthesized by Sol-Gel Method", *IFMBE Proceedings*, vol. 55, pp. 111 – 114 (2016).

Enhancing the seebeck coefficient of Zn-doped MoS₂ grown over carbon fabrics via band engineering

V. SHALINI^{1,3}, S. HARISH², H. IKEDA^{1,2}, J. ARCHANA³, M. NAVANEETHAN^{3,4}

¹Graduate School of Science and Technology, Shizuoka University, 3-5-1 Johoku, Naka-Ku, Hamamatsu, Shizuoka 432-8011, Japan

²Research Institute of Electronics, Shizuoka University, 3-5-1 Johoku, Naka-Ku, Hamamatsu, Shizuoka 432-8011, Japan

³Functional Materials and Energy Devices Laboratory, Department of Physics Nanotechnology, SRM Institute of Science and Technology, Kattankulathur, Chennai 603203, Tamil Nadu, India

⁴Nanotechnology Research Center, SRM Institute of Science and Technology, Kattankulathur, Chennai 603203, Tamil Nadu, India

Abstract

Among various 2D materials, molybdenum disulfide semiconductors have gained much attention in various applications such as electronics, supercapacitors and optoelectronics due

to their unique transport properties. But the nature of charge transport remains indefinable as they show lower mobility compared to theoretical values. In the present work, we report a possible method for enhancing the thermoelectric properties of MoS₂ by effectively growing pristine MoS₂ and Zn-doped MoS₂ on carbon fabrics (CFs) by a simple hydrothermal method. The uniform growth of pristine MoS₂ and Zn-doped MoS₂ on CFs was confirmed by structural and morphological analysis. Various concentrations of Zn doped MoS₂ nanosheets grown on CFs showed significant enhancement thermoelectric performances. It was found that the electrical conductivity (1.69×10^2 S/cm) was significantly increased for Sample Zn2 with temperature.

Introduction

Recently the demand for electronic devices has been attracted worldwide in various applications such as mobile devices, energy vehicles and smart device applications. With this, it has fascinated the growth of self-powered flexible devices [1]. To reach the integrity of self-powered devices, a flexible power supply plays a vital role for future flexible energy devices. Though various kinds of flexible devices have been developed, designing an independent and maintenance-free self-powered electronic device is necessary. Among them, wearable thermoelectric generators (WTEGs) are the most extensively recognized technology for powering wearable devices. However, developing an excellent flexible energy storage device is very challenging. So, we intend to integrate the self-powered electronic devices with fabrics as a binder-free substrate, which proposes a possible solution for flexible electronic devices. Therefore, self-powered WTEGs have gained huge attention in academics as well as in industrial applications [2]. These devices are solid-state devices that convert waste heat energy into appropriate electrical energy. The thermoelectric performance of these materials is analyzed by

$$ZT = \frac{S^2 \sigma}{\kappa}$$

where S is the Seebeck coefficient, σ is the electrical conductivity and κ is the total thermal conductivity [3].

Molybdenum disulfide nanosheets have gained enormous interest due to their unique two-dimensional (2D) layered structure as well as superior physical and chemical properties. As a thermoelectric material, MoS₂ nanosheets have large effective mass, valley degeneracy, low thermal conductivity and anisotropic property. The layered MoS₂ helps to transfer charge carriers due to weak Vander walls interaction [4]. Whereas bulk and thin-film-based MoS₂ has been studied extensively in the field of thermoelectrics. For example, Abinaya et al. have synthesized MoO₃/MoS₂ nanocomposite by hydrothermal method and achieved the highest ZT of 1.18 via tuning the sulfur vacancies in MoS₂ [5]. Jiang et al. have designed and fabricated MoS₂/PDOT: PSS thin films via vacuum filtration method and achieved the highest power factor of 45.6 mW/K²m at 550 K [6]. However, the research works on flexible thermoelectric devices from MoS₂ were rarely reported, but they have been used in various applications such as supercapacitors, photocatalysis, flexible solar cells and biological applications [2].

In this work, we have synthesized Zn doped MoS₂ nanosheets grown on CFs via the hydrothermal method for flexible thermoelectric applications. The structural, morphological and elemental composition analyses were carried via X-ray diffraction and high-resolution field emission spectroscopy. The thermoelectric properties such as electrical conductivity, Seebeck coefficient were measured using the ADVANCE RIKO ZEM-3 series. The power factor was calculated by the relation of $S^2 \sigma$.

Results:

The structural analysis was carried out using a powder X-ray diffraction spectrometer as shown in Fig. 1(a). The peaks located at $2\theta = 13.53^\circ$, 32.23° , 35.28° , and 57.27° have been assigned

to the (0 0 2), (1 0 1), (1 0 2), and (1 1 0) planes of the hexagonal MoS₂ phase, respectively [5]. No secondary phases of Mo, Zn and S were formed. Whereas the peaks of MoS₂ in CF confirmed the growth of MoS₂ on the fabric and it was in good agreement with the JCPDS file number 01-075-1539 [6]. The diffraction peaks located at 2θ = 25.4° and 43.3° correspond to typical diffraction peaks of CF. Compared to ZnO, it was found that the diffraction peak of MoS₂ at (1 0 0) and (0 0 2) of Zn2, Zn4 and Zn6 was slightly shifted to the higher angle side, respectively. This shift indicates that the zinc ions have interacted with Mo and S atoms successfully during synthesis. The chemical bonding between Mo, S, Zn, and C was characterized by Raman spectroscopy. Figure 1(b) shows the Raman spectra of MoS₂ and Zn-doped MoS₂ and peaks at 378 cm⁻¹ and 404 cm⁻¹ correspond to E_{12g}¹ and A_{1g} modes, respectively. In general, E_{12g}¹ corresponds to in-plane vibrations of Mo and S atoms in the basal plane and A_{1g} corresponds to out-plane vibrations of Mo and S atoms along the c-axis.

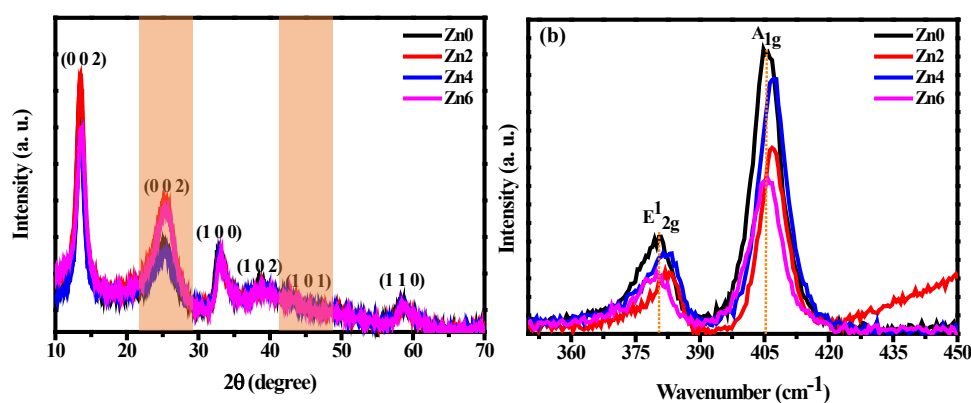


Fig. 1. (a) XRD analysis of MoS₂ and Zn-doped MoS₂ grown on carbon fabrics and (b) Raman analysis of MoS₂ and Zn-doped MoS₂ grown on carbon fabrics

Conclusion

Pristine and Zn-doped MoS₂ nanosheets grown on CFs were successfully synthesized via a one-step hydrothermal method. The structural and morphological analysis confirmed the formation of layered MoS₂ on CFs

References

- [1] T. Stephenson et al., Energy & Environmental Science 7, no. 1 (2014): 209 – 231.
- [2] V. Shalini et al., Journal of Alloys and Compounds 868 (2021): 158905.
- [3] V. Shalini et al., Applied Surface Science 493 (2019): 1350 – 1360.
- [4] K. Hippalgaonkar et al., Physical Review B 95, no. 11 (2017): 115407.
- [5] M. Wu et al., Journal of Materials Chemistry A 5, no. 27 (2017): 14061 – 14069.
- [6] D. Joseph et al., Applied Surface Science 505 (2020): 144066.

Polyaniline-based food quality markers

A. E. SHUMSKAYA¹, H. A. NOVIK¹, T. V. ZHIDKO¹, L. V. FILIPPOVICH²,
J. V. IGNATOVICH¹, A. A. ROGACHEV¹

¹Institute of Chemistry of New Materials, National Academy of Sciences of Belarus

²Institute of Physical and Organic Chemistry, National Academy of Sciences of Belarus

Abstract

Markers have been developed to indicate the quality of food products ((meat, poultry, fish, sausages) on the basis of a nanostructured polyaniline/ copper composite in a polyvinyl alcohol

matrix. The marker is a film with a thickness of 15 – 20 μm . Upon contact with ammonia vapors, they significantly change their optical and electrical characteristics, which are confirmed by UV-, FTIR-ATR spectra and voltammograms. The proposed composite material, as well as PVA films based on it can be used as an indicator of the presence of ammonia.

Introduction

Among high-speed gas sensors, chemoresistive type is very common. One of the actively developing trends in the design of gas sensors is the development of “smart packaging” (SP), which, using internal and external indicators, monitors the interaction between food, packaging and the environment. In SP, two control methods are used: data systems and sensors in packaging, which allows controlling the environment and product packaging using chemical, physical or biological processes [1]. To create the basis for such sensors, nanostructures (NS) can be used to detect molecules, liquids, gases and microorganisms both in the environment and inside the package. Polymers such as polypyrrole (PP) and polyaniline (PANI), in combination with various inorganic materials, including metal nanoparticles (Ag, Au, Cu and Pd), due to their developed surface form nanocomposites with high conductivity, catalytic activity, thermoelectric properties [2], which dictates their application in electrocatalysis, for the development of protective coatings, in the production of sensors [5]. The purpose of this work was to improve the free-stage films technology deposition of coatings for selective gas sensors on the base of PANI and Cu nanoparticles and to determine their main characteristics.

Materials and methods

Matrix polymerization of aniline was carried out under homogeneous conditions; two solutions were prepared: The first (solution A) contained 2.5 ml of aniline, 6 ml of HCl, 3.5 ml of the distilled water. The second (solution B) contained 0.4 ml of HCl, 0.7 g of ammonium persulfate and 9.6 ml of distilled water or an aqueous solution of PVP-360 (concentration 50 mg / ml). To solution B, while stirring on a magnetic stirrer, 0.2 ml of solution A (13 additions) was added every 10 min for 2 h. The mixture was incubated with stirring for 4 hours. The total reaction time was 6 hours. 2 g of PANI were obtained. Synthesis of Cu NPs [3]: 120 ml of a 1.5% starch solution was added to a solution of 0.85 g (0.005 mol) $\text{CuCl}_2 \cdot 2\text{H}_2\text{O}$ in 50 ml of distilled water, stirred at room temperature for 30 min, then 50 ml 0.2 M ascorbic acid solution and slowly added dropwise 30 ml of 1 M NaOH solution. Then the resulting emulsion was heated at 75 – 80 $^{\circ}\text{C}$ for 100 min, after which it was cooled to 6 – 8 $^{\circ}\text{C}$ and kept at this temperature for another 12 h. NPs (the average size of nanoparticles is 25 – 28 nm) were separated on a Schott filter, washed water and ethanol, stored at ~ 6 $^{\circ}\text{C}$. When carrying out the synthesis of Cu NPs under ultrasonic action, copper particles were oxidized to 28-30%.

The composite (11 ml) was mixed with a solution containing: polyvinyl alcohol (PVA) – 5 g, ethyl alcohol – 5 ml, boric acid – 1.5 ml, glycerin – 1.5 ml, dimethylformamide – 2.5 ml in 25 ml of water. Before being added to the composition, the nanocomposites were treated with US for 30 min (US bath, ULTRON, Poland). The films were cast in a 4% H_3BO_3 solution at 45 $^{\circ}\text{C}$. After rinsing them in distilled water, they were dried for 1 h in a heat chamber at 60 – 70 $^{\circ}\text{C}$. The PVA films were 150 – 170 μm thick.

Structure and morphology were determined using scanning electron microscopy (SEM, Hitachi TM3030), energy dispersive X-ray analysis (EDA, Bruker XFlash MIN SVE). To study the effect of ammonia vapors on the film optical properties, the samples were placed in a sealed box with a tissue inside with a drop of 10% ammonia solution (100 μL). The spectra were recorded using a spectrofluorimeter SOLAR (CM2203) in the range from 200 to 800 nm.

Results and Discussions

For the production of markers sensitive to gases (including ammonia) to indicate the quality of food, the PANI+Cu composite was chosen. According to the synthesis method, the resulting composite is PANI grains (up to 50 μm) surrounded by copper particles (Fig. 1,a). Energy dispersive analysis confirms the following composition of the composite: C – 63%, N – 5%, Cu – up to 30% (excluding oxygen). Films with a thickness of 15 – 20 μm were cast from a solution

of the composite in PVA. The films were placed in a sealed box, where a cloth soaked in a drop (100 μL) of 10% aqueous ammonia solution was placed. Within two minutes, the film changed color from bright green to saturated blue (Fig. 1,b and Fig. 1,c).

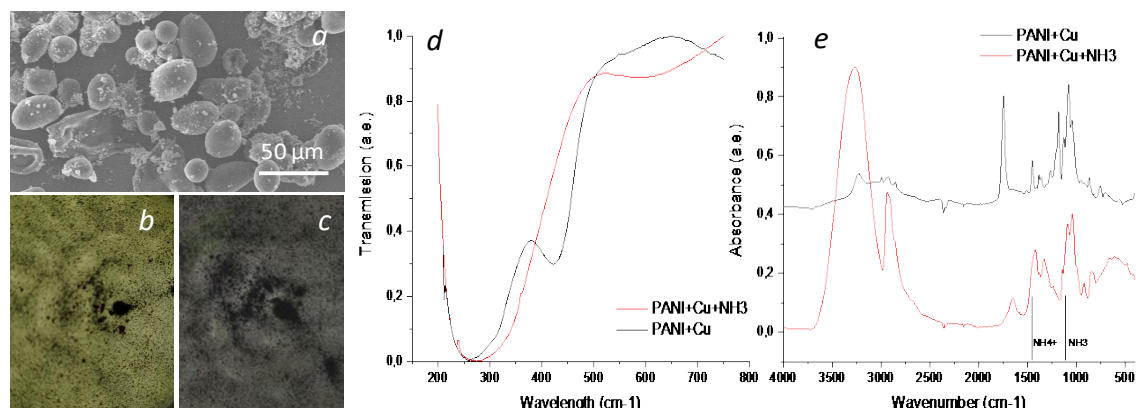


Fig. 1. SEM-image of the PANI + Cu composite (a), and PVA film with the composite before (b) and after treatment with ammonia vapor (c), the change of the film in the presence of ammonia vapor in the UV spectra (d), the change FTIR-ATR spectra (e)

The initial film has a typical absorption range of 380-440 cm^{-1} for PANI, which disappears upon ammonia adsorption [4]. The ART-FTIR tests of the films (Fig. 1,e) before and after treatment with ammonia also recorded changes: the broadening of the peaks in the region of 1110 and 1458 cm^{-1} is probably due to the presence of ammonia adsorbed by the film. A peak in the region of 3000 – 3500 cm^{-1} indicates the saturation of the film with water vapor and indirectly indicates the absorption of ammonia vapors, which is found there. The conductivity of the film that adsorbed ammonia increases by a factor of 10 compared to the original film. In addition, the shape of the I-V characteristic has changed: the hysteresis loop takes on a more symmetric form.

Conclusion

To produce markers sensitive to gases (including ammonia) to indicate the quality of food products, we used a nanostructured composite PANI+Cu. Films with a thickness of 150 – 170 μm were designed from the composite in the polyvinyl alcohol matrix. When treated with ammonia vapor, the films significantly changed their optical characteristics, which were confirmed by UV-, FTIR-ATR spectra. In addition, a significant change in the conductivity of the sample was recorded (by a factor of 10). The proposed composite material, as well as PVA films based on it, can be used as an indicator of the presence of ammonia in the gas mixture

References

- [1] A. Bagchi and T. He, "Intelligent Sensing and Packaging of Foods for Enhancement of Shelf life : Concepts and Applications", *Int. J. Sci. Eng. Res.*, vol. 3, no. 10, pp. 1 – 13, 2012.
- [2] A. A. Rogachev *et al.*, "Structure and electrical properties of polyaniline-based copper chloride or copper bromide coatings deposited via low-energy electron beam Wavenumber cm^{-1} ", *Appl. Surf. Sci.*, vol. 483, no. November 2018, pp. 19 – 25, 2019, doi: 10.1016/j.apsusc.2019.03.159.
- [3] A. Khan, A. Rashid, R. Younas, and R. Chong, "A chemical reduction approach to the synthesis of copper nanoparticles", *Int. Nano Lett.*, vol. 6, no. 1, pp. 21 – 26, 2016, doi: 10.1007/s40089-015-0163-6.
- [4] F. Gu, X. Yin, H. Yu, P. Wang, and L. Tong, "Polyaniline / polystyrene single-nanowire devices for highly selective optical detection of gas mixtures", *Opt. Express*, vol. 17, no. 13, pp. 816 – 819, 2009.

AFM topography of ZnO_x:MgO nanocomposite sol-gel films on the surface of silicon

V. V. SIDSKI, A. V. SEMCHENKO, K. D. DANILCHENKO, O. I. TYULENKOVA
Francisk Skorina Gomel State University, Gomel, Belarus

Abstract

The results of determining by AFM the parameters of sol-gel synthesis influence for the formation of nanocomposite coatings ZnO_x:MgO with a band gap greater than 5 eV and with high sensitivity to UV and visible radiation are presented. It is shown that depending on the magnesium concentration, change in the surface of the ZnO_x: Mg films is observed.

Introduction

The search for new materials for such sensors with sensitivity to UV radiation is an urgent task. Among the requirements imposed on such materials, along with high thermal stability, radiation and chemical resistance, the value of the band gap is important. It should be noted that the structural parameters of oxide layers of complex composition are determined mainly by the conditions and modes of their formation. An analysis of the technological methods used in the synthesis of wide-gap semiconductor materials [1, 2] indicates a number of advantages when using the sol-gel method for these purposes.

When choosing an alloying addition, the radius of the alloying element must be approximately equal to the radius of the element to be replaced and, as a result, a compound with slight distortions of the crystal lattice is formed. The radius of the Mg²⁺ ion (0.57 Å) is comparable to the radius of the Zn²⁺ ion (0.60 Å), which makes magnesium suitable as a dopant to replace Zn in its lattice and facilitate the increase in the band gap [2].

Experimental

Layers based on ZnO:Mg films were obtained by sol-gel method using separate hydrolysis. The application method was centrifugation. The starting materials used were zinc acetate dihydrate (ZnAc) [Zn (CH₃COO)₂ × 2H₂O]; magnesium acetate (Mg (CH₃COO)₂); isopropyl alcohol; distilled water [H₂O]; diethanolamine (DEA) [HOCH₂CH₂NHCH₂CH₂OH]. The film-forming solution (POR) was prepared as follows: zinc acetate and magnesium acetate were separately dissolved in isopropyl alcohol and stirred at 60 °C for 10 minutes. When the solution was transformed into an emulsion, diethanolamine was added at a molar ratio DEA / ZnAc 1: 1 and H₂O / ZnAc 2:1, respectively. A sol based on magnesium acetate was prepared in a similar way. Then the sols were mixed in different concentrations to obtain films with different component ratios (1:1, 1:2, 1:5). Three variants of the sol were prepared: hydrochloric acid was additionally added to sol № 1 and nitric acid to sol № 3. The deposition of the film was carried out by centrifugation at a rotation speed of 2000 rpm for 40 s, followed by drying each layer at 60 °C for 10 minutes (2 layers). The final heat treatment was carried out at temperatures of 250 °C and 450 °C for 30 minutes. Sols containing acetic acid (series 2) did not provide adhesion to the substrate surface.

Results and discussion

Fig. 1 shows typical AFM images of the surface topography of ZnO_x:MgO films on the surface of monocrystalline silicon. The surface of the obtained oxide film №3(1:1) is characterized by developed relief with a high degree of roughness and packing of crystallites according to the "moiré" structure. The topography of the surface of this sample indicates the formation of two separate phases, as evidenced by the data in Table 1. Film №1(1:1) without visible pores and punctures is formed by pyramidal crystallites with the same growth direction perpendicular to the plate. The synthesized films had high adhesion to monocrystalline silicon surfaces. The average grain size on the surface of ZnO_x:MgO films is about 200 μm, and the roughness is

0.114 μm . For films №. 3 (1:1) ZnO, the size and shape of the grains increases 6 times, the roughness – 1.5 – 2 times.

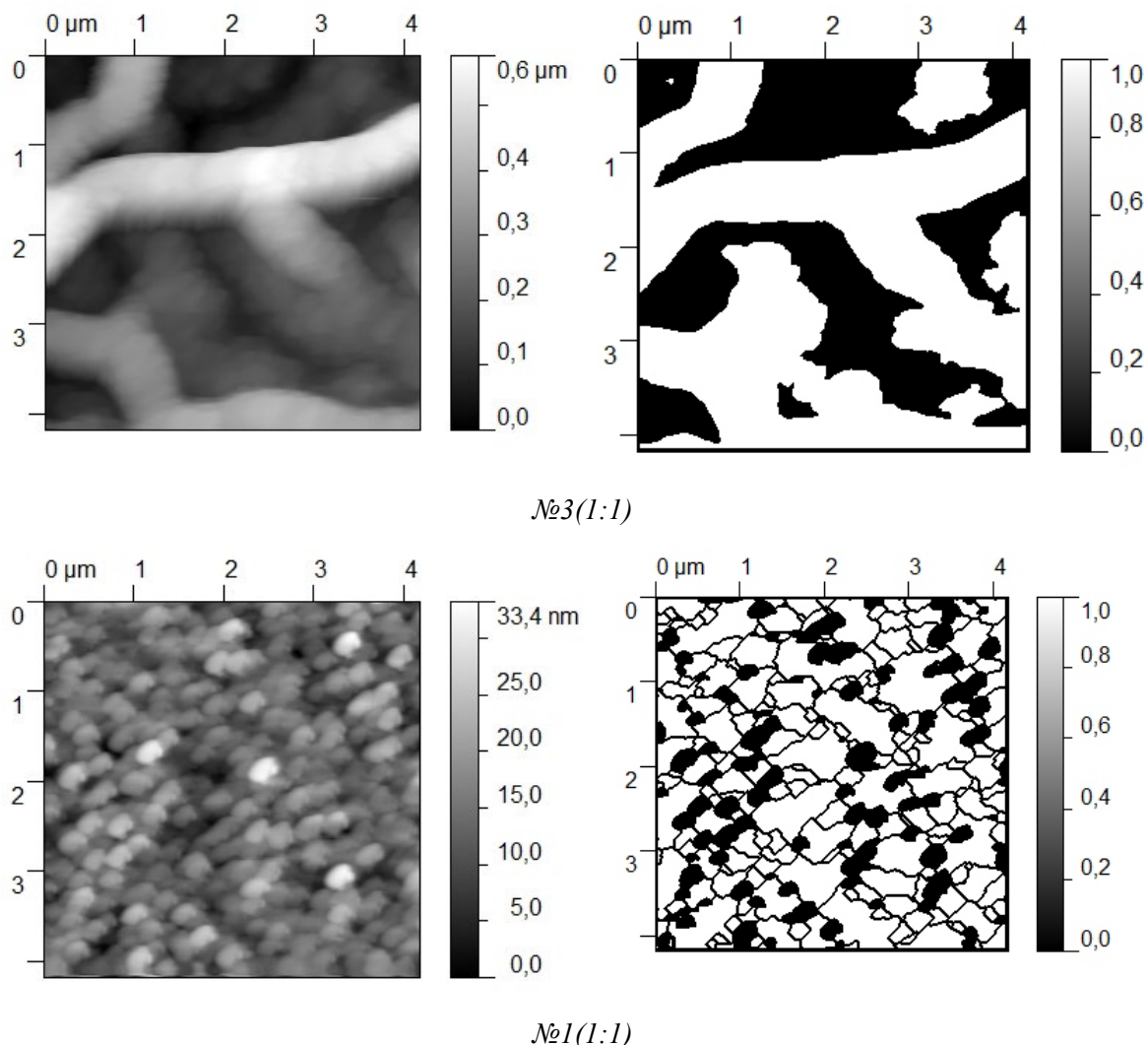


Fig. 1. AFM images of the surface topography of $\text{ZnO}_x:\text{MgO}$ films

Table 1. Parameters of the surface and band gap of $\text{ZnO}_x:\text{MgO}$ films

ZnO:Mg sample №	№1 (1:1)	№3 (1:1)
Ra, nm	3.5	114
Average grains size, nm	174	1060
Band gap, E_g , eV	3.31	3.28/4.72

Conclusion

Samples of coatings based on $\text{ZnO}_x:\text{MgO}$ were studied using AFM. The Gwyddion program calculated the surface roughness, the number of grains and their average size. It was found that the average grain size on the surface of ZnO films is about 200 μm , and the roughness is 0.114 μm . For films №. 3(1:1) $\text{ZnO}_x:\text{MgO}$, the size and shape of grains increases 6 times, roughness – 1.5 – 2 times compared to sample № 1(1:1). The use of nitric acid leads to appearance of two separate oxide phases and to change of the size and shape of the particles $\text{ZnO}_x:\text{MgO}$.

References

- [1] S. J. Priscilla [et al.] "Effect of magnesium dopant on the structural, morphological and electrical properties of ZnO nanoparticles by sol-gel method", *Materials Today: Proceedings.* – 2020; doi:10.1016/j.matpr.2020.07.005.
- [2] K. Gu [et al.] "Tailoring microstructure and optical properties of MgZnO film on glass by substrate temperature", *Materials Letters.* P– 128416. 2020.

Digital materials science

M. M. SYCHOV^{1,2}

¹*Saint-Petersburg State Institute of Technology, Russia*

²*Institute of Silicate Chemistry of the Russian Academy of Sciences, Russia*

"Industry 4.0" (4th industrial revolution) – the concept of digital production, all stages of the product life cycle are carried out on the basis of digital technologies. It should be supported by Digital Materials Science.

Digital Materials Science:

1. Design and construction of materials at the atomic level of the structure (nanostructure).
2. Modeling the processes of synthesis of materials and the formation of a given composition and microstructure.
3. Modeling the macrostructure and properties of materials.
4. Equipment for digital technologies for the manufacture of substances (materials) with desired properties
5. Research of materials using modern digital methods (3D scanning, computed tomography, etc.).

Industry 4.0:

1. Design of products.
2. Computer modeling of properties; behavior under operating conditions in interaction with other elements of the product.
3. Design of manufacturing equipment and products.
4. Manufacturing of products, including 3D printing.
5. Digital interaction with other objects (Internet of things, Big data, AI).

The implementation of the "Industry 4.0" concept at the St. Petersburg State Technological Institute (SPbSTI (TU)) is carried out by the Department of Theoretical Foundations of Materials Science as a complex of educational programs and research programs, implemented in close coordination.

Educational activities:

1. The bachelor's program in "Design, synthesis and application of nanomaterials" has been developed (03/28/03).
2. The Master's program in "Nanomaterials for Industry 4.0" has been developed (28.04.03).
3. The Master's program in "Materials and technologies of additive manufacturing" has been developed (04.22.03).
4. In 2016 the Department of Chemistry, Physics and Biology of the Nanoscale State was organized on the basis of the Institute of Silicate Chemistry of the Russian Academy of Sciences (ISC RAS), headed by Academician of the Russian Academy of Sciences Vladimir Yaroslavovich Shevchenko.
5. With the University of Shizuoka (Japan), a double degree program for PhD students has been implemented.

ISC RAS has a modern instrumentation base for laboratory studies, a multimedia lecture room, a computer class and specialized software for modeling. The peculiarity of the lecture courses

is that the cycle of lectures is delivered not by one lecturer as a whole, but each section is presented by a specialist in this particular field. Laboratory classes are organized in a similar way. For example, students study supercapacitors in the laboratory that directly develops them, whose specialists have the most up-to-date information on this topic.

Over the past years, the basic department has carried out research and graduate qualification works of students on a variety of topics, including the production of nanopowders and nanocomposites, biocompatible ceramic materials, supercapacitors, the development and application of new materials for additive technologies.

The final qualifying work of the master's degree student Polina Matveychikova, recognized as the best graduate of the St. Petersburg State Technological Institute (TU), is devoted to the creation of new composite materials based on multiferroics of the "core-shell" structure. The dispersed phase was formed by modifying ferroelectric barium titanate by applying a magnetic shell of the composition $\text{CoFe}_2\text{O}_4\text{-SiO}_2$ using sol-gel technologies developed under the guidance of Professor O. A. Shilova.

A number of works are devoted to the creation of promising materials for biomedical purposes:

- development of a new class of nanosized porous carriers for targeted drug delivery based on zeolites with a magnetic core; improvement of biocompatible ceramic materials based on zirconium dioxide with additives of oxides of rare earth elements (cerium, yttrium), promising for the manufacture of dental and bone implants.
- development of special materials for generation and storage of electricity: synthesis and optimization of the composition of nanocrystalline ceramics in the $\text{CeO}_2\text{-Sm}_2\text{O}_3$ system for electrolytes of solid oxide fuel cells, improvement of composite electrode materials based on oxygen-containing compounds of cobalt and iron, as well as cathodes for fuel cells with catalytic layers based on metal and bimetallic nanoparticles (Ni, Ag, Cu, Pt, Pd) on various supports as an alternative to traditionally used platinum catalysts.
- development and improvement of materials of complex topology and microstructure using additive technologies. In particular, using the reaction-diffusion Turing transformations, materials with the microstructure of triple periodic surfaces of minimum energy have been created, which have unique mechanical properties.

The research was carried out within the state assignment of Ministry of Science and Higher Education of the Russian Federation (theme No. AAAA-A19-119022290092-5) and supported by Russian Science Fund project No. 21-73-30019.

The effect of SiO_2 content rate in simulated lunar regolith on ablation plume temperature and the feasibility assessment of Al_2O_3 reduction

K. UESUGI¹, K. ISHIGURO², R. OISHI¹, M. MATSUI¹

¹*Department of Engineering, Shizuoka University*

²*Department of Mechanical Engineering, Shizuoka University*

Abstract

We considered the application of lunar regolith for the construction of a lunar base. To obtain aluminum as building materials, the reduction of simulated lunar regolith composed of alumina and silicon dioxide was performed using 1-kW-class continuous-wave diode laser ablation. The temperature dependence of the ablation plume on the content rate of silicon dioxide was investigated, and irradiated surface analysis was conducted using EDX. In addition, the same experiment was conducted with a mixture of silicon and alumina. The silicon dioxide and silicon ratio were set to 25 – 50%, respectively. The plume temperature and Al(I) spectra decreased with silicon dioxide ratio, but not for silicon. EDX results did not show any reduction of alumina in the simulated regolith but did detect aluminum in the silicon mixture.

Introduction

A lunar base is one of the key technologies to expand human activity on the moon. The biggest challenge in building a lunar base is the construction materials. It costs too much to bring all the materials from the earth to the moon. Then, In-Situ Resource Utilization (ISRU) is an important technique for lunar base construction.

Among lunar regolith, alumina is confirmed to be present in about 10% in the whole moon and 23%, especially in the highlands of the moon. Then, alumina is one of the representative substances of lunar minerals. Although alumina itself is not a very versatile material, reduced aluminum has a lot of applications, including lunar base construction materials. In the conventional reduction process, called the Hall-Héroult process, carbon electrodes are required as a reducing agent. However, there is no carbon on the moon. Therefore, a reduction method without carbon has been indispensable because of the huge transport cost of carbon. Komurasaki et al. reported the alumina reduction by laser ablation using continuous-wave CO₂ laser [1]. However, the CO₂ laser has difficult maintenance due to the gas laser, low wall-plug efficiency (10%).

We studied the temperature of the alumina ablation plume and found that it ranged from 2700 – 4500 K. In this study, we investigated the temperature of the plume and the possibility of alumina reduction for simulated regolith composed of alumina and silicon dioxide and for mixed powders of silicon and alumina.

Experimental Procedure

Figure 1 shows a schematic of the experimental setup. A direct diode laser was used, whose maximum power, wavelength was 1.1 kW, 940 nm, respectively. The laser beam was focused on the mixed powder in the crucible, which was installed in the chamber using a focusing lens with a focal length of 100 mm. The laser intensity was set to 1.3 GW/m². The chamber was filled in the argon gas of 100 kPa.

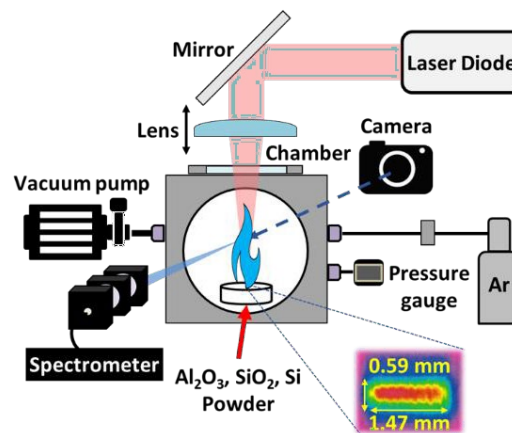


Fig. 1. Schematic of the experimental apparatus

The ablation test was conducted three times for each condition to estimate the standard deviation. The emission spectroscopy was applied to the ablation plume to estimate the plume temperature. The spectrum was measured at a position 2 mm from the powder surface. The plume temperature was estimated by fitting the emission spectrum to the blackbody radiation.

Results and Discussion

Figure 2 shows photos of ablation plumes when ablating a sample of silicon dioxide or silicon mixed powder. As shown in these photos, the emission region decreased with silicon and silicon dioxide ratio. In the case of silicon dioxide mixed powder, the plume turned red, suggesting that the temperature decreased. This is because silicon absorbs laser energy more easily than silicon dioxide. The measured emission spectra were shown in Figure 3. The reduced aluminum line of 394 and 396 nm was observed. This means that the alumina could

be reduced to the aluminum in the ablation plume. The strong AlO vibrational, rotational band was also observed. However, under the condition of silicon dioxide content of 50%, which is close to the actual composition ratio of regolith, the atomic spectrum of aluminum could not be detected. Here, the ablation of pure silicon dioxide was investigated with a spectrometer, and only a small amount of SiO band spectra was obtained, which was thought to be responsible for the decrease in emission.

As a result of EDX, it was investigated that the product by the laser-irradiated mixed powder of silicon dioxide and alumina was just a molten material of each powder. On the other hand, in the case of silicon mixed powder, the presence of aluminum was confirmed. Through the results of this study, it was investigated that alumina laser reduction in simulated regolith containing silicon dioxide is impractical. Therefore, in the future, we will experiment with alumina and silicon dioxide reduction using methane gas as a reusable reducing agent.

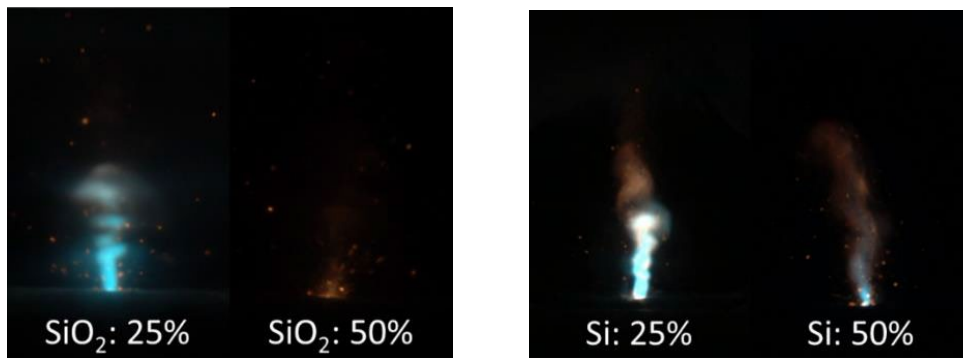


Fig. 2. Photos of ablation plumes as a function of the alumina ratio

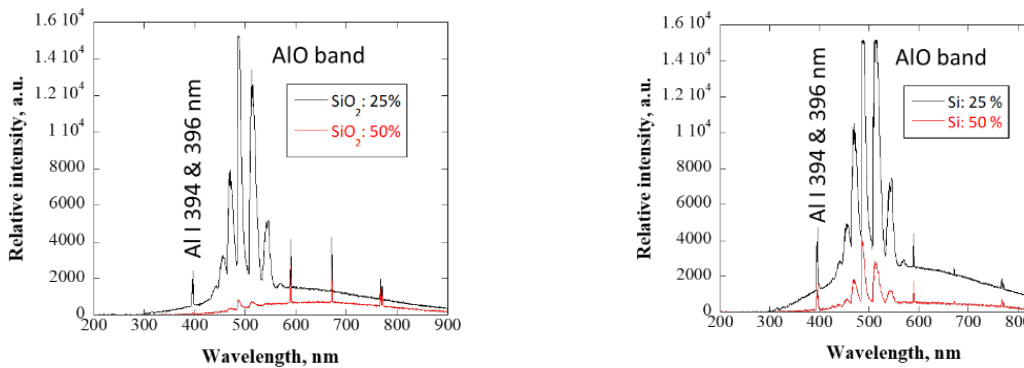


Fig. 3. Measured emission spectra

Conclusion

The plume temperature and Al(I) spectra decreased with silicon dioxide ratio, but not for silicon. EDX results did not show any reduction of alumina in the simulated regolith but did detect aluminum in the silicon mixture. In the meeting, we will also report the results of the plume temperature estimation.

References

- [1] Y. Shin, T. Seiya, K. Kimiya, K. Rei and K. Hiroyuki "Characterization of Reduction Products Generated by Laser Ablation of Alumina", J. IAPS, pp. 26 – 1, 33 – 38, (2018).

Vacuum coatings based on miramistin and their biological properties

YIMING LIU^{1,2}, I. I. KONTSEVAYA², A. A. ROGACHEV^{1,3},
XIAOHONG JIANG¹, M. A. YARMOLENKO^{1,2}

¹*International Chinese-Belorussian Scientific laboratory on Vacuum-Plasma Technology, Nanjing University of Science and Technology, 200, Xiaolingwei street, Nanjing 210094, China;*

²*Francisk Skorina Gomel State University, 104, Sovetskaya street, Gomel 246028, Belarus;*

³*Institute of Chemistry of New Materials of the National Academy of Sciences of Belarus, 36, F. Skoriny, Minsk 220141, Belarus;*

Abstract

This paper provides the first studies of genotoxicity and the ability of miramistin-based coatings to stimulate regenerative processes in eukaryotic cells. The coating testing in the *Allium cepa* system revealed the absence of pathological mitoses beyond the level of normal spontaneous mutation and an increase in the proliferating activity of the meristematic tissue cells in comparison with the control.

Keywords: electron-beam deposition, miramistin, polymer coatings, antibacterial and antifungal properties

Introduction

The problem of drug resistance is steadily increasing every year around the world [1]. This calls for complex use of various combinations of medicinal compounds: antibiotics, metal nanoparticles (Ag, Cu, etc.), antiseptics in medical practice. This is due to the fact that over the past few decades, not a single new antibiotic molecule has been produced. In this regard, miramistin is of interest as an alternative to standard topical drug compounds. Miramistin is an antiseptic with high antifungal and antimicrobial activity. At present, the open literature provides no comprehensive comparative analysis of the results of in vitro and in vivo studies of the antibacterial and antifungal miramistin activity. The aim of these studies is to study the genotoxicity of miramistin-based coatings and its (miramistin) ability to stimulate regeneration processes in eukaryotic cells.

Materials and methods

The technique of coatings vacuum deposition by a low-energy electron beam has been described in a series of papers, in particular [2]. Miramistin powders of (Tocopharm Co., Ltd, China) were used as a target material. The effective thickness was monitored directly during deposition using quartz crystal microbalance (QCM).

Biotesting was performed to study the miramistin genotoxicity and its ability to stimulate regenerative processes in eukaryotic cells. The common onion (*Allium cepa* L., Schtutgarter Riesen sort) was chosen as a model [3]. It should be emphasized that the results of studies on onion cells can be extrapolated to cells of other organisms, including humans [4]. Moreover, onion cells are currently used to test antibacterial drugs. Before the *Allium* test, miramistin-based coatings were deposited on substrates of a given size. The geometric thickness of the coating was measured using a scanning electron microscope (Quanta 200 F). This helped to determine the mass of the deposited layer. To obtain the aqueous solution of an antiseptic (1 mg/l), the substrate was placed in a vessel with distilled water, shaken vigorously for 1 minute. Distilled water was used as the control. Slides for cytogenetic analysis were made according to the S. B. Tedesco and H. D. Laughinghouse protocol [5]. In each case, 10 – 30 root-tips were analyzed. The examination of the squashed slides was carried out at a karyological station equipped with a Leica DMR microscope (Germany). At least 10,000 cells were scanned for each version. The mitotic index (MI) was calculated according to R. Sehgaletal [6]. Phase indices (prophase, metaphase, anaphase, telophase) in the cells of

the meristematic tissue were determined according to [7]. Cells with pathology of mitosis (PM) were expressed as a percentage of abnormal dividing cells of the total number of dividing cells.

Results and Discussion

The use of the drug component to inhibit the growth of pathogenic microorganisms and fungi should not be accompanied by toxic tissue damage. Pathological mitosis (PM) in cells of the body is one of the reasons for mutations and the aneuploidy development. The test results revealed the absence of differences in the experimental versions in terms of the «mitosis pathology» indicator (Fig. 1, a). The determination of the correlation between PM taking into account prophase and PM excluding prophase revealed a high positive value of 0.99.

The possibility of delaying cell division and violating chromosome segregation at any stage of mitosis due to damage to cellular structures such as the spindle apparatus, kinetochores and cell membranes under the influence of aneugenic factors has been studied. To achieve this, the calculation of various types of mitotic index has been performed, and the fractions of dividing cells for each phase have been determined (phase indices (PI)). The absence of noticeable differences between the values of phase indices has been established (Fig. 1, b).

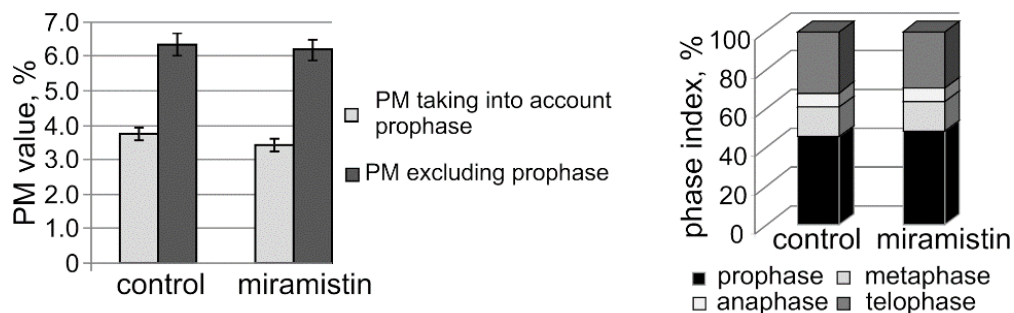


Fig. 1. The miramistin effect on the pathology of mitosis (PM) (a) and on the phase index (PI) (b)

The proportion of cells distribution at different stages of mitosis corresponded to the generally accepted distribution under physiological conditions for plant cells. At the same time, cells at the prometaphase stage were also referred to the metaphase stage. The obtained values of the metaphase-prophase index indicate the absence of mitosis delay in metaphase. The value of this parameter was in the range of 0.32 – 0.33. It should be noted that the pathology “forwarding/lagging chromosomes”, “polar deviation”, “chromosome losses”, “c-anaphase” are found both in the experimental version and in the control one (Fig. 2).

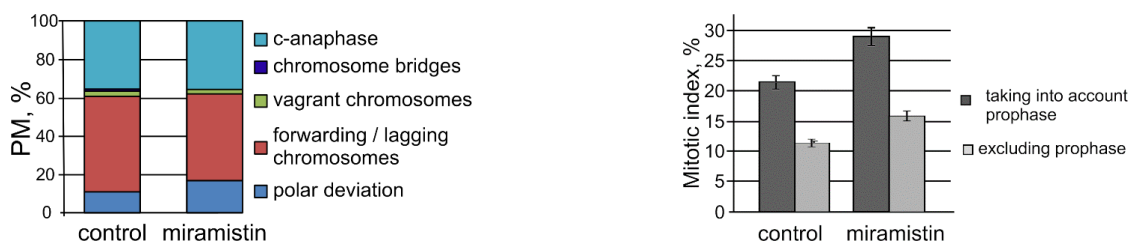


Fig. 2. Composition and spectrum of mitosis pathologies in the root meristem *Allium cepa*

Fig. 3. The influence of miramistin on the mitotic index (MI)

The mitotic index is used as an indicator of adequate cell proliferation. The index indicates the normal mitosis behavior, inhibition of the cell division process or an increase in the mitotic activity of tissues. All this proves the mitotic or mitotic stimulating effect of the factor under study. In the analyzed versions, a rather high mitotic activity of the cells of the formative tissue was observed in the experiment (Fig. 3), but in the case with miramistin, MI was 1.4 times higher.

Conclusions

The miramistin-based coating testing with the *Allium cepa* system showed the absence of pathological mitoses above the level of normal spontaneous mutation and an increase in the proliferating activity of the formative tissue cells compared to the control.

References

- [1] D. I. Andersson, N. Q. Balaban, F. Baquero Antibiotic resistance: turning evolutionary principles into clinical reality, *FEMS Microbiol Rev.* 44, pp. 171 – 188, 2020.
- [2] Beibei Li, Y. Liu, A. V. Rogachev Features of electron beam deposition of polymer coatings with the prolonged release of the drug component, *Materials Science & Engineering C.* 110, 110730, 2020.
- [3] G. Fiskesjö The Allium test as a standard in environmental monitoring, *Hereditas.* 102, pp. 99 – 112. 1985.
- [4] V. E. P. Vicentini, M. Camparoto, R. O. Teixeira *Averrhoa carambola* L., *Syzygium cumini* (L.) Skeels and *Cissus sicyoides* L.: Medicinal herbal tea effects on vegetal and test systems, *Acta Scientiarum Agronomy.* 23, pp. 593 – 598, 2001.
- [5] S. B. Tedesco, H. D. Laughinghouse, *Bioindicator of Genotoxicity: The Alliumcepa Test // Environmental Contamination*, J. K. Srivastava (Ed.). Croatia: InTech Publisher, 2012, pp. 137 – 156.
- [6] R. Sehgal, S. Roy, V. L. Kumar Evaluation of cytotoxic potential of latex of *Calotropis procera* and podophyllotoxin in *Allium cepa* root model, *Biocell.* 30, pp. 9 – 13, 2006.
- [7] N. A. Sutan, I. Fierascu, R. C. Fierascu Comparative analytical characterization and in vitro cytogenotoxic activity evaluation of *Asplenium scolopendrium* L. leaves and rhizome extracts prior to and after Ag nanoparticles phytosynthesis, *Industrial Crops and Products.* 83, pp. 379 – 386, 2016.

Unit 7 “Measurement, identification, and control”

Discovering the *Sicilian byzantine Icons* through a combination of imaging and spectroscopic techniques

F. ARMETTA¹, V. CIARAMITARO¹, G. CHIRCO¹, G. LO RE², M. MIDIRI²,
D. HRENIAK³, E. CAPONETTI^{1,4}, M. L. SALADINO^{1,a}

¹*STEBICEF Department, University of Palermo, Viale delle Scienze and INSTM UdR – Palermo, Bld. 17, I-90128 Palermo (Italy)*

²*Biomedicine, Neuroscience and Advanced Diagnostics, University of Palermo, Via del Vespro 129, I-90127 Palermo (Italy)*

³*Institute of Low Temperature and Structure Research, Polish Academy of Sciences (ILT&RS PAS), ul. Okólna 2, Wrocław (Poland)*

⁴*Labor Artis C.R. Diagnostica S.R.L. Palermo (Italy)*

^a*corresponding author: marialuisa.saladino@unipa.it*

Abstract

The iconographic heritage is one of the treasures of Byzantine art and spirituality that have enriched Sicily (Italy) since the early 16th century. In this work, for the first time, an investigation of some Sicilian *Icons* of Greek-Byzantine origin is reported. The diagnostic studies were carried out using non-invasive Imaging techniques such as photography (grazing vis-light, UV Fluorescence, Infrared, Infrared False Color), Radiography, and Computed Tomography and Spectroscopic techniques such as X-ray Fluorescence, Infrared, and UV-vis Reflectance Spectroscopy. The identification of the constituents (support, pigments, and binders) provides a decisive contribution to the correct historical and artistic placement of the *Icons*, treasure of east Europe historical community in Sicily. Furthermore, the obtained information allows defining their conservation state, the presence of foreign materials and to drive their protection and restoration for future prospective.

Introduction and Motivation

In the Byzantine tradition, *Icons* represent documents of historical, theological and philosophical, as well as artistic interest. For the Eastern faithful, the *Icon* is *Anàmnēsis* (remembrance-recall), it is *Kêrīsmā* (announcement-catechesis), it is *Theoria* (contemplation-prayer), it is a reference to *Tradition*, it is an announcement-declaration of a presence, it is contemplation-involvement vital for a journey of hope. So that, the study of the Byzantine *Icons* constitutes an immense historical heritage and their safeguarding contributes to the knowledge of the religious customs of ancient civilizations [1–5].

The study of some Sicilian *Icons* of Greek-Byzantine origin, here reported, was carried out for the first time. The investigated *Icons*, sacred images that with colours and gold release the prestigious heritage of Greek art, testimony and treasure of east Europe historical community in Sicily, are saved in some important Sicilian town where, since the early 16th century, the ancient Byzantine tradition has been saved and considered the treasures of Byzantine art and spirituality.

The main goal of the research was to understand the painting techniques used by the iconographers in a given historical period, the originality of the *Icon* itself, and the definition of its conservation state.

Approach, Results and Conclusions

The diagnostic studies were carried out following a virtuous protocol based on the use of various analytical techniques (Imaging and Spectroscopic techniques), non-invasive and mainly applicable in situ by using portable instruments.

The main advantage of this choice lies in the possibility of carrying out a large number of measures on a finding in the guarantee of respect for its integrity [6, 7].

A multispectral investigation (grazing vis-light, UV Fluorescence, Infrared, Infrared False Color) was performed by using a modified photocamera and illuminating the *Icons* with different lights and by using some filters. Iconographic details and conservation problems were highlighted by photographic shots in visible light in macro mode and in grazing light. Observation in ultraviolet light permitted us to examine the nature and the state of the surface and the location of pictorial retouching. The examination through Infrared Reflectography at 1100 and 1700 nm and in False Colour gave information on painting techniques and allowed to identify the presence of preparatory drawings, rethinking and / or retouching. Radiography and Computed Tomography gave information about the wooden support and its conservation state, revealed hidden structures, and some integrations made in the previous restoration. The Spectroscopic techniques (X-ray Fluorescence, Infrared, and UV-vis Reflectance Spectroscopy) were useful for the identification of inorganic pigments and gold coating and of the binders and varnishes. Pigments and the realization technique were discriminated on the basis of their typical features and enable us to recognize the palette used by the iconographers.

In detail, concerning an *Icon* saved in the Basilica of Biancavilla di Sicilia (CT), the imaging techniques permitted identifying the different layers of the painting. Some hidden Greek letters were also discovered. Concerning an *Icon* from Piana degli Albanesi (PA), the investigation mapped the previous restoration identifying the different gold area and pigments.

Summarizing, the applied approach provided support for art historians to distinguish the *Icons* for authors/traditions and time and to distinguish the original and false ones as well as to verify the previous restoration works performed in the past.

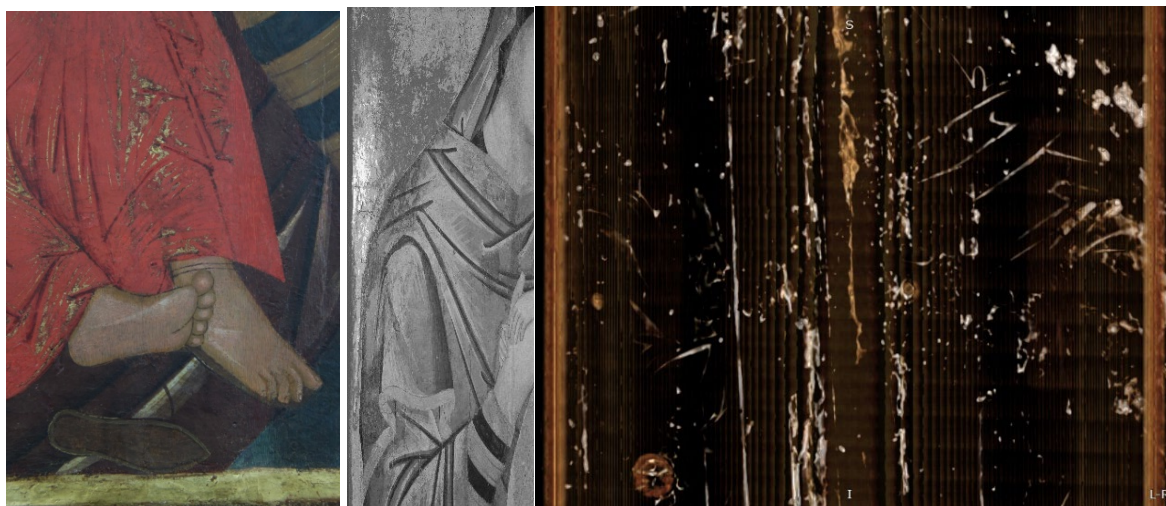


Fig. 1. Details. left) Vis - feet of the Child Jesus, in which the color overlaps, the mission gilding and some retouching are observed. centre) IR-Shoulder of the Madonna; right) greek letters in the retro of the Icon

Funding

The ICONS project (“Old Believer Faith Icons” of VETKA Museum (Gomel Region, Vetka)” – Ref. No. 1206.008-19) is co-financed by the CEI Know-how Exchange Programme sponsored by the CEI Fund at the EBRD.

References

- [1] N. Civici, "Non-destructive identification of inorganic pigments used in 16–17th century Albanian icons by total reflection X-ray fluorescence analysis" *Journal of Cultural Heritage*, 7, pp. 339 – 343 (2006).
- [2] N. Civici, O. Demko, R. J. H. Clark, "Identification of pigments used on late 17th century Albanian icons by total reflection X-ray fluorescence and Raman microscopy" *Journal of Cultural Heritage*, 6, pp. 157 – 164 (2005).
- [3] E. Franceschi, D. Nole, S. Vassallo, "A Comparative Study of Two Albanian Post-Byzantine Icons Attributed to Simoni i Ardenices" *J. of Scientific Research & Reports*, 2, 1, pp. 17 – 34 (2013).
- [4] M. Franceschi, E. Franceschi, D. Nole, S. Vassallo, L. Glozheni, "Two Byzantine Albanian icons: a non-destructive archaeometric study" *Archaeol Anthropol Sci*, 3, pp. 343 – 355 (2011).
- [5] G. P. Mastrotheodoros, M. Theodosios, E. Filippali, K. G. Beltsios, "By the Hand of Angelos? Analytical Investigation of a Remarkable 15th Century Cretan Icon" *Heritage*, 3, pp. 1360 – 1372 (2020).
- [6] M. L. Saladino, S. Ridolfi, I. Carocci, G. Chirco, S. Caramanna, E. Caponetti, "A multi-disciplinary investigation of the "Tavolette fuori posto" of the "Hall of Barons" wooden ceiling of the "Steri" (Palermo, Italy)" *Microchemical Journal*, 126, pp. 132 – 137 (2016).
- [7] M. L. Saladino, S. Ridolfi, I. Carocci, D. Chillura Martino, R. Lombardo, A. Spinella, G. Traina, E. Caponetti, "A multi-analytical non-invasive and micro-invasive approach to canvas oil paintings. General considerations from a specific case" *Microchemical Journal*, 133, pp. 607 – 613 (2017).

Unit 8 “Metamaterials and metasurfaces”

Optical chirality enhancement with dielectric metasurfaces

I. A. FANIAYEU¹, I. A. FANYAEV², V. S. ASADCHY³

¹Department of Physics, University of Gothenburg, 412 96 Gothenburg, Sweden

²Department of Radiophysics and Electronics, Francisk Skorina Gomel State University, 246028 Gomel, Belarus

³Ginzton Laboratory and Department of Electrical Engineering, Stanford University, Stanford, CA 94305, USA

Light-molecule interactions with metallic and dielectric nanostructures make it possible to effectively enhance their sensitivity. For example, circularly polarized light (CPL) interacts with chiral molecules in different ways that allow determining their handedness and structural information. Circular dichroism (CD) spectroscopy (measures the different absorption of light from the left and right circular waves) is used as an effective tool to study chiral molecules. However, CD signal from molecules is very difficult to detect due to their weak internal chirality. These problems impose significant restrictions on the achievable measurement sensitivity. To enhance the CD response from low concentrations or even a single molecule, a new approach based on the formation of superchiral fields interacting with molecules to enhance their optical chirality has been used [1–3].

In this work, we numerically investigate the generation of superchiral fields with achiral dielectric metasurface for further enhancement of CD signals from chiral molecules. The high-refractive-index dielectric metasurface is used to enhance localized electric and magnetic fields simultaneously inside the disk under the CPL excitation at visible wavelengths (Figure 1(a)). As a result, the spatially overlapped electric and magnetic fields with an appropriate phase condition lead to the generation of superchiral fields that in a result maximized optical chirality. The design of a dielectric metasurface consists of TiO₂ disks arranged into a lattice with a period of 450 nm. By changing the diameter (d) of the disk with remaining the height ($h = 195$ nm), we can spatially overlap electric and magnetic fields (Figure 1(b)). Due to the low lossy TiO₂ invisible range, the transmittance of metasurface with optimized parameters ($d = 200$ nm) at the wavelength of 598 nm tends to one while the reflection remains zero. Meanwhile, the optical chirality enhancement reaches up to 485-fold (Figure 1(c)), which can amplify the CD signal from molecules by over two orders of magnitude. We believe that our work could inspire novel on-chip photonic components for surface-sensing in CD spectroscopy, enantioselectivity, and sorting applications.

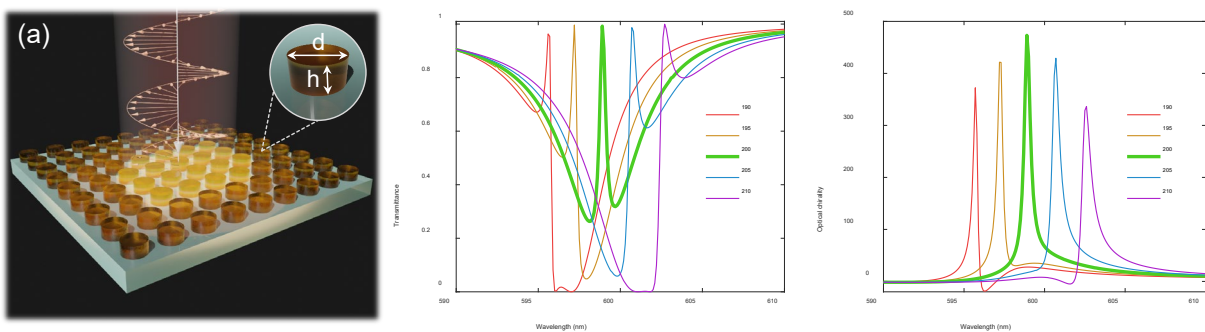


Fig. 1. (a) An illustration of the dielectric metasurface excited by CP light. (b) Simulated transmittance spectra at different diameters of TiO₂ disks. (c) Spectra of optical chirality enhancement

References

- [1] Y. Tang and A. E. Cohen, “Enhanced enantioselectivity in excitation of chiral molecules by superchiral light”, *Science*, 332, 6027, pp. 333 – 336 (2011).
- [2] K. Yao and Y. Liu, “Enhancing circular dichroism by chiral hotspots in silicon nanocube dimers”, *Nanoscale*, 10, 18, pp. 8779-8786 (2018).
- [3] M. L. Solomon, J. Hu, M. Lawrence, A. García-Etxarri, and J. A. Dionne, “Enantiospecific optical enhancement of chiral sensing and separation with dielectric metasurfaces”, *ACS Photonics*, 6, 1, pp. 43 – 49 (2018).

Production and experimental study of a weakly reflecting absorbing metamaterial based on planar spirals in the microwave range

I. SEMCHENKO, A. SAMOFALOV, A. KRAVCHENKO, S. KHAKHOMOV
*Department of General Physics and Department of Optics,
Francisk Skorina Gomel State University
Sov'yetskaya Str. 104, 246028, Gomel, Belarus, e-mail isemchenko@gsu.by*

Abstract

The work aims to produce and experimentally study an absorbing and at the same time weakly reflecting metamaterial consisting of conducting planar two-turn spirals on a dielectric substrate. Such a pre-designed metamaterial is manufactured within the framework of printed circuit board technologies.

Introduction

In articles [1, 2], metamaterials with 3D elements of a special configuration, commonly called planar spirals, were modeled based on the calculation method described in [3]. In contrast to article [1], article [2] designed a metamaterial with a reduced resonant frequency close to 2.5 GHz. The results obtained in article [2] during modeling demonstrate the optimality of a separate planar spiral and the metamaterial as a whole for the parameters found. These simulation results confirmed the high absorbing properties of such a structure and, at the same time, its weak reflecting properties near the resonant frequency (2.5 GHz) and for higher frequencies.

Results of the experiment

Based on the modeling results carried out in article [2], we made an experimental sample of a weakly reflecting absorbing metamaterial consisting of planar spirals on a substrate (Fig.1), with which experimental studies were conducted. The sample material is double-sided FR4 fiberglass with a thickness of 2.93 mm with a copper foil with a thickness of 35 microns.

Article [2] performed the simulation only for the normal incidence of waves. This paper demonstrates experimental studies with an oblique incidence of waves, while the angle of incidence of waves reached 30 degrees. We measured the complex transmission and reflection coefficients in an anechoic chamber for the experimental characterization of the manufactured metasurface sample.

The experimental research was performed in the frequency range of 2 – 3 GHz in the anechoic chamber of Francisk Skorina Gomel State University, Belarus. The experimental setup for transmission coefficient measurement, as shown in Fig. 2, consists of two linearly polarized broadband horn antennas at a distance of 5 m from each other with the metasurface sample between them. The sample was installed into a window in the wall covered with microwave pyramidal absorbers. The antenna was connected to the first port of a vector network analyzer (VNA) by a 50 Ohm coaxial cable. The transmitted wave was detected by a receive horn antenna connected to the second port of the VNA, and S-parameters were stored.

The results of experimental studies are shown in Fig. 3 and 4.

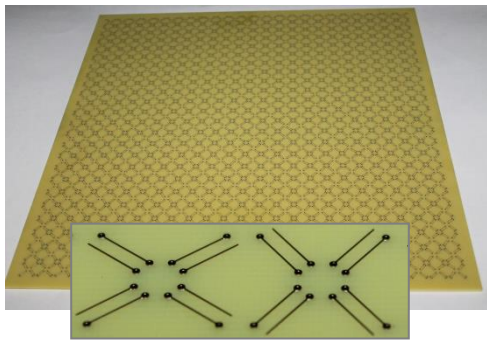


Fig. 1. Photo of a manufactured weakly reflecting absorbing metamaterial in the microwave range and its element on an enlarged scale

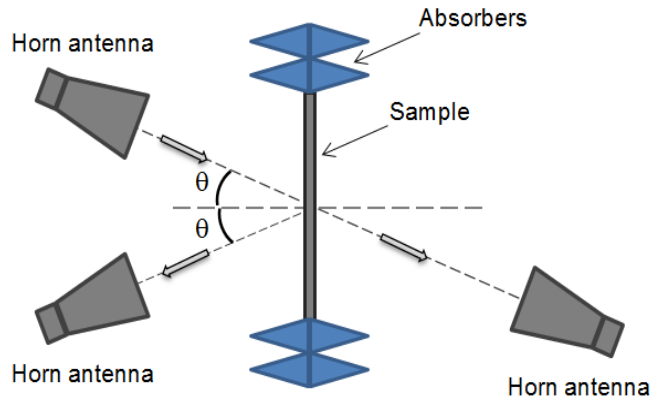


Fig. 2. Experimental setups for measurements of transmission and reflection coefficients

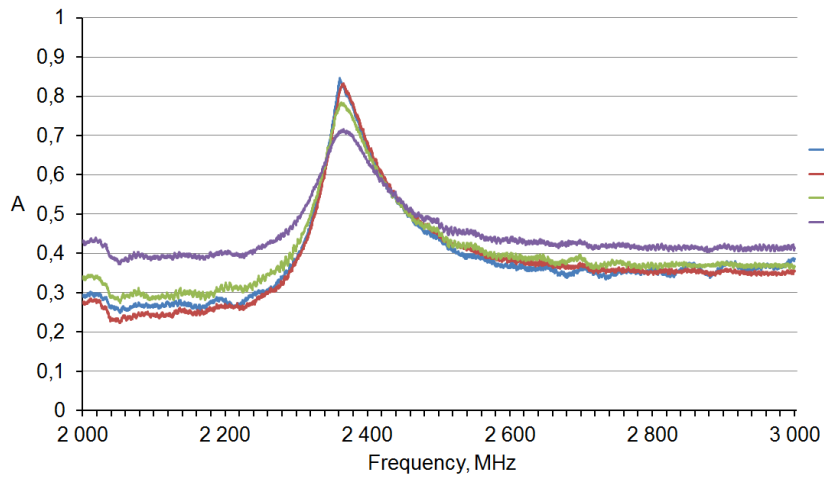


Fig. 3. Frequency dependence of the absorption coefficient at different incidence angles of waves (θ)

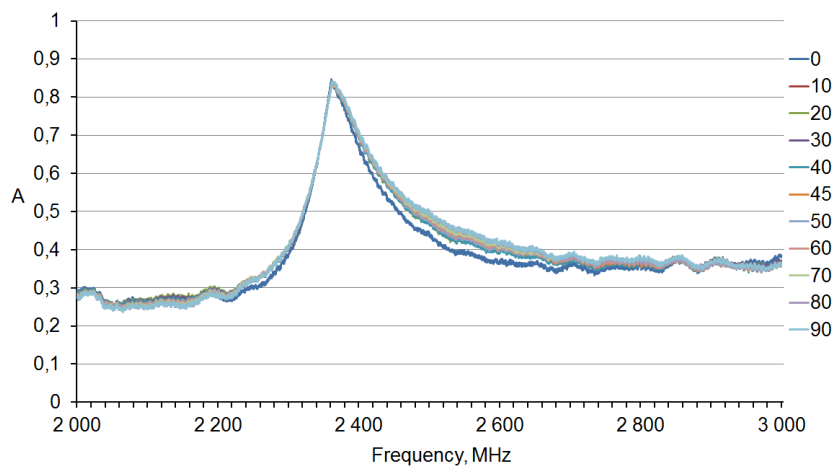


Fig. 4. Frequency dependence of the absorption coefficient at different azimuth angle values on the polarization of the emitting and receiving antennas at normal incidence (the receiving planes of both antennas are rotated by the same azimuth angle relative to the vertical)

Conclusions

The frequency dependence of the absorption coefficient at different incidence angles of the wave on a weakly reflecting metamaterial consisting of conducting planar spirals on a dielectric substrate has been investigated. Good angular stability of the absorbing properties of the sample near the resonant frequency has been shown. When increasing the incidence angle of the wave to 30 degrees, the absorption coefficient of the metamaterial decreased by 15% compared to the normal incidence of the wave (Fig. 3). It has been verified experimentally that the absorbing properties of the metamaterial do not depend on the azimuth of the polarization plane of the incident wave (Fig. 4). Therefore, the manufactured metamaterial is isotropic in the plane of its surface.

As follows from Figures 3 and 4, the experimentally observed resonant absorption frequency is shifted by 0.115 GHz, that is, by 5%, compared with the simulation results. Such a shift in the resonant frequency can be explained by different values of the permittivity for the actual substrate material and the FR4 material considered in the standard software package for modeling.

References

- [1] F. S. Cuesta, I. A. Faniayeu, V. S. Asadchy, S. A. Tretyakov Planar broadband Huygens' metasurfaces for wave manipulations, IEEE Transactions on antennas and propagation, volume 66, number 12, pp. 7117 – 7127 (2018).
- [2] I. V. Semchenko, A. Yu. Kravchenko, A. L. Samofalov, I. A. Fanyaev, Design of metamaterials based on planar spirals in the microwave range, Proceedings of Francisk Skorina Gomel State University, number 3 (120), pp. 154 – 160 (2020) (In Russian).
- [3] V. S. Asadchy, I. A. Faniayeu, Y. Ra'di, S. A. Tretyakov, Determining polarizability tensors for an arbitrary small electromagnetic scatterer, Photonics and Nanostructures – Fundamentals and Applications, volume 12, number 4, pp. 298 – 304 (2014).

Modeling of a three-peak absorber in the 9 – 13 GHz range

D. SLEPIANKOU, A. BALMAKOU, S. KHAKHOMOV, I. SEMCHENKO
*Department of Optics, Department of General Physics,
Francisk Skorina Gomel State University
Sovetskaya Str. 104, 246028, Gomel, Belarus, e-mail Slepenkov95@mail.ru*

Abstract

The aim of this work is to model and theoretically describe an absorbing metamaterial consisting of an array with holes and discs. The simulation is implemented in the Ansys HFSS software product. This work is a preliminary result. Based on this work, we will try to simulate and then create a metamaterial in the 1 – 6 GHz range.

Introduction

During the analysis of the scientific literature, various metamaterials and metasurfaces designed to absorb electromagnetic radiation were studied [1–7]. The most interesting from the point of view of the operating range was the structure of a three-peak absorber proposed by scientists from Jiangnan University, Wuxi, China [1]. The metamaterial is a multilayer structure in which layers alternate, allowing precise tuning of the absorption band. Adjustment is made by varying the radius of the disc R_1 , the radius of the hole R_2 and the distance between them h_1 , as well as the thickness of the insulator h_2 (Fig. 1).

Results of the simulation

An important structural element is the material of the disc and the hole. In the course of modeling in the Ansys HFSS program (Foreign partners provided a High-Frequency Structural

Simulator for non-commercial educational use), copper was chosen as the material of the disc and the hole due to its electrical conductivity properties and use as a metal layer in printed circuit boards as well as the accessible and cheap material. The model of a three-layer absorber in a program Ansys HFSS as well as the parameters of metamaterial's elements are presented in Fig. 2 and Table 1.

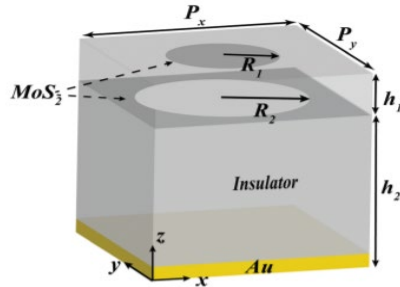


Fig. 1. Schematic representation of a three-layer absorber [1]

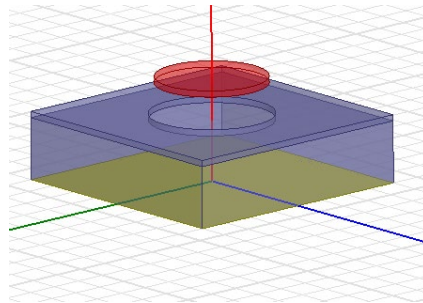


Fig. 2. Model of a three-layer absorber in a program Ansys HFSS

Table 1. Parameters of metamaterial's elements

Element	Material	Dimension, mm
Disc	Copper	$R_1=9$
Hole	Copper	$R_2=10$
Insulator	Air	$h_2=10$

The results of simulation are presented in Fig. 3, 4. Each of these peaks represents the absorption by a specific element of the material. The highest peaks correspond to absorption by the hole and disc. The third smallest peak is the result of absorption by the insulator layer and the thin substrate (Fig.1, 2).

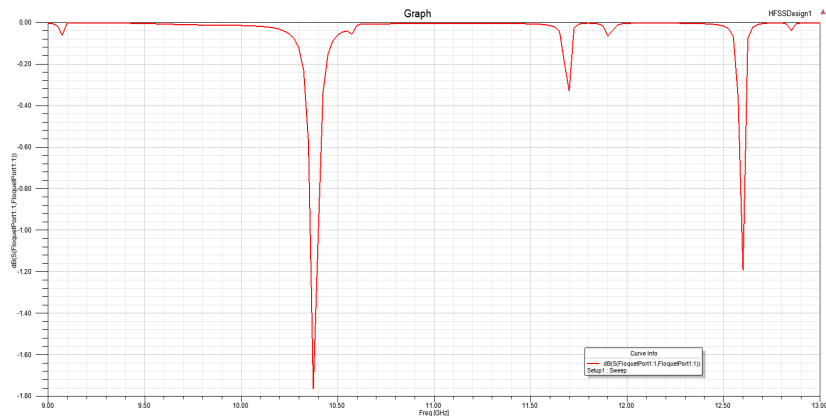


Fig. 3. Graph of power versus radiation frequency

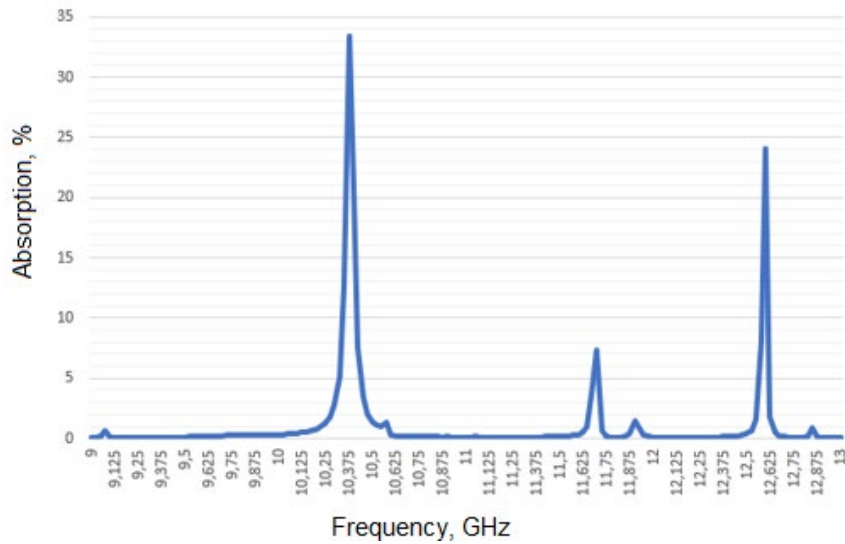


Fig. 4. Graph of absorption versus radiation frequency

It should be noted that further research is needed. To carry out the experiment in the laboratory “Physics of wave processes” of the Francisk Skorina Gomel State University (see Fig. 5), it is necessary to select the parameters so that the absorption maxima are in the range of 1 – 6 GHz. The scheme of the experiment is shown in Fig. 6.



Fig. 5. Anechoic chamber with a control unit of the YUST FarField hardware and software complex with a laptop, as well as a rotary support with an antenna P6-126

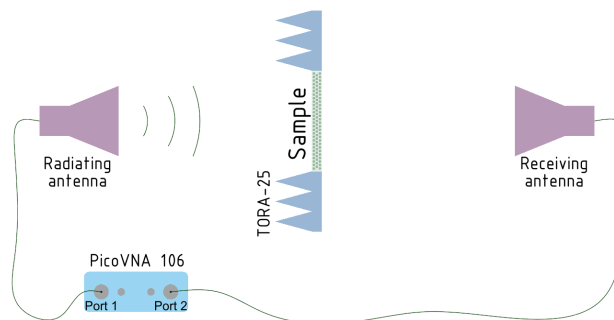


Fig. 6. Schematic of experimental studies to measure the absorption coefficient of radiation by an experimental sample of a metasurface when the radiation is incident along the normal to the metasurface

Conclusions

In summary, we introduce a three-peak absorber based on an array of holes and discs. The proposed structure can be used in related applications such as sensors and detectors. In the near future, we will try to find ways to reduce the operating frequency range for further development of a practical model and research in an anechoic chamber.

Acknowledgment

The work was partly supported by Belarusian Republican Foundation for Fundamental Research (BRFFR) Projects No. F19KITG-017, F20PTI-007.

References

- [1] Wang J., Wang X., Hu Z. D., Tang Y., Balmakou A., Khakhomov S., Liu D., Independent tunable multi-band absorbers based on molybdenum disulfide metasurfaces // *Physical Chemistry Chemical Physics*. 2019. Vol. 21. No. 43. P. 24132 – 24138.
- [2] Ditlbacher H., Krenn J. R., Schider G., Leitner A., Aussenegg F. R. Two-dimensional optics with surface plasmon polaritons // *Applied Physics Letters*. 2002. Vol. 81. No. 10. P. 1762 – 1764.
- [3] Liu Y., Zhong R., Huang J., Lv Y., Han C., Liu S. Independently tunable multi-band and ultra-wide-band absorbers based on multilayer metal-graphene metamaterials // *Opt. Express*. 2019. Vol. 27. No 5. P. 7393 – 7404.
- [4] Feng Y., Hu Z.-D., Balmakou A., Khakhomov S., Semchenko I., Wang J., Liu D., Sang T. Perfect Narrowband Absorber Based on Patterned Graphene-Silica Multilayer Hyperbolic Metamaterials // *Plasmonics*. 2020. Vol. 15. P. 1869 – 1874.
- [5] Bao Z., Tang Y., Hu Z.-D., Zhang C., Balmakou A., Khakhomov S., Semchenko I., Wang J. Inversion Method Characterization of Graphene-Based Coordination Absorbers Incorporating Periodically Patterned Metal Ring Metasurfaces // *Nanomaterials*. 2020. Vol. 10. No. 1102. P. 1 – 10.
- [6] Hu J., Hu Z., Wang J., Khakhomov S., Semchenko I., Wang Z., Li M. High-performance terahertz refractive index sensor based on hybrid graphene Tamm structure // *Journal of the Optical Society of America B*. 2021. Vol. 38. No.9. P. 2543 – 2550.
- [7] del Risco J. P., Mikhalka I. S., Lenets V. A., Sidorenko M. S., Sayanskiy A. D., Glybovski S. B., Samofalov A. L., Khakhomov S. A., Semchenko I. V., Ortiz J. D., Baena J. D. Optimal angular stability of reflectionless metasurface absorbers // *Phys. Rev. B*. 2021. Vol.103. P. 115426.

Unit 9 “Modeling and diagnostics”

Investigation of acoustic wave propagation in complex geometry

M. Yu. ARSENTEV¹, E. I. SYSOEV¹, A. I. MAKOGON²

¹*Institute of Silicate Chemistry, Russian Academy of Sciences,
St. Petersburg, 199034, Russia*

²*Department of Theory of Materials Science, Saint-Petersburg State Institute of Technology,
Technical University, St. Petersburg 190013, Russia*

Abstract

The study of the interaction of acoustic waves with objects of complex geometry is a topic of significant interest in many areas of science and engineering, including aeroacoustics, civil industries, and in military and defence applications, particularly for detection and survivability. In this work, using stable and explicit second-order accurate finite difference method for the elastic wave equation, we investigated the propagation of acoustic waves in such samples (material – corundum). The results of the study show how the wave being reflected from the walls and refracted. Ultimately, active absorption of the wave amplitude and sound pressure was observed.

Introduction

Environmental noise can adversely affect all aspects of our daily life: study, communication with people, quality of sleep. Also, noise has a very detrimental effect on human health. It affects such systems of the body as the nervous system (causes general irritability, reduces concentration and performance), the cardiovascular system and causes many psychophysical effects.

With all of this in mind, product designers and engineers at some of the world's most advanced and successful companies have recognized this fact and incorporate effective noise mitigation elements into their product design process.

It is necessary to consider the fact that despite the intensity of the noise from the source, if a person is constantly exposed to it from the environment, then this leads to annoyance, which reflects how noise can affect our daily life.

Susceptibility to noise and the degree of irritability from it can also be influenced by the individual social circumstances of people.

Computational Details

In the process of modeling elastic waves propagation in objects with complex geometry, two problems should be considered. First, there are curvilinear interfaces since the free surface condition must be met. Secondly, accuracy, since it is necessary to correctly adopt the mesh to the object under study.

The propagation of an elastic wave was studied using a complex second-order differential equation. If the object has a complex geometry, that is, has curvilinear interfaces, then the elastic wave equation is written relative to the curvilinear coordinate system. Within the framework of this model, three types of boundary conditions are used: free surface, Dirichlet condition, and translation conditions. Discretization of the elastic wave equation on a curvilinear grid (discretization of the wave propagation space) is self-adjoint.

Using computer modeling based on the finite element method (COMSOL software package), we investigated the propagation of acoustic waves in the object with complex geometry (material - corundum). In this model, the propagation of acoustic vibrations inside the studied object, which can be caused by a collision with a projectile (bullet), was studied by the application of an acoustic pulse to the top surface of the object under study. Reflections of

waves from periodic boundaries are suppressed by adding absorbing layers, as well as imposing a weak reflection boundary condition. As a result of the application of this load, various types of elastic waves propagate in the volume of the sample. These include longitudinal and transverse waves. In the process of modeling, we used the Elastic Waves module (elastic waves). The methodology of work is presented in work [1].

Results and Discussion

The results of the study show how at different moments the wave runs inside the sample, reflected from the walls and refracted (Fig. 1 – 2). Changes in the pressure distribution have been found. It is assumed that areas containing the highest values of compressive and tensile stresses will be subjected to the highest mechanical stresses, with the possibility of subsequent fracture and cracking. It can also be assumed that these redistributions will depend on the point (surface) of application of the acoustic pulse to the surface of the object under study. Over time, due to refraction and reflection, reflection from the walls, as well as the imposition of the boundary condition of weak reflection, the amplitudes of the waves and the magnitude of the sound pressure decrease.

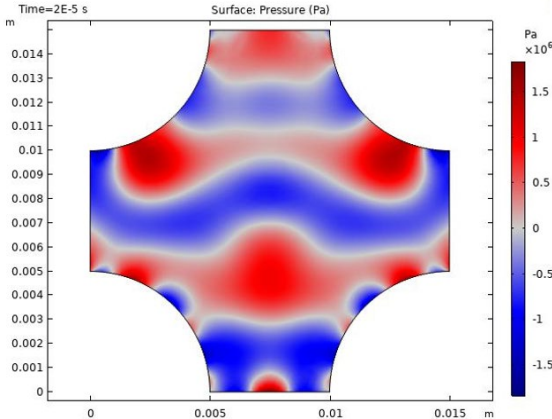


Fig. 1. Distribution of the sound pressure

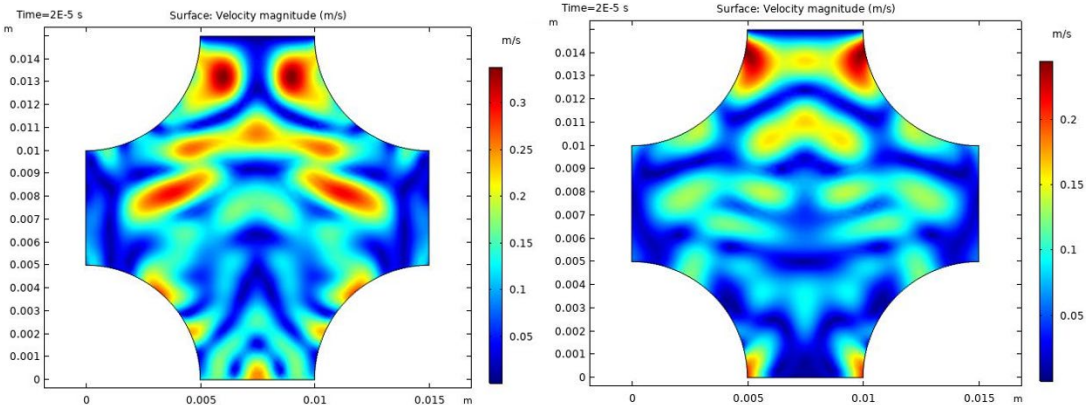


Fig. 2. Distributions of the of the velocity amplitude at different time instants. Initial (left) and subsequent (right) distribution

Conclusion

Thus, we studied the interaction of acoustic waves as they pass through the object under study. This model makes it possible to obtain information about the level of the sound pressure arising at each point of the studied system with a complex geometry, as well as to predict the destruction and cracking caused by the sound wave.

The studies were carried out within the framework of the State Assignment of the Institute of Chemistry of the Russian Academy of Sciences (state registration number of the topic AAAA-A19-119022290092-5).

References

- [1] S. E. Kishore, R. Sujithra, B. Dhatreyi, "A review on latest acoustic noise mitigation materials", *Materials Today: Proceedings*, In press, (June, 2021).

Optimization of quartz glass laser polishing parameters using the computational experiment planning method

V. A. EMELYANOV, E. B. SHERSHNEV, Y. V. NIKITJUK, S. I. SOKOLOV
Francisk Skorina Gomel State University, Sovyetskaya Str. 104, 246028 Gomel, Belarus

Abstract

This paper demonstrates the optimization of the laser polishing process of quartz glass. It was performed using the method of a complete factorial experiment with a two-level variation of factors and the parameters search method. After simulation, the laser polishing modes of quartz glass have been determined. These modes ensure the temperature set points in the processing zone at the minimum values of thermoelastic stresses in quartz plates.

Introduction

The quartz glass properties ensure its wide application in various technical fields. In this case, laser polishing is a promising method for processing quartz glass [1, 2]. The authors previously investigated the laser polishing process of quartz glass using finite element modeling and a complete factorial experiment by creating the appropriate regression model of the material laser processing [3, 4]. This research concentrates on optimizing the parameters of quartz glass laser polishing via the search method using finite element modeling and the method of planning computational experiments [5–7].

Numerical experiment

When using numerical simulation, the technique of a complete first-order factorial experiment was used with a two-level variation of factors (processing speed V , scanning pitch h , laser beam radius R) with output parameters (maximum temperature in the laser processing zone T and principal stress σ_1). The statistical model of the object for analysis was the response functions (T) and (σ_1), connecting the output parameters with the factors (V, h, R), which varied within the specified limits during numerical experiments. Table 1 was created after converting the independent variables in natural scale to dimensionless variables with coded values: -1, +1.

Table 1. Coded values of independent variables

Independent variables	Dimensionless variables	-1	+1
Processing speed, mm/s	X_1	2	4
Scanning pitch, mm	X_2	0.25	0.5
Laser beam radius, mm	X_3	1	2

Table 2 shows the numerical experiment results on quartz glass laser polishing, given for all values of the factors. According to the data presented in Table 2, the models were created. They determine the dependences T and σ_1 on the processing parameters. The scanning pitch turned out to be a non-influencing parameter for the selected variation ranges of technological parameters.

After the appropriate calculations, the equations for T and σ_1 in the transition to actual values are as follows:

$$T = 2098.5 \cdot R - 163.25 \cdot V - (R - 1.5) \cdot (237.5 \cdot V - 712.5) + 159.75 ,$$

$$\sigma_1 = 104615000 \cdot R + 19697500 \cdot V + (R - 1.5) \cdot (38505000 \cdot V - 115515000) + 156272500$$

Table 2. Numerical experiment results

Factor combination number	T, K	σ_1 , MPa
1	1813	7.0
2	1724	7.9
3	1813	7.0
4	1724	7.9
5	4149	73.1
6	3585	151.0
7	4149	73.1
8	3585	151.0

Results of modeling and their discussion

The optimization of the parameters of quartz glass laser polishing was carried out using the search method. This method is an alternative to the direct optimization method when solving extremum problems. In this case, the range of the temperature values T, required for effective polishing, was taken equal to 2000 – 2005 K. Then, the temperatures in the processing zone were calculated using the formula mentioned above. The speed varied in the range of 1 – 20 mm/s with a pitch of 1 mm/s, and the radius of the laser beam varied within 0.1 – 2 mm with a pitch of 0.1 mm. The stresses σ_1 were calculated after determining the parameters that ensure the formation of a given temperature in the laser processing zone (table 3).

Table 3. Calculated parameters of the quartz glass laser polishing

№	V, mm	R, mm	T, K	σ_1 , MPa
1	5	1.2	2004	45
2	8	1.5	2001	160
3	17	0.3	2004	400

As Table 3 shows, the formation of temperatures in a given range is carried out when choosing three settings of speed and radii of the laser beam. In this case, critically high stresses are formed in the processing zone in the third setting.

Conclusion

The numerical experiment resulted in establishing the optimal parameters of laser polishing of quartz plates. These plates provide the minimum values of thermoelastic stresses at temperature set points. The technique proposed in this research can be used to optimize quartz glass laser processing.

References

- [1] D. Wang, F. Fan, M. Liu, T. Tan, H. Li, Y. Li “Top-hat and Gaussian laser beam smoothing of ground fused silica surface, Optics & Laser Technology, Vol. 127, 106141, pp. 1 – 9 (2020).
- [2] J. Hildebrand, K. Hecht, J. Bliedtner, H. Müller, “Advanced analysis of laser beam polishing of quartz glass surfaces”, Physics Procedia, Vol. 39, pp. 277 – 285 (2012).

- [3] E. B. Shershnev, Y. V. Nikitjuk, S. I. Sokolov, A. E. Shershnev “Investigation of laser macro- and microform formation of brittle nonmetallic materials by the method of full factor experiment”, Problems of physics, mathematics and technics. Vol. 4 (33). pp. 30 – 32. (2017)
- [4] A. P. Dostanko [et al.] “Innovative technologies and equipment for submicron electronics” (Minsk. Belaruskaya Navuka, 2020. – pp. 260)
- [5] Y. P. Adler, E. V. Markova, Y. V. Granovsky “Planning an experiment in the search for optimal conditions” (M. Science., 1976, pp 278).
- [6] F. Gill, W. Murray, M. Wright “Practical optimization” (M. Mir, 1985.pp. 383).
- [7] N. N. Shabrov, “The finite element method in calculating the details of heat engines” (Leningrad: Mashinostroenie, 1983. pp. 212).

Investigation of the effect of observation window on the sensitivity enhancement in the multi-pass cell outside the expansion wave tube chamber

R. KOBAYASHI¹, H. SAKAI¹, M. MATSUI^{1,2}

¹ *Department of Engineering, Shizuoka University*

² *Department of Mechanical Engineering, Shizuoka University*

Abstract

Although expansion tubes have been used to simulate atmospheric entry environment, the flow conditions have not been completely characterized. In our previous research, the sensitivity of laser absorption spectroscopy (LAS) using multi-pass cell outside the chamber was not high enough to diagnose ISAS/JAXA expansion tube flows because the inclination of the observation window. In this study, the sensitivity enhancement of multi-pass cells in the inclination of interior cell window was investigated by calculation using the ray-tracing method considering laser spread. As a result, the higher the sensitivity, the smaller the acceptable range of slope. The inclination tolerance of the observation window is larger than the inclination tolerance of the concave mirror.

Introduction

An expansion tube is a promising facility to simulate atmospheric entry conditions in which the velocity would be achieved as 15 km/s [1]. Since the expansion tube flow is generated without high-pressure and high-temperature stagnation conditions, the flow conditions might be close to actual conditions [2, 3]. However, they have not been fully characterized mainly due to its short operation time of typically several tens micro-seconds [4, 5]. Therefore, our group has applied diode laser absorption spectroscopy (DLAS) to expansion tube flows. In our previous study, we diagnosed two expansion tubes flows in Kakuda Space Center and Institute of Space and Astronautical Science in JAXA using molecular oxygen line of 763.43 nm. The maximum fractional absorption was 0.6 %, which is comparable with that of the atmosphere outside the chamber [6]. Then, Herriott type multi-pass system was developed to enhance the sensitivity of DLAS by increase the absorption length. As a result, we succeeded in improving the sensitivity by 44 times [7]. However, the observation windows were moved by the shock wave, so it was not possible to measure with higher sensitivity. In this study, the sensitivity enhancement of multi-pass cells in the inclination of interior cell window was investigated by calculation using the ray-tracing method considering laser spread.

Calculations Conditions

In the calculations, the ray-tracing method does not use paraxial approximation and gives the initial beam diameter to account for beam spread. The coordinate system of the multi-pass cell is shown on the left side of Fig.1 (left). The beam diameter, the focal length of concave mirrors, concave mirror diameter, and the diameter of both entrance and exit hole size were set to

1.0 mm, 200 mm, 50.4 mm and, 2.0 mm. The initial position (Sr), the initial angle of horizontal (θ) and vertical (δ) of the beam, and mirror distance(d) were varied as the parameter when making a multi-pass cell. The coordinate system of the window is shown on the right side of Fig. 1, where α is the angle in the x-axis, β is the angle in the y-axis. The window distance, the refractive index of the window, and the window thickness were set to 170 mm, 1.513, 4.0 mm. α and β were varied as the parameter after making a multi-pass cell. The minimum inclination at which the sensitivity does not change by inclining the observation window from the state where there is no window inclination ($\alpha = \beta = 0^\circ$) is defined as the tolerance.

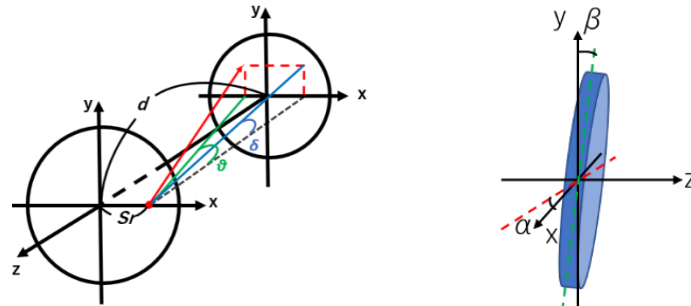


Fig. 1. Coordinate system of multi-pass cell(left) and window(right)

Result and Discussion

The left side of Fig. 2 shows the relationship between sensitivity and tolerance in observe window. The points shown here represent the tolerance for all multi-pass cells generated and the tolerance is less than 5.57 degrees and the resolution is 0.0057 degrees. Even when three orders of magnitude increase the sensitivity, the sensitivity is maintained even when the window is tilted by a few degrees. As the sensitivity increases, the tolerance decreases. While the relationship between the sensitivity and tolerance when the concave mirrors are inclination is shown on the right side of Fig. 2 [8]. The inclination tolerance of the observation window is larger than the inclination tolerance of the concave mirror.

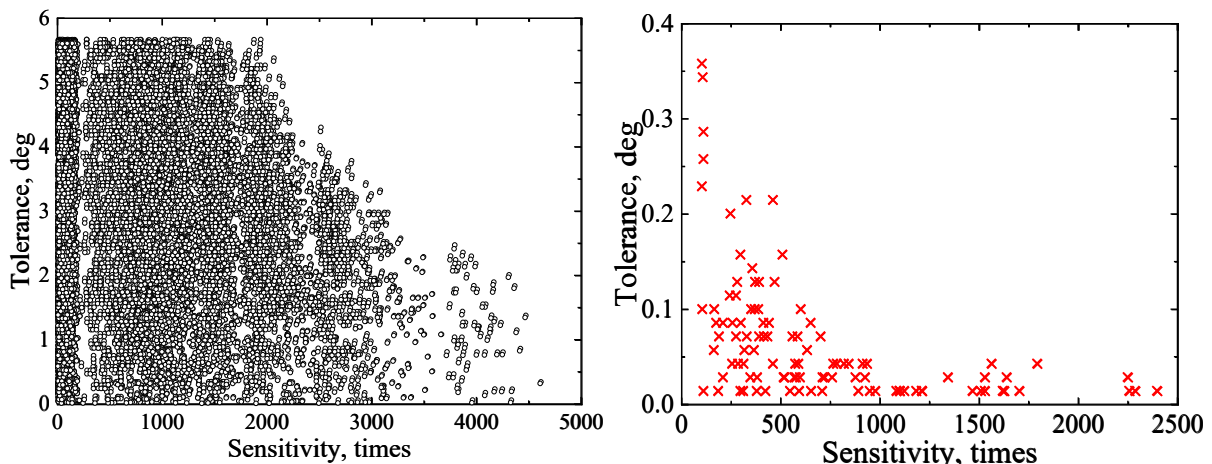


Fig. 2. The relationship between sensitivity and tolerance in observe window(left) and in concave mirror (right)

Conclusion

In the conclusion, even when the sensitivity is increased by three orders of magnitude, the sensitivity is maintained even when the window is tilted by a few degrees. In future work, we will conduct experiments to reproduce the calculation by inserting a window.

References

- [1] T. Yamada, K. Kawahara, T. Ito, and S. Nakazawa “Return and Recovery Operation of the Hayabusa2 Sample Return Capsule”, Proc. 32nd ISTS, Japan (06, 2019).
- [2] Y. M. Abul-Huda and M. Gamba, “Design and Characterization of the Michigan Hypersonic Expansion Tube Facility (MHEXT)”, AIAA Paper 2015-1785 (01, 2015).
- [3] H. Tanno, T. Komuro, K. Sato, K. Itoh, K. Arai, and K. Yamada “Basic characteristics of the free-piston driven expansion tube JAXA HEK-X”, AIAA Paper 2016-3817 (01, 2016).
- [4] Sasoh, Y. Ohnishi, D. Ramjau, K. Takayama, H. Otsu, and T. Abe, “Effective Test Time Evaluation in High-Enthalpy Expansion Tube”, *AIAA J.*, 39, 2141 – 2146 (01, 2001).
- [5] K. Shimamura, A. Okamoto, Y. Fujiwara, Y. Higo, K. Yamada, T. Komuro, and H. Tanno “High-speed visualization for test-time evaluation of a JAXA HEK-X free-piston driven expansion tube”, AIAA Paper 2019-1556 (01, 2019).
- [6] M. Matsui, T. Okamoto, H. Tanno, and K. Yamada “HEK-X Expansion Tube Flow Diagnostics by Laser Absorption Spectroscopy”, 51th Fluid Dyna. Conf, Japan, (07, 2019).
- [7] R. Kobayashi, T. Okamoto, M. Matsui, and K. Yamada “Influence of Multi-pass Configuration on Diagnostics in Laser Absorption Spectroscopy”, Symposium on the Dynamics of Space Navigation, Japan (12, 2019).
- [8] R. Kobayashi, T. Yashui, T. Ishikawa, M. Matsui, K. Yamada, “Investigation of The Enhancement Limit of Multi-pass Cells in Laser Absorption Spectroscopy at Expansion Tube”, Symposium on Shock Waves in Japan. Conf, Japan, (03, 2021).

Simulation of laser splitting of bilayer structures made of silicon wafers and glass substrates

Y. V. NIKITJUK¹, A. N. SERDYUKOV¹, I. Y. AUSHEV²

¹*Francisk Skorina Gomel State University, Sovyetskaya Str. 104, 246028 Gomel, Belarus*

²*University of Civil Protection of the Ministry for Emergency Situations of the Republic of Belarus, Mashinostroiteley Str 25, 220118 Minsk, Belarus*

Abstract

The paper presents the results of a finite-element simulation of the laser splitting process of bilayer structures of monocrystalline silicon and glass under the influence of laser beams with wavelengths equal to 0.808 μm and 10.6 μm and a refrigerant on the workpiece. The calculation of thermoelastic fields formed in a bilayer wafer as a result of laser heating was performed for three cuts of silicon crystals, i.e. (100), (110), (111). The outcomes of this research can be used to optimize the process of laser separation of bilayer structures of monocrystalline silicon and glass.

Introduction

The main methods of separating glass products and instrument wafers into crystals include: cutting with diamond disks, mechanical and laser scribing [1–3]. One of the effective ways to cut silicate glasses and monocrystalline silicon is laser splitting [1–5]. In some cases, the successful implementation of laser splitting technologies for silicon wafers and glass products can be achieved by using double-beam processing methods [7–10]. The use of bilayer structures made of monocrystalline silicon and glass has become widespread in the manufacture of semiconductor microelectromechanical devices [2, 11]. Paper [2] provides a study of the laser splitting process of bilayer structures made of silicon and glass via a laser beam with a wavelength of 1.06 μm . Paper [10] presents a study when the workpiece was exposed to laser beams with wavelengths equal to 1.06 μm and 10.6 μm and a refrigerant. The current paper demonstrates the results of finite element simulation of laser splitting of similar bilayer structures under laser heating with beams with wavelengths equal to 0.808 μm and 10.6 μm and exposure to a refrigerant.

Numerical modeling

The finite-element modeling of the laser splitting process of bilayer structures made of monocrystalline silicon and glass was carried out within the framework of an uncoupled thermoelasticity problem in the quasi-static formulation using the ANSYS program. For comparative analysis, calculations of the thermoelastic field distribution were performed for six spatial variants of laser and refrigerant exposure zones. Thermoelastic fields in the bilayer structure for each of the six spatial variants of the laser and refrigerant exposure zones were calculated for six different variants, taking into account the anisotropy of the silicon layer, i.e. I a is the analysis of the (100) cut when cutting in the [001] direction; I b is the (100) cut analysis when cutting in the [011] direction; II a is the (110) cut analysis when cutting in the direction $[1\bar{1}0]$; II b is the analysis of the (110) cut when cutting in the [001] direction; II c is the (110) cut analysis, when cutting in the $[1\bar{1}1]$ direction, III is the analysis of the (111) cut, when cutting in the $[1\bar{1}0]$ direction.

Results of modeling and their discussion

Figure 1 shows the distribution of temperature fields and fields of thermoelastic stresses formed in a bilayer structure when cutting in the [001] direction of the (100) cut of monocrystalline silicon under sequential laser heating with beams with wavelengths equal to 0.808 μm and 10.6 μm and the influence of a refrigerant from the side of monocrystalline silicon. The maximum temperature values are in the range necessary for the realization of brittle fracture of the bilayer wafer under the action of thermoelastic stresses. The analysis of the spatial configuration of the boundary between tensile and compression stresses in the bilayer structures in the treatment zone (see isosurfaces at $\sigma_{yy}=0$), makes it possible to predict the success of crack propagation in both layers of the bilayer structure. In this case, the most effective of the six calculated treatment options seems to be the use of laser splitting of the bilayer structure in a sequential double-beam laser heating and exposure to the refrigerant from the side of the monocrystalline silicon.

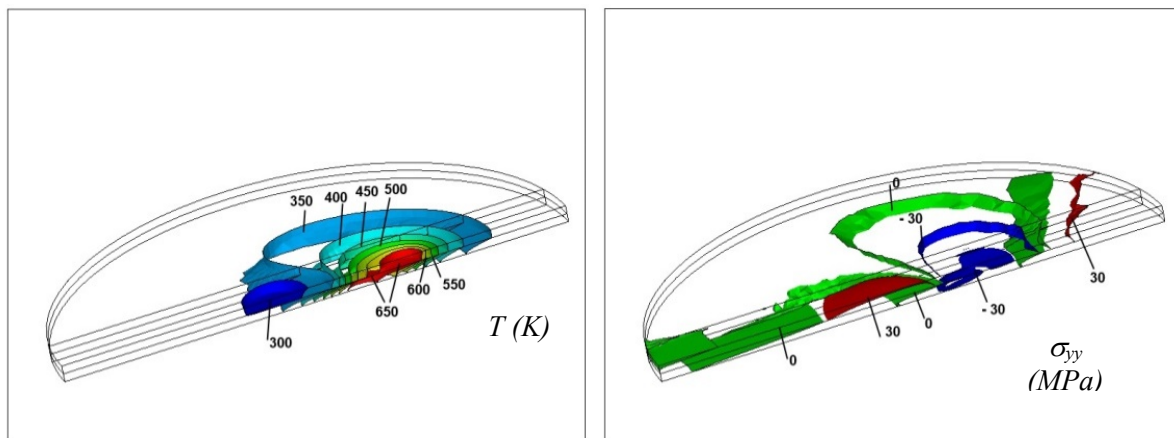


Fig. 1. Distribution of temperature T (K) and stresses σ_{yy} (MPa) in the volume of the processed bilayer sample during double-beam treatment from the side of the monocrystalline silicon

Conclusion

The results obtained show the necessity to take into account the anisotropy of elastic properties of monocrystalline silicon when choosing the parameters of laser splitting of bilayer structures. The paper shows the feasibility of implementing laser splitting of a bilayer structure with sequential laser heating and exposure to a refrigerant from the side of monocrystalline silicon.

References

- [1] S. Nisar, L. Li, and M. Sheikh “Laser Glass Cutting Techniques - A Review”, J. Laser Appl., Vol. 25, No. 4, pp. 042010-1 – 042010-11 (August 2013).
- [2] Y. Cai, L. Yang, H. Zhang, Y. Wang “Laser cutting silicon-glass double layer wafer with laser induced thermal-crack propagation”, Optics and Lasers in Engineering, Vol. 82, pp.173 – 185 (July 2016).
- [3] V. S. Kondratenko, A. S. Naumov “Method of cutting plates from fragile materials”, Patent 2404931, Russian federation, (2010).
- [4] A. N. Serdyukov, S. V. Shalupaev, Yu. V. Nikitjuk “Features of Controlled Laser Thermal Cleavage of Crystalline Silicon”, Crystallography, 55(6), 933 – 937 (2010).
- [5] A. M. Saman, T. Furumoto “Evaluation of separating process for different materials by thermal stress cleaving technique”. International Journal of Engineering & Technology. Vol. 7, No. 4.27, pp. 158 – 161 (2018).
- [6] V. K. Sysoev, P. A. Vyatlev, A. V. Chirkov, V. A. Grozin, D. A. Konyashchenko “Two laser thermo cleavage of glass elements for space-craft conception”, SPACE JOURNAL of «Lavochkin association», 1, pp. 38 – 44 (2011).
- [7] J. Liu, J. Lu, X. Ni, G. Dai, L. Zhang, Y. Chen “Numerical study on thermal stress cutting of silicon wafer using two-point pulsed laser”, Optica Applicata, Vol. XLI, №.1, pp. 247 – 255 (2011).
- [8] J. Junke, W. Xinbing, “Cutting glass substrates with dual-laser beams” Optics and Lasers in Engineering, Vol. 47, pp. 860 – 864. (2009).
- [9] S. V. Shalupaev, E. B. Shershnev, Yu. V. Nikityuk, and A. A. Sereda “Two-beam laser thermal cleavage of brittle nonmetallic materials”, J. Opt. Technol. Vol 73, No.5, pp. 356 – 359 (May 2006).
- [10] Y. V. Nikitjuk “Investigation of the process of laser splitting of two-layer structures of silicon plates and glass substrates”, Problems of Physics, Mathematics and Technics, Vol 44, No.3, pp. 44 – 49 (2020).
- [11] L. S. Sinev, “Calculation and selection of silicon to glass anodic bonding modes based on the criterion of minimum residual stress”, Dissertation in support of candidate of engineering sciences degree: Speciality 05.27.06, Bauman Moscow State Technical University, (2016).

The use of artificial neural networks for determining the parameters of laser processing of fused quartz

Y. V. NIKITJUK¹, A. N. SERDYUKOV¹, V. A. PROKHORENKO¹, I. Y. AUSHEV²

¹*Francisk Skorina Gomel State University, Sovyetskaya Str. 104, 246028 Gomel, Belarus*

²*University of Civil Protection of the Ministry for Emergency Situations of the Republic of Belarus, Mashinostroiteley Str 25, 220118 Minsk, Belarus*

Abstract

This paper provides the simulation of the laser splitting process of fused quartz using artificial neural networks. The calculations of temperatures and thermoelastic stresses were performed by the finite element method in the ANSYS program to create a training data array and an array data for testing neural networks. The paper studies the influence of neural network architecture, the size of the training data array, and the training time on the accuracy of determining thermoelastic stresses and temperatures in the zone of laser processing of quartz sol-gel glass.

Introduction

The implementation of the fused quartz processing is based on the use of a diamond tool, a water-jet, or laser radiation for cutting in the mode of material evaporation [1]. Laser splitting is one of the most effective methods for processing glass, ceramics and crystals. The main advantages of laser splitting are high separation accuracy, high processing speed and increased strength of the resulting products [2]. Paper [3] presents the research results of the laser splitting process of glass sol-gel plates. Artificial neural networks are widely used in

science and technology, including simulating laser processing processes [4]. Paper [5] provides a comparison of the modeling efficiency using an artificial neural network and finite-element modeling of the laser splitting process of glass. This paper uses an artificial neural network to calculate the values of temperatures and thermoelastic stresses generated by laser splitting of quartz plates.

Finite element analysis

The training data array and data for testing the neural network were performed with ANSYS. Simulation was carried out for a plate with geometric dimensions of 20x10x0.5 mm. The calculations used the properties of fused quartz obtained with the help of a colloidal version of the sol-gel method [3]. When simulating, the cutting speed varied from 40 to 70 mm/s; the laser power was from 100 to 300 W; the semi-major axis of the elliptical laser beam was from 1 to 3 mm; the semi-minor axis of the elliptical laser beam was from 0.5 to 1.5 mm. Table 1 presents some of the input parameters and calculation results.

Table 1. Input parameters of the finite element model and calculated values of maximum temperatures and thermoelastic stresses in the laser processing zone

N	V, mm/s	A, mm	B, mm	P, W	σ , Pa	T, K
1	60	1	1.25	100	2134379	609
2	40	3	1	100	2651899	587
3	60	2.5	1.5	100	1516934	468
4	50	1	1.25	300	7304059	1335
5	55	1.5	0.75	250	7047292	1388

The use of artificial neural networks

Fully connected feedforward neural networks with various architectures created in the open software library for computer-assisted instruction TensorFlow were used to determine the parameters of laser processing of sol-gel glass [6].

The activation function ReLu (Rectified Linear Unit) was used when creating the networks. The optimizer was Adam, which is an extension of the stochastic gradient descent algorithm. The network was compiled with the mse (mean squared error) loss function, which calculates the squared difference between the predicted and target values. There was a change in the number of epochs in training networks and their architecture. Mean Absolute Percentage Error (MAPE) was used to assess the efficiency of neural networks

$$MAPE = \frac{1}{n} \sum_{i=1}^n \left| \frac{d_i - y_i}{d_i} \right| \times 100,$$

where d_i is the desired network output, y_i is the actual network output [7]

The MAPE values when determining the maximum thermoelastic tensile stresses and maximum temperatures in the treatment zone did not exceed 8% and 5% for the worst option of the neural network (option 1). In general, option 3 of the neural network configuration seems preferable to be used, which provides the MAPE values of 3.7% and 2.5%, respectively, when determining the maximum tensile stresses and maximum temperatures in the treatment zone (Table 2).

Table 2. Results of training and testing neural networks

N	Data	Architecture	Epochs	σ	T
				MAPE	MAPE
1	800	[4-5-3]	50	7.7 %	4.9 %
2	800	[4-15-10-3]	50	5.4 %	3.3 %
3	800	[4-15-10-3]	100	3.7 %	2.5 %

Conclusion

The results have shown that it is possible to determine the modes of laser splitting of quartz sol-gel glass based on a combination of the finite element method and artificial neural networks. The numerical experiment helped to identify the architectures of neural networks, which give the best result in determining the thermoelastic stresses and temperatures in the laser processing zone.

References

- [1] V. E. Borisovskiy “Development of the theory and development of a complex of technologies and equipment for laser processing of quartz glass” Dissertation in support of doctors of engineering sciences degree: Speciality 05.11.14, MGUPI, (2011).
- [2] S. Nisar, L. Li, and M. Sheikh, “Laser Glass Cutting Techniques – A Review”, J. Laser Appl., Vol. 25, No. 4, pp. 042010-1 – 042010-11 (August 2013).
- [3] S. V. Shalupaev, A. V. Semchenko, Y. V. Nikitjuk “Silica gel glasses after laser radiation”, Material Science., Vol. 21, № 4. pp. 495 – 501 (2003).
- [4] A. N. Bakhtiyari, Z. Wang, L. Wang, H. Zheng “A review on applications of artificial intelligence in modeling and optimization of laser beam machining”, Optics & Laser Technology., Vol.135, pp 1 – 18 (2021).
- [5] M. B. Kadri, S. Nisar, S. Z. Khan, W. A. Khan “Comparison of ANN and finite element model for the prediction of thermal stresses in diode laser cutting of float glass”, Optik – Int. J. Light Electron Optics., Vol. 126. No 19. pp. 1959 – 1964. – 2015.
- [6] F. Chollet “Deep Learning with Python” (Manning Publications Co., 2018, pp 400).
- [7] M. Madić, M. Radovanović, B. Nedić, V. Marušić “Multi-objective optimization of cut quality characteristic in CO₂ laser cutting stainless steel”, Tehnički vjesnik, Vol/ 22, No 4, pp. 885 – 892 (2015).

Characterization of laser welding of steel 30XГCH2A by combining artificial neural networks and finite element method

Y. V. NIKITJUK¹, G. A. BAYEVICH¹, V. N. MYSHKOVETS¹,
A. V. MAXIMENKO¹, I. Y. AUSHEV²

¹Francisk Skorina Gomel State University, Sovyetskaya Str. 104, 246028 Gomel, Belarus

²University of Civil Protection of the Ministry for Emergency Situations of the Republic of Belarus, Mashinostroiteley Str 25, 220118 Minsk, Belarus

Abstract

The paper presents the calculation of the temperature fields, created at different depths, via artificial neural networks and the finite element method during laser welding of steel 30XГCH2A. The training data array and the array data for testing neural networks were created using ANSYS.

Introduction

The manufacture of structural steel products using electric arc and gas-flame welding is sometimes complicated by high residual stresses and deformations. Laser welding is used to produce joints of various metallic materials. In this case, using laser welding provides minimal deformation of welded joints due to the high energy density, high rate of the process, and narrow fusion zone [1, 2]. In [3], the dynamics of forming thermal cycles during pulsed laser welding and surfacing of high-strength structural steel 30XГCH2A was determined based on the results of finite element modeling. Artificial neural networks are widely used in science and technology, including simulating laser processing [4]. Paper [5] uses neural network simulation to predict the laser welding parameters. It has been found that the developed neural network provides more accurate predictions compared to the regression model. This study determines

the values of temperatures, formed at different depths during laser processing of steel 30XГCH2A, using the artificial neural network.

Finite Element Analysis

The training data array and data for testing the neural network were performed with ANSYS. The simulation was carried out for a plate with geometric dimensions of 2×3×0.6 mm. The calculations took into account the temperature dependences of the thermophysical properties of 30XГCH2A steel. The time dependence of the heat flux was set in the form of rectangular pulses [3]. During finite element modeling, the duration of laser pulses t varied from 1 to 10 ms, the power density of laser radiation P_0 was from 10^8 to 10^9 W/m². The calculations were performed for 100 variants of input parameters, 90 of which were used to train the neural network. The input parameters and the calculation results of the test set are presented in Table 1. T_1 , T_2 , T_3 are the temperatures on the sample surface at a depth of 250 μm and 500 μm, respectively.

Table 1. Input parameters of the finite element model and temperature values in the laser processing zone

N	$P_0, 10^8$ W/m ²	t, ms	T_1, C	T_2, C	T_3, C	N	$P_0, 10^8$ W/m ²	t, ms	T_1, C	T_2, C	T_3, C
1	7	8	1689.1	1170.6	803.4	6	1	3	196.7	144.9	108.0
2	1	5	204.9	152.8	115.6	7	2	10	415.1	306.5	228.9
3	8	2	1556.2	1036.2	673.6	8	2	7	405.3	297.3	220.1
4	3	8	623.8	452.2	329.7	9	9	5	2255.6	1506.7	982.7
5	8	10	2141.0	1462.8	984.2	10	2	8	409.1	300.9	223.5

The use of artificial neural networks

A fully connected feedforward neural network with the architecture [2-10-5-3], created in the open software library for computer-assisted instruction TensorFlow, was used to determine the temperature values during laser welding [6]. The activation function ReLu (Rectified Linear Unit) was used when creating the networks. The optimizer was Adam, which is an extension of the stochastic gradient descent algorithm. The network was compiled with the mse (mean squared error) loss function, which calculates the squared difference between the predicted and target values. The number of epochs in training the networks was 50. The results of the created neural network are shown in Table 2. The relative errors were considered as the values characterizing the accuracy of determining the required parameters. The values of the largest relative errors in determining the temperatures T_1 , T_2 , T_3 were 14.2%, 20.6%, and 8.9%, respectively.

Table 2. Temperature values in the laser processing zone, defined by neural network

N	T_1, C	e, %	T_2, C	e, %	T_3, C	e, %
1	1571.9	6.9	1162.1	0.7	812.1	1.1
2	196.1	4.3	155.9	2.0	125.9	8.9
3	1424.1	8.5	927.1	10.5	605.3	10.1
4	620.1	0.6	454.8	0.6	314.4	4.6
5	2016.3	5.8	1461.1	0.1	1002.7	1.9
6	168.7	14.2	114.9	20.6	98.3	8.9
7	418.3	0.8	326.1	6.4	223.3	2.4
8	411.8	1.6	318.7	7.2	231	5.0
9	2257.8	0.1	1494.5	0.8	971.5	1.1
10	419.1	2.4	325.6	8.2	231.9	3.8

Conclusion

The paper shows the possibility of determining the modes of laser welding of structural steels based on a combination of the finite element method and artificial neural networks. The results can be used in developing technological processes for pulsed laser welding and metal surfacing.

References

- [1] O. V. Sizova, E. A. Kolubaev, A. A. Zaikina, A. V. Vorontsov, Yu. A. Denisova, V. E. Rubtsov "Features of the weld seam structure during laser welding of 09G2S structural steel", Metal processing (technology, equipment, tools), Vol. 20, №. 3, pp. 123 – 133 (2018).
- [2] A. G. Grigoryants, I. N. Shiganov, A. I. Misyurov "Technological processes of laser processing" (Moscow: Bauman Moscow State Technical University, 2006, pp 663).
- [3] G. A. Bayevich, A. V. Maximenko, V. N. Myshkovetz "The Dynamics of the Thermal Cycle Formation in Impulse Laser Welding and Surfacing of High-Strength Structural Steel", Bulletin of GSTU named after PO Sukhoi: scientific – practical journal., No. 1. pp. 38 – 44, (2016).
- [4] A. N. Bakhtiyari, Z. Wang, L. Wang, H. Zheng "A review on applications of artificial intelligence in modeling and optimization of laser beam machining", Optics & Laser Technology., Vol.135, pp 1 – 18 (2021).
- [5] M. Ismail, Y. Okamoto and A. Okado "Neural network modeling for prediction of weld bead geometry in laser microwelding", Advances in Optical Technologies, Vol. 2013, 7 pages, (2013).
- [6] F. Chollet "Deep Learning with Python" (Manning Publications Co., 2018, pp 400).

Modeling and optimization of a microgrid for a midrise apartment and industry

R. RITURAJ¹, A. R. VÁRKONYI-KÓCZY²

¹Doctoral School of Applied Inf. and Applied Math., Óbuda University, Budapest, Hungary

²Institute of Software Design and Software Development, Obuda University, Budapest, Hungary rituraj88@stud.uni-obuda.hu, varkonyi-koczy@uni-obuda.hu

Abstract

To meet the energy demand of an area having a midrise apartment and industry, a microgrid model is proposed. Its sensitivity analysis is performed to assess the impact of fuel price on the least-cost system design. The proposed microgrid system has an overall energy consumption of 24.188 kWh/day and 2129 kW during peak time. The original grid search algorithm and proprietary derivative-free algorithm are used to simulate all of the feasible system configurations defined by the search space and to search for the least-costly system, respectively. On this basis, estimation for the lifecycle cost of the system, accounting for the capital, replacement, operation and maintenance, fuel, and interest costs are discussed. The result shows an efficient rate of return on investment and the internal rate of return for the designed microgrid is 72.6% and 75.9%, respectively. The simulation result of the HOMER optimization tool showed that a PV-diesel system with battery storage would most cost-effectively supply the energy required by the given setup. The achieved result shows hourly energy flows for each component as well as annual cost and performance summaries.

Index Terms- Microgrid, Sensitivity Analysis, Homer Optimization Tool, Rate of Return on Investment, Internal Rate of Return.

Introduction

The word micro means small. As the name implicates, "Microgrid" is a small network of electricity users. It has a local source of supply that is connected to a centralized national grid but functions independently. This helps to improve the function and stability of the regional

electric grid. It also intensifies the local flexibility of the microgrid [1]. Therefore, they have an increasing demand nowadays. Many microgrids are not related to undeveloped sites for commercial exploitation. These are built upon the existing electrical infrastructures. This helps to reduce the overall cost of the grid. Three main components of the microgrid are 1) generation, 2) infrastructure automation, 3) control. The generation of microgrids costs a huge amount. The microgrid controller is the smallest part of the overall project budget. The cost of the construction of a microgrid also depends on the location and size of the microgrid. The cost will increase if it is in a place where construction is not easy [2]. For example, if a place is a dense urban environment and requires lots of distribution reconfiguring then the cost for constructing the microgrid will increase. The scale of microgrids also influences their cost. Generally, larger microgrids are assumed to be more expensive than smaller ones. In gross terms, on a “per kilowatt basis,” the smaller microgrids can cost more than the larger ones. For example, a 50-kW solar array is more expensive per kW than a 1-MW solar array. In the case of the control system, the smaller microgrid will likely cost less. However, smaller microgrids consume more of the overall project budget than the control system for the larger one. Consumers need a perfect reason for switching from a traditional grid system to a microgrid system. They always focus on value over cost. They can switch if the operator identifies what they need, decreases outages, possible resiliency, and avoids fuel costs. Then the operator can help the consumer to optimize the microgrid’s assets and identify the possible value streams. For example, in a grid-connected microgrid, the customer may be able to use the asset. This helps to lower utility demand charges. It also gains revenue by selling capacity or providing ancillary services to the grid.

Component of Microgrid

There are five main components of microgrids. These are:

- a) existing assets: it is a start point of any microgrid. This includes all existing loads, generation sources, and utility connections. These three elements and microgrid operation vision will determine the necessity of new technology to achieve the goals. Determining whether the operator can use the existing assets directly affects how much the islanded microgrid will cost and how long it can keep the lights on in islanding mode.
- b) hardware: it includes various types of technologies and equipment. The choices are vast and depend mainly on the microgrid's use plan. Microgrid hardware cannot be plug-and-play. It will need to be carefully evaluated for a variety of considerations.
- c) integration service: the microgrid cannot work without integration services. Its essential role is to ensure hardware, software, and control communication clearly and respond quickly. A variety of services from the system studies testing. It is necessary to bring the microgrid from concept to completion and guarantee it works properly.
- d) controls: It controls essential components to coordinate different microgrid elements. Three levels of controls are required. The cycle-level control detects and communicates almost instantaneous events on the microgrid. The second-level control takes this information and makes intelligent decisions. This constantly balances and adapts the microgrid system. The minute and hour-level controls react slower after the hard work. This enables customers to make longer-term changes to their microgrid.
- e) deployment services: These are the services and considerations required to build a microgrid and keep it running in the future. The first step is building the microgrid and preparing a team to take over the operation. The second step ensures the long-term operation of a microgrid. This can be enhanced and maintained to reduce the risk from issues that come with age [3].

Conclusion

The work has presented a microgrid model for a midrise apartment and industry, altogether having a capacity of 24.188 kWh/day and 2129 kW during peak time. Designing the microgrid with such a high capacity is quite difficult. The Homer pro tool is used to optimize the microgrid with maximum efficiency. July is taken as a peak month for maximum energy consumption.

Homer optimizer calculates the number of PV arrays, wind turbines, batteries, and converters. The 'Fronius Symo 24.0-3-M with Generic' PV arrays with a rated capacity of 24 kW are used in the microgrid. The microgrid is proved to be efficient, having the rate of return on investment and internal rate of return for the designed microgrid is 72.6% and 75.9%, respectively. The optimization tool took around 180 seconds to provide the optimized new microgrid model. This is optimized for the lowest net present cost. The proposed model is validated through an optimized system with both high simulation speed and accuracy. Further work can be designing this new microgrid into an on-grid system. This can help to sell the extra power after consumption. The optimized combination of power resources and elements is taken for microgrid modeling which gives maximum efficiency at minimum cost.

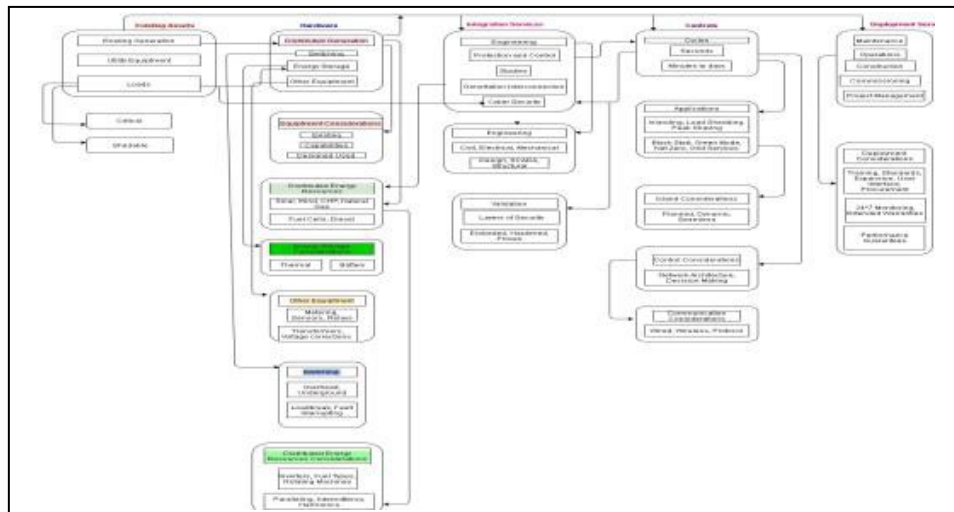


Fig. 1. Flowchart of microgrid components

References

- [1] Yanine F. F., Sauma E. E., "Review of grid-tie micro-generation systems without energy storage: Towards a new approach to sustainable hybrid energy systems linked to energy efficiency", *Renewable and Sustainable Energy Reviews* 26, 60 – 95, Oct-2013.
- [2] Bullich-Massague E, Díaz-González F, Aragüés-Peñalba M, Girbau-Llistuella F, Olivella-Rosell P, Sumper A, "Microgrid clustering architectures", *Applied energy*, 212:340-61, Feb 2018.
- [3] Raji A. K., Luta D. N. "Modeling and optimization of a community microgrid components", *Energy Procedia*, 156:406-11, Jan 2019.

Development of material for 3D printing based on thermoplastic elastomer

M. V. TIMOSHENKO^{1,a}, S. V. BALABANOV¹, M. M. SYCHEV^{1,2}, D. I. NIKIFOROV²

¹*Institute of Silicate Chemistry, Russian Academy of Sciences 199034, Russia, St. Petersburg, Makarova emb. 2*

²*Saint-Petersburg State Institute of Technology 190013, Russia, St. Petersburg, Moskovskiy prospect 26*

^a*e-mail: timoshe-mikhail@mail.ru*

Abstract

Thermoplastic elastomer based on styrene-butadiene rubber was developed for 3D printing using fused deposition modelling. 3D modeling of simple and complex geometric structures

from the developed material is performed. Optimal 3D printing parameters for this material were obtained.

Keywords: thermoplastic elastomer; TPE; 3D printing; FDM technology; styrene-butadiene rubber; g-code.

Introduction

Thermoplastic elastomers are hybrid materials, usually made of thermoplastics and elastomers. They have a lower hardness compared to other plastics, but they can withstand large deformations without breaking [1–3].

The development of a material for 3D printing based on thermoplastic elastomers is an urgent task for the further development of the industry since it will reduce the cost of creating products using this method. In addition, this material can be modified, which will allow creating products with unique useful properties.

2 Materials and Methods

The purpose of this work is to develop, create and study the properties of a mixed thermoplastic elastomer for 3D printing based on styrene-butadiene rubber of three different brands.

The selection was made according to the resistance of the feedstock to the influence of UV radiation. Three rubber brands were selected: SEBS YH503, SEBS Europrene Sol 2315, SBS LG 501. The samples were tested with a UV lamp OUFK-320/400-03 “Sun” with a wavelength of 300 nm. The tests were carried out continuously; their duration was 21 days. The test results revealed that styrene-butadiene rubber of the SEBS YH503 brand is the most resistant to the influence of UV rays. The rubbers of the SEBS Europrene Sol 2315 and SBS LG 501 brands were destroyed and turned yellow under the influence of radiation, while SEBS YH503 remained without external changes.

The selection of the melt flow index of the compound was carried out by using various mass ratios of components. Stable printing with the least number of defects was observed at the compound flow rate in the range from 2 to 6 g/10 min with a piston load of 5 kg at a temperature of 190°C. Thermoplastics were selected from the following range: low-pressure polyethylene, polypropylene, polystyrene, and polymethylmethacrylate. For compounds based on polymethylmethacrylate and polystyrene, an uneven passage of the material through the forming head was observed. For low-pressure polyethylene, a high degree of shrinkage was observed during 3D printing and a high distortion of the finished products compared to the specified print sizes.

The combination of polypropylene (PP) and styrene (ethylene butylene)-styrene (SEBS) in thermoplastics based on the mixing method preserves the advantages of PP printing and the elasticity of SEBS. Polypropylene is widely used for various commercial and industrial applications due to its low cost, excellent machinability, mechanical properties, recyclability, etc. [4–5]. On the other hand, SEBS is an important polymer elastomer with high elongation at break, low processing temperature, low melt viscosity and low extrusion deformation.

Results

The standard blades of the second standard size according to ISO37–2017 [6], cylinders with a diameter of 29 mm ± 0.5 mm and a height of 12.5 mm ± 0.5 mm and Schwartz primitive with side 30 mm were taken as a basis.

Control programs blades and cylinders with alternating application of layers and Schwartz primitive (Fig. 1) for printing (g-code) were generated in the program “Cura”.

3D products printed on «Wanhao duplicator i3» using FDM technology with a nozzle diameter 0.4mm. The most optimal printing parameters from this material: nozzle temperature 230°C, table temperature 70°C, print speed 20 mm/s; rollback of the rod in the extruder is disabled. Blades, cylinders and Schwartz primitives (fig. 2) with 100% filling were made on a 3D printer.

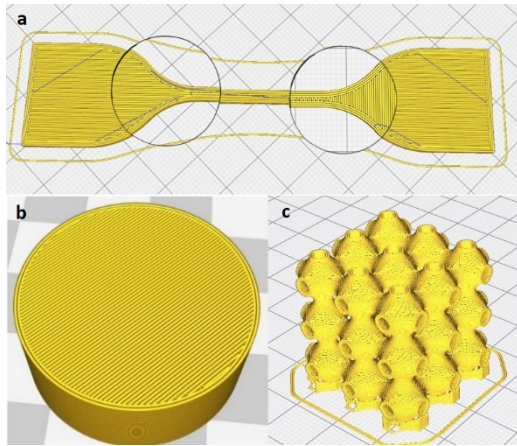


Fig. 1. Render of the blade – a, cylinder – b and Schwartz primitive – c

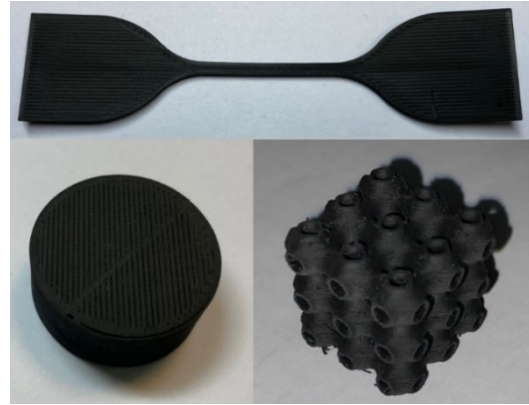


Fig. 2. Photo of the blade, cylinder and Schwartz primitive obtained by FDM printing

Conclusions

Materials with high elasticity and strength characteristics are increasingly used in additive technologies. This study shows that the material can significantly expand the range of products and properties used for additive technologies.

The developed thermoplastic elastomer is suitable for 3D printing not only simple products, but also complex geometric structures with a triple periodic surface, which impossible to perform more simple molding methods.

The study was supported by a grant from the Russian Science Foundation (project No. 20-73-10171).

References

- [1] Banerjee S. S., Bhowmick A. K. High-temperature thermoplastic elastomers from rubber–plastic blends: A state-of-the-art review. *Rubber Chem. Technol.* 2017;90:1 – 36.
- [2] Banerjee S. S., Bhowmick A. K. Novel nanostructured polyamide 6/fluoroelastomer thermoplastic elastomeric blends: Influence of interaction and morphology on physical properties. *Polymer.* 2013;54:6561 – 6571.
- [3] Coran A. Y., Patel R. Rubber-Thermoplastic Compositions. Part IV. Thermoplastic Vulcanizates from Various Rubber-Plastic Combinations. *Rubber Chem. Technol.* 1981;54:892 – 903.
- [4] Banerjee S. S., Bhowmick A. K. Tailored Nanostructured Thermoplastic Elastomers from Polypropylene and Fluoroelastomer: Morphology and Functional Properties. *Ind. Eng. Chem. Res.* 2015;54:8137 – 8146.
- [5] Setz S., Stricker F., Duschek T. Morphology and mechanical properties of blends of isotactic or syndiotactic polypropylene with SEBS block copolymers. *J. Appl. Polym. Sci.* 1996;59:1117–1128.
- [6] ISO 37-2017 Rubber, vulcanized or thermoplastic — Determination of tensile stress-strain properties. Publication date: 2017-11-01 2017. 30 p.

Unit 10 “Multimedia and E-learning techniques and materials”

Project architecture and data model for AR application development

N. AKSIONOVA

Francisk Skorina Gomel State University, Sovyetskaya Str. 104, 246028 Gomel, Belarus

Abstract

Augmented reality is an intuitive approach to displaying models. Instead of controlling the position and rotation of virtual cameras with primitive controls, users can look at the model by inspecting them through the cameras of their devices. Since this project represents an SDK, the project structure appears as a set of files and instructions on how to use them. In order to implement the architecture that is easy to use and maintain, separation of concerns principle should be used during architecture planning. This will enable users of this library to use only the functionality they need, which also corresponds to Single-responsibility principle.

Introduction

The correct approach to this problem would be splitting the implied workflow into indivisible phases, select phases that are supported by the BluePrint SDK, and create corresponding sub-folders for each phase. The implied workflow is displayed in Figure 1:

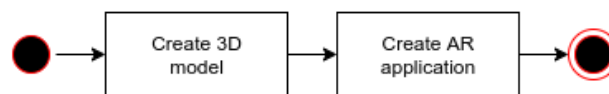


Fig. 1. Implied workflow for SDK usage

Considering this workflow, the preferred project structure can be represented as a set of communicating layers. Input data for the BluePrint SDK is simply an image containing an augmented reality marker. This image might be used for model creation only, or it could also be used as an augmented reality marker. The image used as a reality marker should be easy to print and contain fewer minor details. For an augmented reality marker, all text notations, thin lines, arrows and labels are recommended to be removed. The example of the input image that would fit to create 3D, but would not represent a good augmented reality marker, is shown in Figure 2:

As you can see, the following example contains all sorts of possible information about the building: room types, staircases, windows, doors, and furniture. This image contains too many details to be tracked by computer vision in real-time. Nevertheless, this image would be good to base a 3D model on because it contains much useful information that could be used to create a more detailed model.

Each sub-folder should contain a text file with usage instructions. Library root should also contain a text file that contains SDK description, expected workflow, SDK modules and a brief description of each of these modules. Considering the implied workflow, the following project structure will be used. Each sub-folder should contain a recognizable structure: source directory, containing source code for SDK module, binaries directory, containing executable binary files, precompiled for out-of-the-box usage, and instructions text file.

The first module is called “modelling-assistance”, which represents an addon for 3D modeling software. Addons can not be run by themselves, they need to be imported into the software, and thus, this module does not contain a binaries directory. It only contains a source code

directory, a module package and a text file with instructions on how to import this module into modeling software and how to package the module from the source if needed.

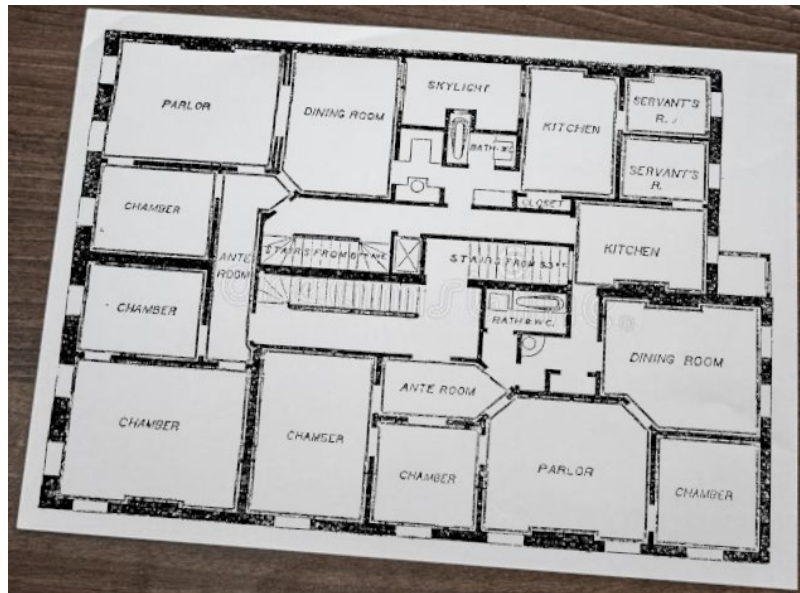


Fig. 2. Example of input image

The second module is called “application-generation” and is the most complicated module among others. Since it will be based on top of the augmented reality library that implies its own application generation workflow, this module will have the most detailed instruction file than those from other modules. These instructions will contain a specific augmented reality library usage guide, a subset of generic library usage instruction that implies the workflow of the BluePrint SDK. It will also contain a set of scripts that may automate some steps of this guide or run a health check in order to alert if additional configuration is required. The scheme of the project layers is displayed in picture 3:

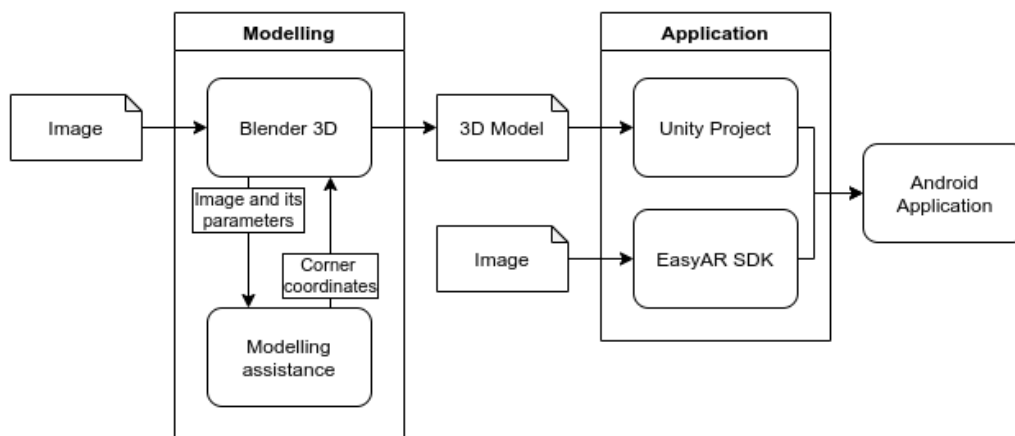


Fig. 3. Project structure represented as layers

Conclusion

In order to install the application on an Android device, the generated file needs to be packaged into an installation file. “Android Package” is the package file format used by the Android operating system, and a number of other Android-based operating systems for the distribution and installation of mobile apps, mobile games and middleware. To make an APK file, a program for Android is first compiled using Android Studio, and then all of its parts are

packaged into one container file. An APK file contains a program's code, resources, assets, certificates, and manifest file. As is the case with many file formats, APK files can have any name needed, but it may be required that the file name ends in the file extension for being recognized as such.

References

- [1] Aksionova N. A., Kucharav A. I. Development of SDK for a mobile application using augmented reality technology. Bulletin of F. Skorina Gomel State University, 2021. No. 3 (126). S. 81 – 84.
- [2] Aksionova N. A., Kucharav A. I. Presentation and implementation of educational material using augmented reality technology. Electronic collection of materials of the International scientific conference "Trends and prospects for the development of science and education in the context of globalization." – Ukraine, 2021.
- [3] Voruev A. V. Information capacity of objects in conjunction with augmented reality. Bulletin of F. Skorina Gomel State University, 2021. No. 3 (126). S. 92 – 95.

Online lesson “Academic English I” for students

S. R. OTA

Division of Technical Service, Shizuoka University

Abstract

Since 2019, I have been providing technical support for the required third-year students' class “Academic English I” in the Department of Electrical and Electronic Engineering, Faculty of Engineering, Shizuoka University. The teaching team includes Professor Damon M. Chandler (Now Ritsumeikan University) of the Department of Electrical and Electronic Engineering and Professor Emerita Valerie A. Wilkinson of the Faculty of Informatics, Shizuoka University. It was a face-to-face lecture in 2019, but an online lecture was held in 2020 and 2021 due to the spread of the new coronavirus infection (COVID-19). I report on the results of questionnaires to students and faculty members from the preparation for the online lecture to the implementation as well as post-lecture feedback. We used Moodle system “LecShizu” to check student’s attendance and so on.

Introduction

The goal of Academic English I is to create an intensive 15-week course in which students are immersed in an international-style conference setting, where they must regularly participate in mini-poster presentations on various technical topics. This department consists of two programs: the Course of Information Electronics and the Course of Energy and Electronic Control. In 2019, the class was offered on Wednesday and Friday, with EE Control group on Wednesday and E Information group on Friday. The note: students in both classes were divided into teams of three or four. In 2020, two groups were combined for the registration of one hundred and fifteen students. Our hybrid online class used Zoom software (Zoom Video Communications, Inc.) and Moodle. The class system includes the professional staff, i.e., Professors, Technical Support and Mentor (senior student). A team of volunteer citizen coaches provided the audience and feedback. “Team learning starts with 'dialogue'” (citation) and trains the capacity of members of a team to suspend assumptions and enter into genuine 'thinking together'.

Class in 2020

We started the class on May 4th and announced that as a Course overview. The following week was the assessment of English (May 10th). Students began the presentation (Theme: About online meeting software). The next theme was “About drones to solve social problems”. The last theme was to chose one academic article and free robotics contents. All teams were

able to finish in 3 weeks on each topic. The senior coaches-volunteers left comments and questions about their presentations.

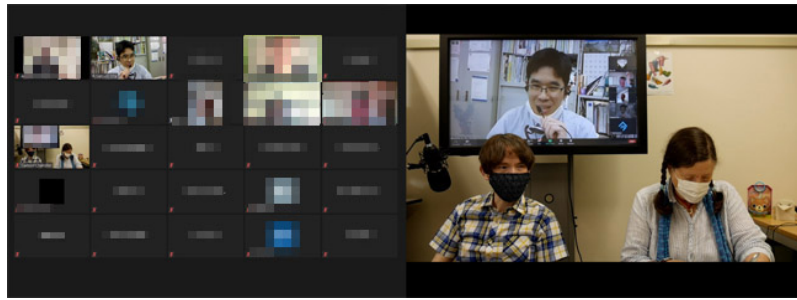


Fig. 1. From online “Academic English I” class in 2020

Conclusion

From the student’s final survey in Moodle system, we could get the results. Now I support the class in 2021 and want to find a way to improve their English speaking and listening skills when communicating with Professors.

References

- [1] Valerie Wilkinson, Damon Chandler “Flipping Out in Japan: Engineering the Academic English Classroom for Innovation”, *Advances in Intelligent Systems and Computing*, pp 326 – 333 (9, 2017).
- [2] Peter M. Senge "The fifth discipline – The Art & Practice of The Learning Organization", (1990).

Unit 11 “Nanotechnology and nanometrology”

Two-steps formation of ZnO-loaded TiO₂ nanotube array films with enhanced photocatalytic performance

M. DOBROMIR¹, C. T. KONRAD-SOARE^{2,3}, R. P. APETREI², A. AIRINEI⁴,
A. V. SEMCHENKO⁵, D. L. KOVALENKO⁵, D. LUCA²

¹*Institute of Interdisciplinary Research, Department of Exact and Natural Sciences,
Alexandru Ioan Cuza University of Iasi, 11 Carol I Blvd., 700506, Iași, Romania*

²*Faculty of Physics, Alexandru Ioan Cuza University of Iași,
11, Carol I Blvd., 700506, Iasi, Romania*

³*Institute for Ion Physics and Applied Physics, University of Innsbruck,
Technikerstr. 25, A-6020, Innsbruck, Austria*

⁴*“Petru Poni” Institute of Macromolecular Chemistry,
41A, Grigore Ghica Voda Alley, 700487, Iasi, Romania*

⁵*Faculty of Physics and Information Technology, Francisk Skorina Gomel State University,
Sovetskaya Str. 104, 246028 Gomel, Belarus*

Abstract

Recent results are reported on the investigation of the optical properties of ZnO-loaded TiO₂ nanotubes array layers. TiO₂ nanotubes layers formed by electrochemical anodization of the Ti surface were subsequently loaded with controllable amounts of ZnO, originating from a magnetron sputtering source. Structural and optical analyses of the ZnO-TiO₂ composite films with different ZnO coverage were carried out to further investigate the electronic properties of the composite films. The results are discussed in terms of the occurrence of the ZnO-TiO₂ heterojunctions and the bandgap modification. These effects increase the photocatalytic yield and activation duration of the films.

Introduction

TiO₂ semiconductors feature peculiar advantages as photocatalytic materials, in spite of two main drawbacks, which diminish their area of applications: (a) less than 5% of the energy of the incident solar radiation can be harvested for surface photoactivation, and (b) the high recombination rate of photo-generated electron-hole pairs in pristine titania reduces the photocatalytic yield of the surface. A red-shift of the absorption edge of titania by doping with various chemical elements was reported extensively [1]. To increase the lifetime of the charge carriers, one can manipulate their spatial separation, such as inside p-n junctions, which can be formed on the TiO₂ surface by growing ultra-thin oxide islands of materials with convenient band gap (WO₃, ZnO, etc.) [2, 3]. Besides enhanced charge separation, our current results point to the alteration of the band gap of ZnO/TiO₂ nanocomposites, and suggest a synergic effect in terms of widening the photoactivation range.

Materials and Methods

The synthesis of the samples is described in detail elsewhere [3]. Briefly, on top of the anodized TiO₂ nanotube layers, ultra-thin ZnO thin films with gradually increasing thickness were deposited by RF magnetron sputtering. ZnO films coverage was adjusted *via* growth duration, from 10 to 30 min, with a step of 10 min. A Shimadzu LabX XRD-6000 diffractometer was used for structural characterization, while the diffuse reflectance spectra (DRS) were recorded (within the 200 – 1100 nm wavelength range) using an Analytik Jena Specord 210 Plus spectrometer, equipped with a collecting integrating sphere, at an angle of 8°.

Results and Discussion

The X-ray diffraction patterns of the TZN_x samples are presented in Fig. 1, where TZN stands for ZnO/TiO₂ layers, and *x* – for the ZnO deposition time (in minutes). Two distinct diffraction peaks are evident, at $2\theta = 25.30^\circ$ and 27.43° , corresponding to the reflections on the anatase A(101) and rutile R(110) planes. The diffraction peaks at $2\theta = 35.05^\circ$, 38.42° , 40.16° , and 52.98° originate in the reflections on the Ti planes, namely T(100), T(002), T(101), and T(102), respectively. The intensity of the A(101) peak decreases with the increase of the amount of ZnO coverage. The average crystalline grain size in the TiO₂ nanotube wall, derived from the A(101) signal, fluctuates between 28.9 nm and 27.3 nm.

Fig. 2 shows a detail of the UV–Vis absorbance spectra (within the 350 – 500 nm range) of the same samples, where a noticeable shift in the absorption edge of the ZnO-loaded films occurs. The band gap energy (E_g) was determined using the equation $E_g = 1240/\lambda_g$ (eV), where λ_g is the absorption edge wavelength, which was obtained from the intercept of the tangent of the absorption curve with the abscissa.

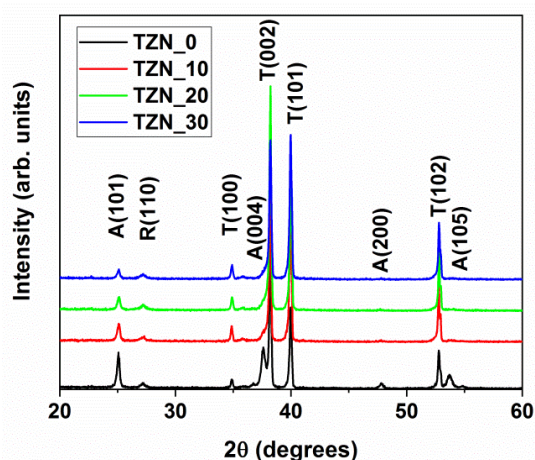


Fig. 1. X-ray diffraction patterns of the TZN_x samples

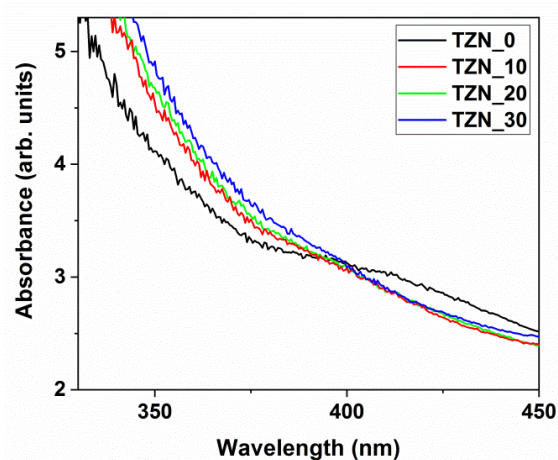


Fig. 2. Absorbance spectra of the investigated samples

The calculated band gap energy (E_g) for the four ZnO loading conditions decrease from $E_g = 3.25$ eV (for TZN₀) to 3.16 eV (for TZN₃₀). We ascribed this alteration to the dual effect of local doping of titania with Zn species and structural changes (anatase-to-rutile ratio) in the interface region.

Conclusion

ZnO/TiO₂ heterojunctions have been fabricated by sputtering ZnO films on top of anodized TiO₂ nanotube array layers. Anatase and rutile crystalline phases with different ratios were detected in the nanotube volume. A slight decrease of the crystalline grain size in the sample with a higher amount of ZnO thin film was noticed. As demonstrated by the DRS data, loading ZnO material on top of TiO₂ nanotubes results in shifting the absorption edge of materials by 2.76 percent, most probably as the effect of local modification of crystallinity and chemical environment.

Based on cyclic voltammetry and surface wettability techniques, future research is foreseen to evaluate the potential synergic effect of the heterojunctions development as a path for higher-performance photocatalytic applications.

Acknowledgements

This research was supported by the Romania - Belarus AR-FRBCF-2020-2021 and Belarus-Romania T20RA-019 bilateral research grants.

References

- [1] A. Fujishima, X. Zhang, D. A. Tryk “TiO₂ photocatalysis and related surface phenomena” Surf. Sci. Rep. 63, pp. 515 – 582 (2008).
- [2] M. Dobromir, R. P. Apetrei, S. Rebegea, A. V. Manole, V. Nica, D. Luca “Synthesis and characterization of RF sputtered WO₃/TiO₂ bilayers” J. Surf. Coat. Technol. 285, pp. 197 – 202 (2016).
- [3] M. Dobromir, C. T. Konrad-Soare, G. Stoian, A. Semchenko, D. Kovalenko, D. Luca “Surface Wettability of ZnO-Loaded TiO₂ Nanotube Array Layers” Nanomaterials 10, 1901 (2020).

Raman investigation of multiferroic BiFeO₃ and Bi_{1-x}Sm_xFeO₃ materials synthesized by the sol-gel method

O. FESENKO¹, T. TSEBRIIENKO¹, A. YAREMKEVYCH¹,
V. V. SIDSKI², A. V. SEMCHENKO², V. E. GAISHUN²,
D. L. KOVALENKO², S. A. KHAKHOMOV²

¹*Institute of Physics NASU, Nauki av., 46, Kyev, Ukraine*

²*Francisk Skorina Gomel State University, Sovetskaya 104, Gomel, 246028, Belarus*

Abstract

The current work presents the investigation results of multiferroic materials (BiFeO₃ and Bi_{1-x}Sm_xFeO₃) with perovskite structure, which possesses two types of orderings: ferromagnetic and ferroelectric. Also, the obtained samples were investigated by Raman spectroscopy to provide detailed information about chemical structure, phase purity and polymorphism, crystallinity and molecular interactions. To enhance the magnetoelectric interaction of bismuth ferrite samples, Bi cations were substituted by isovalent Sm cations with the formation of systems with the general formula Bi_{1-x}Sm_xFeO₃, where x = 7.0; 10.0; 20.0 and 25.0. The interest was to study the features of the formation of ferromagnetic composites both in the form of powders and in the form of films on a silicon substrate, as well as to explore the effect of the formation method on their magnetoelectric properties.

Introduction

To develop new effective materials for various applications, donor and / or acceptor cationic substitutions are used to achieve the required properties. In this work, we investigated multiferroic materials (BiFeO₃ and Bi_{1-x}Sm_xFeO₃) with perovskite structure via Raman spectroscopy to provide detailed information about chemical structure, phase purity and polymorphism, crystallinity and molecular interactions.

Experimental

The synthesis of BiFeO₃ and Bi_{1-x}Sm_xFeO₃ composites was carried out by the sol-gel method. Among the available chemical methods, sol-gel synthesis is known as a universal method that allows the synthesis of nanoparticles with chemical composition and crystallography similar to particles obtained by solid-state reactions but with better morphology including BiFeO₃ and Bi_{1-x}La_xFeO₃ films and powders [1–4]. The synthesis of BiFeO₃ and Bi_{1-x}Sm_xFeO₃ composites was carried out using separate hydrolysis of each of the precursors (iron nitrate nanohydrate Fe(NO₃)₃×9H₂O, 99% purity; bismuth nitrate pentahydrate Bi(NO₃)₃×5H₂O, 99% purity, and Sm(NO₃)₃×6H₂O all from Merck) with their subsequent mixing. First, Fe(NO₃)₃ × 9H₂O was mixed in the diluted lemon acid (C₆H₈O₇) and glycerol C₃H₈O₃ (volume ratio 1:4) solution to form a Fe precursor solution. The solution was continuously stirred for 30 min at 50°C to completely dissolve the ferric nitrate. Bi and Sm precursor solution was obtained through a similar process. Secondly, Fe precursor solution was mixed with Bi and Sm precursor solution

(in case of formation $\text{Bi}_{1-x}\text{Sm}_x\text{FeO}_3$), followed by continuous ultrasonic stirring for 30 min at 25 °C.

BiFeO_3 and $\text{Bi}_{1-x}\text{Sm}_x\text{FeO}_3$ films were formed on a silicon substrate by spin coating method. Heat treatment in the air of each layer of BiFeO_3 or $\text{Bi}_{1-x}\text{Sm}_x\text{FeO}_3$ was carried out at a temperature of 250 °C for 5 minutes.

After that, obtained nanopowders and films were annealed in a muffle furnace for 1 hour.

Results and discussion

The dependence of the Raman spectra of samples prepared at 600 C and 650 °C temperatures on the concentration of Sm is shown in Figure 1. For the samples with lower concentration of Sm we obtained 9 Raman modes (3A+5E) which indicate the rhombohedral perovskite structures [5]. With increasing number of doping atoms, A1-1 and A1-2 modes almost merge together demonstrating the existence of the tetragonal phase with higher crystal symmetry [6]. It can be observed that for higher calcination time, the transformation from the rhombohedral to tetragonal structure takes place with a higher concentration of doping atoms. The positions of Raman modes for the samples are presented in table 1.

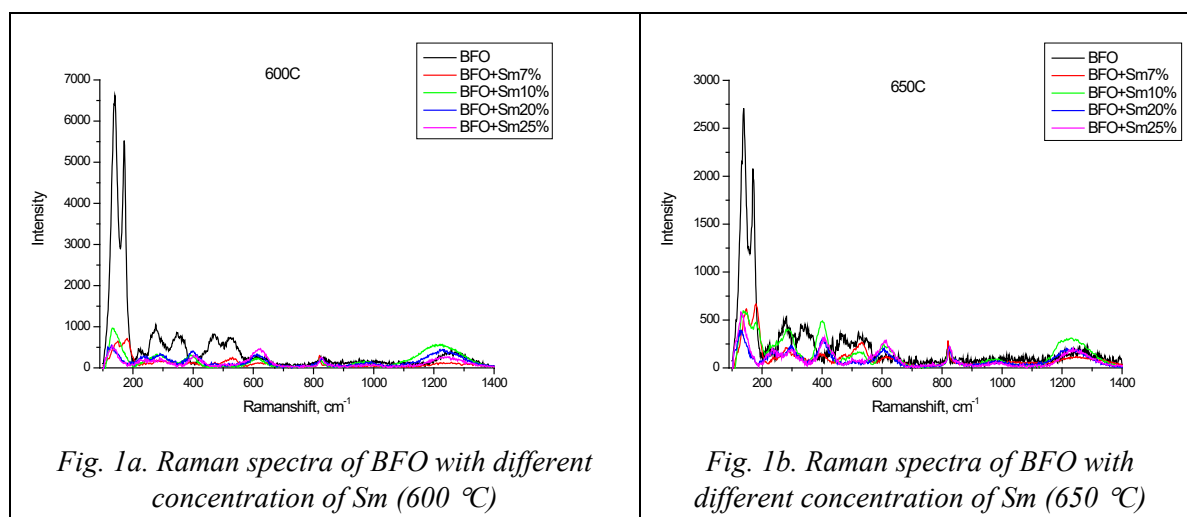


Table 1. Positions of Raman modes for the samples

Raman mode (cm ⁻¹)	600C					650C				
	BFO	BFO+Sm 7%	BFO+Sm 10%	BFO+Sm 20%	BFO+Sm 25%	BFO	BFO+Sm 7%	BFO+Sm 10%	BFO+Sm 20%	BFO+Sm 25%
A1-1	140	148	133	130	133	139	147	137	132	130
A1-2	171	179	-	-	-	170	180	181	-	-
A1-3	220	230	-	-	-	225	236	240	238	235
E	276	290	291	290	289	276	281	288	295	296
A1-4	346	399	394	398	402	344	400	401	404	403
E	470	472	-	-	-	469	478	474	-	-
E	525	530	-	-	-	524	530	527	-	-
E	614	615	616	617	619	612	613	611	612	613

Conclusion

Multiferroic materials (BiFeO_3 and $\text{Bi}_{1-x}\text{Sm}_x\text{FeO}_3$) with the perovskite structure (600 °C and 650 °C annealing temperature) with different Sm content from 7% to 25% were synthesized by sol-gel method and were investigated by Raman spectroscopy. It was established that with the increasing number of doping atoms, A1-1 and A1-2 modes almost merge demonstrating the existence of the tetragonal phase with higher crystal symmetry.

Acknowledgments

The work was performed within the European Union's Horizon 2020 research and innovation programme under the Marie Skłodowska-Curie grant (agreement No 778070). The project was partly supported by BRFB, project number T20R-359.

References

- [1] Shirsath S. E., Mane M. L., Yasukawa Y., Liu X., Morisako A. *J Nanopart Res.* 2013;15:1976. DOI 10.1007/s11051-013-1976-8.
- [2] Brinker C. J., Scherer G. W. *Sol-gel science: The physics and Chemistry of Sol-Gel Processing*, Academ. Press, San Diego, 1990.
- [3] Semchenko A. V., Sidsky V. V., Bdikin I., Gaishun V. E., Kopyl S., Kovalenko D. L., Pakhomov O., Khakhomov S. A., Kholkin A. L. *Materials.* 1 (2021) 1694.
- [4] A. V. Semchenko, S. A. Khakhomov, V. V. Sidsky, V. E. Gaishun, D. L. Kovalenko, et al. *International Conference on Global Research and Education*, 9/4 ,(2019) :113 – 118.
- [5] Rodrigues, H. O., et al. *Physica B: Condensed Matter* 406.13 (2011): 2532 – 2539.
- [6] Zhang, Cheng, et al. *Journal of Advanced Dielectrics* 5.03 (2015): 1550025.

Localized surface plasmon resonance liquid sensors based on array gold nanoparticles fabricated on 36XY-LiTaO₃ substrate

T. FIRMANSYAH^{1,2}, G. WIBISONO², E. T. RAHARDJO², J. KONDOH¹

¹*Shizuoka University, Hamamatsu, Japan,*

²*Universitas Indonesia, Depok, Indonesia*

Abstract

Localized surface plasmon resonance (LSPR) has excellent performance for sensor application. It usually composes base on metal nanoparticle (MeNP) and deposits it on a glass substrate. Therefore, the primary application has focused on refractive index sensors only. As a novelty, we propose to develop an LPSR sensor based on an array of gold nanoparticles (AuNPs) fabricated on 36XY-LiTaO₃, which is a piezoelectric substrate. Complete data such as plasmonic electric field (E-field) simulation, fabrication devices, and implementation as sensor data were provided. Finally, the proposed method has functions for bridging between LSPR and piezoelectric material.

Introduction

Localized surface plasmon resonance (LSPR) phenomena were produced when the metal nanoparticle (MeNP) resonances with light with a particle size of MeNP has much lower than the wavelength of the light. This phenomenon was utilized for LSPR sensors, such as refractive index detectors [1–4]. The refractive index changes correlate with the changes in wavelength peak position [5–7]. In detail, Z. Geng et al. propose to combine Si/Quartz substrate with gold nanoparticle (AuNPs) [1]. Moreover, T. Handoyo [5] and T. Karakouz [6] developed LSPR based on AuNPs and Nanoisland deposited on a glass substrate, respectively. Therefore, the application has focused on refractive index sensors only. Here, we propose to develop an LPSR sensor based on an array of gold nanoparticles (AuNPs) fabricated on 36XY-LiTaO₃, which is a piezoelectric substrate. The proposed method has functions for bridging between LSPR and piezoelectric material in order to develop a multifunctional sensor.

Result and discussion

Figs. 1(a), 1(b), and (1c) show plasmonic electric field (E-field) simulation, implementation of devices as sensors, and measurement result, respectively. In brief, the finite-difference time-domain (FDTD) simulation was utilized to investigate the E-field plasmonic distribution at array

AuNPs on the 36XY-LiTaO₃ substrate. We can see that the E-field plasmonic has successfully been produced even at the piezoelectric material substrate.

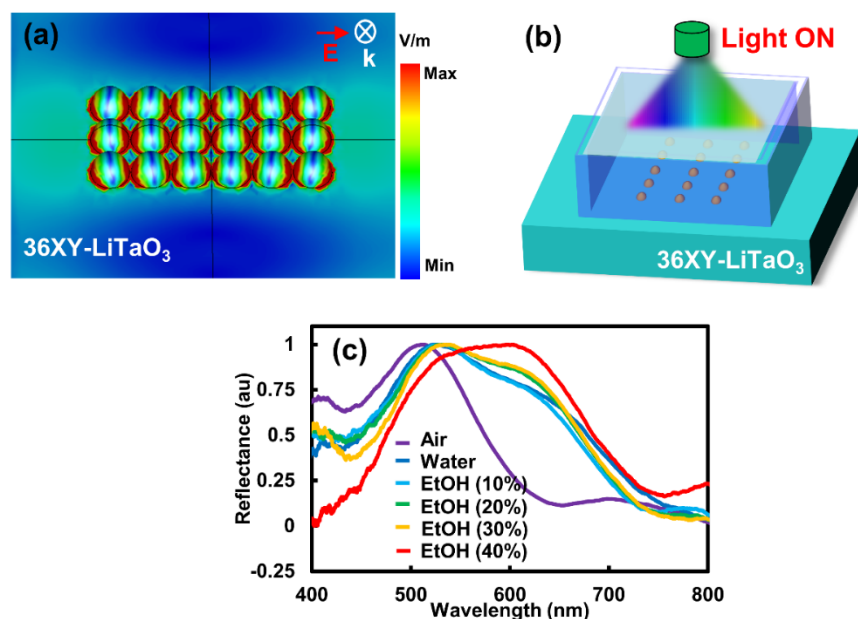


Fig. 1. (a) 2D plasmonic electric field (E-field) simulation, (b) implementation of devices as sensors, and (c) measurement result

Moreover, the high interaction between near neighbors of AuNP has produced high E-field plasmonic. Furthermore, Figure 1(b) shows the implementation of the device as a liquid sensor. Here, we use ethanol (EtOH) as a liquid sample from 0% to 40%. As a result, we can clearly see that the difference of environment has changed wavelength peak position, as shown in Figure 1(c). This result indicates that the piezoelectric material such as 36XY-LiTaO₃ can be used as an LSPR sensor substrate.

Conclusion

LSPR liquid sensors based on array gold nanoparticles fabricated on the 36XY-LiTaO₃ substrate were successfully simulated, fabricated, and implemented. The FDTD simulation shows that plasmonic phenomena can be generated on array AuNP with 36XY-LiTaO₃ substrate. Finally, the measurement result indicates that the piezoelectric material such as 36XY-LiTaO₃ can be utilized as a substrate for the LSPR sensor. The proposed method has functions for bridging between LSPR and piezoelectric material in order to develop a multifunctional sensor.

References

- [1] Z. Geng, Q. Kan, J. Yuan, and H. Chen "A route to low-cost nanoplasmonic biosensor integrated with optofluidic-portable platform," *Sensors Actuators, B Chem.*, vol. 195, pp. 682 – 691, 2014, doi: 10.1016/j.snb.2014.01.110.
- [2] A. Bonyar, B. Wimmer, and I. Csarnovics "Development of a localised surface plasmon resonance sensor based on gold nanoparticles," *Proc. 2014 37th Int. Spring Semin. Electron. Technol. ISSE 2014*, pp. 369 – 374, 2014, doi: 10.1109/ISSE.2014.6887627.
- [3] T. Karakouz, B. M. Maoz, G. Lando, A. Vaskevich, and I. Rubinstein "Stabilization of gold nanoparticle films on glass by thermal embedding," *ACS Appl. Mater. Interfaces*, vol. 3, no. 4, pp. 978 – 987, 2011, doi: 10.1021/am100878r.
- [4] O. Kedem, A. Vaskevich, and I. Rubinstein "Improved sensitivity of localized surface plasmon resonance transducers using reflection measurements," *J. Phys. Chem. Lett.*, vol. 2, no. 10, pp. 1223 – 1226, 2011, doi: 10.1021/jz200482f.

- [5] T. Handoyo and J. Kondoh "Enhancement of ultrathin localized surface plasmon resonance sensitivity using sequential temperature treatment for liquids sensing," *Sensors Actuators, A Phys.*, vol. 307, p. 112006, 2020, doi: 10.1016/j.sna.2020.112006.
- [6] T. Karakouz, D. Holder, M. Goomanovsky, A. Vaskevich, and I. Rubinstein "Morphology and refractive index sensitivity of gold island films," *Chem. Mater.*, vol. 21, no. 24, pp. 5875 – 5885, 2009, doi: 10.1021/cm902676d.

Studies of magnesium – hydroxyapatite micro/nano film for drug sustained release

JINXING CAO¹, XIAOHONG JIANG¹, A. V. ROGACHEV²

¹Nanjing University of Science and Technology, Nanjing 210094, China

²Francisk Skorina Gomel State University, Gomel 246028, Belarus.

Abstract

It is challenging to fabricate the bioactive films containing magnesium (Mg) particles to obtain a film with a porous structure. These microporous structures facilitate the diffusion of the drug covered by the Mg-HA film to achieve sustainable drug release. Herein, ciprofloxacin hydrochloride (CIP) film as the drug representative is obtained by low energy electron beam deposition (LEBD) to verify the sustained release effect of Mg-HA film. Therefore, the four-layer composite films with a distribution of the CIP are obtained using the layered growth of CIP film and Mg-HA film by the PLD-LEBD coupling technology. The results showed that Mg-HA film not only prolonged the CIP release period, but also enhanced the drug release in the middle and late stages.

Introduction

In the previous works [1], it was found that porous structure appeared on the surface of Mg-HA film after soaking in simulated body fluid (SBF) for seven days. This is due to the precipitation of Mg in Mg-HA film and the formation of interconnected pores similar to the network structure. Besides, it has been proved in previous studies that low-energy electron beam deposition technology (LEBD) can effectively protect the original structure of materials from destruction, such as the deposition of polymer materials (polylactic acid, polycaprolactone, polyvinyl chloride, etc.) and some drugs (ciprofloxacin hydrochloride, norfloxacin, etc.) [2–5]. Therefore, ciprofloxacin hydrochloride (CIP) was used as the target drug to construct multilayer drug-loaded composite film by PLD-LEBD coupling technology, and the sustained release behavior of CIP in the composite films in phosphate buffer saline (PBS) was evaluated. The sustained release of drug therapeutics for bone defect restoration has become an attractive design strategy for accelerating the rate of bone healing and for reducing the risk of a chronic wound.

Materials and methods

Mg-HA film was prepared by PLD ($\lambda = 1024$ nm) with a mixture of magnesium and hydroxyapatite (mass ratio = 2:1) as the target material. The thickness of Mg-HA film could be controlled by adjusting the deposition time. CIP film was formed by continuous irradiation of LEBD on the target. The target material was composed of CIP powder (5 mg), and the target area was in the irradiation range of the electron beam. Detailed deposition parameters and procedures are presented in paper [5]. Multilayer composite films were prepared layer by layer by PLD-LEBD coupling technique.

Results and discussions

The four-layer composite film was immersed in PBS for different times. Then the antibacterial performance was tested with *Staphylococcus aureus* as strains, and CIP film as a control

group. As can be seen from the diameter of the bacteriostatic zone in Fig. 1a, the diameter of the inhibition ring of CIP film reached 29.45 ± 0.74 mm before soaking. However, there was no obvious bacteriostatic ring after soaking for 3 days, indicating that the CIP film showed a burst release at the initial stage of soaking. The surface of CIP film became smooth after soaking (R_q value drops from 54.6 ± 0.3 nm to 30.1 ± 0.5 nm), which can be obtained by SEM and AFM images. In contrast, the four-layer composite film showed a sustained drugs release pattern. These pores played a vital role in the release of the third layer (CIP film).

The kinetic release behavior of CIP in the four-layer composite film is investigated in PBS. Fig. 1b shows the kinetic release curve of CIP during the four-layer composite film soaked in PBS for 14 days and the concentration-absorbance standard curve of CIP in PBS. According to the CIP kinetic release curve in Fig. 1b, the CIP release can be divided into two stages: the first stage is soaking for 0 ~3 days, and the first layer (CIP film) is mainly released; The second stage is soaked for 3 ~ 14 days. With the gradual degradation of the second layer (Mg-HA film), the third layer (CIP film) enters the release stage and the release rate is significantly lower than that of the first layer (CIP film). Therefore, it can be inferred that the degradation process of Mg in Mg-HA film plays a decisive role in the kinetic release of CIP.

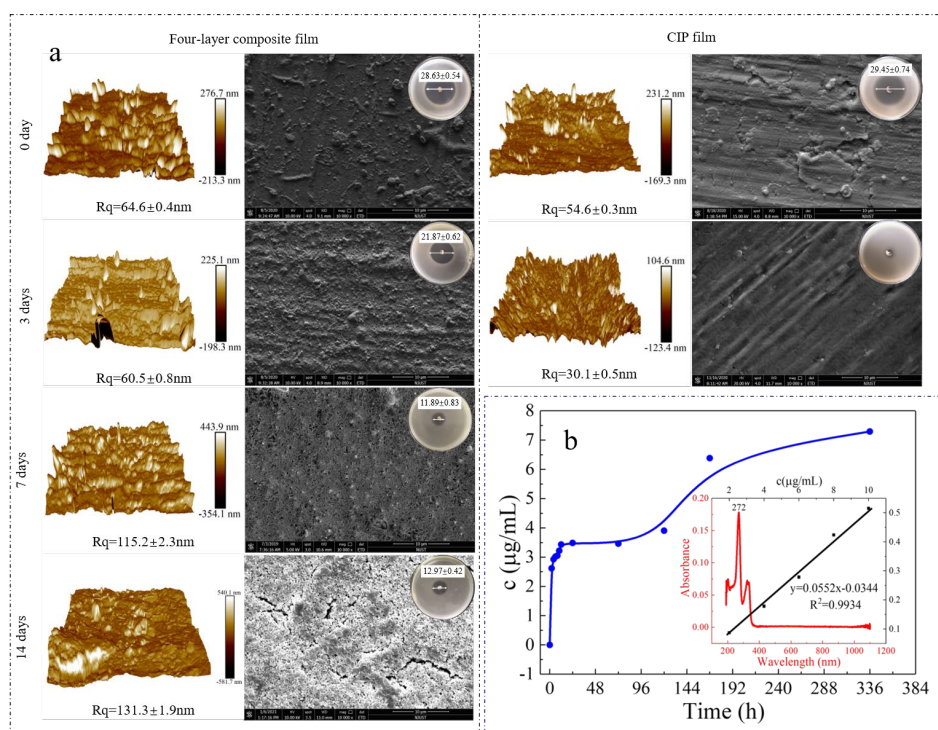


Fig. 1. (a) AFM and SEM morphology and antibacterial properties of the four layers of composite film soaked for different times with CIP film as the control group; (b) The kinetic release curve of CIP in the four layers of composite film and concentration-absorbance standard curve of CIP in PBS

Conclusion

In this study, Mg-doped hydroxyapatite (Mg-HA) films with uniform distribution of Mg particles were obtained by pulsed laser deposition (PLD). Mg in Mg-HA membrane was preferentially degraded in simulated body fluids for ion exchange, thus forming microporous structures on the surface of Mg-HA film. Thus, as the drug representative, ciprofloxacin hydrochloride (CIP) film was obtained by low energy electron beam deposition (LEBD) to verify the sustained release effect of Mg-HA film. Herein, four-layer composite films with a distribution of the CIP were obtained using the layered growth of CIP film and Mg-HA film by the PLD-LEBD coupling technology. The results showed that Mg-HA film not only prolonged the CIP release period, but also enhanced the drug release in the middle and late stage.

References

- [1] J. Cao, R. Lian, and X. Jiang “Magnesium and fluoride doped hydroxyapatite coatings grown by pulsed laser deposition for promoting titanium implant cytocompatibility”, *Applied Surface Science*, 515, pp. 146069 – 146079, 2020.
- [2] C. He, Q. Chen, M. A. Yarmolenko, A. A. Rogachev, D. G. Piliptsov, X. Jiang, and A. V. Rogachev “Structure and antibacterial activity of PLA-based biodegradable nanocomposite coatings by electron beam deposition from active gas phase”, *Progress in Organic Coatings*, 123, pp. 282 – 291, 2018.
- [3] C. He, A. V. Rogachev, B. Li, V. A. Yarmolenko, A. A. Rogachev, D. V. Tapal'Skii, X. Jiang, D. Sun, and M. A. Yarmolenko “Synthesis and structure of antibacterial coatings formed by electron-beam dispersion of polyvinyl chloride in vacuum”, *Surface and Coatings Technology*, 354, pp. 38 – 45, 2018.
- [4] Q. Xu, Z. Xu, X. Jiang, M. A. Yarmolenko, A.A. Rogachev, and A. V. Rogachev “Antibacterial coatings based on polycaprolactone and polyurethane with prolonged release of ciprofloxacin”, *Surface and Coatings Technology*, 405, pp. 126584 – 126594, 2021.
- [5] B. Li, Y. Liu, A. V. Rogachev, V. A. Yarmolenko, A. A. Rogachev, A. E. Pyzh, X. Jiang, and M. A. Yarmolenko “Features of electron beam deposition of polymer coatings with the prolonged release of the drug component”, *Materials Science and Engineering: C*, 110, pp. 110730 – 110742, 2020.

Photocatalytic activity and wettability of TiO₂ nanotube arrays coupled with WO₃ and ZnO

C. T. KONRAD-SOARE^{1,2}, M. DOBROMIR³, G. STOIAN⁴,
M. LUCA⁵, A. CIOBANU⁵, D. LUCA¹

¹*Faculty of Physics, Alexandru Ioan Cuza University, Carol I Blvd. 11, 700506, Iasi, Romania*

²*Institute for Ion Physics and Applied Physics, University of Innsbruck, Technikerstr. 25, A-6020, Innsbruck, Austria*

³*Institute of Interdisciplinary Research, Department of Exact and Natural Sciences, Alexandru-Ioan-Cuza University of Iasi, 11 Carol I Blvd., 700506, Iasi, Romania*

⁴*Institute of Computer Science, Romanian Academy, 2 T. Codrescu Str., 700481, Iasi, Romania*

⁵*National Institute of Research and Development for Technical Physics, 47 D. Mangeron Blvd., 700050, Iasi, Romania*

Abstract

New results are presented in this work on the photocatalytic performance of modified titanium dioxide (TiO₂) nanotube arrays prepared *via* electrochemical anodization. TiO₂ semiconductors have a band gap value (3.2 eV), which makes them suitable as photoactivated catalysts. For surface activation, UV-A radiation (315 – 400 nm) can be used. By depositing WO₃ and ZnO nano-coatings on top of titania surface, formation of oxide semiconductor heterojunctions has been reported, with the benefit of longer electron-hole pairs lifetime, due to reduced recombination rate inside such structures. Here, we focus our investigation on titania *nanotube arrays* (TNA) loaded with zinc and tungsten oxide ultra-thin layers. On macroscale, loading TNA with WO₃ and ZnO layers led to significantly time-prolonged photocatalytic activation and, thus, the catalytic performance.

Introduction

Environmental issues related to pollutant degradation can be, among others, addressed by using catalysts based on oxide semiconductors, able to be easily photoactivated by (mainly) UV light. Among these materials, low-cost titania nanostructures featuring large surface to volume ratio (nanoparticles, thin films and nanorods / nanotubes) are key candidates. Titania photocatalytic materials (PCM) feature non-toxicity, high thermal and chemical stability. As

demonstrated in previous studies, a first class of *titania* modification refers to *doping* with appropriate metal or oxide semiconductors, which may result in extending the activation wavelength range, deep into visible part of the spectrum. Macroscopically, this is associated with increased photoactivation yield and with spectacular surface hydrophilicity.

Results are presented here on a second class of modification, namely the *effects of decoration* of anatase TNA surface with tungsten trioxide ($E_g = 2.8$ eV) and zinc oxide ($E_g = 3.3$ eV) non-contiguous layers. This results in the formation of surface $\text{TiO}_2\text{-WO}_3$ [1] and $\text{TiO}_2\text{-ZnO}$ [2] heterojunction structures, with long-duration photoactivation performances.

Materials and Methods

TiO_2 nanotube arrays were prepared by means of electrochemical anodization in 0.5% wt. NH_4F dissolved in glycerin solvent under 30V DC for a time of 3h. The as-obtained nanotubes were subsequently loaded by means of magnetron sputtering with WO_3 and ZnO_2 , respectively, for progressively increasing times of 10, 30, 60 and 90 min.

High-resolution SEM images were acquired by a JEOL FE-SEM instrument (80 kV accelerating voltage, 10 μA emission current) for the morphological characterization of the nanotube arrays. The subsequent loading of the TNA was evaluated by a novel approach for computer-aided morphological analysis, which used the high-resolution scanning electron microscopy of the top-view images. The MATLAB[®] routine, developed within our research groups [1, 3], successfully detected the nanotube openings and validated them by size, solidity and eccentricity, attaining in this manner a rigorous evaluation of the loading.

XRD patterns, recorded using a Shimadzu LabX XRD-6000 diffractometer equipped with a Copper anode ($\lambda = 1.54059$ Å), operated in the Bragg-Brentano configuration, were used to derive the sample crystallinity. The photocatalytic activity of the samples was monitored by the time rate degradation of the aqueous solution of methylene blue (MB) dye in agreement with the ISO10678:2010 standard. The spectra were recorded using a Perkin Elmer UV-Vis Lambda 3 spectrophotometer. The hydrophilic effects were investigated by means of static contact angle measurements (CA) to evaluate the surface wettability during the back-reaction. The experiments were carried out at room temperature and 75% relative humidity, in a sessile drop arrangement, with deionized water drop volumes as low as 0,5 μl , using the Data Physics OCA 15EC goniometer and the associated SCA 20 software package.

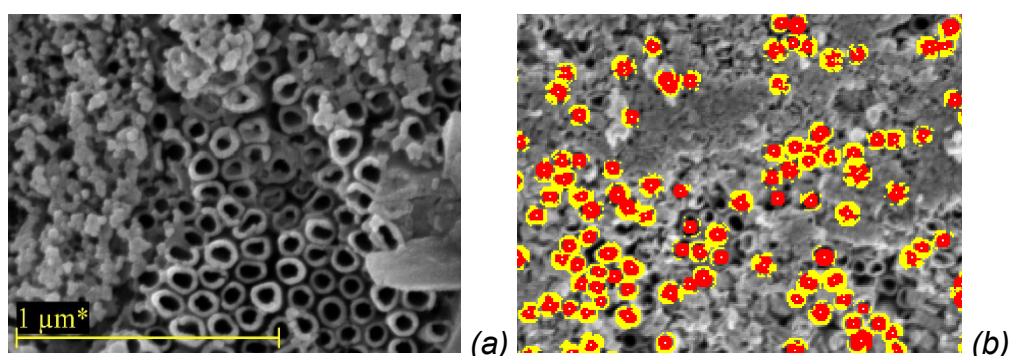


Fig. 1. SEM image (top-view) of (a) TiO_2 nanotube array sample loaded with WO_3 , and (b) overlapped processed images (Red – TNA holes, Yellow – TNA borders) [1]

Results and Discussions

The photocatalytic and hydrophilic characteristics of TiO_2 are closely correlated, following similar evolution under photo-activation and back-reaction conditions.

The photocatalytic performances of the investigated WO_3 and ZnO loaded TiO_2 nanotube array samples were evaluated from the photo-degradation rate of methylene blue (MB) dye in an aqueous solution with initial concentration complying with Lambert-Beer law requirements. Different evolutions were recorded for each of the samples, which maintained similar shapes throughout the decomposition process, with two strong absorption peaks located in the

proximity of 615 nm and 662 nm. As it can be observed, the intensity of the absorption peaks gradually decreases as the exposure time increase.

Contact angle (CA) measurements were used to indirectly follow the photocatalytic efficiency evolution of the TiO₂ layers [4]. All the samples reach a superhydrophilic angle (CA ≤ 12°), after an initial photo-activation up to saturation.

Conclusion

TiO₂ nanotube arrays were obtained through electrochemical anodization and subsequently loaded with non-contiguous ultrathin films of WO₃ and ZnO₂. Maximum areas of approx. 70% of the total array area were covered with deposits after a loading time of 90 min. A loading of the surface with up to approx. 33% coverage lead to the significant enhancement of photocatalytic performance. Upon further loading of the nanotubes, a counter effect is registered due to lowering of the TiO₂ exposure. The mid-range coverage in both WO₃ and ZnO₂ cases is also associated with the slowest decay of the amphiphilic effect, as demonstrated by the contact angle data.

References

- [1] C. T. Teodorescu-Soare, M. Dobromir, A. Ciobanu, M. Luca, G. Stoian, and D. Luca “Synthesis and optimisation of photocatalytic performance of WO₃-loaded TiO₂ nanotube array layers” *Semicond. Sci. Technol.* 34 075027 8pp. (2019).
- [2] M. Dobromir, C. T. Konrad-Soare, G. Stoian, A. Semchenko, D. Kovalenko, D. Luca “Surface wettability of ZnO-loaded TiO₂ nanotube array layers” *Nanomaterials* 10 1901 14pp (2020).
- [3] A. Ciobanu, M. Luca, C. T. Konrad-Soare, G. Stoian, and D. Luca “Computer-aided detection and morphological characterization of nanotube layers using scanning electron microscopy images”, *J. Appl. Phys.* 127 105102 7pp (2020).
- [4] A. Manole, V. Dăscăleanu, M. Dobromir, D. Luca, “Combining degradation and contact angle data in assessing the photocatalytic TiO₂:N surface” *Surf. Interf. Anal.* 42 947 8pp (2010).

Heat treatment effect on the mechanical properties of nanostructured carbon coatings

A. S. RUDENKOV, A. S. POBIYAHA

Francisk Skorina Gomel State University, Belarus

Abstract

The effect of heat treatment temperature on the microhardness and tribotechnical properties of carbon coatings, formed from the plasma of a pulsed cathode-arc discharge on a polyacrylamide sublayer, has been determined. The heat treatment of carbon-based systems leads to a decrease in their microhardness and friction coefficient with a simultaneous increase in the volumetric wear coefficient of the counterbody. It is due to sp³→sp² phase transitions and CN_x-type compounds arising through cyclization processes during heat treatment.

Introduction

Studies devoted to developing technological methods and methods for structuring carbon-based coatings, the introduction of carbon nanostructures into their composition have become highly relevant in recent years [1–2]. The use of laser and plasma technology methods expands tremendously the possibilities for controlling the structure and the properties of nanoscale coatings, which identifies their high potential for solving various technical problems [2].

One of the promising technological methods of structuring carbon layers is the pre-production of a softer nanoscale sublayer based on polymer materials. As a result of subsequent deposition of carbon layers with a high content of sp³-hybridized carbon atoms due to the

difference in thermal conductivity coefficients, mechanical characteristics, and phase transformation processes, their surface is nanostructured.

This paper aims at determining the effect of heat treatment temperature on microhardness and friction coefficient of carbon coatings formed on a polyacrylamide sublayer.

Methodology of the Experiment

Carbon coatings (CC) were deposited from pulsed discharge plasma at a voltage of 250 – 300 V for 2500 pulses with a repetition rate of 5 Hz on a polyacrylamide (PAA) sublayer previously deposited by electron beam dispersion (energy 800 – 1600 eV, density 0.01 – 0.03 A/cm²). The studies of the sublayer phase composition have shown that its structure is similar to that of polyacrylonitrile. The heat treatment of such a sublayer can lead to the formation of cyclic carbon structures, which improve the adhesive interaction. The heat treatment process was carried out in air at 200 °C, 300 °C, 400 °C for 1 hour.

The microhardness of the system under consideration was determined via the Knoop method at various loads of 245 mN, 490 mN, 980 mN.

The tribotechnical tests were performed according to the “sphere-plane” scheme with a load of 490 mN.

Results and discussion

The microhardness of the PAA/CC bilayer systems is found to be higher than that of single-component carbon coatings, which may be due to several factors. First, based on the previously obtained Raman spectroscopy data, such systems are characterized by a higher degree of ordering of sp²-hybridized atoms. Second, the softer PAA layer deforms when heated during the carbon layer deposition under the action of arising internal stresses. Such deformation can contribute to increasing the coating density, which can also cause an increase in microhardness. Apart from the above, one of the reasons for the higher microhardness values of bilayer PAA/CC systems may be the presence of CN_x-type compounds. The coating heat treatment in air leads to the complete disappearance of nitrile groups due to cyclization processes and the formation of C=N bonds. However, in the IR spectrum, stretching vibrations of C=N bonds appear in the absorption range of carboxyl groups (1660 – 1590 cm⁻¹), which makes their identification difficult.

The microhardness of carbon coatings and bilayer PAA/CC systems decreases with an increase in the annealing temperature. It is caused by the sp³→sp² phase transitions and is consistent with the results presented in [3, 4].

During tribotechnical tests, it was established that carbon coatings are characterized by a lower friction coefficient than bilayer PAA/CC systems. This fact is attributable to a more diverse phase composition of the friction track on the PAA/CC, different wear rates and, therefore, the occurrence of a more heterogeneous relief. In the case of carbon coatings, graphite smearing can be observed both on the surface of the counterbody and on the surface of the friction track. The same factors can explain the difference in the behavior of the kinetic dependences of the friction coefficient.

It has been found that the volumetric wear coefficient of the counterbody when interacting with carbon coatings decreases with an increase in the annealing temperature. Graphite acts as a solid lubricant, it smears on the counterbody, and reduces its wear.

On the contrary, the volumetric wear coefficient of the counterbody when interacting with bilayer PAA/CC systems increases after heat treatment. It is likely due to the abrasive action of nanocrystalline structures and more heterogeneous phase composition, and, hence, to a different wear rate of the friction track surface.

Conclusions

It has been shown that carbon coatings, formed on the sublayer deposited by electron beam dispersion of polyacrylamide, are characterized by a higher microhardness than single-layer carbon coatings. It is a consequence of a higher degree of ordering of sp²-hybridized atoms and a higher density due to deformation of the PAA-based sublayer. Besides, one of the

reasons for the higher microhardness values of bilayer PAA/CC systems may be the presence of CN_x -type compounds occurring as a result of cyclization processes during heat treatment. The friction coefficient of carbon coatings and bilayer PAA/CC systems changes significantly after heat treatment at a temperature above 300 °C. It is a result of more intense carbon oxidation, $sp^3 \rightarrow sp^2$ phase transitions, and more heterogeneous phase composition in the case of PAA/CC systems.

The research has been performed with the financial support from the Ministry of Education of the Republic of Belarus as part of the research and development plan "Development of the essentials of a combined technology for the formation of planar-structured carbon coatings from pulsed cathode carbon plasma and products of laser dispersion of polymer materials", task 1.12 "Synthesis of nanocomposite film structures, the formation of materials with high functional properties using electron-beam, ion, laser processing methods".

References

- [1] Heimann R. B., Evsyukov S. E., Koga Y. "Carbon allotropes: a suggested classification scheme based on valence orbital hybridization", *Carbon*, 35, 10 – 11, 1654-1658 (July 1997).
- [2] Booker R., Boysen E. "Nanotechnology For Dummies" (Wiley Publishing Inc, 2005, 366 p.).
- [3] Yan X., Xu T., Wang X., Liu H., Yang S. "Microstructure and mechanical properties of hard carbon films prepared by heat treatment of a polymer on steel substrate", *Surface & Coatings Technology*, 190, 2 – 3, 206 – 211 (January 2005).
- [4] Nobili L., Guglielmini A. "Carbon allotropes: a suggested classification scheme based on valence orbital hybridization", *Surface and Coatings Technology*, 219, 25, 144 – 150. (March 2013).

Piezoelectric properties of $SrBi_2(Ta_xNb_{1-x})_2O_9$ thin films synthesized by the sol-gel method

A. V. SEMCHENKO¹, V. V. SIDSKI¹, O. I. TYULENKOVA¹, A. YU. SHEPELINA²,
D. A. KISELEV², V. A. PILIPENKO³

¹*Francisk Skorina Gomel State University, Sovetskaya 104, Gomel, 246028, Belarus*

²*National University of Science and Technology "MISiS", Leninsky pr.4,
Moscow, 119049, Russia*

³*JSC "INTEGRAL", Kazintsa I.P 121A, Minsk, 20108, Belarus*

Abstract

The present work aims to design and study novel functional thin films with ferro- and properties. $SrBiTa_2O_9$ and $SrBi_2(Ta_xNb_{1-x})_2O_9$ thin films were synthesized by the sol-gel method on Pt/Ti/SiO₂/Si substrates. The influence of the synthesis conditions and the presence of niobium on the features of the piezoelectric properties were determined. The PFM method was applied to visualize not only the morphology of grains, but also their local piezoelectric activity.

Introduction

At the moment, dielectrics and, in particular, ferroelectrics in the form of thin films, which have the greatest prospects for practical applications for miniaturizing devices, due to reduced control fields, good integration of films with semiconductor materials; traditionally used in electronics, as well as for creating reprogrammed memory devices based on ferroelectrics [1]. Ferroelectrics are characterized by the presence of dielectric hysteresis loop, large dielectric constant, high piezomodule, as well as some electro-optical properties. The main practically used property of such materials is their controlled dielectric response to external influence, which, as a rule, is based on polarization switching processes. The widespread practical use of ferroelectric materials is constrained by the incomplete research on polarization switching

dynamics in these structures. Local piezoelectric properties of $\text{SrBiTa}_2\text{O}_9$ (SBT) and $\text{SrBi}_2(\text{Ta}_x\text{Nb}_{1-x})_2\text{O}_9$ (SBTN) thin films are investigated in this work.

Experimental

The main problem in the formation of a homogeneous multicomponent solution is the unequal conditions of hydrolysis and the rate of condensation for each type of metal alkoxides. This can lead to phase separation during hydrolysis or heat treatment and, consequently, to crystallization temperature increase or even to the formation of impurity phases. Thus, choosing such alkoxides and a solvent with sufficient solubility is necessary for the stoichiometric ratio in their joint presence and do not interact at room temperature. Many problems of the above-described variant of preparing a mixture of a working solution can be overcome by replacing the alkoxides of some metals with their salts. These are mainly salts of carboxylic acids, but nitrates, sulfates and chlorides can also be used. The salts of acetic acid and ethyl caproic acid are versatile and can be used for most metals. They are compatible with almost all metal alkoxides. It was found that the use of separate hydrolysis improves the ferroelectric properties of the obtained films. This is due to the fact that when preparing the sol when using the same solvent, separate hydrolysis occurs completely for each of the metal compounds in comparison with joint hydrolysis, where, due to different reaction rates, some metals are not completely hydrolyzed.

Synthesis of $\text{SrBiTa}_2\text{O}_9$ films used nitrate salts of Sr, Bi, Ta, HNO_3 , ethylene glycol, ethylenediamine and citric acid. The $\text{SrBi}_2(\text{Ta}_x\text{Nb}_{1-x})_2\text{O}_9$ films were synthesized using the same procedure. NbCl_5 was used as a niobium source. The thickness of the films can be controlled by the number of layers spin coated. Then the samples $\text{SrBiTa}_2\text{O}_9$ and $\text{SrBi}_2(\text{Ta}_x\text{Nb}_{1-x})_2\text{O}_9$ sol-gel materials were annealed at different temperatures for 20 minutes.

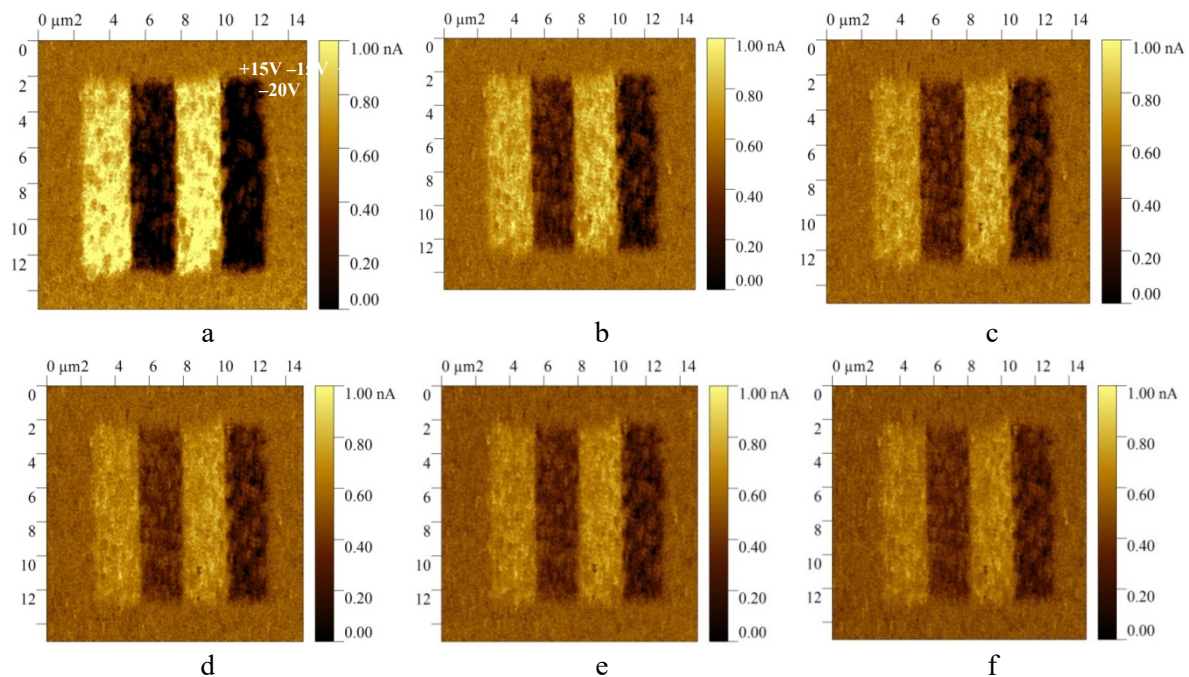


Fig. 1. Polarization of SBTN film with annealing temperature 700°C after polarization with voltage $\pm 15\text{ V}$ and $\pm 20\text{ V}$ (in contact mode): a – immediately after polarization; b – 10 minutes after polarization; c – 20 minutes after polarization; d – 30 minutes after polarization; e – 40 minutes after polarization; f – 50 minutes after polarization

Results and discussion

The vertical or out-of-plane component of the piezoresponse was measured, which is proportional to the effective piezoelectric effect d_{33} [1]. The images showed SBTN thin films

annealed at different temperatures. The convenient way to describe a piezoresponce is to construct it in the form of histograms as the function of the image of pixels in the entire image [2]. In this way, complete polarization distribution in the resulting films can be obtained. Due to the small grain size, the contrast in the grain is constant, and no ferroelectric domains are observed.

Visualization of the induced domain state is possible after polarization of the film by applying constant voltage to the “cantilever - film - substrate” system. For this, the surface of the film, measuring $(2.5 \times 10) \mu\text{m}^2$, was first polarized with a constant voltage of $\pm 15 \text{ V}$ and $\pm 20 \text{ V}$, and then a larger area of the film was scanned in the piezoresponse mode $(15 \times 15) \mu\text{m}^2$. The results are shown in Figure 1. It was established experimentally that the best “memory” for polarization is a sample with niobium content of 40%.

Conclusion

Polycrystalline $\text{SrBi}_2(\text{Ta}_x\text{Nb}_{2-x})\text{O}_9$ (SBTN) films (700 °C annealing temperature) with different Nb content from 10% to 50%, with a step of 10%, as well as 5 samples of SBTN films (20% content Nb) were synthesized. It was experimentally established that the best “memory” for polarization is a sample with niobium content of 40%.

References

- [1] P. K. Panda and B. Sahoo. *Ferroelectrics*, (2015) 474, 128 – 143.
- [2] P. Sharma, Q. Zhang, D. Sando, C. H. Lei, Y. Liu, J. Li, V. Nagarajan, J. Seidel, Nonvolatile ferroelectric domain wall memory. *Sci. Adv.* 3, e1700512 (2017).

Atomic force spectroscopy experiments with amino-functionalized silicon AFM tips and samples

L. SIRGHI, A. BESLEAGA

*Iasi Plasma Advanced Research Center (IPARC), Faculty of Physics, Alexandru Ioan Cuza
University of Iasi, Blvd. Carol I nr. 11, Iasi 700506, Romania*

Abstract

Nanosopic probes in scanning probe microscopy interact with the target surfaces through forces that are vital to applications in microscopy imaging and single-molecule studies of biologic forces. In their turn, the interaction forces depend crucially on the chemistry of the probe and sample surfaces. Therefore, controlling and modifying the surface chemistry of the nanoscopic probes is vital for the success of these microscopic studies [1].

The present work uses plasma technology combined with wet-chemistry functionalization methods to functionalize silicon atomic force microscopy (AFM) probe and sample surfaces with amino ($-\text{NH}_2$) chemical groups. Plasma cleaning, oxidation, and hydroxylation processes are used to chemically activate silicon or silicon nitride surfaces by generating surface silanol (Si-OH) groups. This process is followed by self-assembled monolayer (SAM) deposition of ethanolamine to generate surface amino groups. The amino-functionalized AFM probes and samples were used in atomic force spectroscopy measurements that confirmed successful functionalization by chemical force titration.

Introduction

Atomic force microscopy uses the interaction between a probe with a very sharp tip (apex curvature radius of 5 – 10 nm) and a sample surface in order to acquire the topography image of the surface. In this case, it is important to decrease as much as possible the region of interaction by manufacturing very sharp tips and eliminating long range surface forces. This may lead to an increase of the lateral resolution towards the atomic resolution. In biophysical

studies, the AFM probes are chemically functionalized to investigate specific interactions and mechanical properties at a single molecule level. In this case, chemical functionalization of the AFM probe surface is required to attach biomolecules to it. A similar functionalization procedure is required in optical tweezers and magnetic tweezers studies, where molecules are bounded to nanobeads. Some of these studies used gold-covered nanoprobe functionalized by the wet chemistry technique of SAM deposition of organothiol molecules. This method requires chromium and gold coatings of the probes and generates hazardous chemical waste [2]. On the other hand, plasma functionalization of surfaces uses an electrical discharge in gas or mixture of gases to provide high-energy particles (ions, electrons, metastable molecules and atoms, and radical molecules), which chemically modify the top layer of a solid surface without using of solvents [3]. The type of functionalization depends on gas and operating parameters as pressure, power, time, gas flow rate, etc. The present work uses plasma techniques to activate silicon nitride surface of AFM nanoprobe by generating silanol (Si-OH) terminal groups required for bonding ethanolamine to generate surface amino groups. Success and stability of the AFM nanoprobe functionalized with amino functional groups is evaluated by pH titration atomic force spectroscopy experiments.

Material and methods

Commercial silicon nitride AFM probes (MLCT from Bruker) were first cleaned in chloroform (Sigma-Aldrich, $\geq 98.5\%$) (3 times for 5 minutes), dried and then hydroxylated by exposure for 10 minutes to negative glow plasma of a dc discharge in a mixture of air and water vapor at 20 Pa (discharge voltage and current intensity were 470 V and 3 mA, respectively). This treatment removes contaminant (hydrocarbons) molecules adsorbed on the probe surface and generates surface hydroxyl groups. The plasma hydroxylated AFM probes were immediately functionalized with an amino group ($-\text{NH}_2$) by binding to surface ethanolamine molecules. This was done by dissolving ethanolamine hydrochloride in dimethyl sulfoxide (DMSO) (0.5 g/L) in a crystallization dish at 70°C . After complete dissolution and cooling at room temperature, a Teflon block was immersed in the crystallization dish and molecular sieve beads (4\AA) were added around. The solution was kept for 30 minutes in dessicator for degassing the dissolved air. Then, the AFM probes were placed on the Teflon block and incubated in ethanolamine solution overnight. Then, the AFM probes were washed in DMSO (3 times for 1 min) and ethanol (3 times for 1 min), and dried in a gentle stream of nitrogen gas [4]. The same functionalization protocol was followed for amino functionalization of polished silicon substrates. The amino-functionalized AFM probe and samples were kept in a vacuumed dessicator until their use in atomic force spectroscopy measurements.

Results

The presence of $-\text{NH}_2$ groups on the AFM probe and sample surfaces was evaluated by chemical titration experiments, which probe the electrical charging of the surfaces under different pH conditions (Wallwork 2001). Figure 1 shows the results of the chemical force titration experiment for AFM tip and sample, both modified with ethanolamine. Force-displacement curves were acquired on the arrays of 8×8 equidistant points on an area of $0.5 \mu\text{m} \times 0.5 \mu\text{m}$ for each value of pH, the adhesion force values being used to determine the average and standard deviation values. At low pH, a small adhesion ($< 1 \text{ nN}$) is observed. A sudden increase of the adhesion force between amino-functionalized AFM tip and silicon sample was recorded at isoelectric point ($\text{pI} = 4.2$) (Smith 2001). For $\text{pH} > 9$, the adhesion force starts to decrease and approaches zero above $\text{pH} = 11$. A simple explanation for this behavior is that at low pH, the amino group on both tip and sample surfaces are protonated (NH_3^+). The net positive charge results in the formation of electric double layers on both surfaces which leads to electrostatic repulsion and a low adhesion force. With the increase of pH, the amino groups become deprotonated; a larger adhesion arises because of the hydrogen-bond formation between neutral amino groups on the tip and sample surface. At a very high pH, the adhesion force falls to zero and this drop could be explained by electrostatic repulsion between two surfaces containing ionized acid groups as well as neutral amines.

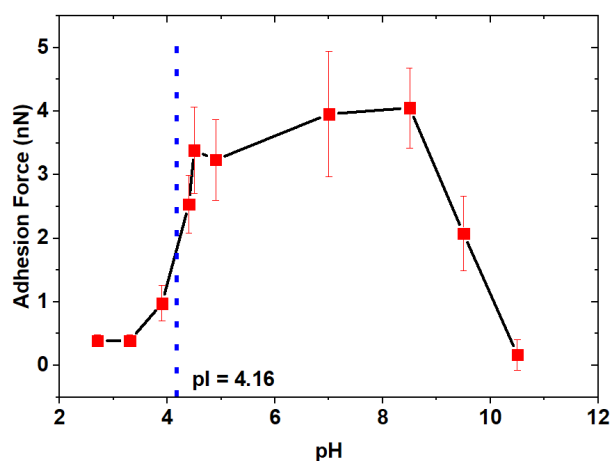


Fig. 1. Variation of AFM tip-sample adhesion force with solution pH showing the isoelectric point pI of amino-functionalized surfaces at 4.16

Conclusion

In summary, the surfaces of silicon nitride AFM probes and silicon samples were hydroxylated in discharge plasma and then covered with a monolayer of ethanolamine by SAM deposition. The success of surface functionalization with amino terminal groups was assessed by atomic force spectroscopy titration force measurements.

References

- [1] Y. F. Dufrêne, P. Hinterdorfer "Recent progress in AFM molecular recognition studies", *Eur J Physiol.* 256, 237 – 245 (12, 2007).
- [2] M. Fiorini, R. McKendry, M. A. Cooper, T. Rayment, C. Abell "Chemical Force Microscopy with Active Enzymes", *Biophys. J.* 80, 2471 – 2476 (05, 2001).
- [3] C. Volcke, R. P. Gandhiraman, V. Gubala, C. Doyle, G. Fonder, P. A. Thiry, A. A. Cafolla, B. James, D. E. Williams "Plasma functionalization of AFM tips for measurement of chemical interactions", *J. Colloid and Interface Scie.* 348 322 – 328 (04, 2010).
- [4] A. Ebner, P. Hinterdorfer, H. J. Gruber "Comparison of different aminofunctionalization strategies for attachment of single antibodies to AFM cantilevers", *Ultramicroscopy* 107, 922 – 927 (2007).

Atomic force microscopy indentation of supported lipid bilayers

G. TIFUI, S. TEODOROFF-ONESIM, L. SIRGHI

Iasi Plasma Advanced Research Center (IPARC), Faculty of Physics, Alexandru Ioan Cuza University of Iasi, Blvd. Carol I nr. 11, Iasi 700506, Romania

Abstract

Because of the small size of the cells, investigation at the sub-cellular level of their physical properties remains difficult. Atomic force microscopy (AFM) has proved to be a valuable technique used not only to acquire high-resolution 3D topography of cell surface, but also to measure locally the elastic and hardness properties of cells by using the AFM instrument as a nanoindentation tool.

In this work, AFM indentation experiments of supported lipid bilayers (SLB) on mica are performed to investigate their hardness. In such measurements, the strain response of the SLB to the compression stress applied by the sharp tip of the AFM probe (curvature radius of

10 nm) is analyzed. It was observed that under the compression stress, the SLB deformed first elastically and then plastically (with a lateral disruption of the lipid bilayer). The transition between elastic and plastic deformation is characterized by the SLB breakthrough force. It is shown that plasma hydroxylation of the AFM tips decreases slightly the SLB breakthrough force.

Introduction

In the last decades, the AFM nanoindentation techniques contributed decisively to the progress in understanding the mechanical properties of the cell membranes [1]. The value of breakthrough force recorded in AFM indentation of SLB depends on the curvature radius and chemistry of the AFM tip surface, the compactness, chemical composition, and temperature of SLB, ionic strength of aqueous solution and nature of the substrate [2]. In this work, we study the effect of hydroxylation of the AFM tip on the breakthrough force.

Material and methods

High purity (>99%) 1-palmitoyl-2-oleoyl-sn-glycero-3-phosphocholine (POPC) lipids were purchased from Avanti Polar Lipids (Alabaster, AL, USA) in powder form. Chloroform (>99%) was purchased from Sigma-Aldrich and ethanol absolute (>99.9%) was purchased from EMSURE®. The lipid was dissolved in chloroform to obtain a lipid solution with the concentration of 25 mg/mL. Then, the solution was placed in vacuum to evaporate the solvent and obtain a thin lipid film. Then, the thin lipid film was dissolved in a solution of 0.1M NaCl and 10 mM HEPES at pH 7 and stirred with a vortex stirrer to form multilamellar vesicles. Finally, the solution was sonicated for a few minutes in a heated bath to obtain a solution of unilamellar vesicles. A drop with the volume of 50 μ l was deposited on a freshly cleaved mica sheet and left to dry in the open air. The AFM measurements were performed at room temperature in PBS at pH 7 using a commercial AFM apparatus (XE-100 from Park Systems, South Korea). The AFM images were obtained in contact mode in PBS using a commercial AFM probe (MLCT from Bruker) with very flexible silicon nitride cantilevers (nominal force constant of 10 pN/m) and sharpened tips (nominal radius < 10 nm). The force spectroscopy measurements were performed with the same AFM probe using the dedicated controlling software of the microscope. The AFM loading and unloading force-displacement curves were acquired at a constant speed of scanner extension (1 μ m/s). The cantilever deflection versus scanner extension curves acquired in the experiments were calibrated and transformed in force versus tip displacement (tip-sample distance). The AFM indentation experiments were performed with as-received and plasma-hydroxylated AFM tips. Before plasma hydroxylation, the as-received AFM probes were washed in chloroform (Sigma-Aldrich, \geq 98.5%) to remove large dust particles from the surface. Then, the AFM probes were exposed for 3 minutes to the negative glow plasma of a d. c. discharge in a mixture of air and water vapor at 40 Pa. The discharge current intensity and voltage were maintained constant at 3 mA and 470 V, respectively. This treatment removes the surface contaminant molecules from the AFM probe surface [3] and generates surface silanol (Si-OH) groups [4]. After plasma treatment, the AFM probes were used immediately in SLB indentation experiments.

Results

Figure 1 shows a typical force-distance curve obtained in SLB indentation experiments. The position of the mica surface has been taken as a reference in this plot. After the AFM tip is brought in mechanical contact with SLB, a constantly increasing force is applied until the AFM tip suddenly breaks through the lipid bilayers (part A-B on the loading force-distance curve) at a threshold value of the impinging force. This event separates the elastic from the plastic regimes of SLB deformation. The breakthrough events are easily identified on approach force-distance curves as sudden jumps in the position of the AFM tip (about 4 nm) at constant compression. After the breakthrough, the AFM tip gets in contact with the mica substrate and cannot move further due to the large hardness of the substrate. During the SLB breakthrough, the lipid bilayers collapse under the compression stress applied by the AFM tip, the constant compression force during the event being named breakthrough force. During the unloading

process, the AFM probe is retracted and the SLB reform quickly under a small compression force (portion C-D on unloading force-distance curve in Fig. 1)

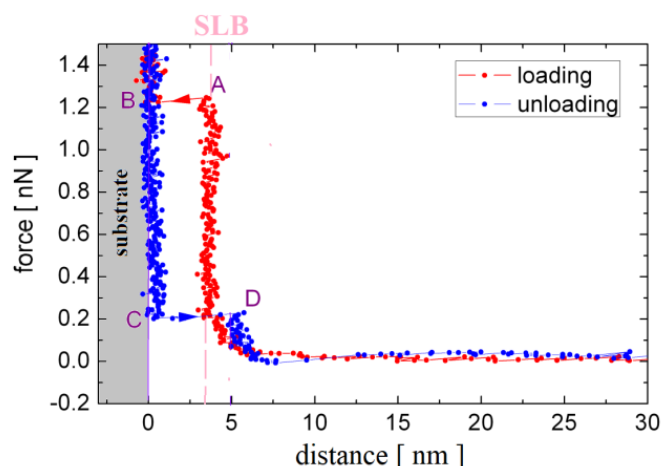


Fig. 1. Example of force-distance curve recorded during loading (increasing force) and unloading (decreasing force) applied on the AFM tip in contact with SLB on mica substrate

AFM spectroscopy measurements were performed on SLBs with as-received and plasma-hydroxylated and PEG functionalized AFM tips. Histograms with breakthrough force values obtained in these measurements are presented in Fig. 2. In this case, the histograms show much larger breakthrough force values, with the most probable values around 1.4 nN, 1.2 nN for as-received and plasma-hydroxylated AFM tips, respectively. These breakthrough force values are consistent with results reported in [5].

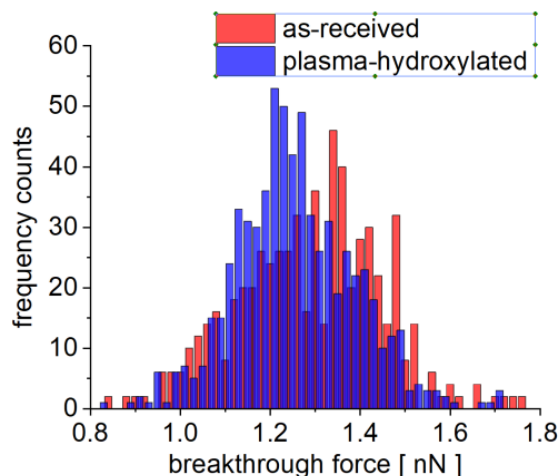


Fig. 2. Histograms of breakthrough force values recorded in force spectroscopy measurements performed with as-received, plasma hydroxylated and PEG functionalized AFM tips on SLB

Conclusion

In summary, mechanical properties of the SLB were studied by AFM indentation in PBS. The experiments revealed that hydroxylation of AFM tips lowers the SLB breakthrough force.

References

- [1] L. Sirghi, J. Ponti, F. Broggi, F. Rossi "Probing elasticity and adhesion of live cells by atomic force microscopy indentation" Eur Biophys J, 37, 935 – 945 (2008).

- [2] Ch. Das, K. H. Sheikh, P. D. Olmsted, S. D. Connell “Nanoscale mechanical probing of supported lipid bilayers with atomic force microscopy”, *Phys. Rev. E et Biophysica Acta* 82, 049120 (2010).
- [3] F. Samoila, V. Pohoata, L. Sirghi “Cleaning Away the Oleic Acid Contaminant from Glass Surface by Negative Glow Plasma”, *Plasma Chemistry and Plasma Processing* 38 (6) 1273 – 1291 (2018).
- [4] A. Apetrei, L. Sirghi “Stochastic adhesion of hydroxylated atomic force microscopy tips to supported lipid bilayers”. *Langmuir* 29(52), 16098 – 16104 (2013).
- [5] A. Alessandrini, H. M. Seeger, A. Di Cerbo, T. Caramaschi, P. Facc What do we really measure in AFM punch-through experiments on supported lipid bilayers?, *Soft Matter* 7, 7054 (2011).

Unit 12 “Photonics”

High power terahertz wave emission using DAST crystal

T. KAWAUCHI¹, G. OHTAKE¹, C. KOYAMA²,
H. UCHIDA², K. TAKEYA³, S. R. TRIPATHI^{1,4}

¹*Department of Mechanical Engineering, Shizuoka University, 3-5-1 Johoku,
Hamamatsu, Shizuoka 432-8561, Japan*

²*ARKRAY Inc., Kamigyo-ku, Kyoto 602-0008, Japan*

³*Institute for Molecular Science (IMS), 38 Nishigonaka, Myodaiji, Okazaki 444-8585, Japan*

⁴*Graduate School of Science and Technology, Shizuoka University, 3-5-1 Johoku,
Hamamatsu, Shizuoka 432-8561, Japan*

Abstract

The power of terahertz wave emitted by non-linear optical crystal via optical rectification of femto-second laser pulses depends upon the power of the laser used to pump the optical crystal. However, a significant amount of pump power is lost due to Fresnel's reflection at the air-crystal boundary during this process. In this study, we used the anti-reflection (AR) coat known as cytop on the surface of non-linear crystal 4-Dimethylamino-N-methyl-stilbazolium tosylate (DAST), which enabled to increase the incident pump power. The power of terahertz wave generated by DAST crystal with AR coating is higher than the power of terahertz wave generated by the crystal without AR coating.

Introduction

Electromagnetic waves between the microwave and infrared regions in the electromagnetic spectrum are known as terahertz waves. These waves possess excellent properties such as higher penetrability than infrared waves and better spatial resolution compared to microwaves. Moreover, the photon energy of the THz wave (~meV) is much smaller in comparison to X-ray (~keV). These waves are considered safe for a human being. Owing to these characteristics, terahertz waves have widely been studied for various applications such as material characterization, information and communication technology, biomedicine, homeland security, non-destructive testing and analysis and scientific studies [1].

High power and broadband THz wave is essential to further expand the applications of THz wave. In the past, there have been large numbers of reports on high power THz wave generation using different methods such as optical parametric generation, quantum cascade laser, laser plasma interaction. Among these methods, optical rectification of femtosecond pulses in the non-linear optical crystal is one of the widely used methods to emit broadband and high-power terahertz waves [2]. In this process, the power of the terahertz wave is directly proportional to the square of the power of the femtosecond pump laser. Therefore, high power terahertz wave can be generated using high power pump laser provided that the non-linear crystal has a high damage threshold and a high optical non-linear coefficient. Although the high-power terahertz wave can be generated using such crystals, the efficiency of terahertz wave generation is limited by the loss of laser power due to Fresnel's reflection at the boundary between air and crystal. However, selecting appropriate anti-reflection coating with proper thickness helps to reduce the laser power reflection, increasing the resultant incident pump power. In this study, we experimentally demonstrate that using an antireflection coat on the surface of optical crystal effectively reduces the reflection loss of the pump laser, thereby increasing the incident laser power. This enables us to enhance the terahertz wave emitted by an optical crystal with the anti-reflection coating.

Experiment

Various non-linear optical crystals such as Zinc Telluride (ZnTe), Lithium Niobate (LiNbO₃), DAST, Gallium Phosphide (GaP), etc. can be used to generate terahertz waves. In this study, we used DAST crystal as it has a high non-linear optical constant and low terahertz wave absorption. This crystal is coated with an amorphous fluoropolymer called Cytop via dip coating [3]. Figure 1 shows the experimental setup used to emit and detect terahertz waves. The DAST crystals with the thickness of 0.5 mm were used, where one crystal is coated with cytop whereas the other crystal is used without an anti-reflection coat for comparison.

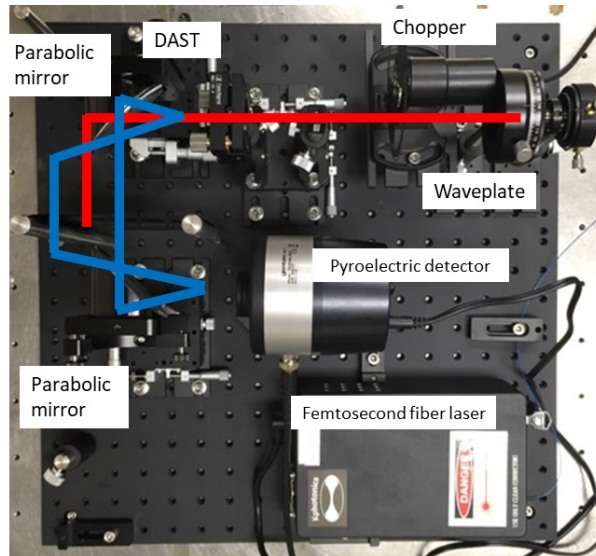


Fig. 1. Experimental setup for the emission and detection of terahertz waves

We used femtosecond fiber laser ($\lambda = 1560$ nm, average power = 80 mW, pulse width < 100 fs, repetition rate = 50 MHz) to pump the DAST crystals. The polarization of the laser was aligned to the a-axis of the crystal by half waveplate. The pump beam is focused on the crystal using a lens with a focal length of 50.8 mm. The terahertz wave emitted by the crystal is collimated and focused on the pyroelectric detector using two off-axis parabolic mirrors. The laser beam transmitted through the crystal is blocked using black polyethylene whose transmittance in the THz frequency band is 70 %, whereas in the optical region, it is close to 0 %. Here, first we measured the transmittance of the laser pulse through the two different crystals and we observed that the transmittance of a laser beam of around 93 % and 79 % for the crystals with and without AR coating, respectively. It indicates that the AR coating is effective in increasing the transmission by reducing the reflection loss. Finally, we measured the terahertz wave emitted by the pyroelectric detector and we confirmed that the AR coated crystal produces around average power of 2 μ W whereas the other crystal produces around 1.6 μ W when excited with 80 mW pump laser.

Conclusion

In the study, we studied the terahertz wave emitted by DAST crystal with and without anti-reflection coating. We found that the power of the terahertz wave generated by DAST crystal with AR coating is higher than the power of the terahertz wave generated by DAST crystal without AR coating.

References

- [1] P. U. Jepsen, D. G. Cooke, M. Koch "Terahertz spectroscopy and imaging – Modern techniques and applications". Las. Phot. Rev. vol. 5, no. 1 pp. 124 – 166 (2011).

- [2] S. R. Tripathi, K. Murate, H. Uchida, K. Takeya, K. Kawase "A fiber laser pumped, high-power terahertz wave source based on optical rectification of femtosecond pulses in 4-Dimethylamino-N-methyl-4-Stibazolium Tosylate crystal". *App. Phys. Exp.* vol. 6, pp. 072703-1, (2013).
- [3] H. Uchida, C. Koyama, T. Takagi, P. Wang, T. Kamei, K. Kawase, and K. Takeya "Antireflection coating on organic nonlinear optical crystals using soft materials". *App. Phys. Lett.*, vol. 115 No. 23, p.231107 (2019).

Unit 13 “Plasma physics”

Oxidation and stability of polymers treated by atmospheric-pressure plasma

E. BÎRLEANU, I. MIHAILA, I. TOPALA, G. BORCIA
Faculty of Physics, Alexandru Ioan Cuza University, Iasi, Romania

Abstract

The influence of atmospheric-plasma exposure on various polymers is studied, aiming to evaluate the plasma capability for efficient, uniform and stable surface modification. The surfaces show a strong increase of the hydrophile character, related to the incorporation of oxygen groups. The limiting level of modification is similar for all polymers, whereas the post-treatment stability is better for non-polar polymers, such as PE and PS.

Introduction

Polymer materials offer a large range of surface properties, thus playing an essential role in many applications. Nonetheless, many polymer properties rest on the surface chemical composition, material structure and surface orientation of specific chemical functionalities, all intrinsically related, and defining the material interaction with its environment. In this respect, the generation of polymer surfaces and interfaces allowing control on the interaction with a specific environment through definite surface properties remains a major challenge in the development of surface processing techniques.

Taking this into account, we investigate the surface modification of polymers treated by an air atmospheric-pressure dielectric barrier discharge (DBD), under conditions simulating continuous processing, also assessing the dynamics and stability of modified surfaces.

Here, polar polymer structures, such as polyethylene-terephthalate (PET) and polysulfone (PSU), are tested, in comparison to non-polar polymers, as polyethylene (PE) and polystyrene (PS), in order to evaluate the plasma capability for efficient modification. The selected polymers offer a variety of chemical structures, in terms of structurally bonded oxygen in their chain, also allowing a comparison between aliphatic polymers, as PE, and aromatic polymers, as PS, PET and PSU, known to exhibit enhanced mechanic characteristics and chemical stability, related to intrinsic rigidity and chemical inertness of the aromatic ring.

Experimental

The plasma exposure was performed on commercial polymer films of PE, PS, PET and PSU (Goodfellow Ltd., Cambridge), 50 μm thick.

The samples were treated in an atmospheric-pressure plasma reactor in the DBD arrangement, working in air. The plasma is created in the gap between the HV electrode, consisting of two thin metal blades, and the ground electrode, which is a moving stage, covered with a polymer film, 0.3 mm thick. The discharge covers 10 cm in length and 3 mm in width. The stage can be displaced at various speeds and the real treatment duration is calculated, taking into account the speed and the discharge width. Here two treatment durations were tested, 0.5 s and 1 s.

The surface of polymers, before and after processing, was analyzed by the contact angle, X-ray photoelectron spectroscopy (XPS) and atomic force microscopy (AFM). The stability of the surface was assessed by monitoring the ageing of samples by contact angle measurement.

Results and discussion

The polymer repeat units are presented in Fig. 1. These represent polar and non-polar structures, related to the presence of bonded oxygen atoms in the chain and in the pending groups.

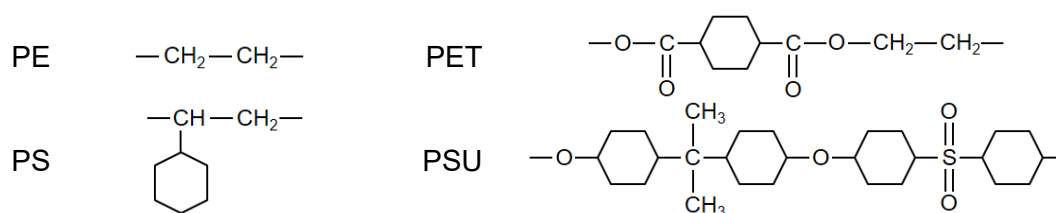


Fig. 1. Repeat units of PE, PS, PET and PSU

The water contact angle measured on the polymers after plasma exposure shows an important decrease, as observed in Fig. 1, which implies a strong increase in the hydrophile character of the surface. Importantly, the dispersion of the measured values is low, within 2 – 3°, showing uniform surface modification over the entire exposed area. Also, the modification of the surface properties is very fast, since the difference between the surfaces treated for the two durations is practically within error bars, showing that after 0.5 s the modifications already level out. The degree of modification of the hydrophilicity is better rendered to evidence by the adhesion work of water W_a , presented in Table 1. Interestingly, although the initial value is different for the four polymers, the limiting level of W_a increase is the same for PS, PET and PSU.

Table 1. Water adhesion work on plasma-treated polymers

Sample	PE			PS		
treated	—	0.5 s	1.0 s	—	0.5 s	1.0 s
W_a (mJ/m ²)	70.7	107.7	110.8	78.5	129.9	126.4

Sample	PET			PSU		
treated	—	0.5 s	1.0 s	—	0.5 s	1.0 s
W_a (mJ/m ²)	92.7	126.3	127.7	103.6	128.6	130.0

The strong modification of the surface hydrophilicity can be related to the creation of carbon-bonded-to-oxygen functional groups, as shown by XPS spectra. The atomic composition, expressed as O/C, is presented in Table 2. An increase in the number of oxygen atoms is visible for all polymers, although it depends on the initial oxygen content of the material.

Table 2. Atomic composition calculated from XPS spectra for plasma-treated polymers

Sample	PE			PS		
treated	—	0.5 s	1.0 s	—	0.5 s	1.0 s
O/C	-/100	8/92	14/86	-/100	14/86	15/85

Sample	PET			PSU		
treated	—	0.5 s	1.0 s	—	0.5 s	1.0 s
O/C	25/75	28/72	33/67	15/82	20/75	22/73

The treated samples show different ageing behavior (Fig. 2). Although the contact angle remains significantly lower than that for untreated surfaces even after two weeks of ageing, in the case of polar polymers, PET and especially PSU, the recovery is more accentuated than for non-polar polymers, such as PE and PS.

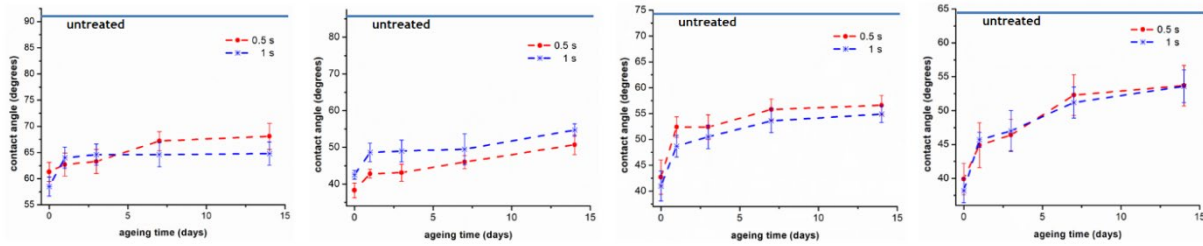


Fig. 2. Ageing of treated polymers: PE, PS, PET and PSU

Conclusion

Atmospheric-pressure plasma provided efficient, uniform and stable surface modification on selected polymers with various chemical structures. The surfaces show a strong increase of the hydrophilic character, related to the incorporation of oxygen groups. The limiting level of modification is similar for all polymers, whereas the post-treatment stability is better for non-polar polymers, like PE and PS. Restraining the ageing process is a necessary condition for polymer operational stability.

Velocity distribution functions at plasma boundary

C. COSTIN

*Iasi Plasma Advanced Research Center (IPARC), Faculty of Physics,
Alexandru Ioan Cuza University of Iasi, Iasi 700506, Romania*

Abstract

The study of bounded laboratory plasmas often requires the knowledge of particle distribution function at the plasma boundary. The distribution function can describe either plasma particles that are reflected on the surrounding surfaces or particles that are injected in plasma due to different surface phenomena: thermionic emission, secondary emission, sputtering, etc. The distribution function is usually defined as a combination of two independent distributions, one angular and one energy-dependent. In the current study, all distributions are discussed as functions of the velocity components. Different combinations of angular (isotropic and cosine-type) and energy (energy-dependent, uniform, and mono-kinetic) distributions are compared based on their effect on subsequent calculations.

Introduction

In the last decades, numerical simulations have been frequently used when experiments are difficult to implement or are too expensive. The choice of input parameters should be based on solid physical assumptions in order to guarantee the accuracy of the simulation. Regardless of the numerical model (fluid, particle-in-cell, Monte Carlo, collisional-radiative, etc.), an important assumption of bounded plasma simulation concerns the particles that are injected in the simulation domain through the boundaries.

The present study is focused on the most common distribution functions used in the literature [1] for the particles mentioned above. Although the distributions are obtained by coupling an angular and an energy distribution, which are independent of each other, they are treated as a whole and they are expressed as functions of the velocity components. Isotropic and cosine-type angular distributions are combined with typical energy distributions (maxwellian, uniform, mono-kinetic, etc.). Macroscopic quantities are estimated with different distributions, evidencing the particularities of each distribution. False definitions of angular distributions are discussed.

Velocity distribution functions

The distribution function on the velocity components, $F(v_x, v_y, v_z)$, is obtained by coupling the energy distribution function, $f(\varepsilon)$, and the angular distribution function, $g_\Omega(\theta)$, where ε is the energy of the particle and θ is the polar angle measured with respect to the surface normal. If the latter two distributions are independent, the whole distribution is obtained by multiplication:

$$F(v_x, v_y, v_z) = F(\varepsilon, \theta) = f(\varepsilon)g_\Omega(\theta). \quad (1)$$

The energy distribution function is defined as the number of particles per unit energy, having the kinetic energy around ε . The angular distribution function is defined as the number of particles having the velocity vector in a unit solid angle, around the polar angle θ . In terms of probability, both isotropic and cosine-type distribution functions are defined by the same formula [1]:

$$g_\Omega(\theta) = \frac{n+1}{2\pi} \cos^n \theta. \quad (2)$$

For $n = 0$ the distribution is isotropic, while for $n = 1, 2, \dots$ the distribution is cosine-type. According to ref. [2], a common error would be to define the angular distribution with respect to the polar angle instead of defining it with respect to the solid angle as in eq. (2). For illustration, the comparison between correctly and false defined isotropic and cosine angular distributions is shown in Fig. 1.

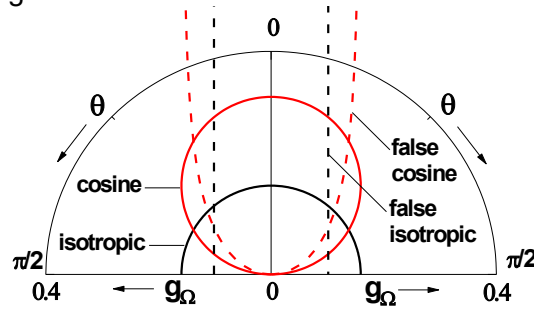


Fig. 1. Polar coordinates plot of four angular probability functions, $g_\Omega(\theta)$: isotropic, cosine, false isotropic and false cosine

An example of velocity distribution functions obtained from isotropic and cosine angular distributions combined with maxwellian, uniform ($f(\varepsilon) = \text{const.}$) and mono-kinetic ($\varepsilon = \text{const.}$) energy distributions is plotted in Fig. 2.

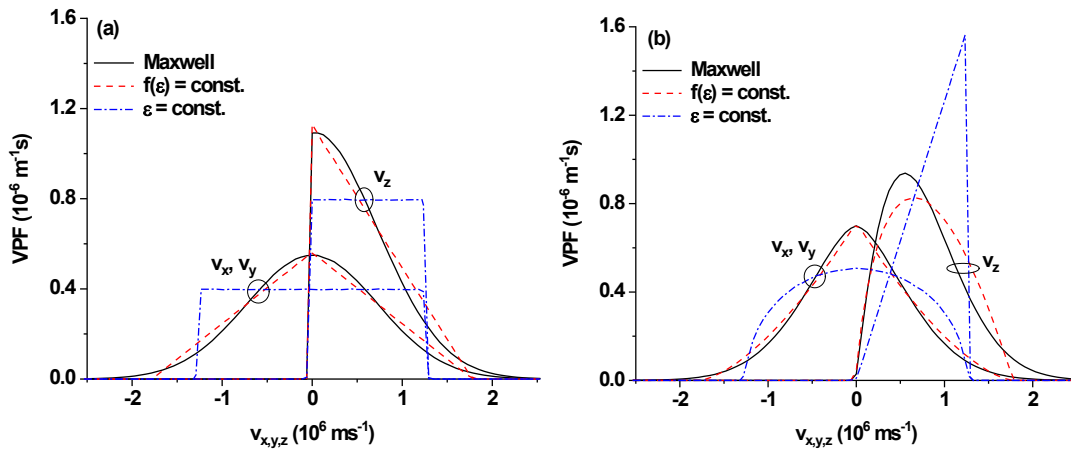


Fig. 2. Examples of velocity probability functions at plasma boundary: (a) isotropic and (b) cosine angular distributions

Velocity components v_x and v_y are parallel, while v_z is perpendicular to the boundary surface. It can be observed that the isotropic uniform energy distribution can be a fair approximation of the isotropic Maxwellian energy distribution. The isotropic mono-kinetic distribution is uniform with respect to all velocity components, while the cosine mono-kinetic distribution increases linearly with the perpendicular velocity v_z . When the distributions plotted in Fig. 2 are used to compute macroscopic quantities, such as the average velocity of the particles in perpendicular direction to the surface [1] or the secondary electron emission yield [3], the results are significantly different.

Conclusion

The proper choice of the particle distribution function at the plasma boundary requires the investigation of the distribution as a whole, expressed as a function of velocity components, instead of just coupling two independent distributions: angular and energy. An inadequate assumption of the distribution function can lead to significantly different results on subsequent calculations.

References

- [1] C. Costin "Particle distribution functions at plasma-surface interface", AIP Adv. 10, 115308 (2020).
- [2] J. Greenwood "The correct and incorrect generation of a cosine distribution of scattered particles for Monte-Carlo modelling of vacuum systems", Vacuum 67, 217 (2002).
- [3] C. Costin "Secondary electron emission under magnetic constraint: from Monte Carlo simulations to analytical solution", Scientific Reports 11, 1874 (2021).

The physicochemical/electrical properties of plasma activated medium by dielectric barrier discharge microplasma

A. G. YAHAYA¹, T. OKUYAMA², J. KRISTOF³, M. G. BLAJAN³, K. SHIMIZU^{1,2,3}

¹*Graduate School of Science and Technology*

²*Graduate School of Integrated Science and Technology,*

³*Organization for Innovation and Social Collaboration Shizuoka University*

Abstract

Plasma activated medium (PAM) is a relatively new approach for bacterial inactivation while ensuring safety and maintaining the properties of the material to be sterilized. Recent research reported that PAM is effective for bacterial sterilization up to 8 log reduction in CFU/mL. In this paper, further physicochemical/electrical properties of PAM generation by dielectric barrier discharge microplasma (DBD) were investigated at relatively low discharge voltage. Temperature, water loss, pH, UV-VIS absorbance after 2 months, nitrite/nitrate concentration, resistivity and conductivity were assessed after treatment. The results suggested that microplasma treatment of PAM causes an increase in resistivity, acidification, dissolved reactive oxygen and nitrogen species (RONS), creating an environment suitable for sterilization of bacteria. These properties could be preserved for a long time under low temperature. Therefore, PAM is an effective method for surface sterilization.

Introduction

Generally, medical devices are sterilized mainly by heat, γ -radiation, or hydrogen peroxide (H_2O_2) [1]. However, heat-sensitive materials, such as bio-compatible polymer and skin, are normally inapplicable using oven or autoclave sterilization processes which have minimal temperature of 121 °C [2]. Microplasma is a type of DBD atmospheric-pressure plasma that

can be generated at a relatively low discharge voltage of about 1 kV. The micrometer order discharge gap allows microplasma to be generated at atmospheric pressure, low temperature, and voltages from 0.4 kV depending on the discharge parameters [3]. Plasma discharge near water creates RONS containing solutions known as PAM. Plasma-treated solutions can remain stable for several days with respect to the storage temperature. Recently, PAM have been widely studied for many biomedical applications such as cancer cell treatment [4], bacterial sterilization [5], wound healing/skin treatment [6], and dental infection treatments [7]. Recent research reported that PAM is effective for bacterial sterilization up to 8 log reduction in CFU/mL [5].

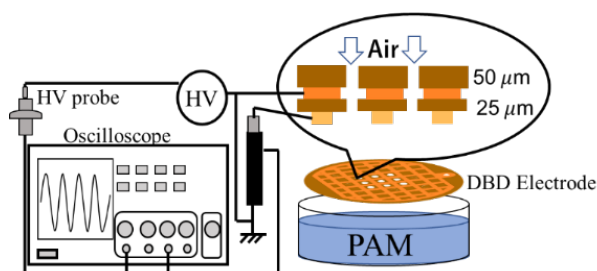


Fig. 1. Experimental setup with electrode geometry

Materials and Methods

The physicochemical/electrical properties of PAM by DBD microplasma were investigated at relatively low discharge voltage. Temperature, water lost, pH, UV-VIS absorbance 2 months after treatment, $\text{NO}_3^-/\text{NO}_2^-$ concentration using Griess reagent kit and resistivity were investigated. Microplasma (Fig.1) used for PAM treatment was generated at a discharge voltage of 1,18 kV and an AC frequency of 20 kHz using a Neon transformer (M-5, Alpha Neon, Gifu, Japan). 2 mL of 0.85% NaCl solution henceforth referred to as “samples” were treated for 1, 2, and 3 min at 2 mm from the plasma source using air at a flow of 2 L/m.

Results and Discussion

The pH value of PAM significantly dropped after 3 minutes of treatment indicating that the water had undergone acidification. Temperature and evaporation of PAM (Fig. 2a) increased from 22.7 – 28.2°C and 1994 – 2007μL after 3 minutes of treatment. However, this temperature is below the boiling point of water and harmless to heat-sensitive medical device/skin; therefore, the evaporation of PAM is attributed to gas flow. The absorption peaks of $\text{NO}_3^-/\text{NO}_2^-$ at 200 – 210 nm (Fig. 2b) slightly decreased 2 months after treatment which implies that these species could last long in PAM depending on storage conditions. Furthermore, the concentration of $\text{NO}_3^-/\text{NO}_2^-$ in PAM increased with treatment time (Fig. 2c). The resistivity of PAM increased from 0.86 – 0.92 Ω/m with an increase in treatment time to 3 min causing conductivity to decrease from 1.16 – 1m05 s/m after 3 min of treatment (see Fig. 2c).

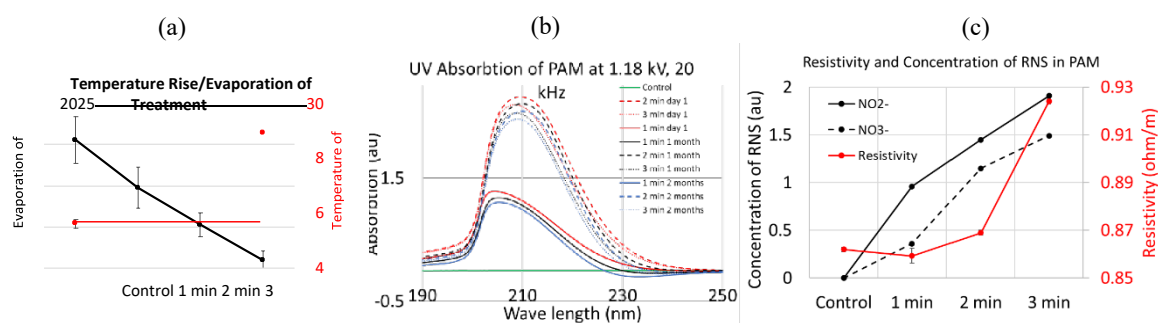


Fig. 2. (a) Temperature rise and Evaporation of PAM during treatment (b)UV-VIS Absorption of PAM (c) Resistivity and Concentration of RNS in PAM

Conclusion

The Physicochemical/electrical properties of PAM treated by DBD microplasma were investigated. An increase in treatment time caused an increase in acidification, temperature, minor evaporation, the concentration of nitrates and nitrites and resistivity. UV-VIS spectroscopy confirms that the dissolved RONS generated using this setup could last for more than 2 months. These results suggest that PAM could be suitable for the sterilization of heat-sensitive materials/skin. Further research on the properties of PAM will be conducted.

References

- [1] Halfmann H., Bibinov N., Wunderlich J., Awakowicz P. "A double inductively coupled plasma for sterilization of medical devices", *J. Phys D: Appl. Phys.*, 40, 4145, 2007.
- [2] Coulter W. A., Chew-Graham C. A., Cheung S. W., Burke F. J. T. "Autoclave performance and operator knowledge of autoclave use in primary care: a survey of UK practices", *J. Hospital Infection*, 48, 180 – 185, 2001.
- [3] Shimizu, K., Tran, N.A, Hayashida K., Blajan, M. G "Comparison of atmospheric microplasma and plasma jet irradiation for increasing of skin permeability", *J. Phys. D Appl. Phys.*, 49,315201, 2016).
- [4] Azzariti A., Iacobazzi R. M., Di Fonte R., Porcelli L., Gristina R., Favia, P., Sardella E. "Plasma-activated medium triggers cell death and the presentation of immune activating danger signals in melanoma and pancreatic cancer cells", *Scientific Reports*, 9, 1, 2019.
- [5] Yahaya A. G., Okuyama T., Kristof J., Blajan M. G., Shimizu K. "Direct and Indirect Bactericidal Effects of Cold Atmospheric-Pressure Microplasma and Plasma Jet", *Molecules*, 26, 2523, 2021.
- [6] Xu D., Wang S., Li B., Qi M., Feng R., Li Q., Zhang H., Chen H., Kong M. G. "Effects of Plasma-Activated Water on Skin Wound Healing in Mice", *Microorganisms*, 8, 1091, 2020.
- [7] Kaushik N. K., Ghimire B., Li Y., Adhikari M., Veerana M., Kaushik N., Choi E. H. "Biological and medical application of plasma-activated media, water and solutions", *Biological Chemistry*, 2018.

Unit 14 “iA Young Researcher”

Green functions of relativistic quasipotential equations for complex values of energy

A. V. BUZHAN, V. N. KAPSHAI

Francisk Skorina Gomel State University, Gomel, Republic of Belarus

Abstract

Green functions of quasipotential equations for scattering states of a two-particle system are investigated for complex values of energy. Green functions of quasipotential equations in the relativistic configurational representation for complex values of energy are found. Limits for implementing the complex-scaling method for investigating resonance states of scattering cross-sections of a relativistic two-particle system are defined.

Partial two-particle equations in the relativistic configurational representation for scattering p -states in the case of a superposition of two δ -function potentials

V. N. KAPSHAI, A. A. GRISHECHKINA

Francisk Skorina Gomel State University, Gomel, Republic of Belarus

Abstract

Exact solutions of two-particle equations are considered in the relativistic configurational representation for scattering p -states in the case of superposition of two δ -function potentials. Scattering amplitudes and cross sections are determined. Comparative analysis is carried out with the case of scattering s -states.

Introduction

Partial wave equations in the relativistic configurational representation for scattering p -states (orbital angular momentum $l = 1$) of system of two particles are defined as [1]

$$\psi_{(j)}(r) = m \operatorname{sh} \chi_q p_1(\chi_q, r) + \int_0^\infty G_{(j)}(r, r') V(r') \psi_{(j)}(r') dr', \quad (1)$$

$$p_1(\chi_k, r) = r(mr + i)^{-1} \operatorname{sh}^{-2} \chi_k \left(\operatorname{ch} \chi_k \sin(\chi_k mr) (mr)^{-1} - \operatorname{sh} \chi_k \cos(\chi_k mr) \right). \quad (2)$$

In expressions (1) – (2) $\psi_{(j)}(r)$ – is the wave function, χ_q – is the rapidity connected with the system energy by the formula $2E = 2m \operatorname{ch} \chi_q$, m – is the mass of each particle, and the index j indicates the corresponding equation ($j=1$ – the modified Kadyshevsky equation, $j=2$ – the Logunov-Tavkhelidze equation, $j=3$ – the modified the Logunov-Tavkhelidze equation, $j=4$ – the Kadyshevsky equation). The explicit form of the partial Green's functions (GF) $G_{(j)}(r, r')$ was defined earlier [2].

When $r \rightarrow \infty$ the GF $G_{(j)}(r, r')$ take the following form:

$$G_{(j)}(r, r') \Big|_{r \rightarrow \infty} \cong K_{(j)}(r') e^{i\chi_q m r}, \quad (3)$$

$$K_{(1)}(r') = K_{(3)}(r') = -ir' \left((mr' - i) \operatorname{sh} \chi_q \right)^{-1} \left(\cos(\chi_q m r') - (mr')^{-1} \operatorname{cth} \chi_q \sin(\chi_q m r') \right),$$

$$K_{(2)}(r') = K_{(4)}(r') = -ir' (mr' - i)^{-1} \left(2 \cos(\chi_q m r') (\operatorname{sh}(2\chi_q))^{-1} - \sin(\chi_q m r') (mr' \operatorname{sh}^2 \chi_q)^{-1} \right).$$

1. Solution of the equations for a superposition of two δ -function potentials

For the following superposition of two δ -function potentials:

$$V(r) = V_{01} \delta(r - a_1) + V_{02} \delta(r - a_2) \quad (4)$$

equation (1) takes the following form:

$$\psi_{(j)}(r) = m \operatorname{sh} \chi_q p_1(\chi_q, r) + G_{(j)}(r, a_1) V_{01} \psi_{(j)}(a_1) + G_{(j)}(r, a_2) V_{02} \psi_{(j)}(a_2). \quad (5)$$

In order to determine the values of $\psi_{(j)}(a_1)$ and $\psi_{(j)}(a_2)$ in (5), it is necessary to consider the wave function at the points $r = a_1$ and $r = a_2$, and then solve the resulting system of linear algebraic equations. Expressions for $\psi_{(j)}(a_1)$ and $\psi_{(j)}(a_2)$ can be then represented as

$$\psi_{(j)}(a_1) = \Delta_{1(j)}(\chi_q) / \Delta_{(j)}(\chi_q), \quad \psi_{(j)}(a_2) = \Delta_{2(j)}(\chi_q) / \Delta_{(j)}(\chi_q); \quad (6)$$

$$\Delta_{(j)}(\chi_q) = \prod_{n=1}^2 \left[1 - V_{0n} G_{1(j)}(\chi_q, a_n, a_n) \right] - V_{01} V_{02} \left(G_{1(j)}(\chi_q, a_1, a_2) \right)^2,$$

$$\Delta_{1(j)}(\chi_q) = m \operatorname{sh} \chi_q p_1(\chi_q, a_1) \left[1 - V_{02} G_{1(j)}(\chi_q, a_2, a_2) \right] + V_{02} m \operatorname{sh} \chi_q p_1(\chi_q, a_2) G_{1(j)}(\chi_q, a_1, a_2),$$

$$\Delta_{2(j)}(\chi_q) = m \operatorname{sh} \chi_q p_1(\chi_q, a_2) \left[1 - V_{01} G_{1(j)}(\chi_q, a_1, a_1) \right] + V_{01} m \operatorname{sh} \chi_q p_1(\chi_q, a_1) G_{1(j)}(\chi_q, a_2, a_1).$$

Taking into account the asymptotic expressions for GF (3), we obtain

$$\psi_{(j)}(r) \Big|_{r \rightarrow \infty} = m \operatorname{sh} \chi_q \left(p_1(\chi_q, r) \right) \Big|_{r \rightarrow \infty} + f_{1(j)}(\chi_q) (-i) e^{im\chi_q r} m \operatorname{sh} \chi_q. \quad (7)$$

In this case the relativistic scattering amplitude $f_{1(j)}(\chi_q)$ corresponding to the equation with the model potential (4) can be expressed analytically:

$$f_{1(j)}(\chi_q) = i \left(m \operatorname{sh} \chi_q \right)^{-1} \left(K_{(j)}(a_1) V_{01} \psi_{(j)}(a_1) + K_{(j)}(a_2) V_{02} \psi_{(j)}(a_2) \right). \quad (8)$$

The partial scattering cross section for the p -wave is expressed by the scattering amplitude $f_{1(j)}(\chi_q)$ as follows: $\sigma_{1(j)}(\chi_q) = 12\pi \left| f_{1(j)}(\chi_q) \right|^2$. Figure 1 shows the graphs of the dependence of the scattering cross sections on the rapidity for the following parameter values: $a_1 = 3$, $V_{01} = 1$, $a_2 = 4$, $V_{02} = 2$, $m = 1$.

2. Comparison of results for scattering s- and p-states

Earlier [3], the scattering cross sections were obtained for the equations under consideration in the case of an s-wave. Let us give the graphs of the scattering cross section for the Logunov-

Tavkhelidze equation in the case of $l = 0.1$ for $a_1 = 3$, $V_{01} = 1$, $a_2 = 4$, $V_{02} = 2$, $m = 1$ (Figure 2). Analyzing Fig. 2, we see that the local maxima of the scattering cross section for the p -state compared to the maxima for the s -state are shifted in the direction of high rapidity values. This feature is a consequence of the presence of a centrifugal barrier.

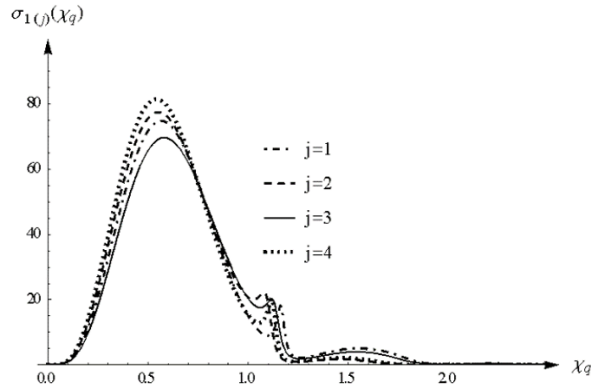


Fig. 1. Dependence of the partial scattering cross section $\sigma_{1(j)}$ on χ_q

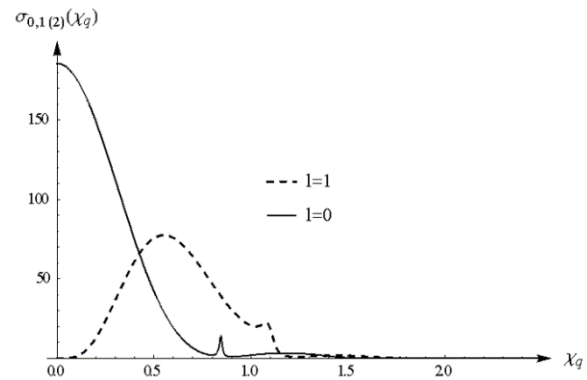


Fig. 2. Dependence of the partial scattering cross section $\sigma_{0,1(2)}$ on χ_q

Conclusion

Thus, in this paper, we consider the determination of the wave functions of partial two-particle equations in the relativistic configurational representation in case of a unit orbital angular momentum. On the basis of the obtained wave functions the partial scattering amplitudes and scattering cross sections for the superposition of two δ -function potentials are found.

References

- [1] V. N. Kapshai, S. I. Fialka "Solution of relativistic two-particle equations with arbitrary orbital angular momentum", Russ. Phys. Journal, Vol. 60, № 1, P. 37 – 49 (2017).
- [2] V. N. Kapshai, A. A. Grishechkina "Partial relativistic Green's functions for scattering states in the case of a unit orbital angular momentum" [in Russian], Materials of the international jubilee scientific and practical conference dedicated to the 90th anniversary of the Francisk Skorina Gomel State University, p. 3, Gomel: Francisk Skorina Gomel State University, p. 224 – 229 (november 2020).
- [3] V. N. Kapshai, Yu. A. Grishechkin "Relativistic scattering s-states problem for superposition of two potentials " δ -sphere" type" [in Russian], P, №2 (23), c. 7 – 12 (2015).

Analysis of the spatial distribution of the second-harmonic radiation generated in a thin surface layer of a spheroidal dielectric particle

V. N. KAPSHAI, A. A. SHAMYNA, A. I. TALKACHOV
Francisk Skorina Gomel State University, Gomel, Republic of Belarus

Abstract

Based on Rayleigh–Gans–Debye model, the spatial distribution of the second-harmonic radiation generated in a thin surface layer of a spheroidal dielectric particle is presented using three-dimensional directivity patterns. The peculiarities of forms of the directivity patterns are described for the key values of the parameters. The symmetries of the directivity patterns are

revealed, as in the case of second-harmonic generation in a surface layer of a spherical particle. The relationship between the polarization of the generated radiation and the polarization of the incident wave is described.

Introduction

Second-order nonlinear optical effects are widely used for the investigation of anisotropic properties of molecules and different structures. The second-harmonic generation (SHG) as the special case of nonlinear optical phenomenon of the even order may be used to get information about the thin surface layer of dielectric particles. The investigations of SHG were mostly devoted to generation in the surface layer of spherical [1, 2] and cylindrical particles [2, 3]. Some authors described the SHG in spheroidal dielectric particles [2]. Despite that, the analytical solution of the latter problems cannot be used to determine the spatial distribution of the generated radiation in some partial cases: if the particle has the form of an oblate spheroid, if the exciting radiation has the elliptical polarization, if one has to account the dispersion properties of the media in the problem. Some of these issues are solved during the research described in this paper.

Problem statement

Let an elliptically polarized electromagnetic wave propagate through a spheroidal dielectric particle covered by an optically nonlinear layer. Using the dipole model, the SHG radiation can be described by the second-order term in the expression for the polarization vector expressed using components of the electric field strength $E_{j,k}$:

$$P_i^{(2)} = \chi_{ijk}^{(2)} E_j E_k. \quad (1)$$

The tensor $\chi_{ijk}^{(2)}$ is the second-order nonlinear susceptibility tensor that depends on the components of the unit vector n_i perpendicular to the surface of the layer as follows:

$$\chi_{ijk}^{(2)} = \chi_1^{(2)} n_i n_j n_k + \chi_2^{(2)} n_i \delta_{jk} + \chi_3^{(2)} (n_j \delta_{ki} + n_k \delta_{ij}) + \chi_4^{(2)} n_m (n_k \varepsilon_{ijm} - n_j \varepsilon_{imk}). \quad (2)$$

The coefficients $\chi_{1-4}^{(2)}$ are independent components of the tensor $\chi_{ijk}^{(2)}$. For SHG, there are only four independent components in $\chi_{ijk}^{(2)}$.

Spatial distribution of the second harmonic radiation

The expression for the electric field strength of the generated radiation may be written as in [1]:

$$\mathbf{E}^{(2\omega)}(\mathbf{x}) = \mu_{2\omega} \frac{(2\omega)^2}{c^2} \frac{\exp(ik_{2\omega}r)}{r} (1 - \mathbf{e}_r \otimes \mathbf{e}_r) \int_V \exp(-i\mathbf{k}^{(2\omega)}(\mathbf{x}) \cdot \mathbf{x}') \mathbf{P}^{(2)}(\mathbf{x}') d\mathbf{x}' \quad (3)$$

where $\mathbf{k}^{(2\omega)}$ ($k_{2\omega} = |\mathbf{k}^{(2\omega)}|$) is the wave vector of the second-harmonic (SH) wave, the multiplier $(1 - \mathbf{e}_r \otimes \mathbf{e}_r)$ eliminates the radial component of the value of the integral, ω is the cyclic frequency of the incident wave, r is the distance from the particle to the point of observation. The integration is performed within the volume of the thin optically nonlinear layer on the spheroidal particle. The integral in (3) may be found analytically using infinite series like in paper [2] where the case of prolate spheroid was considered.

Let us consider the radiation patterns for the SHG from the particles of different forms.

One can see in Fig. 1 the directivity patterns for the size of minor semiaxis of spheroidal particle characterized by the condition $k_\omega a_x = 0.1$ (k_ω is the magnitude of the wave vector of the

incident wave, a_x – the length of minor semiaxis), the ratio of semiaxes equals 0.1 (oblate spheroid). These radiation patterns are plotted for the case when the incident wave has linear polarization and the electric field vector (the red arrow) is parallel to the symmetry axis of the spheroidal particle. The wave vector of the incident wave (the black arrow) is oriented perpendicularly to the symmetry axis. The polarization of the second-harmonic radiation is also linear (white color of the radiation patterns). The forms of radiation patterns differ from each other for different values of coefficients $\chi_{1-4}^{(2)}$ and have their own mirror and axial symmetries.

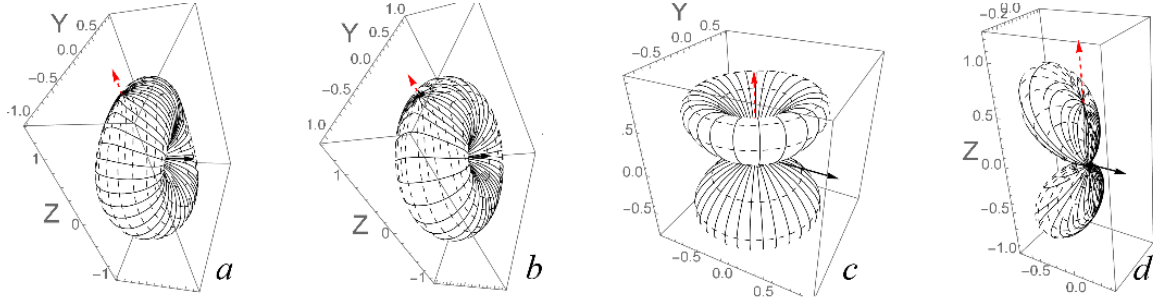


Fig. 1. The diagram of the second-harmonic radiation in the surface layer of the spheroidal particle:

$$a - \chi_1^{(2)} \neq 0, \chi_{2-4}^{(2)} = 0, b - \chi_2^{(2)} \neq 0, \chi_{1,3,4}^{(2)} = 0, c - \chi_3^{(2)} \neq 0, \chi_{1,2,4}^{(2)} = 0, d - \chi_4^{(2)} \neq 0, \chi_{1-3}^{(2)} = 0$$

The following directivity patterns in Fig. 2 are plotted for the elliptically polarized incident wave and the prolate form of the dielectric particle (the ratio of semiaxes is 1.5).

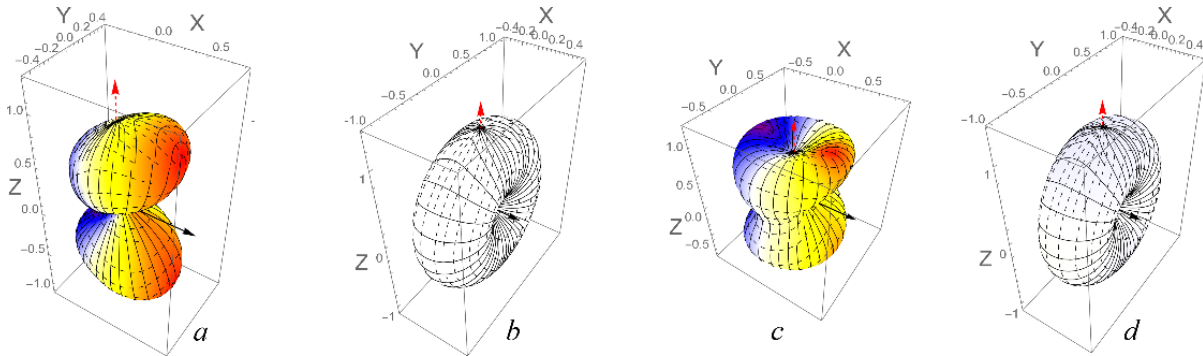


Fig. 2. The diagram of the SH-radiation spatial distribution caused by the elliptically polarized wave:

$$a - \chi_1^{(2)} \neq 0, \chi_{2-4}^{(2)} = 0, b - \chi_2^{(2)} \neq 0, \chi_{1,3,4}^{(2)} = 0, c - \chi_3^{(2)} \neq 0, \chi_{1,2,4}^{(2)} = 0, d - \chi_4^{(2)} \neq 0, \chi_{1-3}^{(2)} = 0$$

The main differences between the directivity patterns in Fig. 1 and Fig. 2 are:

- the polarization of the SH waves (elliptically/linearly polarized incident wave causes generation of elliptically/linearly polarized radiation (non-white color) for $\chi_1^{(2)} \neq 0$, $\chi_3^{(2)} \neq 0$ or $\chi_4^{(2)} \neq 0$);
- the form of the directivity pattern depends on the polarization of the incident wave and on the ratio of the semiaxes of the spheroidal particle.

Conclusion

The connection between the polarization of the incident waves and the polarization of the second-harmonic radiation is revealed. The dependence of the form of the directivity patterns on the form of the dielectric particle is also observed. The symmetries of the spatial distribution of the generated radiation are found for each considered case. Similar symmetries were previously discovered for the spherical and cylindrical form of the dielectric particle [1, 3].

This work was supported by Belarusian Republican Foundation for Fundamental Research (project No. F20M–011).

References

- [1] V. N. Kapshai, A. A. Shamyna “Second-Harmonic Generation from a Thin Spherical Layer and No-Generation Conditions,” *Optics and Spectroscopy*, Vol. 123, No. 3, pp. 440 – 453 (2017).
- [2] A. G. F. de Beer, S. Roke, J. I. Dadap “Theory of second-harmonic and sum-frequency generation from arbitrarily shaped particles,” *J. Opt. Soc. Am. B*, Vol. 28, No. 6, pp. 1374 – 1384 (June 2011).
- [3] V. N. Kapshai, A. A. Shamyna “Second-Harmonic Generation from a Thin Cylindrical Layer. II. Analysis of Solution,” Vol. 126, No. 6, pp. 653 – 660 (2019).

Maxima of the power density of the second–harmonic generation from a linear structure of long cylindrical dielectric particles

V. N. KAPSHAI, A. I. TALKACHOV, A. A. SHAMYNA
Francisk Skorina Gomel State University, Gomel, Republic of Belarus

Abstract

The problem of second–harmonic generation by a plane electromagnetic wave from a linear structure of long cylindrical dielectric particles coated by an optically nonlinear substance is solved for the far field region using the Rayleigh–Gans–Debye approximation. The directions in which maximal intensity of the generated radiation occurs and the directions in which no generation occurs have been found. It is revealed that the maximal power density of second harmonic generation from the structure is proportional to the square of the number of cylinders.

Introduction

The phenomenon of second-harmonic generation (SHG) has been widely applied to study surfaces of dielectric nanoparticles. The paper focuses on the analysis of the signal generated from the lateral surfaces of long dielectric cylinders coated with an optically nonlinear substance and ordered in a linear structure. The structure under consideration is similar to ordered nanotubes.

One cylindrical particle

Let a cylindrical particle with height h and radius of its base a be coated with a nonlinear layer with the thickness d_0 ($d_0 \ll a$, $d_0 \ll h$). We arrange the particle so that the cylinder axis would coincide with the Oz axis and define incident plane electromagnetic wave propagation direction as the x -axis (Fig. 1a). As previously shown using Rayleigh–Gans–Debye model [1], the second harmonic field in the far-field region can be written as follows:

$$\mathbf{E}^{(2\omega)} = 2\pi\mu_{2\omega} \frac{(2\omega)^2}{c^2} d_0 a h E_0^2 (1 - \mathbf{e}_\rho \otimes \mathbf{e}_\rho) \mathbf{f}_{\text{lat}}^{(2\omega)}(\varphi) \frac{\exp(ik_{2\omega}\rho)}{\rho}, \quad (1)$$

where E_0 is the incident wave complex amplitude, $\mathbf{f}_{\text{lat}}^{(2\omega)}$ is the vector characterizing the spatial distribution of the generated radiation, ρ is the distance between the center of the particle and the place of observation. SHG power density is written as

$$S^{(2\omega)} = \frac{c}{8\pi} \frac{n_{2\omega}}{\mu_{2\omega}} \left| \mathbf{E}^{(2\omega)} \right|^2 = 8\pi c \frac{\mu_{2\omega} n_{2\omega}}{n_\omega^4} \frac{d_0^2}{\rho^2} (k_\omega a)^2 (k_\omega h)^2 E_0^4 \cdot \left| (1 - \mathbf{e}_\rho \otimes \mathbf{e}_\rho) \mathbf{f}_{\text{lat}}^{(2\omega)}(\varphi) \right|^2. \quad (2)$$

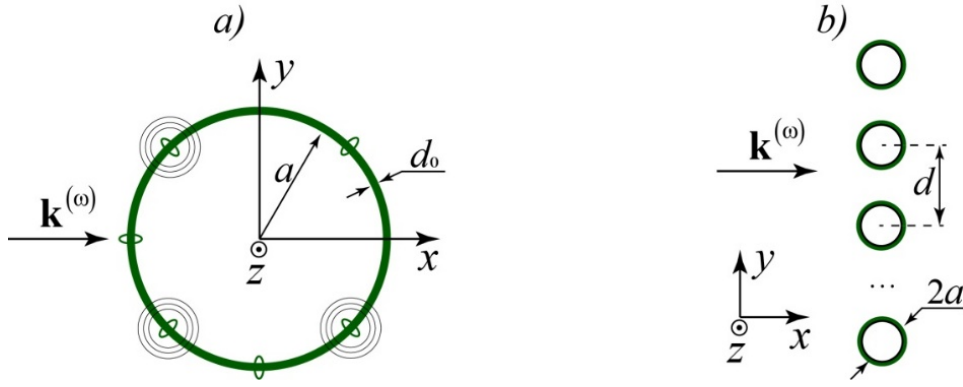


Fig. 1. a) Scheme of the problem of the SHG from the lateral surface of a cylindrical particle; b) Scheme of the problem of the SHG from the linear structure of cylindrical particles

Linear structure of cylindrical particles

Let us consider SHG from the linear structure of N cylinders with distances between their axes d at normal incidence of a plane wave (Fig. 1b). We calculate generated field in the far region assuming that the azimuth angles φ are the same for different particles. Similarly to article [1], using the principle of superposition and taking into account the phase shift, it is possible to write the vector of the electric field strength of the second harmonic from the structure as

$$\begin{aligned} \mathbf{E}_N^{(2\omega)} &= 2\pi\mu_{2\omega} \frac{(2\omega)^2}{c^2} d_0 a h E_0^2 \sum_{j=1}^N \frac{\exp(ik_{2\omega}\rho_j)}{\rho_j} (1 - \mathbf{e}_\rho \otimes \mathbf{e}_\rho) \mathbf{f}_{\text{lat}}^{(2\omega)}(\varphi) = \\ &= 2\pi\mu_{2\omega} \frac{(2\omega)^2}{c^2} d_0 a h E_0^2 (1 - \mathbf{e}_\rho \otimes \mathbf{e}_\rho) \mathbf{f}_{\text{lat}}(\varphi) \sum_{n=1-N/2}^{N/2} \frac{\exp(ik_{2\omega}(\rho + \frac{d}{2}\sin\varphi - nd\sin\varphi))}{\rho + \frac{d}{2}\sin\varphi - nd\sin\varphi}, \end{aligned} \quad (3)$$

where ρ is the distance between the center of the structure and the place of observation. Let us introduce the notation $\Phi = k_{2\omega}d\sin\varphi$. Taking into account the fact that the distance to the observation point is large in comparison with the width of the structure ($\rho \gg Nd$), the sum in (3) can be simplified as follows

$$\begin{aligned} &\sum_{n=1-N/2}^{N/2} \frac{\exp(ik_{2\omega}(\rho + \frac{d}{2}\sin\varphi - nd\sin\varphi))}{\rho + \frac{d}{2}\sin\varphi - nd\sin\varphi} \approx \frac{\exp(ik_{2\omega}\rho)}{\rho} \sum_{n=1-N/2}^{N/2} \exp(i(\frac{1}{2} - n)\Phi) = \\ &= \frac{\exp(ik_{2\omega}\rho + i\frac{N+1}{2}\Phi)}{\rho} \sum_{n'=1}^N \exp(-in'\Phi) = \frac{\exp(ik_{2\omega}\rho + i\frac{N+1}{2}\Phi)}{\rho} \exp(-i\Phi) \frac{1 - \exp(-iN\Phi)}{1 - \exp(-i\Phi)} = \\ &= \frac{\exp(ik_{2\omega}\rho + i\frac{N-1}{2}\Phi) \exp(-i\frac{N}{2}\Phi) \sin(-\frac{1}{2}N\Phi)}{\rho \exp(-i\frac{1}{2}\Phi) \sin(-\frac{1}{2}\Phi)} = \frac{\exp(ik_{2\omega}\rho) \sin(\frac{1}{2}N\Phi)}{\rho \sin(\frac{1}{2}\Phi)}. \end{aligned} \quad (4)$$

The vector of the electric field strength and power density of the second harmonic generated from the linear structure of long cylindrical dielectric particles can be written in the form

$$\mathbf{E}_N^{(2\omega)} = 2\pi\mu_{2\omega} \frac{(2\omega)^2}{c^2} d_0 a h E_0^2 (1 - \mathbf{e}_\rho \otimes \mathbf{e}_\rho) \mathbf{f}_{\text{lat}}^{(2\omega)}(\varphi) \frac{\exp(ik_{2\omega}\rho) \sin(\frac{1}{2}N\Phi)}{\rho \sin(\frac{1}{2}\Phi)} = \mathbf{E}^{(2\omega)} \frac{\sin(\frac{1}{2}N\Phi)}{\sin(\frac{1}{2}\Phi)}, \quad (5)$$

$$S_N^{(2\omega)} = S^{(2\omega)} \frac{\sin^2(\frac{1}{2}N\Phi)}{\sin^2(\frac{1}{2}\Phi)}. \quad (6)$$

Analysis of the SHG power density

Global maxima of the function $\frac{\sin^2\left(\frac{1}{2}N\Phi\right)}{\sin^2\left(\frac{1}{2}\Phi\right)}$ are equal to N^2 . They are reached at

$\frac{1}{2}\Phi = \frac{1}{2}k_{2\omega}d \sin \varphi = m\pi$, where $m = 0, 1, 2, \dots$. Global minima of the function are equal to zero and reached at $\frac{1}{2}N\Phi = \frac{1}{2}Nk_{2\omega}d \sin \varphi = m'\pi$, where $m' = 1, 2, 3, \dots$ (except $N, 2N, 3N, \dots$).

SHG power density from the structure $S_N^{(2\omega)}$ is maximum when the maximum of the function $\frac{\sin^2\left(\frac{1}{2}N\Phi\right)}{\sin^2\left(\frac{1}{2}\Phi\right)}$ coincides with the maximum of the function $S^{(2\omega)}(\varphi)$ (SHG power density from

one cylinder). There is no generation from the structure ($S_N^{(2\omega)} = 0$) for the directions $\frac{1}{2}N\Phi = m'\pi$ or for the directions in which there occurs no generation from one cylinder ($S^{(2\omega)} = 0$).

Conclusion

The problem of SHG by the plane electromagnetic wave from the linear structure of long cylindrical dielectric particles coated by optically nonlinear substance has been solved in the far field. The directions in which maximal intensity of the generated radiation occurs and the directions in which no generation occurs have been found. Our analysis showed that the maximal power density of SHG from the structure is proportional to the squared number of cylinders.

This work was supported by Belarusian Republican Foundation for Fundamental Research (project No. F20M-011).

References

- [1] A. A. Shamyna, V. N. Kapshai "Second-Harmonic Generation from a Thin Cylindrical Layer. I. An Analytical Solution", *Optics Spectroscopy*, Vol. 126, No. 6, pp. 645 – 652 (2019).

Diamond radiation detector with built-in boron-doped neutron converter layer

T. MIYAKE¹, H. NAKAGAWA², T. MASUZAWA², T. YAMADA³,
T. NAKANO², K. TAKAGI², T. AOKI², H. MIMURA²

¹Graduate School of Science and Technology, Shizuoka University, Japan

²Research Institute of Electronics, Shizuoka University, Japan

³Nanomaterials Research Institute, National Institute of Advanced Industrial Science and Technology (AIST), Japan

Abstract

We report on the fabrication and characterization of a solid-state neutron detector made of polycrystalline diamond, grown by hot-filament chemical vapor deposition (HFCVD). The detector consists of an undoped free-standing polycrystalline diamond layer and a heavily boron (B)-doped polycrystalline diamond top layer that serves as an electrical contact and a converter for neutron- alpha conversion, respectively. The boron impurity captures (thermal) neutrons and generates alpha particles, which excite electron-hole pairs in the diamond detector to form signal pulse current. Detection of radiation particles was demonstrated using alpha particles from americium-241.

Introduction

Neutron imaging is gathering attention as a tool for non-destructive inspection in medical and security applications [1]. One of the requirements for neutron image sensors is the selectivity of a neutron signal over that of an environmental gamma-ray. Since the neutron turns stable elements to radioactive isotopes, the gamma-ray is a major source of noise in neutron detection.

Diamond is a suitable material for neutron detectors: it has good neutron/gamma selectivity because of small capture cross-section of carbon against gamma-ray. It also has good tolerance against radiation dose and allows high temperature operation by its wide bandgap (5.47 eV). In addition, diamond can be heavily doped with boron (B), which can be used as a neutron- α conversion using nuclear reaction $^{10}\text{B}(n, \alpha)^7\text{Li}$. Previous studies on diamond-based neutron detectors utilize single-crystal diamonds for the best carrier transport. On the contrary, we focus on polycrystalline diamond as a radiation sensor material for its advantage in wide-area deposition using chemical vapor deposition (CVD). This study presents the fabrication and characterization of a radiation detector made of polycrystalline diamond. The detector is designed to detect both α -ray and neutron, where neutrons are converted to α -ray in the heavily B-doped converter layer. Detection of α -ray particles is demonstrated by using α -ray from americium-241 as an input.

Experimental and result

The detector structure was fabricated by synthesizing undoped self-standing polycrystalline diamond substrate and forming a B-doped layer by HFCVD, followed by contact formation. The undoped self-standing diamond films were first grown on Si(100) substrates. The substrates were prepared by ultrasonic cleaning in acetone, ethanol, and deionized water, and then seeded by ultrasonication in a detonation-diamond dispersed solution. The substrates were introduced in the HFCVD chamber, and undoped polycrystalline diamond films were synthesized with the following conditions: reactant gases are hydrogen and methane with a flow rate of 60 and 0.3 sccm, respectively. The pressure of the reaction chamber was 200 Torr. The filament temperature measured by a pyrometer was 2300 °C. An average growth rate was approximately 0.4 $\mu\text{m h}^{-1}$. After the synthesis, the undoped diamond layer was removed from the Si substrate by mechanical exfoliation. The typical thickness of the film was 44 μm .

The B-doped polycrystalline diamond layer was grown on the undoped diamond film to serve as a neutron converter. The source gas for B-doped diamond growth was prepared by dissolving trimethyl borate (TMB) in acetone and evaporated at room temperature (RT). The source gas was introduced into the chamber by bubbling using H_2 as a carrier gas. H_2 (100 ccm) was also supplied separately into the chamber to maintain a total pressure of 100 Torr. The B/C ratio in the source gas was calculated to be 1%. B-doped diamond films were grown for 2 h to achieve a typical thickness of 2 μm .

Electrical contacts were formed by vacuum evaporation. The 25 nm-thick aluminum (Al) electrodes were deposited on both undoped and B-doped sides of the detector. After the evaporation, thermal oxidation was conducted at 450 °C in mixed N_2 and O_2 gas (4:1) to passivate the conductive layers on the as-deposited surfaces of the diamond layers.

The fabricated detector was connected to a preamplifier and multi-channel analyzer (MCA) to measure the radiation signal. In α -ray detection, the incident α -ray particle generates electron-hole pairs in the detector. Since the incident energy is as large as MeV order, the excited carriers are extracted as a current pulse. The height of the current pulse is proportional to the incident energy of the radiation. The current pulse is converted to voltage using a T-Z amplifier and counted for each pulse height by the MCA. As a result, the channel-count spectrum is obtained, where the channel number reflects the incident energy of the radiation. Figure 1 shows a typical spectrum obtained by α -ray detection. In this experiment, α -ray from americium-241 (^{241}Am) is used for the input. Since the α -ray particles have an electrical charge, they are repeatedly scattered in the detector to lose its kinetic energy. The scattering process results in a broad Gaussian-like peak in Fig. 1. In neutron detection, thermal and epi-thermal

neutrons are captured in the boron (boron-10), and generate α -ray and Li-7. Detection of the α -ray particle converted from neutron was demonstrated, which will be published elsewhere [2]. We also examined gamma-ray detection using cobalt-60 and cesium-137 for comparison, but these gamma-rays were not detected due to the small capture cross-section of the diamond against gamma-ray.

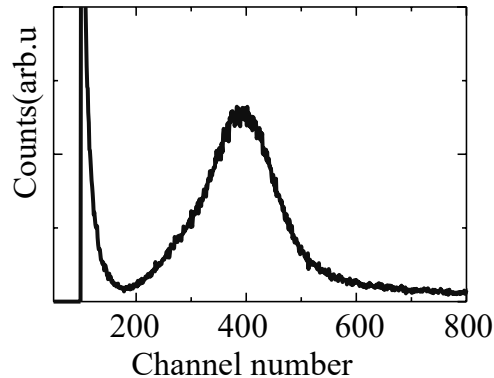


Fig. 1. A typical spectrum obtained for α -ray detection using ^{241}Am as α -ray source

Conclusion

A radiation detector has been fabricated. It consists of undoped polycrystalline diamond film and B-doped built-in neutron converter. The concept of utilizing the B-doped layer as a neutron- α converter, and undoped layer to collect the carriers generated by the α -ray particles, has been demonstrated. The present results suggest that the combination of polycrystalline diamond and a B-doped polycrystalline diamond built-in neutron converter is a viable choice to achieve a large-scale flat-panel detector for neutron imaging, whose application ranges from medical diagnosis to industrial non-destructive inspection.

References

- [1] S. Almaviva, M. Marinelli, E. Milani, G. Prestopino, A. Tucciarine, C. Verona, G. Verona-Rinati, M. Angelone, M. Pillon "Improved performance in synthetic diamond neutron detectors: Application to boron neutron capture therapy", Nuclear Instruments and Methods in Physics Research A, 612, pp.580 – 582 (2010).
- [2] T. Miyake, H. Nakagawa, T. Masuzawa, T. Yamada, T. Nakano, K. Takagi, T. Aoki, H. Mimura, submitted

Numerical solution of the two-dimensional Logunov – Tavkhelidze equation with the sum of two separable potentials in the momentum representation

A. V. PAULENKO, Yu. A. GRISHECHKIN
Francisk Skorina Gomel State University, Gomel, Republic of Belarus

Abstract

A numerical solution of the two-dimensional quasipotential Logunov – Tavkhelidze equation describing the bound states of systems of two identical scalar particles when simulating their interaction by the sum of two separable potentials in the momentum representation is found. The results obtained are illustrated by plots of the dependences of the partial wave functions and the energy of the system on the momentum and the coupling constant, respectively.

Problem Statement

The two-dimensional partial equation for the wave function $\psi_\mu(p)$ describing the bound states of a system of two scalar particles of the same mass m , in the momentum representation, has the following form ($\hbar = c = 1$):

$$\psi_\mu(p) = -\frac{\sqrt{p}}{2\pi} G(E, E_p) \int_0^\infty \sqrt{k} V_\mu(p, k) \frac{m}{E_k} \psi_\mu(k) dk, \quad (1)$$

where $G(E, E_p)$ is the Green's function which for the Logunov – Tavkhelidze equation has the form

$$G(E, E_p) = \frac{1}{E_p^2 - E^2}. \quad (2)$$

In this work, we model the potential in the coordinate representation as a superposition of two δ -potentials:

$$V(\rho) = -\lambda_1 \delta(\rho - a) - \lambda_2 \delta(\rho - b), \quad (3)$$

where $\lambda > 0$, $a > 0$ are the constants. The partial potential in the impulse representation is related to the two-dimensional potential in the coordinate representation $V(\rho)$ by the integral relation [1]:

$$V_\mu(p, k) = 2\pi \int_0^\infty \rho J_\mu(p\rho) V(\rho) J_\mu(k\rho) d\rho, \quad (4)$$

where $J_\mu(z)$ is the Bessel function.

Numerical solution

Substituting (3) into (4) and performing integration, we obtain an expression for the partial potential in the momentum representation

$$V_\mu(p, k) = -\lambda_1 2\pi a J_\mu(pa) J_\mu(ka) - \lambda_2 2\pi b J_\mu(pb) J_\mu(kb). \quad (5)$$

Potential (5) is separable. Substituting (5) into (1), we can transform the integral equation to the following form:

$$\psi_\mu(p) = C_1 \lambda_1 a \sqrt{p} G(E, E_p) J_\mu(pa) + C_2 \lambda_2 b \sqrt{p} G(E, E_p) J_\mu(pb), \quad (6)$$

where the notation is introduced

$$C_1 = \int_0^\infty \sqrt{k} \frac{m}{E_k} J_\mu(ka) \psi_\mu(k) dk, \quad (7)$$

$$C_2 = \int_0^\infty \sqrt{k} \frac{m}{E_k} J_\mu(kb) \psi_\mu(k) dk. \quad (8)$$

To determine the energy spectrum of the two-particle system, we multiply equality (6) by the function $\sqrt{p} m/E_p J_\mu(pa)$ and integrate the resulting expression in the interval $p \in [0; \infty)$. As a result, we obtain the system of equations

$$C_1 = C_1 \lambda_1 a \int_0^\infty p G(E, E_p) J_\mu^2(pa) dp + C_2 \lambda_2 b \int_0^\infty p G(E, E_p) J_\mu(pb) J_\mu(pa) dp, \quad (9)$$

$$C_2 = C_1 \lambda_1 a \int_0^\infty p G(E, E_p) J_\mu(pa) J_\mu(pb) dp + C_2 \lambda_2 b \int_0^\infty p G(E, E_p) J_\mu^2(pb) dp. \quad (10)$$

The solution of this system of equations has the form

$$\frac{\lambda_2 b \int_0^\infty p G(E, E_p) J_\mu(pa) J_\mu(pb) dp}{1 + \lambda_1 a \int_0^\infty p G(E, E_p) J_\mu^2(pa) dp} = \frac{1 + \lambda_2 b \int_0^\infty p G(E, E_p) J_\mu^2(pb) dp}{-\lambda_1 a \int_0^\infty p G(E, E_p) J_\mu(pa) J_\mu(pb) dp}. \quad (11)$$

Based on equation (11), it is possible to determine the required energy spectrum of the two-particle system. The results of the numerical solution of this problem are graphically illustrated in Fig. 1. They show the dependences of the energy of a system of two particles on the parameter λ_2 corresponding to each of the equations of the quasipotential approach under consideration at the particular values of the parameters μ , a and b .

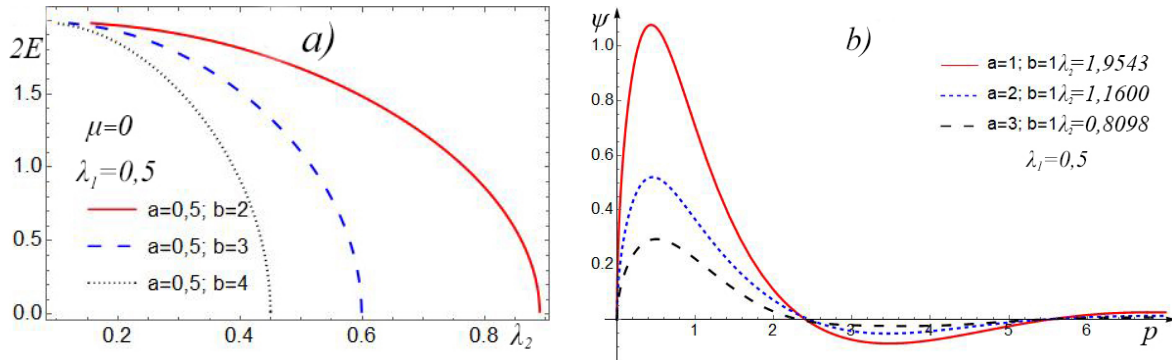


Fig. 1. a) The condition for quantizing the energy of a two-particle system; b) Partial wave functions for various values of system parameters

Conclusion

The numerical solution of the two-dimensional quasipotential equation of Logunov – Tavkhelidze is found, which describes the bound states of systems of two identical scalar particles when modeling their interaction by the sum of two potentials separable in the momentum representation. The results obtained are illustrated by plots of the dependence of the partial wave functions and the energy of the system on the momentum and the coupling constant, respectively. It has been found that when separable potentials are taken into account, there is only one bound state, and the partial wave functions have an infinite number of zeros. Analyzing Fig. 1, b, we found that the growth of the parameter a (for a fixed parameter value b) leads to decrease in the amplitude values of the wave functions.

References

- [1] S. A. Ktitorov., N. E. Firsova “Scattering of electrons in monolayer graphene: a model of a ring-shaped well”, *Solid State Physics*, Vol. 53, No. 2, pp. 384 – 388. (2011).

Spatial resolution of X-ray Imaging using 80 μ m pitch TIBr Detector

K. TOYODA¹, K. TAKAGI³, H. KASE³, T. TAKAGI³, K. TABATA³,
T. TERAO², H. MORII², A. KOIKE², T. AOKI³, M. NOGAMI⁴, K. HITOMI⁴

¹*ANSeeN Inc., Hamamatsu 4328011, Japan; E-mail: toyoda@anseen.com.*

²*ANSeeN Inc., Hamamatsu 4328011, Japan.*

³*Shizuoka University, Hamamatsu 4328011, Japan.*

⁴*Tohoku University, Sendai 9808577, Japan.*

Abstract

This study introduces an X-ray imager that uses TIBr detectors and demonstrates its potential for X-ray imaging applications. Although TIBr detectors are suitable for X-ray imaging applications because of the associated large attenuation coefficients and direct conversion behavior, realizing a flat-panel detector with TIBr involves developing processes. The proposed imager is constructed utilizing a combination of existing technologies; it comprises a plate electrode containing thallium metal to suppress the polarization phenomenon, pixelated silver electrodes with 80 μ m pitch, and a photon-counting-type readout integrated circuit (ROIC) that can work in the hole as well as electron collection modes. The modulation transfer function (MTF) of the imager is calculated based on the imaging results of an X-ray test chart, and the result corresponds to 180 μ m sampling. The measured high-MTF shows the immense potential of TIBr detectors for X-ray imaging applications.

Introduction

Thallium bromide (TIBr) is a compound semiconductor that is attractive for fabricating X- and gamma-ray detectors because of the high atomic numbers and high density. TIBr detectors act as X-ray photoconductors that directly convert X-ray photons into electron-hole pairs. Unlike indirect detectors that convert X-rays into scintillation, the spatial resolution is high, in principle, because there is no light diffusion. A comparison of the spatial resolution of direct/indirect flat panel detectors (FPDs) for commercial off-the-shelf (COTS) products has been published by Datta et al. [1]. Figure 2 in their paper shows that a direct conversion detector has a higher modulation transfer function (MTF) value than indirect detectors (The MTF value of indirect FPDs at 2 lp/mm is around 30 %, and it is 90 % for the direct FPD).

Compared to other semiconductor detectors, the higher efficiency of TIBr detectors above 100 keV [2, 3], and spatial resolution [4] have been verified with large electrodes. However, developing an FPD with TIBr involves more processes, such as fabricating small electrodes pixelated to the limits of the detector geometry [4], designing a readout integrated circuit (ROIC), and stacking. These processes cannot be easily solved. Therefore, this study presents an X-ray imager using TIBr with small electrodes assembled by combining existing technologies.

Structure of the Imager

Semiconductor detectors were fabricated using a grown TIBr crystal. The resulting wafer size was approximately 3.2 mm \times 3.2 mm \times 0.8 mm. A plate electrode was constructed on the 3.2 mm \times 3.2 mm surfaces through vacuum evaporation of the metal containing thallium. The opposite side did not have electrodes before stacking. The readout architecture of the ROIC was designed by our group [5, 6], the transistor-level circuit was designed by Brookman Technology Inc., and it was fabricated using a TSMC 0.13 μ m CMOS process. The stacking

process utilizes silver paste with MONSTER PAC® Core Technology (CONNECTEC JAPAN Corporation, Japan). Figure 1 depicts the stacking of the assembled TlBr imager and the stacked structure.

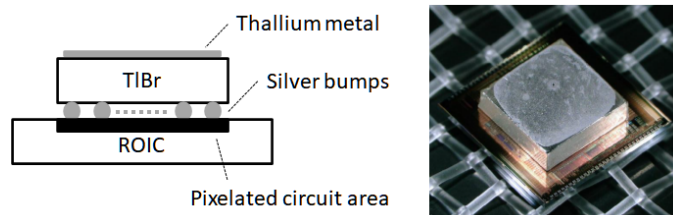


Fig. 1. Structure of the assembled TlBr X-ray imager (left) and the structure after stacking (right)

Experimental Results

X-ray images of larger objects than the detector can be captured by moving the imager, similar to line sensors. Figure 2 depicts the imaging result and the column-averaged line profile of an X-ray test chart that includes various line pairs for calculating the MTF. The MTF of our imager, depicted in Figure 3, is calculated based on the imaging result. The solid line denotes the sinc function corresponding to an MTF of 80 μm sampling without degradation. The cross-marks denote the measured MTF values of the proposed imager. The measured MTF was fitted to 180 μm sampling, denoted by a dashed line. The deviations at high spatial frequencies are due to the fluctuations in the pixel values during measurement. The MTF value at 2 lp/mm is approximately 80 %; which is higher than that of indirect FPDs and close to that of direct FPDs [1]. Thus, a high MTF value was achieved without optimized process development, demonstrating the immense potential of the TlBr detector in X-ray imaging applications.

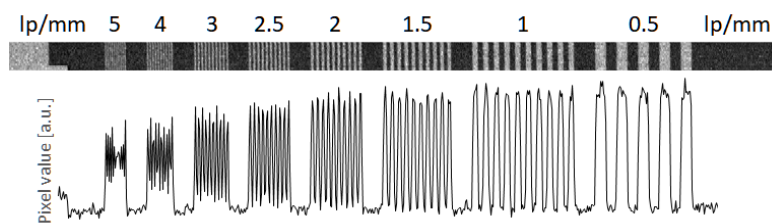


Fig. 2. Imaging result of an X-ray test chart that includes 0.5-5 lp/mm line pairs. The bottom graph shows the averaged line profile

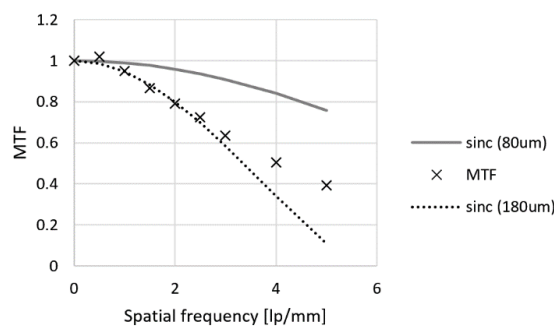


Fig. 3. Calculated MTF based on the X-ray test chart results

Conclusion

This study introduced a method for assembling X-ray imagers using TlBr detectors, and demonstrated its imaging behavior. The measured MTF corresponded to 180 μm sampling, which is a sufficient result considering that the imager was not designed specifically for the TlBr detector.

References

- [1] Datta, A., Zhong, Z., and Motakef, S. "A new generation of direct X-ray detectors for medical and synchrotron imaging applications". *Sci Rep* 10,20097 (2020). <https://doi.org/10.1038/s41598-020-76647-5>
- [2] Hitomi, Keitaro, et al. "Characterization of pixelated TlBr detectors with TI electrodes". *Nuclear Instruments and Methods in Physics Research Section A: Accelerators, Spectrometers, Detectors and Associated Equipment* 747 (2014): 7 – 12.
- [3] Ariño-Estrada, Gerard, et al., "Development of TlBr detectors for PET imaging". *Physics in Medicine & Biology* 63.13 (2018): 13NT04.
- [4] Owens, Alan, et al. "Hard X-ray spectroscopy using a small-format TlBr array". *Nuclear Instruments and Methods in Physics Research Section A: Accelerators, Spectrometers, Detectors and Associated Equipment* 497.2-3 (2003): 359 – 369.
- [5] Takagi, Katsuyuki, et al. "Readout Architecture Based on a Novel Photon-Counting and Energy Integrating processing for X-ray imaging". *IEEE Transactions on Radiation and Plasma Medical Sciences* (2020).
- [6] K. Takagi, et al. "Study of an X-ray/Gamma Ray Photon Counting Circuit Based on Charge Injection". *Sensors and Materials* 30.7 (2018): 1611 – 1616.

Scientific electronic publication

INTER-ACADEMIA 2021

*The 19th International Conference on
Global Research and Education*

(Gomel, Belarus, 20 – 22 October, 2021)

Collection of abstracts

Signed for use on 12.10.2021.

The volume of the publication is 11 MB.

Publisher and printing execution:
Educational institution “Francisk Skorina Gomel State University”
Certificate of state registration of the publisher, manufacturer,
distributor of printed publications No. 3/1452 dated 17.04.2017.
Special permit (license) No. 02330 / 450 dated 18.12.2013.
Sovetskaya str., 104, 246028, Gomel.

<http://www.gsu.by>